Thermomechanically Coupled Processes for Functionally Graded Materials:
Experiments, Modelling, and Finite Element Analysis using High-Order DIRK-Methods

Doctoral Thesis
(Dissertation)

to be awarded the degree

Doctor of Engineering (Dr.-Ing.)

submitted by

Dipl.-Ing. Karsten J. Quint

from München
(place of birth)

approved by the Faculty of
Mathematics/Computer Science and Mechanical Engineering,
Clausthal University of Technology

Date of oral examination
14.10.2011

Für Constanze

Vorwort

Die vorliegende Arbeit enstand im Rahmen des Teilprojektes C1 des Sonderforschungsbereichs SFB/TR TRR 30 "Prozessintegrierte Herstellung funktional gradierter Strukturen auf der Grundlage thermo-mechanisch gekoppelter Phänomene". Die Projektleiter Prof. Dr.-Ing. Stefan Hartmann und Prof. Dr.-Ing. Detlef Kuhl haben wesentlich zum Umfang dieser Arbeit beigetragen.

Meinem Doktorvater Prof. Dr.-Ing. Stefan Hartmann bin ich für seine engagierte Betreuung mit vielen Hinweisen, Anregungen und Korrekturen zu besonderem Dank verpflichtet.

Darüber hinaus haben noch weitere Personen zum Gelingen meiner Arbeit beigetragen: Die vielen Gespräche mit Dipl.-Ing. Ahmad Wahadj-Hamkar über Numerik, insbesondere über die Finite Elemente Methode, waren eine wichtige Grundlage und Inspirationsquelle dieser Arbeit.

Auf dem Gebiet der iterativen Löser für lineare Systeme hat die Zusammenarbeit mit Dr. Jurjen Duintjer Tebbens, Dr. Philipp Birken und Prof. Dr. rer. nat. Andreas Meister mir viel Freude bereitet und den Fortgang meiner Arbeit unterstützt. In diesem Rahmen wurden gemeinsam mit Dr. Philipp Birken, Prof. Dr. rer. nat. Andreas Meister und Dr. Rainer Niekamp auch wichtige Grundlagen zur thermischen Fluid-Struktur-Kopplung mit DIRK-Verfahren erarbeitet.

Experimente mit Rundstahlproben zum induktiven Erwärmen und anschließenden Abkühlen durch freie Konvektion wurden zusammen mit Dr.-Ing. Ursula Weidig und Dr.-Ing. Nicolas Saba durchgeführt. Dipl.-Ing. Günter Linek und Dr.-Ing. Lothar Schreiber bereiteten Prüfkörper vor und führten einachsiale Zug- und Druckexperimente aus. Die Ergebnisse dienten der Parameterbestimmung in dieser Arbeit.

Viele Studenten haben meine Arbeit durch herausfordernde Fragen und ihre eigenen Ideen vorangebracht. Für die wissenschaftlichen Arbeiten von Dipl.-Ing. Ammar Al-Baldawi, Dipl.-Ing. Björn Büchling, Dipl.-Ing. Torben Netz und Dipl.-Ing. Steffen Rothe bin ich sehr dankbar. Zusätzliche Unterstützung haben die studentischen Hilfkräfte Dipl.-Math. Benjamin Badel, Dipl.-Ing. Ehsan Hajyheydari, Dipl.-Ing. Martin Langebach, Dipl.-Ing. Francis Nakam, Dipl.-Ing. Rudolf Neumann, Dipl.-Math. Marouen Ben Said und Dipl.-Ing. Bettina Schröder mit ihrer Arbeit geleistet. Insbesondere Dipl.-Ing. Steffen Rothe war bei seinen zwei wissenschaftlichen Arbeiten und als studentische Hilfskraft sehr engagiert.

Allen Genannten danke ich für die gute Zusammenarbeit und Unterstützung.

<div align="right">Karsten J. Quint</div>

Abstract

Today, a trend towards lightweight components is seen in many industrial fields. Functionally graded products with tailored mechanical properties, load profile adapted geometries, and reduced joining operations can be used to master today's challenges. For three dimensional products an innovative metal forming process, based on a differential thermomechanically coupled process, can be employed. Here, the workpiece is locally heated up to $1200\,^\circ\mathrm{C}$, forged in a hydraulic press, and rapidly cooled down. This leads to different material phases with different mechanical properties.

The complexity and strong interdependency of thermal, mechanical, and metallurgical fields on each other are difficult to predict with standard procedures. To efficiently use this production technique, engineers have to be supported in the process design by simulation tools which account for the new requirements. The purpose of this thesis is to further the understanding and prediction of advanced thermomechanically coupled forming processes. It is part of a twelve year joint research effort, has its main focus on the numerical treatment, and does not yet include metallic phase transformations.

For the low alloy steel used in the forming process (51CrV4) the mechanical and thermal properties were not available. Thus, basic experiments are conducted that characterize some principle features. Based on these results, a thermomechanically consistent material model is developed. It captures the main thermomechanical behavior in monotonous loading. The deformation gradient is multiplicatively decomposed into a thermal, an elastic, and a plastic part. Additionally, relevant material properties are modeled as temperature-dependent quantities.

An accurate prediction of the temperature distribution and the material evolution in time and space plays an important role in the studied processes. The vertical method of lines (semi-discrete approach) is applied using isoparametric finite elements for the spatial discretization. It is shown that this approach leads to a nonlinear differential-algebraic equation system, where the differential part stems from the evolution of the internal variables (describing viscous and plastic material effects) and the time-dependent temperature field. The algebraic part of the system comes from the quasistatic balance of linear momentum. The new point of view allows the consistent application of higher order time integration methods. Stiffly accurate diagonally implicit Runge-Kutta methods (SDIRK-methods) with step size control are applied. To account for the yield condition and to ensure objectivity, the time integration is performed in the reference configuration in combination with a return mapping consisting of an elastic predictor and a plastic corrector. Contrary to popular myth, the numerical results show that high-order methods are suitable for thermomechanically coupled problems, are more efficient than standard

procedures, and allow an error control, respectively a time step adaptivity.

Due to the strong coupling of the intended application and to exploit the advantages of high-order accuracy and time-adaptivity, a monolithic scheme is employed. This results in a large global system of equations, with an unsymmetric iteration matrix. Several approaches are considered to accelerate the solution process. To enhance the quality of the initial iterate a linear extrapolator is proposed. It significantly improves the robustness of the Newton process allowing larger time steps and accelerates the iteration process. Doing so, the number of required iterations can be reduced by one third. At the heart of the Newton process is the solution of the global linear system, which can consume over 80% of the total computation time. Here, different approaches for direct and iterative solvers are studied. If the multilevel-Newton algorithm (MLNA) is used in combination with the chord-method, the tangent is kept constant if possible. This spoils the second order rate of convergence, but reduces the total CPU time by 60% to 85%.

Contents

List of Symbols

Symbol	Description	Page
$\boldsymbol{\lambda}$	Thermal conductivity tensor, cur. configuration	65
λ	Isotropic (or one-dimensional) thermal conductivity	26
Λ	Plastic multiplier	61
μ_0	permeability of vacuum (magnetic constant)	172
μ_r	relative permeability of material	172
ω	Open set of a body in the current configuration	41
$\partial\omega$	Boundary of a body in the current configuration	41
$\partial_q\omega$	Boundary with prescribed heat fluxes	83
$\partial_s\omega$	Boundary with prescribed stresses	81
$\partial_\theta\omega$	Boundary with prescribed temperature	83
$\partial_{\theta q}\omega$	Boundary with prescribed combination of temperatures and heat fluxes	83
$\partial_u\omega$	Boundary with prescribed displacements	81
Ω	Open set of a body in the reference configuration	41
$\overline{\Omega}$	Closed set of body $\overline{\Omega} = \Omega \cup \partial\Omega$, see fn. 4 on p. 81	100
$\partial\Omega$	Boundary of a body in the reference configuration	41
$\partial_q\Omega$	Boundary with prescribed heat fluxes	82
$\partial_s\Omega$	Boundary with prescribed stresses	81
$\partial_\theta\Omega$	Boundary with prescribed temperatures	82
$\partial_{\theta q}\Omega$	Boundary with prescribed combination of temperatures and heat fluxes	82
$\partial_u\Omega$	Boundary with prescribed displacements	81
ψ	Helmholtz free energy	50
π_θ	Weak form of heat conduction	92
π_u	Weak form of moment of momentum	92
ϱ	Density in the current configuration	44
ρ	electrical resistivity of material	172
ϱ_R	Density in the reference configuration	44
σ	Stefan-Boltzmann constant	28
ϑ	Temperature change	57
θ	Absolute temperature	49
$\boldsymbol{\theta}$	Vector of unknown nodal temperatures	98
θ_f	Absolute temperature of surrounding fluid	84
$\boldsymbol{\Theta}_i$	Stage vector of unknown nodal temperatures	115
$\dot{\boldsymbol{\Theta}}_i$	Stage derivatives of unknown nodal temperatures	115
$\boldsymbol{\Theta}_i^S$	Starting vector of unknown nodal temperatures	115
Θ_j	Temperature at node j	96

Symbol	Description	Page
θ_s	Absolute temperature of surface	28
θ_∞	Absolute temperature of surroundings	28
$\boldsymbol{\zeta}_k$	Quadrature point of numerical integration rule	96
$\mathbf{A}$	Almansi strain tensor	39
$\boldsymbol{a}$	Acceleration vector	38
a	Diffusivity	27
$\mathcal{B}$	Material body	32
$\mathbf{B}$	Left Cauchy-Green tensor	36
$\mathbf{B}_\mathrm{i}$	Inelastic left Cauchy-Green tensor	56
$\check{\mathbf{B}}_\theta$	Thermal left Cauchy-Green tensor	57
$\boldsymbol{C}$	Global capacity matrix of FEM discretization	98
c_d	Specific heat capacity	25
$\mathbf{C}$	Right Cauchy-Green tensor	36
$\hat{\mathbf{C}}_\mathrm{e}$	Elastic right Cauchy-Green tensor	57
$\check{\mathbf{C}}_\mathrm{r}$	Reversible right Cauchy-Green tensor	56
$\mathbf{D}$	Strain rate tensor	38
$\mathrm{d}\boldsymbol{A}$	Material surface element in the reference config.	36
$\mathrm{d}\boldsymbol{a}$	Material surface element in the current configuration	36
Div	Divergence operator with respect to material coordinates	39
div	Divergence operator with respect to spatial coordinates	39
$\mathrm{d}V$	Material volume element in the reference configuration	36
$\mathrm{d}v$	Material volume element in the current configuration	36
$\mathrm{d}\boldsymbol{X}$	Material line element in the reference configuration	35
$\mathrm{d}\boldsymbol{x}$	Material line element in the current configuration	35
$\mathbf{E}$	Green strain tensor	39
e	Specific internal energy	47
$\mathbf{e}_\mathbf{g}$	Global discretization error of time integration	113
$\mathbb{E}^3$	Three-dimensional Euclidean space of physical observation	33
$\boldsymbol{E}_\alpha$	Cartesian base vectors in the reference configuration	33
$\boldsymbol{e}_i$	Cartesian base vectors in the current configuration	33
$\mathbf{e}_\mathrm{l}$	Local discretization error of time integration	113
$\mathbf{e}_q$	Error measure of internal variables	126
$\mathbf{e}_\theta$	Error measure of temperatures	126

Symbol	Description	Page
$\mathrm{k}_{\theta\theta,\mathrm{q}}^{e,ab}$	Conductivity element components of nodes a and b	143
$\mathbf{k}_{\theta\theta}^{e}$	Thermal element matrix	145
$\mathrm{k}_{\theta\theta}^{e,ab}$	Thermal element components of nodes a and b	144
$\boldsymbol{K}_{\theta\mathrm{u}}$	Global stiffness matrix, $\boldsymbol{K}_{\theta\mathrm{u}} = \partial\boldsymbol{G}_{\theta}/\partial\boldsymbol{U}$	142
$\mathbf{k}_{\theta\mathrm{u}}^{e}$	Element stiffness matrix	145
$\mathbf{k}_{\theta\mathrm{u}}^{e,ab}$	Element stiffness submatrix of nodes a and b	144
$\boldsymbol{K}_{\mathrm{u}\theta}$	Global stiffness matrix, $\boldsymbol{K}_{\mathrm{u}\theta} = \partial\boldsymbol{G}_{u}/\partial\boldsymbol{\Theta}$	136
$\mathbf{k}_{\mathrm{u}\theta}^{e,ab}$	Element stiffness submatrix of nodes a and b	139
$\boldsymbol{K}_{\mathrm{uu}}$	Global stiffness matrix, $\boldsymbol{K}_{\mathrm{uu}} = \partial\boldsymbol{G}_{u}/\partial\boldsymbol{U}$	136
$\mathbf{k}_{\mathrm{uu}}^{e}$	Element stiffness matrix	138
$\mathbf{k}_{\mathrm{uu}}^{e,ab}$	Element stiffness submatrix of nodes a and b	138
$\mathbf{k}_{\mathrm{uu,C}}^{e,ab}$	Constitutive element stiffness submatrix	138
$\mathbf{k}_{\mathrm{uu,G}}^{e,ab}$	Geometric element stiffness submatrix	137
$\mathbf{L}$	Spatial velocity gradient	38
L	Power of external forces	47
$\mathbf{L}_{\mathrm{i}}$	Inelastic spatial velocity gradient	56
$\mathbf{L}_{\theta\mathrm{i}}$	Thermal-inelastic spatial velocity gradient	57
$\boldsymbol{n}_{\mathrm{R}}$	Unit normal vector in the reference configuration	42
$\boldsymbol{n}$	Unit normal vector in the current configuration	42
$\hat{N}_i$	Global shape function of ith global node	95
N_a	Element shape function of ath element node	100
n_{el}	Number of finite elements of given mesh	100
n_{eq}	Number of equations	115
n_{ip}	Number of integration points	106
n_{en}	Number of nodes of element	101
n_{nod}	Number of nodes of given mesh	95
n_{q}	Number of internal variables of complete structure	98
$n_{\mathrm{n}\theta}$	Number of nodes with unknown temperature	95
n_{nu}	Number of nodes with unknown displacement	95
$n_{\mathrm{p}\theta}$	Number of prescribed temperature values	98
n_{pu}	Number of prescribed displacement values	99
$\check{\mathbf{P}}$	Mandel stress tensor in inelastic configuration	60
$\mathcal{P}$	Material point or particle	32
p	Plastic arc length (equivalent or effective inelastic strain)	61
p_{d}	Dissipative part of plastic arc length	61
p_{s}	Energy storing part of plastic arc length	59

Symbol	Description	Page
Q	Resultant heat supply	47
$\boldsymbol{q}$	Vector of internal variables of complete body	98
q	Cauchy heat flux vector	47
$\mathbf{q}$	Vector of internal variables at a material point	64
$\overline{q}_{\text{con}}$	Convective heat flux	83
$\boldsymbol{Q}_i$	Stage vector of internal variables	123
$\boldsymbol{Q}_i^{\text{S}}$	Starting vector of internal variables	123
$\boldsymbol{q}_{\text{R}}$	Piola-Kirchhoff heat flux vector	48
$\overline{q}_{\text{rad}}$	Radiative heat flux	84
$\mathbf{R}$	Rotation tensor of polar composition of $\mathbf{F}$	36
R	Change of yield stress due to isotropic hardening	60
$\mathcal{R}$	Reference configuration of material body	33
r	Thermal energy production due to radiation or internal processes	47
$\mathbb{R}$	Set of real numbers	32
$\boldsymbol{R}_{\text{e}}$	Equivalent external force vector	134
$\boldsymbol{R}_{\text{i}}$	Equivalent internal force vector	134
S	Entropy of material body	49
s	Specific entropy	49
$\mathcal{S}_{\theta,t}$	Set of temperature trial functions	87
$\mathcal{S}_{\theta,t}^h$	Finite-dimensional set of temperature trial functions	94
$\check{\mathbf{S}}$	Stress tensor in inelastic configuration	57
$\hat{\mathbf{S}}$	Stress tensor in thermal configuration	57
$\boldsymbol{S}_{u,t}$	Set of displacement trial functions	87
$\boldsymbol{S}_{u,t}^h$	Finite-dimensional set of displacement trial functions	95
$\mathbf{T}$	Cauchy stress tensor	45
$\boldsymbol{t}$	Cauchy stress vector	45
t	Time	32
$\text{tol}_{\boldsymbol{G}}$	Newton error tolerance of residual	191
$\text{tol}_{\boldsymbol{Q}}$	Newton error tolerance of internal variables	191
$\text{tol}_{\boldsymbol{V}}$	Newton error tolerance of global variables	191
$\mathbf{T}_{\text{R}}$	First Piola-Kirchhoff stress tensor	45
$\tilde{\mathbf{T}}$	Second Piola-Kirchhoff stress tensor	48
$\boldsymbol{t}_{\text{R}}$	First Piola-Kirchhoff stress vector	45
$\mathbf{U}$	Right stretch tensor	36
$\boldsymbol{u}$	Displacement of material point	34

Symbol	Description	Page
$\boldsymbol{u}$	Vector of unknown nodal displacements	98
$\boldsymbol{U}_i$	Stage vector of unknown nodal displacements	123
$\dot{\boldsymbol{U}}_i$	Stage derivatives of unknown nodal displacements	123
$\boldsymbol{U}_i^{\mathrm{S}}$	Starting vector of unknown nodal displacements	123
$\mathbf{u}_j$	Displacement at node j	96
V	Left stretch tensor	36
$\boldsymbol{v}$	Velocity vector	37
$\mathcal{V}_\theta$	Set of temperature test functions, variations	87
$\mathcal{V}_\theta^h$	Finite-dimensional set of temperature test functions, variations	94
$\boldsymbol{\mathcal{V}}_u$	Set of displacement test functions, variations	87
$\boldsymbol{\mathcal{V}}_u^h$	Finite-dimensional set of displacement test functions, variations	95
W	Spin or vorticity tensor	38
w	Thermal energy production due to internal processes	67
w_{e}	Thermoelastic stress power	67
w_{p}	Plastic stress power	67
w_{s}	Stress power due to a change of internal variables	67
BiCGSTAB	Biconjugate gradient stabilized method	152
CMLNA	Chord-Multilevel-Newton algorithm	147
CSC	Compressed sparse column storage format	139
CSE	Computational science and engineering	3
CSR	Compressed sparse row storage format	139
DAE	Differential-algebraic equations	99
dG	Discontinous Galerkin time integration method	108
DIRK	Diagonally implicit Runge-Kutta methods	115
DSC	Differential scanning calorimetry	25
FEM	Finite element method	94
GMRES	Generalized minimal residual method	152
IBVP	Initial boundary value problem	79
ILUT	Incomplete LU factorization with threshold	154
ILU	Incomplete LU factorization	154
IR	infrared	27
IVP	Initial value problem	109
LFA	Laser flash apparatus	27
MLNA	Multilevel-Newton algorithm	129

Symbol	Description	Page
MOL	Method of lines	91
ODE	Ordinary differential equations	7
PDE	Partial differential equations	84
POM	Polyoxymethylene	193
PSE	Problem-solving environments	3
RK	Runge-Kutta methods	108
SSOR	Symmetric successive overrelaxation	13

1. Introduction

Today, a trend towards lightweight components is seen in many industrial fields, particularly in the automotive industry. Tailoring of mechanical properties, load profile adapted geometries, and reduction of joining operations are employed to master today's environmental and economical challenges.

An encouraging approach to achieve these objectives are functionally graded products, cf. [Koizumi, 1997] and [Miyamoto, 1999]. However, state-of-the-art processes are either limited to two-dimensional products, such as metal sheets (see e.g. [Tušek et al., 2001] and [Ryabkov et al., 2008]), or are restricted to academic studies. Up to now, three-dimensional products are based on powder metallurgy or metal casting techniques, cf. [Kieback et al., 2003]. These concepts allow only simple gradients and are difficult to process due to extremely differing flow resistance and formability, see for instance [Raßbach and Lehnert, 2000]. Thus, labor-intensity and cost-ineffectiveness limit their use in commercial production. This deficiency is overcome by a promising and highly innovative process, which is based on a differential thermomechanically coupled process. To efficiently use this production technique in large scale, engineers have to be supported in the process design by a problem-solving environment, a simulation tool which accounts for the requirements specific to the new process.

1.1. Significance of Thermomechanical Processes

A coupled process is characterized by two or more fields which affect each other. In various engineering applications mechanical parts are subjected to a combination of thermal and mechanical loads. Well-known examples are power piping, blades of gas turbines, and automotive parts such as pistons, combustion chambers, and exhaust systems.

While thermomechanical loads are common conditions in daily action of many technical devices, thermomechanical coupling also occurs during many production processes, [Altan, 1998]. In this context the coupling yields several advantages; in the case of warm forging these are for example a decreased yield strength (thus reduced forming forces), an increased ductility (allowing more complex shapes), an increased tool life time, a reduction of pores, and a reduction of chemical inhomogeneities (due to increased diffusion), [Altan et al., 2004, p. 233]. In particular in advanced metal forming applications such as press hardening, cf. [Nicolas, 2005] and [Maikranz-Valentin et al., 2008], the mutual effects of thermal, mechanical, and metallurgical fields on each other are harnessed.

The aforementioned thermomechanical process was recently proposed in [Steinhoff et al., 2005]. It is another example with an extraordinary complex interaction of different mechanisms and received considerable scientific and industrial attention, [Steinhoff et al., 2009]. The innovative approach combines the possibilities of thermomechanical coupling to obtain bulk steel products with tailored properties. In contrast to conventional integral thermomechanical processing, a highly heterogeneous temperature profile is imposed on the workpieces. This new differential thermomechanical process allows the generation of workpieces with functionally graded mechanical properties as demonstrated in [Weidig et al., 2008]. Further characteristics are a three-dimensional geometry, a thermally controlled material flow, and a three-dimensional gradation due to local microstructural transformations. The procedure, which is described in detail in [Weidig et al., 2009], is shown for the demonstrator "shaft with flange". This demonstrator resembles an example of typical products in engineering such as pistons in pumps and hydraulic systems, gearbox shafts, cam shafts, and eccentric shafts. The procedure

(a) Heating

(b) Transfer and positioning

(c) Open die forming

(d) Closed die forming
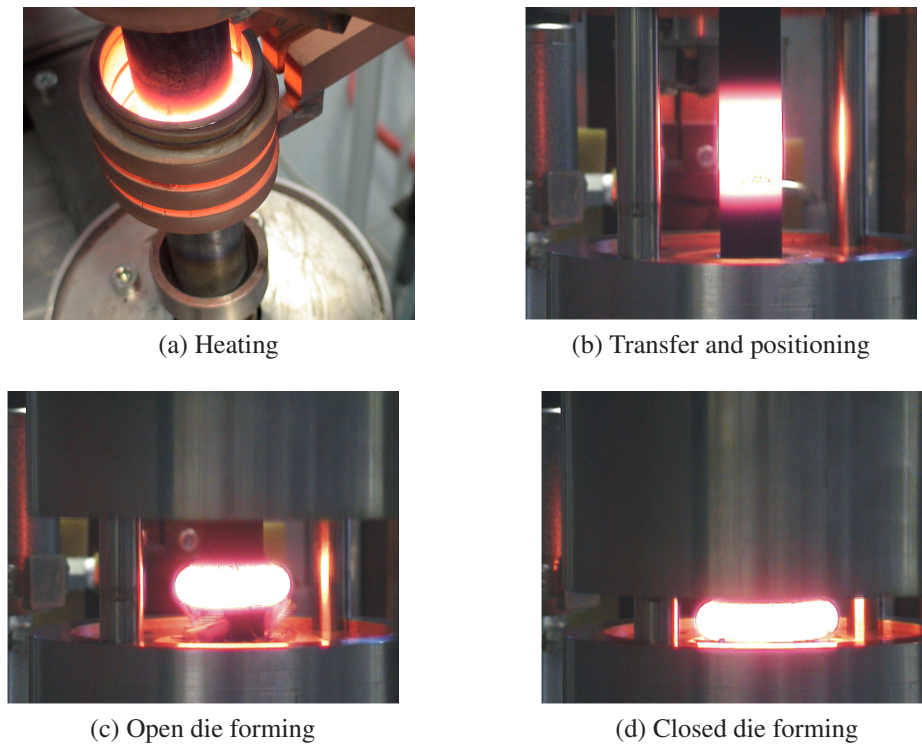
Figure 1.1.: Thermomechanically coupled forming process

consists of four sequential steps. In the first step, Fig. 1.1a, the induction facility heats the workpiece locally (in the center) up to a temperature of 1200 °C. The resulting temperature profile varies strongly in axial direction. Subsequently, the electro-pneumatic transfer unit, Fig. 1.1b, pulls the workpiece upward and positions it automatically in a forging die. Transfer and positioning take approximately 4 s. Immediately commences

the forging process with the hydraulic press (capacity of 1000 kN). During the first stage, Fig. 1.1c, open die forming takes place and the workpiece exchanges heat with its surroundings by free convection and radiation. In the following, the forming dies come into contact and closed die forming sets in, Fig. 1.1d. The contact is the driving force for an increased heat exchange by contact cooling. The final product, Fig. 1.2, shows different material phases (metallic), which are associated with different mechanical properties.
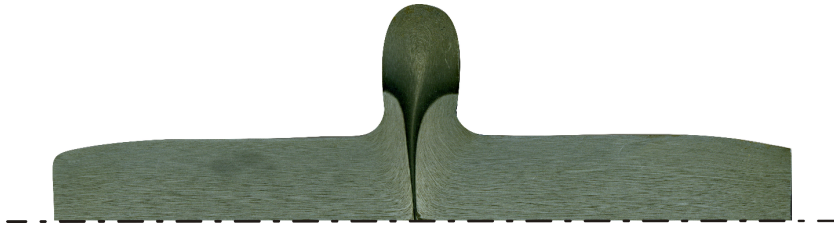
Figure 1.2.: Cut of final workpiece (rotated by $90°$)

1.2. Computational Science and Engineering

During the illustrated manufacturing process, several physical and chemical processes simultaneously take place on various length and time scales. The complexity of these processes renders classical engineering patterns consisting of empirical design-build-test cycles impracticable and uneconomic. The strong dependencies between manufacturing technologies and parameters on one side and final component properties on the other side require new engineering methods. An iterated design-mesh-analyze paradigm on the grounds of physics-based computational tools is on the cusp of superseding the classical engineering patterns and promises several general advantages, [Oden, 2002; Post, 2009]. In particular for the new thermomechanically coupled manufacturing process it seems mandatory. Its application is needed to gain a complete understanding of the interaction of the single processes and for the design of specific workpieces with tailored properties. Despite early suspicion even from highly respected researchers such as Truesdell [1984], computational science and engineering (CSE) is a rapidly growing area and is now regarded as an equal partner along with experiment and theory. CSE is a multidisciplinary area where three domains intersect, namely applied mathematics, computer science and engineering/science. Its main business is the development of problem-solving environments (PSE), [Gallopoulos et al., 1994]. According to [Gallopoulos, 1997], the process in CSE and of a particular PSE can be viewed as concentric layers as depicted in Fig. 1.3.

The success of the CSE methodology depends on its performance regarding computation time and first of all on its reliability. With an exponential growth in computing capability (with respect to floating-point operations), the first aspect seems at first sight
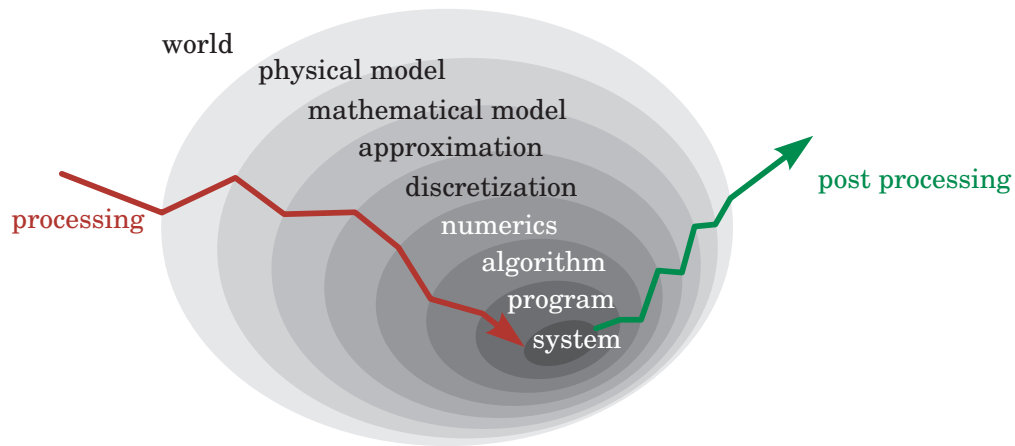
Figure 1.3.: Computational science and engineering as concentric layers, according to [Gallopoulos, 1997]

secondary. Nevertheless, successful PSEs can have as much economic impact as higher performance hardware, [Gallopoulos et al., 1994]. In fact, during the last four decades the improvement in performance for scientific computing problems derived from computational methods has been of the same order as the improvement derived from supercomputer hardware, [Schäfer, 2006, p. 6]. Thus, an investment in numerical methods gives a good return and should not be disregarded. Furthermore, numerical methods and software have to be continuously adapted to new trends in computer technology. Otherwise improvements in computer hardware remain ineffectual.

As mentioned before, another important issue for PSEs is reliability of the numerical results. Apparently, there are many simplifications and abstractions involved in the CSE approach, which are a source of potential errors. However, high reliability is crucial for the successful application of PSEs and in the engineering decision making process, [Szabó and Babuška, 1991, Chp. 1]. Unfortunately, it can be difficult and costly to achieve, which is the reason why it is sometimes neglected by PSE builders, [Gallopoulos et al., 1994]. Reliability of computer predictions is the subject of validation and verification, as described in [Babuška and Oden, 2004]. In this context, validation refers to the quality of the physical respectively mathematical model. The quality of the numerical treatment of the particular model (including the implementation on a specific computer hardware) is assessed by verification. To assess the accuracy and validity of computer predictions severe tests have to be done. However, these can only corroborate a model and its implementation. A model can never be validated; it can only be invalidated. The same assertion is true for verification, see [Babuška and Oden, 2004].

1.3. Literature Review

Today the finite element method is used with great success to solve many engineering problems. During the four stages of the thermomechanically coupled production process, shown in Fig. 1.1a - 1.1d, different physical processes take place and pose various challenges for the numerical solution.

The heating stage is mainly governed by pure heat conduction. During the transfer and positioning stage heat conduction with superimposed strong heat transfer to the surroundings determines the temperature profile of the workpiece. The regions of high temperature show fully coupled thermomechanical behavior during the open die forming stage. Other regions of the workpiece are still at room temperature and are dominated by a pure mechanical problem. The behavior in the final stage of closed die forming is dominated by the contact of the workpiece and the tool. This has an impact on the mechanical and thermal problem.

In this work the emphasis is put on the numerical treatment of the pure heat conduction problem, the pure mechanical problem, and finally the fully coupled thermomechanical problem. In all these numerical solution methods emanates a huge sequence of linear systems of equations with special properties.

1.3.1. Heat Conduction Problem

In the induction facility the workpiece is heated locally which results in a temperature profile. It is the cause of pure heat conduction within the workpiece. The heat conduction problem does not seem to be problematic, at least at first sight. It is one topic of many introductory books on the finite element method such as [Becker et al., 1981; Hughes, 2000; Zienkiewicz and Taylor, 2005]. Moreover, even books that have a focus on heat transfer, such as [Lewis et al., 1996] and [Reddy and Gartling, 2000], mention only some minor problems in connection with time integration. Nevertheless the heat conduction problem does pose some unresolved problems. In particular spatial and temporal oscillations can be observed.

In [Damjanić and Owen, 1982] temporal oscillations were found when using the Crank-Nicolson method. Further, spatial oscillations for a low diffusivity parameter were observed at the initial stages of the transient response. Already Fujii [1973] concluded that the spatial oscillations at the initial stages are due to a violation of a discrete maximum principle. To satisfy this discrete maximum principle too small time steps have to be avoided in the semi-discrete Galerkin method. This was further investigated in [Rank et al., 1983], were it is shown that small time steps do not improve the accuracy, but lead to physically unreasonable results. To avoid the loss of accuracy, a minimum time step criterion is derived. Also Thomas and Zhou [1997] and Yang and Gu [2005] investigate the effect of time step size on the accuracy of time integration, in particular with regard to the minimum time step criterion. Kujawski and Wiberg [1987] investigated a different class of time integration methods. They developed a generalized

least-squares time finite element procedure which leads to a four parameter and two time level family of schemes. They investigate accuracy, stability, and oscillatory behavior of the algorithm. Faragó and Horváth [2007] discuss qualitatively adequate numerical methods for linear parabolic problems. They derive lower and upper bounds for time step sizes of the θ-method. Unphysical oscillations can be avoided with the derived time step bounds, but at the same time the attainable accuracy of the time integration is limited by this step size.

Higher-order time integration schemes as described in [Hairer et al., 2000] and [Hairer et al., 2002] have gained attention in connection with the solution of heat conduction problems. Fung [2001] develops a third order accurate A-stable time integration method using the θ-method and two substeps with complex-valued weighting coefficients. Mancuso et al. [2000] apply a continuous Galerkin formulation for the time integration of linear heat conduction problems and obtain A-stable integration schemes of higher-order. Lang and Verwer [2001] develop a third order accurate Rosenbrock (linear-implicit) solver for nonlinear parabolic problems. Loureiro and Mansur [2009] use singly diagonally implicit Runge-Kutta (SDIRK) methods to compute a numerical Green's function matrix for the solution of linear heat conduction problems. In the recent study of Hansen and Ostermann [2010] SDIRK schemes are compared with a backward difference formula of order two (BDF2). For a simple model problem the authors find that the second order SDIRK method yields better accuracy than the BDF2 method and is a good compromise between accuracy and computational effort. In particular, the SDIRK method is in favor in comparison with the backward Euler method.

Often the rate of convergence is derived analytically and is either not tested at all or asserted only in simple test problems, in many cases just one-dimensional. However, from a practical point of view, the ratio of total computation time and numerical accuracy is more important than the theoretical rate of convergence. Also time adaptivity has rarely been studied so far, cf. [Eriksson and Johnson, 1991] and [Eriksson and Johnson, 1995]. Further, the influence of material parameters on the solution and requirements of the material model have not been discussed.

1.3.2. Mechanical Problem

During the forming process the workpiece is plastically deformed. The regions of the workpiece which are at a moderate temperature can be described by an isothermal mechanical problem, whose solution procedure also forms the basis for the fully coupled thermomechanical procedure. To solve the mechanical problem with the finite element method it is necessary to specify a material model. This model is given by so-called constitutive equations which have to be solved along with the balance equations of continuum mechanics. Process, i.e. history-dependent behavior such as metal plasticity is commonly described by material models of evolutionary type, [Dunne and Petrinic, 2005]. In this case the stresses are given by an elasticity relation which in addition to the total strain depends on internal variables. These account for the inelastic effects and

evolve according to ordinary differential equations known as evolution equations which are referred to as flow rules in the case of metal plasticity. The flow rules are governed by additional internal variables, commonly divided into kinematic and isotropic hardening. These variables specify the form and size of the yield surface, which divides the space of stress into an elastic and inelastic region. Nonlinear kinematic hardening in the small strain range is mainly modeled by Armstrong & Frederick-type models where the linear kinematic hardening is modified such that a saturation state is reached, see [Armstrong and Frederick, 1966].

The most popular solution scheme within the realm of implicit finite element computations is the radial return method also known as the elastic predictor and plastic corrector scheme. Algorithms on this basis use a backward Euler like or exponential-type time integration method. For specific material equations it is often possible to construct problem-adapted stress algorithms, which are superior to the standard procedure. Examples and further references in the small strain regime can be found in [Auricchio and Taylor, 1995; Hartmann and Haupt, 1993; Hartmann et al., 1997].

In the case of finite deformations different approaches, based on the multiplicative decomposition of the deformation gradient, have been proposed to achieve nonlinear kinematic hardening behavior [Dettmer and Reese, 2004; Lämmer, 1998; Lion, 2000; Svendsen et al., 1998; Tsakmakis, 1996; Tsakmakis and Willuweit, 2004]. Similar approaches as in the small strain regime are used for the numerical solution. Additionally, in [Simo et al., 1985] the necessity to incorporate the constitutive assumption of plastic incompressibility for finite deformations is mentioned and concretized in [Simo and Miehe, 1992]. However, backward Euler like integration steps destroy the assumption of plastic incompressibility. In [Lührs, 1997] an additional scalar variable is introduced in order to take account of the plastic incompressibility condition. Further investigations were done by Tsakmakis and Willuweit [2003] as well as Dettmer and Reese [2004]. On the basis of geometry preserving integration procedures a discussion has been introduced by Helm [2006]. In [Hartmann et al., 2008b] SDIRK methods are used in combination with a local projection to fulfill the plastic incompressibilty condition. Of course, exponential mapping algorithms are implicitly satisfying the side-condition, see [Weber and Anand, 1990] and [Vladimirov et al., 2007] for further references.

All these investigations have been done in view of local aspects. The applied time integration procedure for a given deformation is defined on element, i.e. Gauss-point level. A similar "local" approach in the framework of elastoplasticity, where the yield condition has to be fulfilled (algebraic constraint) during the evolution of the internal variables given by ordinary differential equations (ODE), is interpreted as a system of differential-algebraic equations (DAE), see [Büttner and Simeon, 2002; Kirchner and Simeon, 1999]. The differential part consists of the system of ODEs given by the evolution equations (flow and hardening rules) and the algebraic part comes from the yield condition.

A different interpretation of nonlinear (implicit) finite elements, in conjunction with constitutive models of rate-type, has been proposed by Ellsiepen and Hartmann [2001].

This interpretation goes back to the investigations of Fritzen [1997]; Fritzen and Wittekindt [1997]. There, the method of vertical lines leads, after the spatial discretization using finite elements, to a system of DAEs. The algebraic part results from both the discretized weak formulation (equilibrium conditions) and the yield conditions which are currently "active". The differential part is given by the ODEs stemming from the evolution equations of the internal variables. The entire DAE-system is solved by means of stiffly accurate diagonally-implicit Runge-Kutta methods (DIRK, see, for example, [Hairer et al., 2002]) in combination with the Multilevel-Newton algorithm (MLNA, see [Rabbat et al., 1979]) having the advantage of obtaining the classical structure of implicit finite elements. This is presented in more detail by Hartmann [2005], where the method leads in a straightforward way to local and global iterations. Furthermore, the so-called consistent tangent operator is embedded in a natural manner.

The application in [Ellsiepen and Hartmann, 2001] is curbed to small strain elasto-plasticity. In [Hartmann, 2002] this is extended to finite strain viscoelasticity and in [Hartmann and Bier, 2008] to a problem of pressure-dependent finite strain elasto- and viscoplasticity. This "global" interpretation of finite elements applied to constitutive models of evolutionary-type, however, using different integration algorithms, can be found in [Eckert et al., 2004; Hartmann and Hamkar, 2010; Hartmann and Wensch, 2007], where on the global DAE-system BDF or Rosenbrock-type methods are applied.

In [Hartmann, 2002] and [Hartmann, 2006a] the expected order of the applied higher-order DIRK methods are sustained which is demonstrated in numerical examples. The constitutive models are formulated as smooth functions, i.e. there are no case distinctions as in yield function based models. In [Ellsiepen and Hartmann, 2001] it was shown that an order reduction is visible in small strain elastoplasticity. In [Hartmann and Bier, 2008] this is numerically observed in a more complex finite strain yield function based model. The reason of this phenomenon is still an open issue, see also [Büttner and Simeon, 2002]. In [Hartmann et al., 2008a] the concept of the global formulation using stiffly accurate DIRK-methods combined with the MLNA is extended and used with a constitutive model of finite strain elasto- and viscoplasticity with several multiplicative decompositions of the deformation gradient. In particular the influence of time-adaptivity and incompressibility is studied including a geometry preserving algorithm in the sense of a projection method, see e.g. [Hairer et al., 2002]. Nevertheless, even with this approach the order reduction phenomenon remains an unresolved issue.

1.3.3. Thermomechanical Problem

The middle section of the workpiece is heated up to $1200\,^\circ$C and shows fully coupled thermomechanical behavior. Thermomechanical coupling is a classical multifield problem, which can be solved by various approaches depending on the degree of coupling, cf. [Schrefler, 2004] and [Kuhl, 2004a, p. 24]. In many cases the influence of one field

on the other can be neglected.[1] A prominent example is negligible heat production due to small deformations. This leads to a one-way coupled problem which can be solved by two single field solvers. Snydera and Bathe [1981] for example simulate thermoelastic-plastic deformations using the α-method, where the transient temperature distribution is known a priori and used in the mechanical computation. Another example with a negligible influence on the thermal field is considered by Kuhl [2004b]; Kuhl et al. [2002]. There, the internal dissipation caused by elasto-plastic deformations of a rocket combustion chamber can be neglected.

Partitioned approaches allow a stronger coupling between the fields, cf. [Felippa and Park, 1980]. In this case the fields are computationally treated as isolated entities, which are separately advanced in time (possibly with different time step sizes). The interaction effects are viewed as forcing effects that are communicated between the components. These approaches are suitable when there is only a small number of fields, which are weakly coupled. In particular for surface coupling, they can lead to very efficient solution schemes. For a more recent review see [Felippa et al., 2001]. Today, the so-called staggered solution procedure is the most commonly used approach for thermomechanical analysis. At each time step data is exchanged between the thermal and mechanical solution procedure, [Perić and Owen, 2004]. Advantages are a relatively simple implementation (code reusability) and the application of independent (optimal) spatial grids for each subproblem, see for example [Rieger, 2002].

An early application is presented in [Argyris et al., 1981], where the staggered solution is used for thermal-heat conduction and elastic-viscoplastic response behavior using finite elements with fully implicit time integrators for both fields. For each time step the mechanical response is linearly extrapolated and used to determine the mechanical heat production. Hereby, the thermal field can be computed. Subsequently, the mechanical response at the current time is computed. However, an iterative correction of the mechanical heat production for the thermal analysis is not applied.

The method has been extensively used by many authors. Metal forming of massive three-dimensional parts are considered for example in [Adam and Ponthot, 2003, 2005; Čanađija and Brnić, 2004; Hakansson et al., 2005] using the backward Euler method in combination with the radial return algorithm. In [Münch, 1989] effects of phase change are additionally handled. An application of the staggered approach to sheet metal forming using small strain theory is presented in [Xing and Makinouchi, 2002]. There the backward Euler method is used for the mechanical field and the trapezoidal rule is applied to the thermal differential equations. The authors suggest different coupling schemes depending on the boundary conditions. A similar solution is presented in [Bergman and Oldenburg, 2004], where the authors use the forward Euler method for the heat equation and the effective-stress-function algorithm, developed in [Kojić and Bathe, 1987], for the mechanical subproblem. See also [Burkhardt, 2008], where the method is

---

[1] Criteria for thermomechanical analysis are given e.g. in [Münch, 1989, p. 39] and the references cited therein.

applied to simulate the press hardening process of body parts in the automotive industry.

A similar approach based on the operator-splitting methodology is proposed in [Simo and Miehe, 1992] and has been applied e.g. in [Miehe, 1993, 1995, 1996]. A product formula algorithm is constructed via an operator split of the nonlinear thermodynamical problem and results in a two-step solution procedure with an isothermal split. Both, the mechanical and thermal subproblem require the integration of the local evolution equations. However, the algorithm is only conditionally stable and first order accurate, independent of the underlying methods applied to each subproblem. Further disadvantages are a mesh dependence of the solution and the subproblems constitute ill-posed problems, [Simo, 1998]. Adiabatic splitting, proposed by Armero and Simo [1992, 1993], resolves the problem of conditional stability. The unconditionally stable algorithm employs also two steps. It starts with an isentropic step, in which the total entropy is held constant, followed by a heat conduction step (with nonlinear source) at fixed configuration. Agelet de Saracibar et al. [1999, 2001] extended the adiabatic split to coupled thermoplastic problems with phase-change. A recent application of operator splitting using different time integrators and steps in each subproblem is presented in [Kassiotis et al., 2009]. There, the adequate choice of time steps leads to a significant speed up of the computation.

General drawbacks of staggered procedures are higher computational costs due to coupling iterations for volume coupling, a degradation of accuracy, and possibly a degradation of time-stepping stability caused by prediction. The most natural approach to multifield problems are direct methods, so-called monolithic or simultaneous procedures. These do not have the aforementioned problems but often lead to higher computational costs due to unsymmetric iteration matrices. In spite of their good stability properties, they are rarely used in thermomechanical analysis. In [Fritsch, 2004; Glaser, 1992; Parisch, 2003] the monolithic approach is used with the backward Euler method for the time integration in combination with the radial return method for large strain plasticity problems coupled with linear heat conduction. Miehe [1988, p. 167] compares the simultaneous and staggered approach for a two-dimensional large strain thermoelastic problem. Even though the staggered approach needs a multiple of global iterations, it is faster than the simultaneous scheme. However, in the thermoelastic case there are no local iterations. The effort of the local iterations depends on the complexity of the material model and can also have a large impact on the total computation time. Up to now the DAE interpretation developed for implicit finite element analysis of quasistatic mechanical problems has not been extended to the thermomechanically coupled setting. The general structure of such an approach is already outlined in [Quint and Hartmann, 2009] but not given in detail. Furthermore, higher-order time integration methods have not been used for thermomechanically coupled problems, neither for the monolithic nor the staggered approach. Even though a modified expression of the staggered approach is given by Simo [1998, p. 459], no results have been reported. The expression turns the staggered approach into a second order accurate scheme.

Another important issue in thermomechanical analysis concerns the material model-

ing. A comprehensive review on small strain viscoplasticity including thermomechanical coupling as well as thermally induced phase changes is given by Chaboche [2008]. Material models for hot working have to account for several physical mechanisms, these include strain rate sensitivity, temperature sensitivity, strain rate and temperature history effects, as well as strain hardening and restoration processes. An example of a classical model for applications in the finite strain regime based on a single scalar internal variable representing isotropic resistance with evolution equations of rate type is given in [Brown et al., 1989]. The model parameters are fit to the data of hot compression experiments and verified in the following. Even though the model is comparatively simple it is capable to predict the response of an independent monotonous test.

More recent approaches for finite deformations are based on a thermodynamic framework and the multiplicative decomposition of the deformation gradient, just as in isothermal finite-strain models. This approach is applied e.g. in [Celigoj, 1998; Glaser, 1992; Ibrahimbegovic and Chorfi, 2002; Jansohn, 1997; Lämmer, 1998; Simo and Miehe, 1992], where a thermoelastic (recoverable) and a plastic intermediate configuration are used. Based on these results a special focus on the mechanical heat dissipation is put in [Hakansson et al., 2005; Helm, 2006]. It is well known that part of the work required to produce plastic deformations is stored as internal energy within the material. The other part is dissipated in the form of heat. The effect is most pronounced for small and moderate plastic deformations; at large plastic strains the ratio of dissipated and plastic deformation energy converges to a value just below one, as already found by Taylor and Quinney [1934]. A mixed kinematic and isotropic hardening model with variable mechanical dissipation is developed in [Hakansson et al., 2005]. Kinematic hardening proved to be important for processes with cyclic mechanical loading, where it leads to a higher temperature rise than isotropic hardening.

On the basis of the multiplicative decomposition of the deformation gradient Lion [2000] describes the deduction of constitutive equations for finite thermoviscoplasticity from nonlinear rheological models. He proposes to use an additional multiplicative split of the deformation gradient for each physical mechanism, i.e. three in the case of thermoviscoplasticity. Due to the increased complexity this formulation is rarely used. Examples are [Ganapathysubramanian and Zabaras, 2002; Srikanth and Zabaras, 1999], where the deformation gradient is decomposed into an elastic, a plastic, and a thermal part (in that order). An alternative multiplicative decomposition of the deformation gradient into a rotational, an elastic, a thermal, and a plastic part for anisotropic material undergoing thermomechanical deformations is proposed in [Huétink, 2006]. Even though successfully used in many applications, there is also criticism on the concept of intermediate configurations. Bertram [2003] mentions several shortcomings such as the lack of a unified format for isotropic and anisotropic modeling, and the missing uniqueness of the split (arbitrary rotations of unloaded placements are possible), among others. He suggests to use a theory based on isomorphisms instead, which does not rely on the notions of unloading, intermediate configurations, and plastic strain.

Metallic phase transformations (solid ↔ solid) and their interaction with the mechan-

ical behavior are crucial for the innovative forming process. On the basis of ordinary differential equations Hömberg [1995, 1996]; Visintin [1987] describe the evolution of different metallic phase fractions due to a prescribed temperature history. A comprehensive review of such and other models for phase transformations is given in [Böhm et al., 2003]. Applications to specific steels are studied e.g. in [Surm et al., 2008, 2004]. The coupled thermoplastic problem with phase transformation (fluid ↔ solid) is considered e.g. in [Agelet de Saracibar et al., 2001]. There, a small strain formulation is chosen and solidification processes are considered. Several solid-solid phase transformations and the interaction with the mechanical field is studied in [Pietzsch et al., 2007; Simsir and Gür, 2008]. There, a small strain formulation and constant material parameters are chosen. A linear temperature dependence of the elastic properties is added by Mahnken et al. [2009]. There, however, only two phases are taken into account for a low alloy steel. The model is later extended to large deformations in [Mahnken and Schneidt, 2010]. A more fundamental approach is given by [Wolff et al., 2008]. There the material properties depend on the ratio of the phase fractions (using mixture rules) and the interaction of plasticity, transformation induced plasticity (TRIP) and phase transformations is included. However, a thermodynamically consistent material model including all relevant phase transformations for large deformations is not yet available.

1.3.4. Solution of Linear Systems

Within the DIRK/MLNA approach a sequence of linear systems of equations emanates. For each global Newton-like iteration at each time step a large linear system has to be solved. To this end, direct or iterative solvers can be used. The applied method can have a significant impact on the overall performance of the method. Frequently, it is stated that for smaller linear systems of equations direct solution schemes are superior (see, for an overview in the context of finite elements, [Crisfield, 1986] and [Ferencz and Hughes, 1998]) and iterative solvers seem to be rarely applied in structural mechanics unless memory demands make direct solutions impossible. Both direct and iterative solution techniques have been substantially improved in the recent past. On the one hand, very efficient direct solvers for sparse non-symmetric linear systems can be used within the Multilevel-Newton algorithm, popular examples are SuperLU [Demmel et al., 1999], UMFPACK [Davis and Duff, 1997], and PARDISO [Schenk et al., 1999]. These packages are based on sparse storage schemes so that all redundant information is removed and only inevitable data are stored. However, these methods are limited to a certain size of the linear system and with growing dimensions iterative solvers have to be employed. Krylov-subspace solvers as GMRES [Saad and Schultz, 1986] and BiCGSTAB [van der Vorst, 1992] can be very efficient for large, sparse and non-symmetric matrices, especially if appropriate preconditioning techniques are applied. A thorough overview on iterative solvers with hints on efficient implementation is also given in the textbooks of Golub and van Loan [1996], Saad [2003], and Meister [2008].

There are some publications reporting on iterative solutions in the finite element lit-

erature on geometrical and physical nonlinear problems. In [van den Boogaard et al., 2003] iterative solvers are applied to sheet forming processes within explicit and implicit integration schemes for dynamical and inelastic systems. There, conjugate gradient (CG, [Hestenes and Stiefel, 1952]), BiCGSTAB and GMRES solvers with and without symmetric successive overrelaxation (SSOR), incomplete Cholesky (IC), and Jacobi preconditioners are investigated for symmetric systems. Other applications using iterative solvers for symmetric system matrices in finite elements are dealt with in [Saint-Georges et al., 1996], [Augarde et al., 2006], and [Augarde et al., 2007]. Note that these articles address the case of symmetric linear systems only, whereas they sometimes apply methods like GMRES and BiCGSTAB which were designed for the non-symmetric case. In [Neff and Wieners, 2003] a multigrid method is applied to various models of viscoplasticity, whereas a similar approach treats the more smooth problem of porous media in [Wieners et al., 2002, 2005]. The single-grid algorithms are based on the GMRES and BiCGSTAB algorithms. A comparison of several direct and iterative solvers used in conjunction with finite elements can also be found [Wriggers, 2009].

1.4. Scope of Thesis

This thesis addresses central open issues in the development and successful application of a PSE for the new thermomechanically coupled process. These include experiments, modeling, and numerics, with a focus on the latter.

The steel used in the forming processes is 51CrV4 (referred to as SAE6150 in the SAE steel grading system). For this low alloy steel the mechanical and thermal properties were not available. Accordingly, in Chp. 2 basic experiments are conducted that characterize the principle material features and form the basis for the development of a material model. The material model as well as the formulation of the thermomechanical problem are based on the general framework of continuum mechanics. In this regard all relevant fundamentals are summarized in Chp. 3.

On the basis of thermomechanically consistent material modeling a large strain thermoviscoplasticity model for 51CrV4 is developed in Chp. 4. It captures the main thermomechanical behavior in monotonous loading and is a consequent extension of the model developed by Helm [2006]. Following the proposal of Lion [2000], the deformation gradient is multiplicatively decomposed into a thermal, an elastic, and a plastic part, which has not been studied before. Additionally, relevant material properties are modeled as temperature-dependent quantities. Their functional dependence is determined by experimental data, thermodynamic calculations, or approximated on the grounds of physical reasoning. This temperature dependence is missing in the original investigations of Helm [2006]. However, it can lead to significant differences in the total behavior as demonstrated in [Čanađija and Brnić, 2004], where the response of the model of Simo and Miehe [1992] is compared for constant and temperature-dependent parameters. Phase transformations are not yet included, but the model is suitable for an

extension along the lines of [Wolff et al., 2008].

With the material model and the governing equations at hand, the thermomechanical forming process can be computed. To this end, the initial boundary value problem that describes quasistatic large strain thermomechanical processes within solids is derived in Chp. 5. With the numerical treatment in mind, it is formulated in the variational form (also known as weak formulation). This forms the starting point for the application of the method of lines. In this semi-discrete approach time and space are discretized separately. Here, in the first step finite elements are used for the spatial discretization. The approach leads to a nonlinear differential-algebraic equation system, where the evolution equations of the internal variables at the integration points are included in the global formulation. This interpretation has been developed in connection with quasistatic mechanical systems but has not been extended to thermomechanical systems yet. The new point of view allows the consistent application of higher-order time integration methods.

The methodology is in the first step applied to the separate energy balance, which forms the basis for the following developments. Local temperatures play the most important role for the evolution of the metallic phases and strongly influence the current mechanical properties of the workpiece. Thus, an accurate computation of temperatures in space and time is crucial for correct predictions and process designs.[2] To this end, adaptive high-order time integration is investigated. Stiffly accurate diagonally implicit Runge-Kutta methods (SDIRK-methods) with step size control are applied. The derivation follows the ideas in [Ellsiepen and Hartmann, 2001; Hartmann, 2002; Hartmann et al., 2008a], where the methods are applied to purely mechanical problems. The procedure has the advantage that backward Euler based finite element implementations are easily extendable to a high-order DIRK-method. Additionally, the DIRK-method approach is of high-order without extending the number of unknowns and offers a step size control technique (time-adaptivity) with negligible extra work. In the case of the purely thermal problem, it is known that an order reduction occurs for time-dependent boundary conditions. This problem is alleviated by correcting the boundary terms at internal stages in a simple manner. The proposed method, see Sec. 5.5, requires a negligible amount of extra time and works very well for linear and moderately nonlinear functions.

In order to carry over the advantages of high-order accuracy and time-adaptivity to the thermomechanical simulation the monolithic scheme is employed. This results in a large unsymmetric iteration matrix on global level, which consumes a lot of computation time. On the other hand this scheme has several additional advantages in comparison to the staggered approach. The commonly applied isothermal split leads to numerical instabilities when a high degree of coupling is considered as shown by [Simo, 1998, p. 474] and Agelet de Saracibar et al. [1999] (there the coefficient of thermal expansion

---

[2]The energy balance of the workpiece is also strongly influenced by the exchange of heat with the surroundings. A highly resolved numerical treatment of this interaction is not presented here. This can be achieved by considering a thermal fluid-structure interaction problem as investigated by the author and collaborators, see [Birken et al., 2010; Hartmann et al., 2009c].

is varied). The degree of coupling between the mechanical and thermal field increases with the number of material parameters that are temperature-dependent. In particular when phase transformations are included in addition, the coupling intensifies.[3] Furthermore, the staggered approach is an inherently sequential process. It stems from a time when sequential computing was standard and does not profit from the current computer architecture which relies heavily on multicore CPUs.

In this work, the Multilevel-Newton algorithm (MLNA) is applied to the fully coupled problem, where the consitutive equations are solved on the local level and the balance equations on the global level. To deal with the drawback of a large global system several aspects are regarded. A linear extrapolator is proposed in Sec. 5.6 for the acceleration of the Newton process, taking advantage of the information from previous time steps. This considerably reduces the number of iterations and total computation time. Furthermore, a modified version of the MLNA algorithm is used, where the iteration matrix is kept constant for several iterations, which leads to additional savings. All simulations are done with the in-house code Tasafem, a finite element program for time and space adaptive computations, [Hartmann, 2006a]. For this program a new data management using modules has been implemented by the author. It is much more efficient with respect to access times and allows larger models. Secondary, the programming is easier to understand, less error prone, and allows a parallelization, which is done using OpenMP in this work, see e.g. [Chapman et al., 2008]. Build on top of this, an efficient assembly routine for the global iteration (stiffness) matrix is constructed. For the storage of the iteration matrix the compressed sparse row format (CSR) is used, which can be handled by several modern solvers for linear systems. Several direct and iterative solvers are implemented and compared by the author. To further accelerate the computation when using iterative solvers two aspects are investigated, that have not been exploited in the context of finite element computations. Namely, flexible stopping criteria and flexible preconditioning are applied in Sec. 5.7.

Another important issue is verification. In CSE this can be done either by code verification or by solution verification. Both approaches are followed in this work. The code verification is done according to the concepts in [Hunt and Thomas, 2003, p. 224] and [Sommerville, 2007, p. 562]. Here in particular unit, integration, and regression tests are done (mainly by hand).[4] Furthermore, error situations are tested and the consumption of resources (memory, disk space, cpu throughput, etc.) is investigated. The solution verification is based on a posteriori error estimates. To this end, analytical solutions, e.g. [Al-Baldawi, 2008], are compared with the numerical solution as reported in [Rothe, 2010]. In many cases (in most relevant ones) an analytical solution is not at hand. To cope with this lack of information the numerical method itself can be used to

---

[3]The algorithm of the adiabatic split is unconditionally stable but uses a special formulation of the material model which differs from the common one. This requires additionally the local solution of nonlinear equations, cf. [Simo, 1998, p. 474].

[4]In future developments this testing could be automated and standardized as shown in [Hunt and Thomas, 2005] and [Clark, 2006].

approximate the error. In the case of time integration this can be done highly efficiently by using an embedded method as described in Sec. 5.5.

To avoid or at least reduce errors already during the development process the author introduced several innovations. A new error handling is included with automatic compiler based message generation. Subroutines have been written and rewritten in Fortran 95/2003 to make use of compiler based checks (variable types, input and output parameters of subroutines and functions) that are offered by the new standard. An automatic documentation generation is added that generates consistent documentation directly from the source code. For the collaborative work and for the assistance in error finding in the program code (by continuous and repetitive comparison with previous version) a version control system has been installed. The development process is further enhanced (less errors by automatizing) and speed up by a make file based compilation. For the evaluation of computational results several output options and tools have been established, including a customization of the GiD pre- and post-processor from the International Center for Numerical Methods in Engineering (CIMNE). These tools are also used for the numerical examples in Chp. 6.

2. Experimental Observations and Physical Models

Steel 51CrV4 (referred to as SAE6150 in the SAE steel grading system) is the reference material used in all presented thermomechanical experiments.[1] This is a typical heat-treatable low alloy steel used in metal forming applications for products that have to combine high strength and wear resistance including shafts, bevels, pinions, and gear-wheels. A material model with identified material parameters for the steel 51CrV4 is not at hand and is developed in the following chapters.

Prior to formulating a model for any material, experiments should be carried out. These allow to identify the principal features of the material behavior. The information at hand guides the construction of mathematical models, so-called constitutive models, for the real material and is used to identify the material parameters in subsequent chapters.

A close inspection of the physical process taking place on a microscopic scale reveals extremely complicated systems. Including these effects in constitutive models is not feasible for predictions in engineering applications. As explained in Chp. 3 and Chp. 4, radically simplified model assumptions are generally used. Nevertheless, the physical processes on a micro scale (physical model) are described, where appropriate, to give additional hints for the construction of the constitutive model.

All specimens used in the experiments come from the same production batch, thus having only minor sample to sample variations in the chemical composition, [Lambers et al., 2010]. The three main components are C (0.58 to 0.59 wt.%), Cr (0.96 to 0.98 wt.%), and Mn (0.83 to 0.88 wt.%).[2] The phase transformation behavior of 51CrV4 is in this work not yet included. It is studied e.g. by Maier et al. [2008]. In [Lambers et al., 2009, 2010] the effect of the previous history, including heat and mechanical treatment, on the transformation behavior is studied.

---

[1]The Transregional Collaborative Research Center SFB/TR TRR30 received a donation of steel bars with a diameter of 35 mm, a length of 3 m, and a total weight of 8000 kg from the company Georgs-marienhütte GmbH. All bars were produced within a single batch.

[2]A complete table of the chemical composition of the studied 51CrV4 specimens is also given in [Lambers et al., 2010]. Even though the specimens used here show only minor sample to sample variations, this is not the general case. The analysis of steel 51CrV4 from different suppliers revealed that there may be significant deviations of the constituents, see for example [Lambers et al., 2009; Maier et al., 2008; Wever et al., 1961]. These differences influence the thermal, mechanical, and transformation behavior. On the last aspect experimental results and conclusions are given in [Orlich et al., 1973].

2.1. Mechanical Properties of 51CrV4 at Room Temperature

To study the basic elastic and plastic material properties of 51CrV4 one-dimensional tests with constant strain rates and multistage relaxation test are considered. In particular, the rate dependence, relaxation behavior, and equilibrium stress state of the material are of interest. For the anticipated application cyclic properties are irrelevant and are not investigated.

It is known that twisting tests of thin-walled tubes, as applied for example in [Haupt and Lion, 1995], are capable of producing uniform simple shear states (the main driving force for metal plasticity) in the specimen and are in that respect superior to tension tests.[3] However, tension test are the most common, for 51CrV4 thin-walled tubes are not available, and their manufacturing would introduce residual stresses which alter the overall behavior. Thus, uniaxial tension and compression tests are carried out, with the advantage that the results can also be compared to the measurements of other groups.[4]

The experimental setup in Fig. 2.1 consists of a personal computer (equipped with an A/D and D/A converter and software for measurement and controlling) and the testing machine with measuring instruments. The testing machine contains a built-in inductive displacement transducer and a sensor for the axial force. To improve the measurement
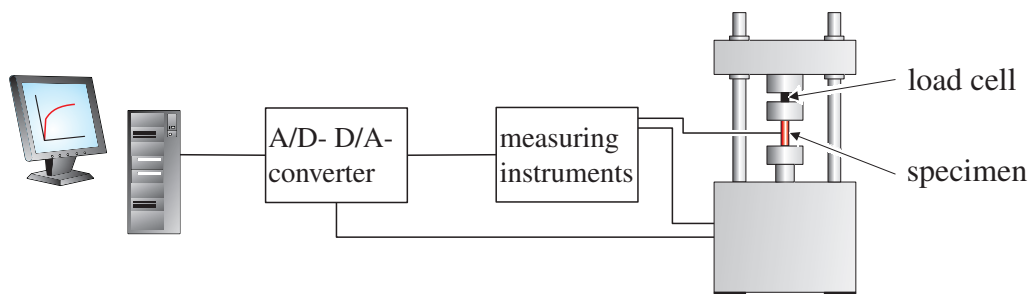
Figure 2.1.: Setup of tension test

accuracy an additional load cell (operating on the basis of a strain gauge) is integrated in the experimental setup.

It is assumed that the inhomogeneity due to the clamping decays rapidly and can be neglected in the middle of the specimen shown in Fig. 2.2a. The middle region is expected to be in a homogeneous state of stress and is, therefore, used as local measuring range. The extensometer, shown in Fig. 2.2b, has an initial length of $25\,\mathrm{mm}$ and is attached at this point to measure the local displacement. The signal from that gauge is also used as actual value for the displacement control. To this end, a PID controller is used

---

[3]Lubliner [2008] discusses the advantages and disadvantages of the two experiments in Chp. 2.

[4]The experiments were done at the laboratory of the Institute of Mechanics at the University of Kassel. The process paths were instructed by the supervisor and evaluated by the author.

(a) Specimen
(dimensions in
mm)

(b) Extensometer
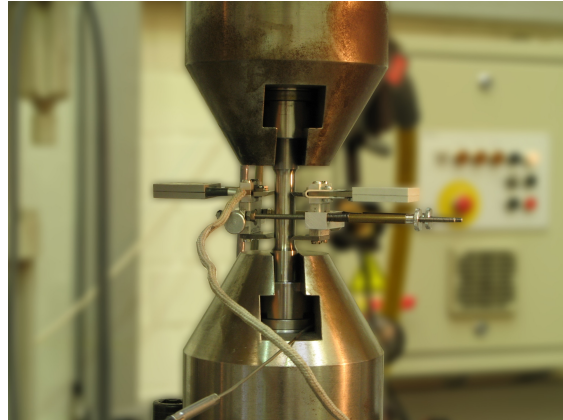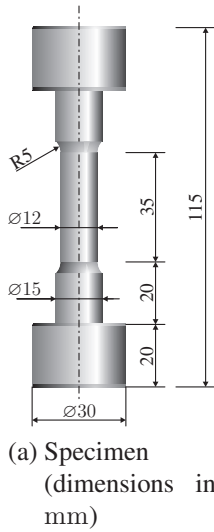
Figure 2.2.: Tension specimen

to adjust the displacement of the lower clamping so that the set path is followed in each instant. The control input and data acquisition are done with the program DASYLab in combination with a 16 bit D/A converter and a 12 bit A/D converter built in the PC. The maximum data rate is 30 Hz.

2.1.1. Tension and Compression Tests

A sequence of tests is chosen along the bottom-up approach proposed in [Lion, 1994]. In the first series strain-controlled tension and compression tests with four different rates, as depicted in Fig. 2.3a, are done. At the beginning a hold time of $t_0 = 3$ s is included to ensure equilibrium initial conditions. Two other hold times of $t_2 - t_1 = 5$ s and $t_4 - t_3 = 8$ s are added in the middle and at the end of each process to return to an equilibrium state. The maximum displacement is $|u_{max}| = 1$ mm, which corresponds to a maximum strain of $|\varepsilon_{max}| = 0.04$ in all tests. The strain rate varies and is given by the loading and unloading times $t_1 - t_0 = t_3 - t_2 = \{2$ s$, 20$ s$, 200$ s$, 2000$ s$\}$, leading to strain rates of $|\dot{\varepsilon}| = \{2 \times 10^{-2}$ s$^{-1}, 2 \times 10^{-3}$ s$^{-1}, 2 \times 10^{-4}$ s$^{-1}, 2 \times 10^{-5}$ s$^{-1}\}$.

Each process is repeated five times and the mean values are displayed in Fig. 2.4a for tension and Fig. 2.4b for compression. The displayed stress is the so-called *true stress*[5] $\sigma = F/A$, where F is the measured force and A refers to the current area. According to Lubliner [2008, p. 77] typical metals do not change significantly in volume[6] and the

---

[5]In a three-dimensional setting this corresponds to the Cauchy stress.

[6]Many metals have a Poisson's ratio of about $\nu = 0.3$ in the linear elastic range. This number gives the ratio of the transversal strain (contraction) to axial strain (extension), when the specimen is stretched in lateral direction. A perfectly incompressible elastic material (at small deformations) would have a

(a) Prescribed displacement

(b) Resultant force
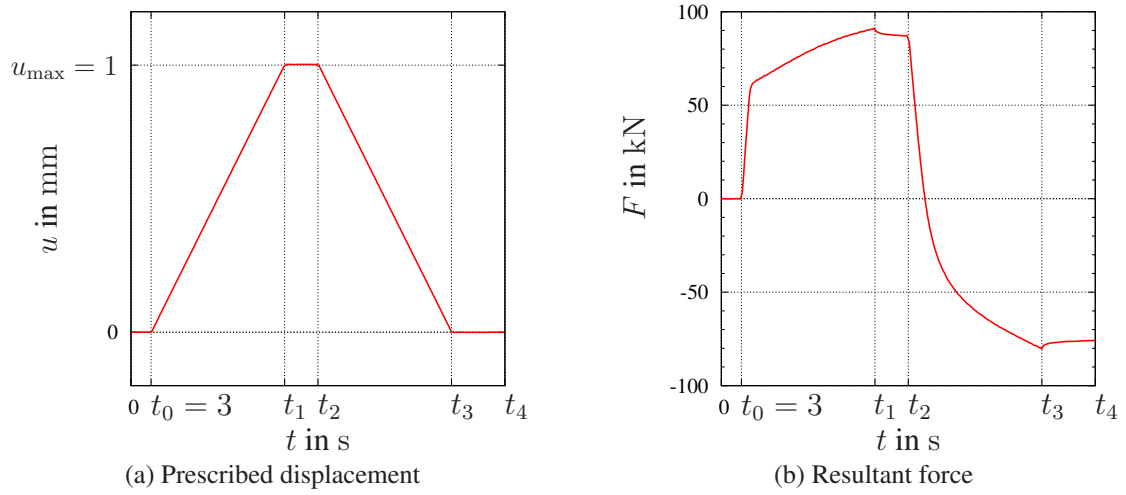
Figure 2.3.: Loading and unloading path with inserted hold times

(a) Tension test

(b) Compression test
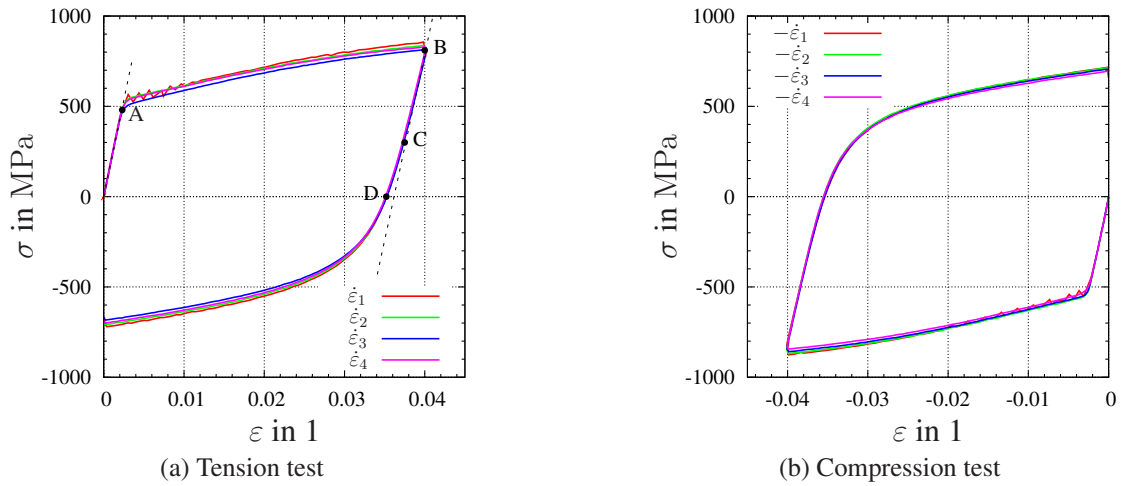
Figure 2.4.: Experimental results

current area can be computed from the volume constancy relation $Al = A_0 l_0$. The computed strain is the conventional or *engineering strain*, the change in length of the extensometer divided by the initial length, $\varepsilon = \Delta l/l_0$.

During the first phase of loading, the specimen behaves linearly elastic, indicated by the dashed line between the origin and point A. The transition from the linearly elastic to plastic behavior is clearly visible at point A with a yield strength of about 460 MPa. After this point the specimen shows nonlinear hardening along the curve A-B. At point B stress relaxation occurs, characterized by a vertical line. The relaxation is only barely visible in this representation and is studied in more detail in the following experiments. The phenomenon is also visible in the force-time diagram Fig. 2.3b, where the tensile and compressive forces decrease during the hold times between $t_2 - t_1$ and $t_4 - t_3$, respectively.

When the specimen is unloaded it behaves linearly elastic again, with the same slope as between the origin and point A. At point C the stress reaches the elastic limit. Yielding starts again and leads to nonlinear hardening. It is found in both tension and compression, that the yield stress is lower than before. This effect is known as the Bauschinger effect, [Tsakmakis, 1994, p. 3] and [Lubliner, 2008, p. 83]. When the stress is reduced to zero at point D, the remaining strain is different from zero. Thus, the material has been deformed plastically. After passing that point pronounced nonlinear hardening occurs.

Each test is repeated five times yielding similar results. In fact, the standard deviation in all tests was below 10 N. Only at the beginning of the fastest strain rate the standard deviation is twice as big, around 19 N. But even this value corresponds only to about $3.3 \times 10^{-4}\%$. Also at this strain rate the stress-strain curve shows fluctuations after the linear elastic range. The reason seems to be nonphysical and can be attributed to the testing machine's limitations.

Between the stress responses at various strain rates only small differences are visible. Thus, at room temperature only a small rate dependence of the material behavior is seen in these diagrams and it is difficult to obtain quantitative values from them. In addition to the overall behavior and the dependence on the strain rate, the degree of the tension-compression asymmetry is of interest. In Fig. 2.5 tensile and compressive stresses during loading with a strain rate of $|\dot\varepsilon| = 2 \times 10^{-4}$ s^{-1} are compared. The material behaves almost identical in both cases and the stress responses coincide to a high degree. Similar results are obtained for the other strain rates. This result agrees with the response of many other metals when the Cauchy stress is considered, as stated by Lubliner [2008, p. 77].

Poisson's ratio of $\nu = 0.5$. However, in the performed tests, the main part of the total deformation is due to plasticity and this deformation satisfies the incompressibility assumption.
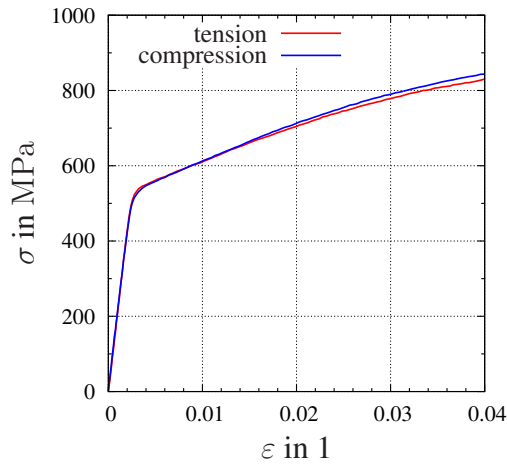
Figure 2.5.: Comparison of tension and compression

2.1.2. Long-time Relaxation Test

To further investigate the relaxation behavior, in particular for long times, the tension and compression test is stopped after reaching the maximum displacement $|u_{max}| = 1$ mm, which corresponds to point B in Fig. 2.4a. The maximum displacement is applied within 2 s, which corresponds to a strain rate of $|\dot{\varepsilon}| = 2 \times 10^{-2}$ s^{-1}. After reaching the maximum displacement, the displacement (respectively strain) is held constant and the time evolution of the stress is recorded. The resulting stress relaxation curves are shown in Fig. 2.6. Obviously the stress relaxes in both cases, tension and compression, over a

(a) Tensile stress

(b) Compressive stress
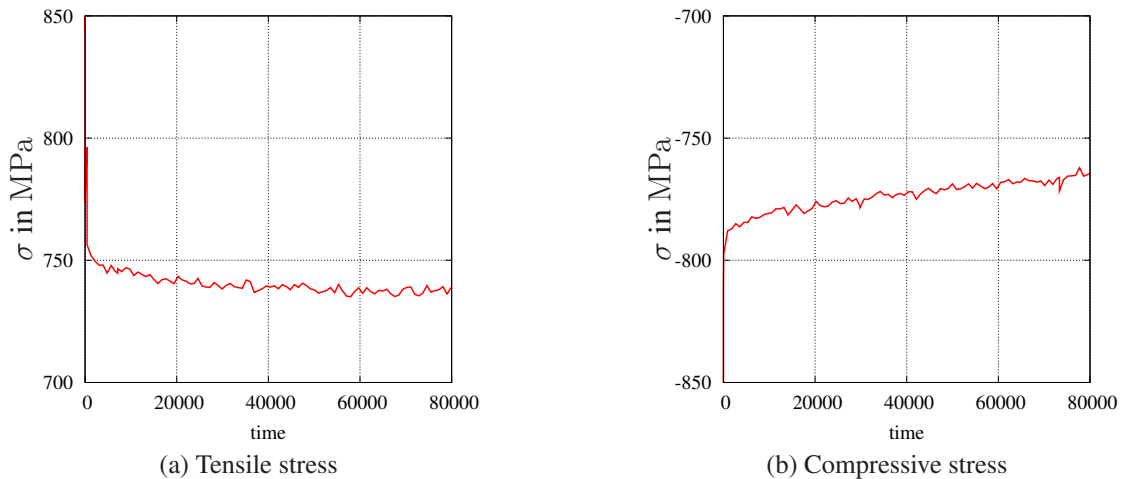
Figure 2.6.: Stress relaxation

long period with a pronounced relaxation at the beginning. Due to the low sampling rate, which was chosen according to the long recording time, the measured signal fluctuates

perceptibly. Similar to the deviations in the stress response (observed when using the highest strain rate $|\dot{\varepsilon}| = 2 \times 10^{-2} \text{ s}^{-1}$), these fluctuations seem to be nonphysical and due to the testing machine's limitations.

2.1.3. Multistage Relaxation Test

To obtain the equilibrium response the multistage process of Fig. 2.7 is investigated. As pointed out in [Lion, 1994, p. 17] these processes have the advantage of a drastically

(a) Complete path

(b) Begin of path in log-scale
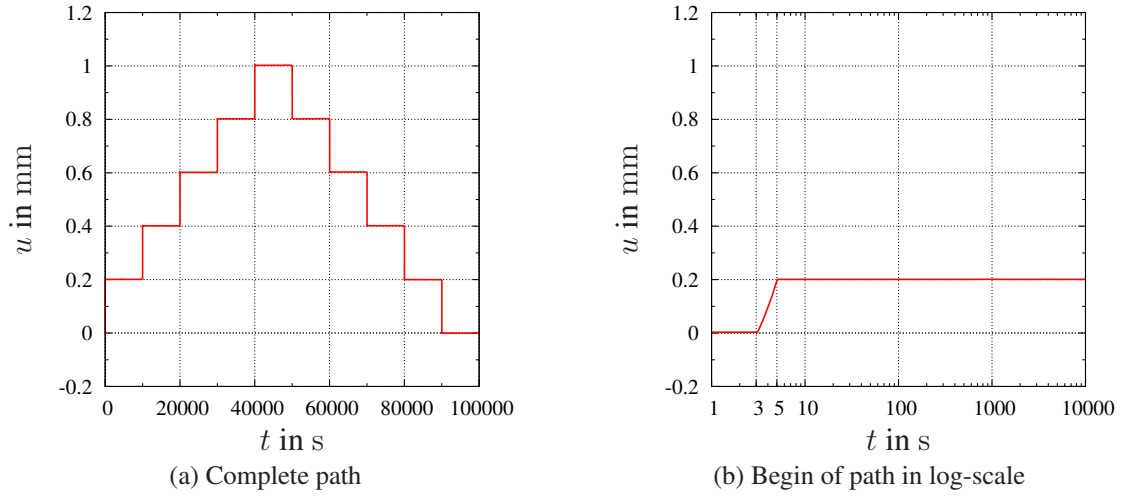
Figure 2.7.: Multistage-relaxation path, $t_{\text{hold}} = 10000$ s, $t_{\text{load}} = 2$ s

reduced experimentation time and offer more accurate results than processes with a slow strain rate.

The process consists of five stages in loading and unloading. At each stage the initial length is extended or reduced by $u = 0.2$ mm as shown for the beginning of the process in Fig. 2.7b. The used load time is $t_{\text{load}} = 2$ s, which corresponds to a strain rate of $|\dot{\varepsilon}| = 4 \times 10^{-3} \text{ s}^{-1}$. After each loading stage the displacement is held constant for $t_{\text{hold}} = 10000$ s, see Fig. 2.7a. During this phase stress relaxation occurs and the measured stress tends towards the equilibrium stress, as can be seen in Fig. 2.8a and Fig. 2.8c for the tension and compression test, respectively. The relaxation phase degenerates into a vertical line when plotted in a stress vs. strain diagram as in Fig. 2.8b and Fig. 2.8d. The end points of the relaxation phases are close to the equilibrium stress. Connecting them leads to a good approximation of the equilibrium hysteresis.
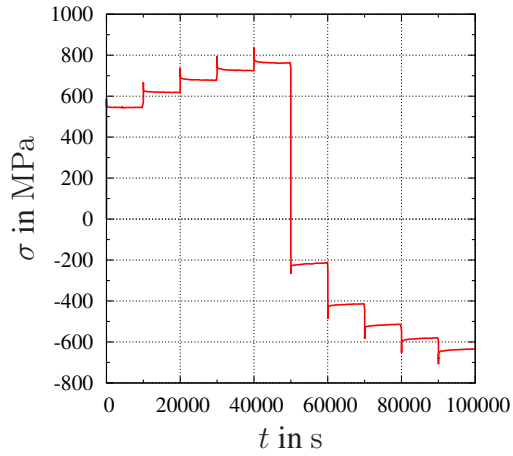
(a) Tension test, stress vs. time
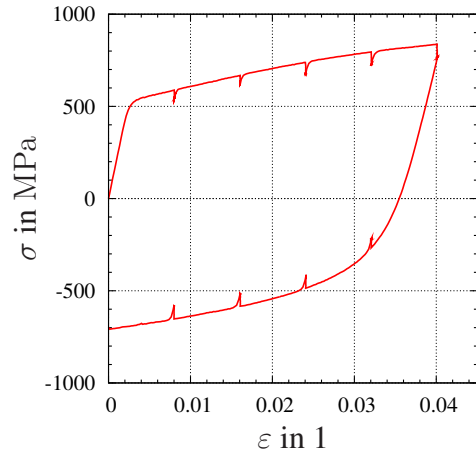
(b) Tension test, stress vs. strain
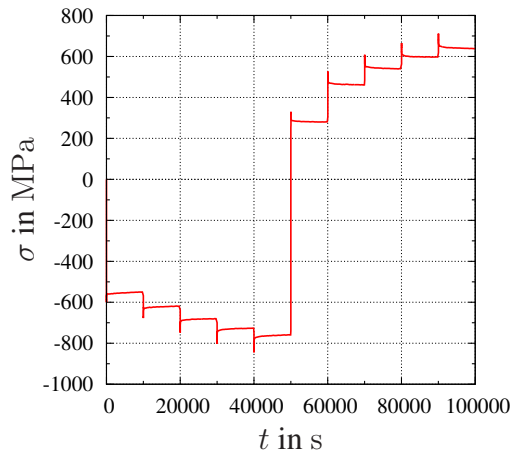
(c) Compression test, stress vs. time
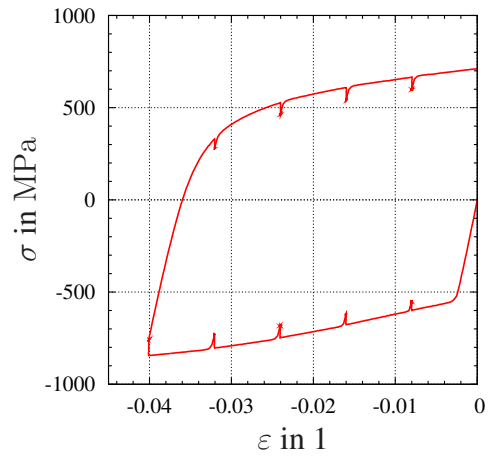
(d) Compression test, stress vs. strain

Figure 2.8.: Multistage-relaxation response

2.2. Thermophysical Properties of 51CrV4

During the production cycle shown in Sec. 1.1 the workpiece is locally heated up to 1200 °C. Thus, the material is in a severe thermal imbalance. It is known from experience that nature strives for balance states. In the present case this compensation is achieved on the one hand by heat flow between the workpiece and its environment and on the other hand by heat flow within the workpiece itself. This exchange of thermal energy is governed by thermophysical properties, in particular by the heat capacity, the heat conductivity and the emissivity of the material.

Due to the large temperature range of the anticipated application, ranging from room temperature up to 1200 °C, the temperature influence on the thermophysical material properties is of particular interest. Three different institutions[7] were instructed with experiments to determine the temperature-dependent heat capacity, heat conductivity, and emissivity.

2.2.1. Specific Heat Capacity

The heat capacity is the measure of the heat (thermal energy) required to increase the temperature θ of a body with mass m by a certain value without encountering a phase transition of the material. Heat is, just like mechanical work, not a system property (state variable, in terms of thermodynamics). Instead it manifests itself only during processes, where energy is exchanged.[8] Thus, it is generally given as differential quotient with respect to time

$$Q = mc_{\mathrm{d}}\frac{\mathrm{d}\theta}{\mathrm{d}t}. \tag{2.1}$$

The heat capacity mc_{d} can be computed from equation (2.1) if the supplied heat as well as the rate of temperature are known.

Differential Scanning Calorimetry (DSC) is employed for the measurement of the specific heat capacity c_{d}. This thermoanalytical technique was developed in 1960 by [Watson and O'Neil, 1966] and operates according to the heat flux principle, see also [Höhne et al., 2003, Chp. 6.1] for details.

A sample and a standard reference sample are subjected to a controlled temperature program by supplying thermal energy, as shown in the schematic drawing in Fig. 2.9a. During this program the temperature of the sample and the reference deviate due to dif-

---

[7]The heat capacity and heat conductivity were measured by the company Netzsch, a renowned manufacturer of thermal testing equipment. The emissivity in the low temperature range was measured at the Bavarian Center for Applied Energy Research (ZAE Bayern). The analysis of the high temperature range (above 700 °C) was done at the Institut für Kernenergetik und Energiesysteme from the University of Stuttgart.

[8]In general, energy forms as work and heat can only be exchanged during a change of state. This is discussed for example in [Stephan et al., 2009, Chp. 3] and [Hemminger and Höhne, 1979, p. 30] as well as the literature cited therein. After completing this change there is no heat or work.

(a) Experimental setup
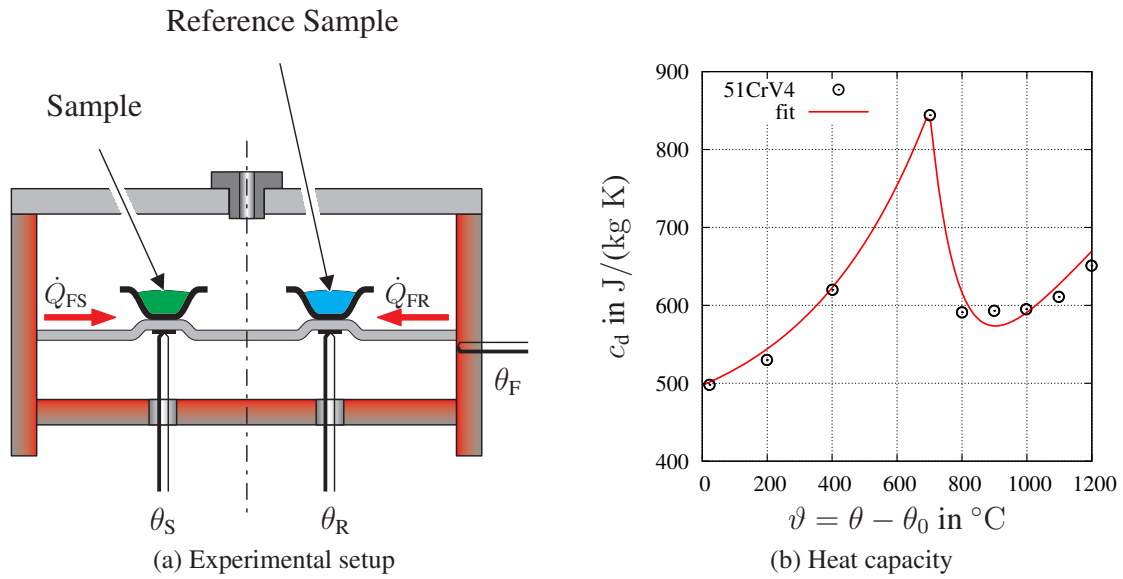
(b) Heat capacity

Figure 2.9.: Measurement of specific heat capacity

ferent heat capacities and phase transformations. Thus, the temperature of the sample and the temperature difference between the two are measured continuously. The experimental setup is as symmetric as possible (same geometries, similar material properties of sample and reference sample). This has the advantage that unavoidable measurement errors, e.g. heat leakage such as convection and radiation, compensate each other to some degree by forming the difference of both signals. Another measurement error is due to the diffusive nature of heat conduction, which leads to "smeared" measurement signals, see [Hemminger and Höhne, 1979, p. 59]. This effect as well as others have to be included in the analysis as described in [Haines, 1995; Höhne et al., 2003].

The samples that were used in all measurements were discs with a diameter of 5 mm and a mass of approximately 100 mg. The reference sample was heated at a constant rate of 20 K/min up to $1250\,°C$. According to the specifications of the manufacturer the measured specific heat has an accuracy better than 2.5% up to $1500\,°C$. The resulting curve in Fig. 2.9b shows a peak around $700\,°C$. This increase is due to the Curie transition, the change in magnetic properties from ferro-magnetic to para-magnetic. At $785\,°C$ there is also an endothermic change of the crystal structure from body-centered cubic (ferrite/ pearlite) to face-centered cubic (austenite). This change is connected with an enthalpy change of 45.74 J/g.

2.2.2. Thermal Conductivity

The thermal conductivity λ of a material describes its ability to conduct heat. To determine the thermal conductivity, the results of the DSC measurement and a laser flash ap-

paratus (LFA) are combined. This apparatus is shown in Fig. 2.10a and consists mainly of three parts: a furnace with a sample holder, a laser underneath the furnace (connected by fiber optics), and an infrared (IR) detector mounted directly on top of the furnace. The cylindrical sample with a diameter of 12.7 mm is heated under dynamic argon (inert gas) atmosphere to a predetermined temperature. When this reference temperature is reached, the base face of the sample is further heated by irradiating it with a short laser pulse (burst of energy). The pulsed laser (Nd:YAG, maximal power: 20 J/pulse, wave length: 1064 nm) irradiation results in a homogeneous heating of the base face and a succeeding temperature rise on the top face. The relative temperature increase is measured as a function of time by the IR detector (Indium antimonide, InSb, photodiode detector). The diffusivity of the sample $a(\theta)$ is computed with this information and the solution of the corresponding heat conduction problem.[9] Subsequently the thermal conductivity is given by

$$\lambda(\theta) = a(\theta)\rho(\theta)c_{\mathrm{d}}(\theta). \tag{2.2}$$

To enhance the emissivity and the absorptivity the samples were coated with graphite prior to each measurement. For each temperature five single measurements were conducted. The mean values are depicted in Fig. 2.10b with an absolute accuracy of the LFA method of about 3%.

(a) Experimental setup

(b) Heat conductivity
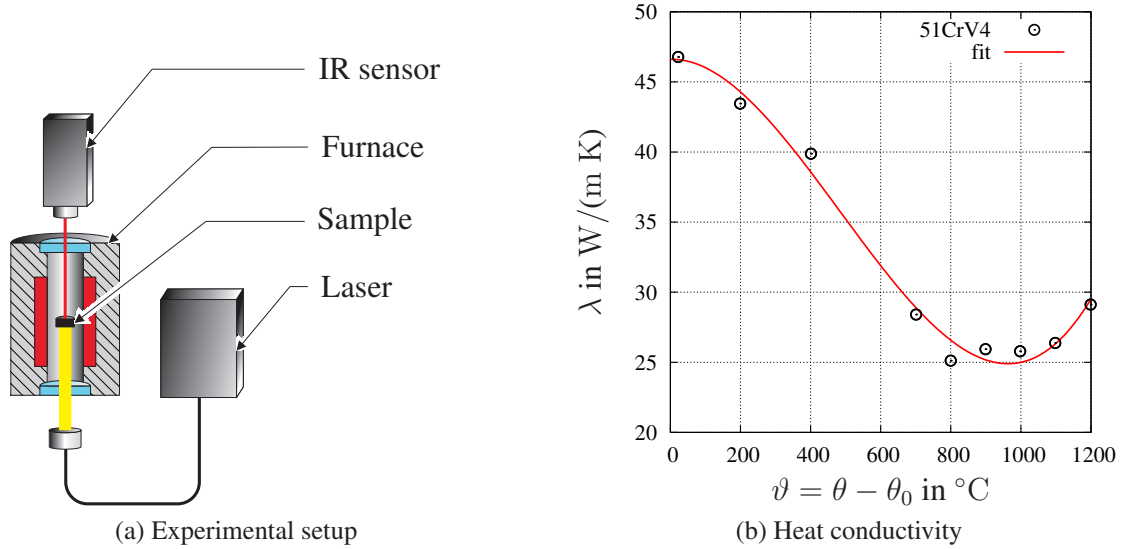
Figure 2.10.: Measurement of heat conductivity

It is known, cf. [Gnielinski et al., 2006, Chp. Dea], that the heat conductivity is sensi-

---

[9]The heat conduction problem can be solved analytically under the assumption of adiabatic conditions and a homogeneous temperature distribution over the radius of the sample. It can be shown, that the thermal diffusivity reads in this case $a = 0.1388\frac{l^2}{t_{0.5}}$, with the sample thickness l and the time needed for 50% of the temperature increase $t_{0.5}$.

tive with respect to changes in composition. Even small additions of alloying elements can lead to a significant decrease of the heat conductivity. Additionally, the thermal and mechanical history of the material have a strong effect on the heat conductivity. These effects are not yet captured by the present experiments. In contrast, the values of heat capacity, thermal expansion, Young's modulus, and Poisson's number vary only little with the constituents.

2.2.3. Emissivity

Matter, that is at a nonzero temperature, exchanges energy with its surrounding environment. This change of energy may require the presence of a material medium as e.g. in the case of heat convection or the aforedescribed heat conduction. In contrast, transfer of energy by radiation does not require any medium and is even most efficient in vacuum. Thermal radiation is energy emitted by matter and transported by electromagnetic waves, see [Incropera et al., 2007, p. 9 and p. 724]. It can be attributed to changes in the electron configurations of the constituent atoms.

In general radiation is a volumetric phenomenon. However, in most solids (opaque matter) radiation emitted from interior molecules is strongly absorbed by adjoining molecules. Accordingly, in such a solid the net radiation emitted by the body originates from the molecules that are within a small distance of the surface (typical is a distance of approximately $1\,\mu m$ from the exposed surface). Thus, radiation can often be treated as a surface phenomenon.

At the end of the 19$^{\text{th}}$ century Stefan and Boltzmann found an upper limit for the emissive power of a surface, which is today known as the Stefan-Boltzmann law

$$E_{\text{b}} = \sigma \theta_{\text{s}}^4, \tag{2.3}$$

where θ_{s} is the absolute temperature of the surface and $\sigma = 5.67 \times 10^{-8}\ \text{W/m}^2\,\text{K}^4$ is the Stefan-Boltzmann constant. A body that emits energy according to (2.3) is called an ideal radiator or blackbody. The heat flux that is emitted by a real surface is less and is given by

$$E = \epsilon \sigma \theta_{\text{s}}^4, \tag{2.4}$$

where ϵ is termed emissivity. This radiative property is a measure of how efficiently the surface emits energy relative to a blackbody and is in the range $0 \leq \epsilon \leq 1$.

A surface does not only emit radiation but it also intercepts and absorbs radiation from its surroundings. The property that describes the portion of the irradiation which is absorbed by the surface is the absorptivity. Often it is assumed that the absorptivity equals the emissivity, which is referred to as a gray surface. In this case the net rate of radiation heat transfer from the surface which is completely enclosed by a blackbody is

$$E = \epsilon \sigma (\theta_{\text{s}}^4 - \theta_{\infty}^4), \tag{2.5}$$

where θ_{∞} is the temperature of the surroundings.

As an electromagnetic wave, thermal radiation encompasses a range of the electromagnetic spectrum. Its wave length ranges from approximately 0.1 μm to 100 μm and includes the upper part of ultraviolet (UV), all the visible, and infrared (IR) light. Only this spectrum is caused by and affects the thermal state of matter. Radiation emitted and absorbed by a surface shows in general a spectral and directional dependency, i.e. the intensity of the emitted radiation varies with wave length and angle of emission respectively incidence, [Baehr and Stephan, 2008, p. 563]. Representative dependencies of the directional and spectral distributions for various materials are depicted in [Incropera et al., 2007, p. 746]. However, in view of the intended application these properties are of minor importance. Instead, the total (hemispherical) emissivity, an integrated average over wavelength and direction, is of practical relevance. This implies the assumption of a diffuse (directionally independent) emitter.

The experimental determination of the emissivity is based on the principle of radiation comparison. To this end, the emitted radiation of the sample is compared with the radiation of a blackbody.[10] The experimental setup is shown in Fig. 2.11a. A disc-shaped

(a) Experimental setup
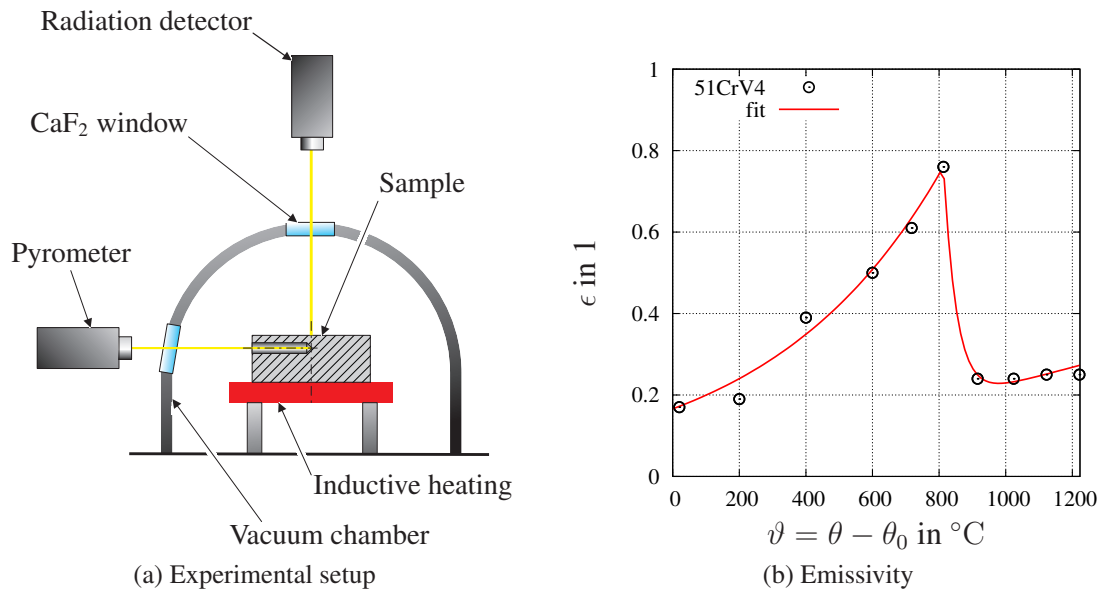
(b) Emissivity

Figure 2.11.: Measurement of total emissivity

sample (diameter of 15 mm and thickness of 5 mm) is mounted in a chamber, which can be evacuated or filled with inert gas. In the present study the chamber is filled with the inert gas argon at a pressure of 960 mbar. The inner surface of the chamber is cooled to room temperature and blackened (coating with an emissivity close to 1.0). Below the sample is a spiral inductor to heat the sample to prescribed temperatures. Its temperature

---

[10]The closest approximation of a blackbody is a cavity with an aperture and whose inner surface is held at uniform temperature. A thermodynamical explanation is given e.g. in [Incropera et al., 2007, p. 736] and [Baehr and Stephan, 2008, p. 586].

is measured within a bore in radial direction (diameter of 1.2 mm and depth of 7 mm). The measured value is extrapolated to the emitting surface (distance between the bore and the emitting surface is 1.3 mm) to yield the corresponding temperature. Mounted on top of the sample is a thermal radiation detector which measures the total radiation. This value is compared to the signal of a blackbody, which has been obtained in a previous measurement.

The actual evaluation of the emissivity also includes the effect of the encapsulating chamber, and absorption in the optical path by the CaF_2 window and gas. The measurement method has been successfully applied to various materials, see e.g. [Neuer, 1993; Neuer and Hoch, 1993]. Further details of the apparatus as well as an analysis of errors are given in [Neuer, 1971].

The final result of the total emissivity is shown in Fig. 2.11b. Again there is an abrupt change in the values around $800\,°C$, which at first sight seems to be connected to the change of crystal structure from ferrite to austenite. However, further investigations have revealed, that this change is permanent and due to an alteration of the material surface. This alteration is even visible with the naked eye and may be connected to thermally activated diffusion processes. The diffusion of soluble constituents is considerably eased within the austenite microstructure, see [Läpple, 2006, p. 83].

3. Fundamentals of Continuum Mechanics

In order to make predictions of the thermomechanical behavior of workpieces, it is necessary to formulate the complete process as a mathematical problem. Continuum mechanics is the basis for this formulation (a thorough and modern description can be found for example in [Haupt, 2000; Hutter and Jöhnk, 2004]). It is a branch of mechanics that is concerned with the analysis of the kinematics and the mechanical behavior of solids and fluids. This theory ignores the discrete nature of matter consisting of grains, molecules, atoms or even more delicate structures, depending on the scale of observation. Instead, a macroscopic point of view is taken and the material is modeled as a continuum which can be described by continuous or piecewise continuous functions. This assumption is justified in many engineering applications that deal with pieces of matter that are very large compared with these particles and leads to the development of field theories.

A field is a scalar-, vector-, or tensor-valued function of space and time. Examples of such fields are the temperature, velocity, and stress distribution, respectively. The fields are governed by general and individual statements. On the one hand the universal laws of nature are considered as general statements, which are formulated as balance equations. On the other hand, models for the material under consideration reproduce typical behavior patterns of the real material within certain restricted situations. These material models are individual statements, which reflect only the material properties of the particular material or class of materials, and are given in the form of constitutive equations.

3.1. Basic Kinematics

Continuum mechanics is concerned with deformable bodies, which change their shape due to external loads. The study of motion without regard to the forces, which drive it, is called kinematics. This branch is further divided into particle kinematics and deformations. Particle kinematics describe the motion of a single particle of a body without reference to the motion of neighboring particles. On the other hand, deformations[1] describe the motion of the entire body which might include a change of shape due to a relative motion of its particles.

---

[1]In continuum mechanics the term deformation is used for general motions, even those that do not involve a change of shape. Because of the ambiguity this terminology is discouraged by Noll [2004, p. 2], who introduced it in the first place. He suggests to use the term "transplacement" instead.

3.1.1. Configuration and Motion

Within the outlined context, a material body is a region of space that is continuously filled with matter. Mathematically, the material body $\mathcal{B} = \{\mathcal{P}\}$ is defined as an infinite set of material points or particles $\mathcal{P}$ which satisfies two essential properties: first, there is a set $\mathcal{K} = \{\boldsymbol{\chi}\}$ of one-to-one mappings, which are called configurations,

$$\boldsymbol{\chi}\colon \begin{cases} \mathcal{B} & \to \boldsymbol{\chi}[\mathcal{B}] \subset \mathbb{R}^3 \\ \mathcal{P} & \mapsto \boldsymbol{\chi}(\mathcal{P}) = (x_1, x_2, x_3) \Longleftrightarrow \mathcal{P} = \boldsymbol{\chi}^{-1}(x_1, x_2, x_3). \end{cases} \tag{3.1}$$

Second, the composition of two configurations $\boldsymbol{\chi}_1 \in \mathcal{K}$ and $\boldsymbol{\chi}_2 \in \mathcal{K}$

$$\boldsymbol{\chi}_2 \circ \boldsymbol{\chi}_1^{-1}\colon \begin{cases} \boldsymbol{\chi}_1[\mathcal{B}] & \to \boldsymbol{\chi}_2[\mathcal{B}] \subset \mathbb{R}^3 \\ (x_1, x_2, x_3) & \mapsto (y_1, y_2, y_3) = \boldsymbol{\chi}_2\big(\boldsymbol{\chi}_1^{-1}(x_1, x_2, x_3)\big) \end{cases} \tag{3.2}$$

is continuously differentiable. The latter ensures that two neighboring material points remain neighbors, while the first guarantees that each material point occupies only one point of space which is not shared by any other material point. This definition also excludes catastrophic situations such as ripping, pinching, or interpenetration of matter.

With the notion of a configuration, the motion of a material body $\mathcal{B}$ can be described as a parametric curve in $\mathcal{K}$ with time $t \in \mathbb{R}$ as parameter

$$t \mapsto \boldsymbol{\chi}_t \in \mathcal{K}. \tag{3.3}$$

The time-dependent configuration $\boldsymbol{\chi}_t$ is called current configuration. As the material body moves and deforms a smooth family of configurations emanates, see Fig. 3.1.
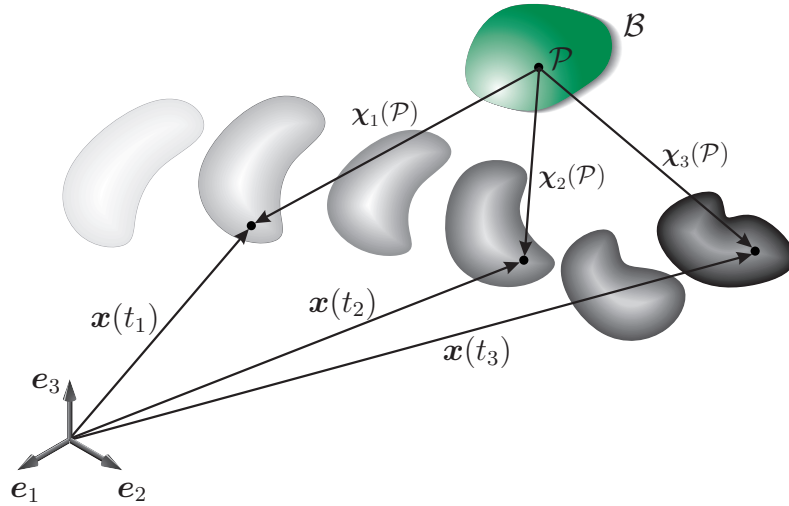
Figure 3.1.: Motion of a body as a parametric curve in $\mathcal{K}$ with t as parameter

In order to eliminate the abstract concept of the material point $\mathcal{P}$ from the formulation, an arbitrary but fixed configuration is chosen as reference.[2] With the reference

---

[2]Often the initial configuration is chosen for convenience, but this is not mandatory.

configuration $\mathcal{R} \in \mathcal{K}$,

$$\mathcal{R} : \begin{cases} \mathcal{B} & \to \mathcal{R}[\mathcal{B}] \subset \mathbb{R}^3 \\ \mathcal{P} & \mapsto \mathcal{R}(\mathcal{P}) = (X_1, X_2, X_3) \Longleftrightarrow \mathcal{P} = \mathcal{R}^{-1}(X_1, X_2, X_3), \end{cases} \tag{3.4}$$

each material point $\mathcal{P}$ is labeled with a corresponding number triple (X_1, X_2, X_3). Furthermore, this ordered triple can be interpreted as the coordinates of the point $P \in \mathbb{E}^3$ of the three-dimensional Euclidean space of physical observation at which the particle $\mathcal{P}$ is located, see Fig. 3.2. To this end, the origin O and base vectors $\boldsymbol{e}_i$ have to be spec-
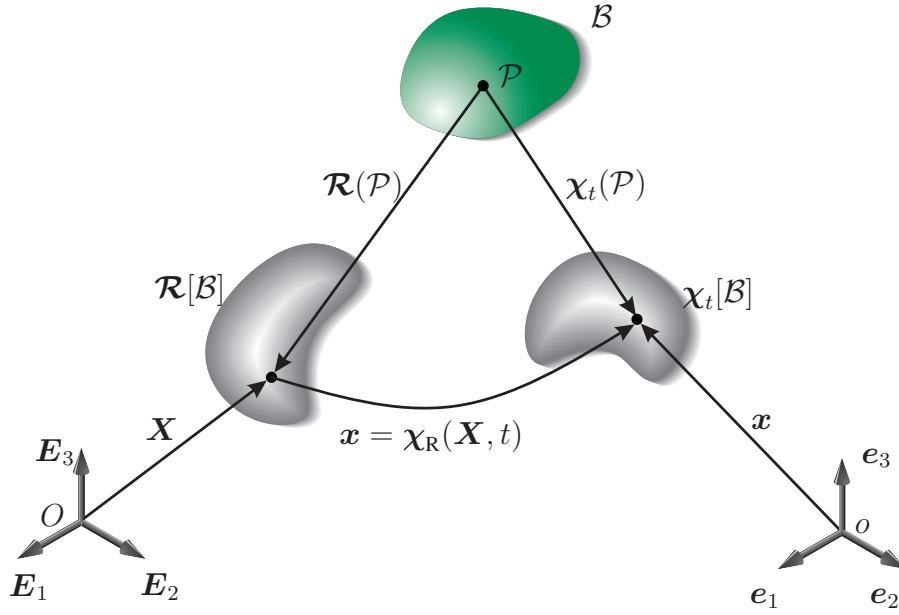
Figure 3.2.: Reference configuration and current configuration

ified to provide a frame of reference.[3] Thus the vectors $\boldsymbol{X} = X_\alpha \boldsymbol{E}_\alpha$ and $\boldsymbol{x} = x_i \boldsymbol{e}_i$ are position vectors, relative to O and o, of the material point within the reference and the current configuration respectively.[4] The corresponding number triples (X_1, X_2, X_3) are called material coordinates and (x_1, x_2, x_3) are termed spatial coordinates. Statements in continuum mechanics can be formulated either with material or spatial coordinates, which is referred to as Lagrangian and Eulerian description respectively.

The motion is represented by means of the vector function

$$\chi_\mathrm{R} : \begin{cases} \mathcal{R} \times \mathbb{R}^+ & \to \chi_t[\mathcal{B}] \\ (\boldsymbol{X}, t) & \mapsto \boldsymbol{x} = \chi_\mathrm{R}(\boldsymbol{X}, t) := \chi_t\big(\mathcal{R}^{-1}(\boldsymbol{X})\big). \end{cases} \tag{3.5}$$

---

[3]In this text orthonormal base vectors and Cartesian coordinates are used.

It is not necessary to introduce a reference system or even an orthonormal one. This is done here only for clarity. A completely system free derivation based on general coordinates and on manifolds can be found in [Marsden and Hughes, 1994] and [Haupt, 2000] .

[4]In general different frames of reference can be used for the reference and current configuration.

In many representations of solid mechanics, the initial configuration, i.e. the configuration of the material body at the time $t = t_0$, is chosen as reference. In this case the motion is described by the displacement of a particle, which is the difference of the position vectors

$$u(X, t) = x - X = \chi_{\mathrm{R}}(X, t) - X. \tag{3.6}$$

The definition of the displacement vector is illustrated in Fig. 3.3.
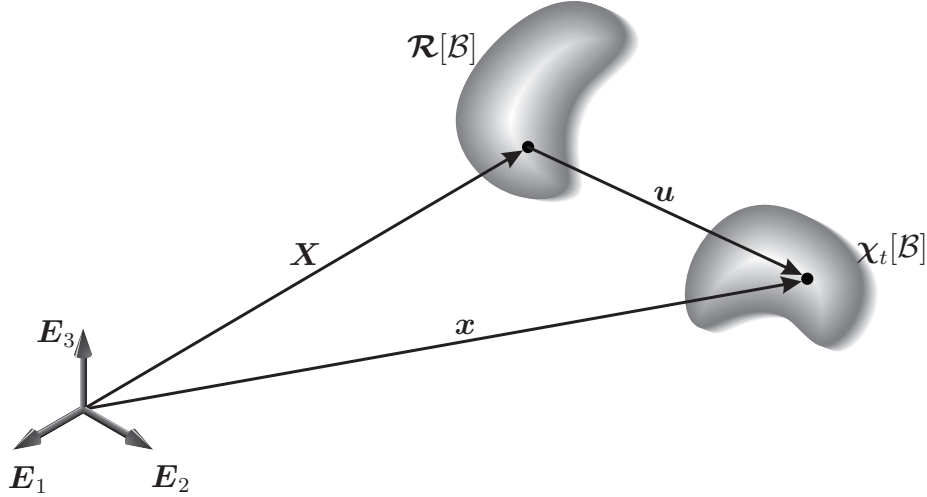
Figure 3.3.: Definition o displacement vector u

3.1.2. Deformation Gradient

Locally, the motion of a material body $\mathcal{B}$ is characterized by the so-called deformation gradient

$$\mathbf{F}(X, t) = \mathrm{Grad}\, \chi_{\mathrm{R}}(X, t). \tag{3.7}$$

Due to the requirement that the composition of two configurations (3.2) is continuously differentiable, there exists a Taylor expansion for the vector function (3.5) of the current position

$$x = \chi_{\mathrm{R}}(X, t) = \chi_{\mathrm{R}}(X_0 + \mathrm{d}X, t) = \chi_{\mathrm{R}}(X_0, t) + \mathbf{F}\,\mathrm{d}X + \|\mathrm{d}X\| r(X_0, t, \mathrm{d}X), \tag{3.8}$$

with the property

$$\lim_{\|\mathrm{d}X\| \to 0} \|r(X_0, t, \mathrm{d}X)\| = 0. \tag{3.9}$$

Here the gradient is evaluated with respect to the material coordinates. With the orthonormal bases $\{E_\alpha\}$ and $\{e_i\}$ the deformation gradient has the component representation

$$\mathbf{F} = \mathrm{Grad}\, \chi_{\mathrm{R}} = \frac{\partial \chi_{\mathrm{R}i}}{\partial X_\alpha} e_i \otimes E_\alpha = F_{i\alpha} e_i \otimes E_\alpha. \tag{3.10}$$

The deformation gradient is the Fréchet derivative of $\chi_R(X, t)$ with respect to X in the direction dX. The direction dX can be interpreted as a tangent vector to a smooth curve in $\mathcal{R}$, consisting of particles in the reference configuration and the material point X. The curve

$$\alpha \mapsto C(\alpha), \quad C(\alpha_0) = X, \tag{3.11}$$

with

$$dX = \frac{d}{d\alpha} C(\alpha) \, d\alpha \bigg|_{\alpha=\alpha_0} = C'(\alpha_0) \, d\alpha \tag{3.12}$$

is called material line. In the current configuration the material line is given by

$$\alpha \mapsto c(\alpha) = \chi_R(C(\alpha), t), \quad c(\alpha_0) = x, \tag{3.13}$$

with the tangent vector

$$dx = \frac{d}{d\alpha} c(\alpha) \, d\alpha \bigg|_{\alpha=\alpha_0} = c'(\alpha_0) \, d\alpha. \tag{3.14}$$

The application of the chain rule leads to

$$dx = \{\operatorname{Grad} \chi_R(C(\alpha), t)\} \, C'(\alpha_0) \, d\alpha. \tag{3.15}$$

Thus, the material elements dX transform according to

$$dx = F \, dX. \tag{3.16}$$

The material lines in the reference and current configuration as well as the transformation of material line elements is depicted in Fig. 3.4. Since dX and dx are associated
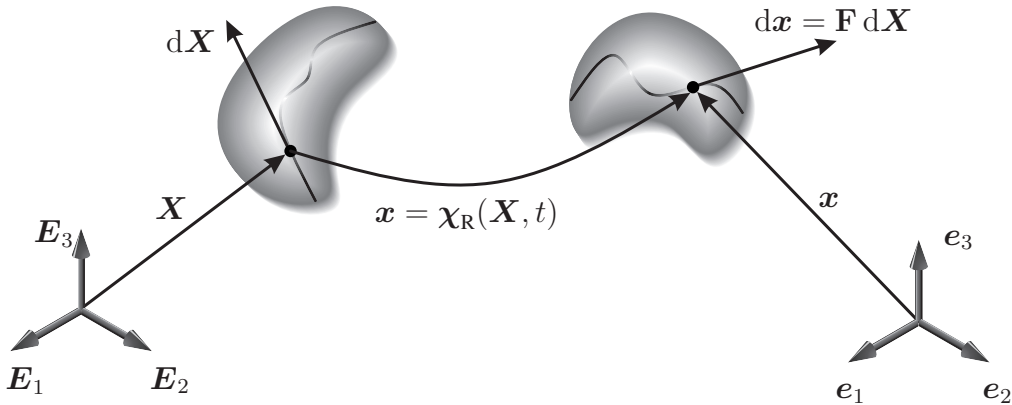
Figure 3.4.: Transformation of material line elements by the deformation gradient

with the reference and current configuration, respectively, F is a two point-tensor, [Ogden, 1997].

This geometrical interpretation of the deformation gradient leads directly to the relations of material surface and material volume elements in the reference and current configuration

$$\mathrm{d}\boldsymbol{a} = (\det \mathbf{F})\, \mathbf{F}^{-\mathrm{T}}\, \mathrm{d}\boldsymbol{A} \tag{3.17}$$

and

$$\mathrm{d}v = (\det \mathbf{F})\, \mathrm{d}V. \tag{3.18}$$

The material elements occur in integrals and are thus a basis for the formulation of balance relations in subsequent chapters. From the invertibility of the configurations (3.2) follows that $\det \mathbf{F} \neq 0$ and it is generally assumed that $\det \mathbf{F} > 0$ holds. The determinant of the deformation gradient is in the case of Cartesian coordinates the Jacobian of the transformation.

Although the deformation gradient contains all the information of the local motion it is not directly used as a strain measure, since it does not vanish for rigid body motions. Instead tensors which emanate from the multiplicative decomposition of $\mathbf{F}$ into orthogonal and symmetric parts are used. This so-called polar decomposition is unique and holds due to the invertibility of the deformation gradient

$$\mathbf{F} = \mathbf{R}\mathbf{U} = \mathbf{V}\mathbf{R}. \tag{3.19}$$

The second order tensors $\mathbf{U}$ and $\mathbf{V}$ are symmetric positive definite[5] and the tensor $\mathbf{R}$ is orthogonal.[6] The orthogonal tensor $\mathbf{R}$ describes a pure rotation of a material line element $\mathrm{d}\boldsymbol{X}$, whereas the so-called right stretch tensor $\mathbf{U}$ and the so called left stretch tensor $\mathbf{V}$ describe a pure elongation of the line elements $\mathrm{d}\boldsymbol{X}$ and $\mathbf{R}\,\mathrm{d}\boldsymbol{X}$ respectively. It can be shown, [Haupt, 2000], that the stretch tensors can be expressed in terms of the deformation gradient

$$\mathbf{U}^2 = \mathbf{C} = \mathbf{F}^{\mathrm{T}}\mathbf{F}, \tag{3.20}$$

$$\mathbf{V}^2 = \mathbf{B} = \mathbf{F}\mathbf{F}^{\mathrm{T}}. \tag{3.21}$$

The symmetric positive tensors $\mathbf{C}$ and $\mathbf{B}$ are called right and left Cauchy-Green tensors respectively and are used for the definition of strain measures later on.

3.1.3. Velocity, Acceleration, and Velocity Gradient

Many relevant processes are time-dependent. Thus, time derivatives of the various fields are required for the formulation of the balance equations and the material models. To this end, a tensor valued function of arbitrary order $w = f(\mathcal{P}, t)$ is considered. The time derivative

$$\dot{w}(t) = \dot{f}(\mathcal{P}, t) = \frac{\mathrm{d}}{\mathrm{d}t} f(\mathcal{P}, t) \tag{3.22}$$

---

[5] A symmetric positive definite tensor $\mathbf{U}$ has the properties $\mathbf{U} = \mathbf{U}^{\mathrm{T}}$ and $\boldsymbol{v} \cdot \mathbf{U}\boldsymbol{v} > 0$ holds for any vector $\boldsymbol{v} \neq \mathbf{0}$.

[6] Tensors with the property $\mathbf{R}^{\mathrm{T}}\mathbf{R} = \mathbf{R}\mathbf{R}^{\mathrm{T}} = \mathbf{1}$ are called orthogonal.

at a material point $\mathcal{P} \in \mathcal{B}$ is called material derivative of f. The physical quantity $w = f(\mathcal{P}, t)$ can be expressed either in terms of spatial coordinates

$$\bar{f} : (\boldsymbol{x}, t) \mapsto w = \bar{f}(\boldsymbol{x}, t) = f(\boldsymbol{\chi}_t^{-1}(\boldsymbol{x}), t) \tag{3.23}$$

or in material coordinates

$$\hat{f} : (\boldsymbol{X}, t) \mapsto w = \hat{f}(\boldsymbol{X}, t) = f(\boldsymbol{\mathcal{R}}^{-1}(\boldsymbol{X}), t). \tag{3.24}$$

The transition from one to the other representation is given by

$$\hat{f}(\boldsymbol{X}, t) = \bar{f}(\boldsymbol{\chi}_{\mathrm{R}}(\boldsymbol{X}, t), t), \tag{3.25}$$
$$\bar{f}(\boldsymbol{x}, t) = \hat{f}(\boldsymbol{\chi}_{\mathrm{R}}^{-1}(\boldsymbol{x}, t), t). \tag{3.26}$$

The time derivative in the material representation follows directly from the definitions (3.22) and (3.24)

$$\dot{w}(t) = \frac{\partial}{\partial t} \hat{f}(\boldsymbol{X}, t). \tag{3.27}$$

The material derivative of the spatial representation is obtained by computing the total derivative of (3.23), i.e. by applying the chain rule

$$\begin{aligned} \dot{w}(t) &= \frac{\mathrm{d}}{\mathrm{d}t} \bar{f}(\boldsymbol{\chi}_{\mathrm{R}}(\boldsymbol{X}, t), t) \\ &= \left\{ \operatorname{grad} \bar{f}(\boldsymbol{x}, t) \right\} \frac{\partial}{\partial t} \boldsymbol{\chi}_{\mathrm{R}}(\boldsymbol{X}, t) + \frac{\partial \bar{f}}{\partial t}. \end{aligned} \tag{3.28}$$

Here, the appropriate product is assumed between the gradient with respect to $\boldsymbol{x}$ and the velocity vector. The velocity of a particle $\mathcal{P} \in \mathcal{B}$ is defined as

$$\boldsymbol{v} = \dot{\boldsymbol{x}}(t) = \frac{\mathrm{d}}{\mathrm{d}t} \boldsymbol{\chi}_t(\mathcal{P}). \tag{3.29}$$

It can be expressed in the material (Lagrangian) representation

$$\boldsymbol{v} = \hat{\boldsymbol{v}}(\boldsymbol{X}, t) = \frac{\partial}{\partial t} \boldsymbol{\chi}_{\mathrm{R}}(\boldsymbol{X}, t) \tag{3.30}$$

or in the spatial (Eulerian) representation

$$\boldsymbol{v} = \bar{\boldsymbol{v}}(\boldsymbol{x}, t) = \hat{\boldsymbol{v}}\left(\boldsymbol{\chi}_{\mathrm{R}}^{-1}(\boldsymbol{x}, t), t\right). \tag{3.31}$$

Accordingly, the material derivative in spatial representation can be expressed as

$$\dot{w}(t) = \left\{ \operatorname{grad} \bar{f}(\boldsymbol{x}, t) \right\} \bar{\boldsymbol{v}}(\boldsymbol{x}, t) + \frac{\partial}{\partial t} \bar{f}(\boldsymbol{x}, t). \tag{3.32}$$

The two summands are often referred to as convective and local derivative. An application of this result is the computation of the acceleration vector $\boldsymbol{a}$. It is the material derivative of the velocity vector (3.29), which leads to

$$\boldsymbol{a} = \hat{\boldsymbol{a}}(\boldsymbol{X},t) = \frac{\partial}{\partial t}\hat{\boldsymbol{v}}(\boldsymbol{x},t) = \frac{\partial^2}{\partial t^2}\boldsymbol{\chi}_{\mathrm{R}}(\boldsymbol{X},t) \tag{3.33}$$

in the material representation and with (3.32) to

$$\boldsymbol{a} = \bar{\boldsymbol{a}}(\boldsymbol{x},t) = \{\mathrm{grad}\,\bar{\boldsymbol{v}}(\boldsymbol{x},t)\}\,\bar{\boldsymbol{v}}(\boldsymbol{x},t) + \frac{\partial}{\partial t}\bar{\boldsymbol{v}}(\boldsymbol{x},t) \tag{3.34}$$

in the spatial configuration.

The deformation gradient $\mathbf{F}$ contains all local information of the motion. In many situations also the rate of change is of interest as described above, where the rate of change of the particle position leads to the velocity vector. The spatial gradient of the velocity vector

$$\mathrm{Grad}\,\hat{\boldsymbol{v}}(\boldsymbol{X},t) = \dot{\mathbf{F}}(\boldsymbol{X},t) \tag{3.35}$$

is called material velocity gradient, while the gradient with respect to spatial coordinates

$$\mathrm{grad}\,\bar{\boldsymbol{v}}(\boldsymbol{x},t) =: \mathbf{L}(\boldsymbol{x},t) \tag{3.36}$$

is the spatial velocity gradient. The relation between the velocity gradients is established by considering the identity between the expressions for the velocity (3.30) and (3.31)

$$\hat{\boldsymbol{v}}(\boldsymbol{X},t) = \bar{\boldsymbol{v}}(\boldsymbol{\chi}_{\mathrm{R}}(\boldsymbol{X},t),t)\,. \tag{3.37}$$

Differentiation with respect to $\boldsymbol{X}$ leads to

$$\mathrm{Grad}\,\hat{\boldsymbol{v}}(\boldsymbol{X},t) = \{\mathrm{grad}\,\bar{\boldsymbol{v}}(\boldsymbol{x},t)\}\,\mathrm{Grad}\,\boldsymbol{\chi}_{\mathrm{R}}(\boldsymbol{X},t). \tag{3.38}$$

With the definition (3.35) follows

$$\dot{\mathbf{F}} = \mathbf{L}\mathbf{F} \tag{3.39}$$

and

$$\mathbf{L} = \dot{\mathbf{F}}\mathbf{F}^{-1}. \tag{3.40}$$

In many formulations only a part of the spatial velocity gradient $\mathbf{L}$ is used. The symmetric part $\mathbf{D}$ is called the strain rate tensor

$$\mathbf{D} := \tfrac{1}{2}\left(\mathbf{L} + \mathbf{L}^{\mathrm{T}}\right), \quad \mathbf{D} = \mathbf{D}^{\mathrm{T}} \tag{3.41}$$

and the antisymmetric part

$$\mathbf{W} := \tfrac{1}{2}\left(\mathbf{L} - \mathbf{L}^{\mathrm{T}}\right), \quad \mathbf{W} = -\mathbf{W}^{\mathrm{T}} \tag{3.42}$$

is called the spin or vorticity tensor. Adding both tensors yields the spatial velocity tensor $\mathbf{L} = \mathbf{D} + \mathbf{W}$. The role of the spatial velocity gradient $\mathbf{L}$ is similar to the geometrical interpretation of the deformation gradient. It represents the rate at which changes of material elements take place. Taking the time derivative of the material elements (3.16), (3.17), and (3.17) and inserting the definition (3.40) leads to

$$(\mathrm{d}\boldsymbol{x})^{\cdot} = \mathbf{L}\,\mathrm{d}\boldsymbol{x}, \tag{3.43}$$

$$(\mathrm{d}\boldsymbol{a})^{\cdot} = \left[(\operatorname{div}\boldsymbol{v})\mathbf{1} - \mathbf{L}^{\mathrm{T}}\right]\mathrm{d}\boldsymbol{a}, \tag{3.44}$$

$$(\mathrm{d}v)^{\cdot} = (\operatorname{div}\boldsymbol{v})\,\mathrm{d}v. \tag{3.45}$$

In these expressions div denotes the divergence operator with respect to spatial coordinates $\boldsymbol{x}$, while Div is used in the following for the divergence operator with respect to material coordinates $\boldsymbol{X}$. In the following the hat and bar (indicating material and spatial representation) are dropped in favor of a more concise notation.

3.1.4. Strain Tensors

A motions deviation from a rigid body motion is termed strain or distortion. Strain tensors provide a measure for the three-dimensional strain state. Therefore, they have to vanish in the case of a rigid body motion, which is generally given by

$$\boldsymbol{x} = \boldsymbol{\chi}_{\mathrm{R}}(\boldsymbol{X}, t) = \mathbf{Q}(t)(\boldsymbol{X} - \boldsymbol{X}_0) + \boldsymbol{x}_0(t). \tag{3.46}$$

The motion consists of a pure rotation about the point $\boldsymbol{X}_0$ given by the orthogonal tensor $\mathbf{Q}(t)$ and a pure translation given by the vector valued function $\boldsymbol{x}_0(t)$, which represents the motion of the material frame of reference point.

The deformation gradient of a rigid body motion according to equation (3.46) is location-independent and equal to the rotation tensor

$$\mathbf{F}(\boldsymbol{X}, t) = \mathbf{Q}(t).$$

Accordingly, the right Cauchy-Green tensor becomes

$$\mathbf{C} = \mathbf{F}^{\mathrm{T}}\mathbf{F} = \mathbf{Q}^{\mathrm{T}}\mathbf{Q} = \mathbf{1}$$

and the left Cauchy-Green tensor reads

$$\mathbf{B} = \mathbf{F}\mathbf{F}^{\mathrm{T}} = \mathbf{Q}\mathbf{Q}^{\mathrm{T}} = \mathbf{1}.$$

The tensor

$$\mathbf{E}(\boldsymbol{X}, t) := \tfrac{1}{2}\left(\mathbf{C} - \mathbf{1}\right) = \tfrac{1}{2}\left(\mathbf{F}^{\mathrm{T}}\mathbf{F} - \mathbf{1}\right) \tag{3.47}$$

vanishes for rigid body motions. It is referred to as the Green strain tensor and operates on tangent spaces of the reference configuration. In contrast the Almansi strain tensor

$$\mathbf{A}(\boldsymbol{x}, t) := \tfrac{1}{2}\left(\mathbf{1} - \mathbf{B}^{-1}\right) = \tfrac{1}{2}\left(\mathbf{1} - \mathbf{F}^{-\mathrm{T}}\mathbf{F}^{-1}\right) \tag{3.48}$$

operates on the current configuration and is related to the Green strain tensor (3.47) by

$$\mathbf{A} = \mathbf{F}^{-T}\mathbf{E}\mathbf{F}^{-1}. \tag{3.49}$$

For the formulation of balance equations and constitutive models also the time derivatives of strain tensors are necessary. The time derivative of the Green strain tensor follows from definition (3.47)

$$\dot{\mathbf{E}} = \tfrac{1}{2}\left(\dot{\mathbf{F}}^{T}\mathbf{F} + \mathbf{F}^{T}\dot{\mathbf{F}}\right) = \mathbf{F}^{T}\tfrac{1}{2}\left(\mathbf{F}^{-T}\dot{\mathbf{F}}^{T} + \dot{\mathbf{F}}\mathbf{F}^{-1}\right)\mathbf{F}. \tag{3.50}$$

With the definition of the strain rate tensor (3.40) the relation

$$\dot{\mathbf{E}} = \mathbf{F}^{T}\mathbf{D}\mathbf{F} \quad \Leftrightarrow \quad \mathbf{D} = \mathbf{F}^{-T}\dot{\mathbf{E}}\mathbf{F}^{-1} \tag{3.51}$$

is established. With this result and the transformation rule (3.49) the relation for the time rate of the Almansi tensor can be computed easily

$$\mathbf{D} = \mathbf{F}^{-T}\dot{\mathbf{E}}\mathbf{F}^{-1} = \mathbf{F}^{-T}\left(\mathbf{F}^{T}\mathbf{A}\mathbf{F}\right)^{\cdot}\mathbf{F}^{-1} = \dot{\mathbf{A}} + \mathbf{L}^{T}\mathbf{A} + \mathbf{A}\mathbf{L}. \tag{3.52}$$

3.2. Balance Equations

The objective of continuum mechanics is the determination of the state of a macroscopic system, i.e. the density $\varrho(\mathbf{X}, t)$, the current position $\boldsymbol{\chi}_R(\mathbf{X}, t)$, and the temperature $\theta(\mathbf{X}, t)$ of all material points $\mathcal{P}$ as a function of time t, [Altenbach and Altenbach, 1994]. The balance equations describe the interaction of the outside world with the material body $\mathcal{B}$ and link the external loads with physical quantities.

3.2.1. General Considerations

The main idea for the formulation of the balance equations is the free-body principle, also called the principle of intersection, [Szabó, 1996]. According to this principle any material body can be cut into two imaginary parts, which are material bodies as well. Each part enjoys the original properties if the interaction between the parts is accounted for properly. The principle is assumed to hold for any body part, independent of its size.

The present state of a material body is represented by the current configuration, the mass, the momentum, the moment of momentum, the temperature, the energy, and the entropy of the body. This state can be represented by physical quantities or variables. These are classified either as intensive or extensive. Intensive quantities are independent of the size of the body (system) and remain constant when the body is divided into subbodies, such as temperature, stress and electric field. Quantities that are proportional to the amount of matter are referred to as extensive, such as volume. These are additive and thus, can be represented by volume integrals over density functions of the mechanical and thermal quantities, [Hutter and Jöhnk, 2004].

The integration over the body can be carried out in the reference configuration $\mathcal{R}[\mathcal{B}]$ or in the current configuration $\chi_\mathrm{R}[\mathcal{B}]$. For an arbitrary physical variable G, which characterizes a partial aspect of the state of the body, this leads to

$$G(t) = \int_\omega \gamma\left(\boldsymbol{x}, t\right) \mathrm{d}v = \int_\Omega \Gamma\left(\boldsymbol{X}, t\right) \mathrm{d}V, \tag{3.53}$$

where γ and Γ denote the corresponding density functions in the current and reference configuration, respectively. In the reference configuration the integration is carried out over the open set Ω of a body with the boundary $\partial\Omega$ (bounding surface). In the current configuration the shape of the body may change with time, thus leading to the time-dependent volume $\omega(t)$ and surface $\partial\omega(t)$, see Fig. 3.5. The density functions are related
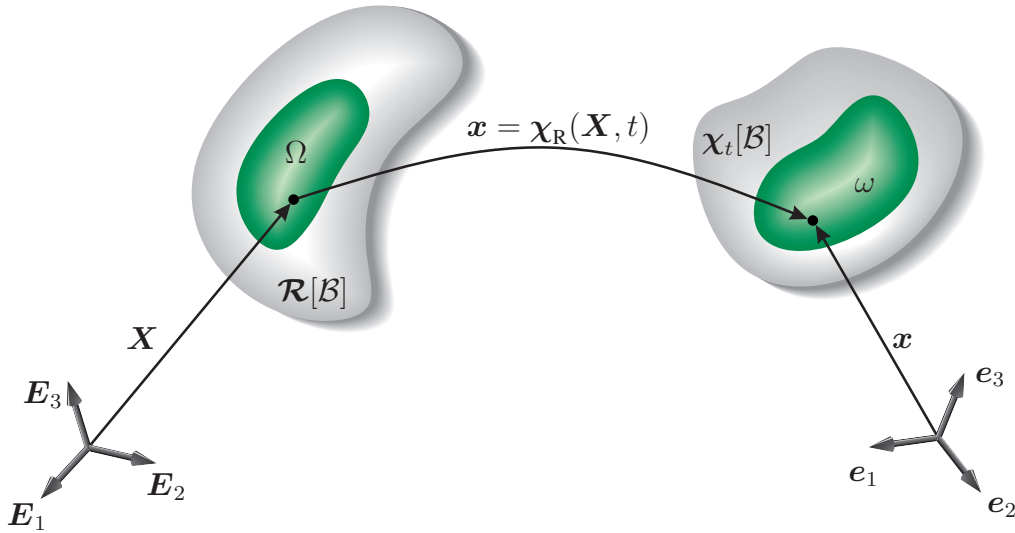
Figure 3.5.: Material domains in the reference and the current configurations with material subsets Ω and ω, respectively

to each other by the definition of motion (3.5) and the transformation of material volume elements (3.18) which yields

$$\Gamma\left(\boldsymbol{X}, t\right) = \gamma\left(\chi_\mathrm{R}(\boldsymbol{X}, t), t\right) \det \mathbf{F}. \tag{3.54}$$

The change of the physical variable G with time is driven by external actions (influence of the surroundings) and by internal processes within the body. These effects are again described as state or process variables. These are denoted as P for production, S for supply, and F for flux. The time rate of change of G is the sum of all effects

$$\frac{\mathrm{d}G}{\mathrm{d}t} = P + S + F. \tag{3.55}$$

Internal processes such as heat production due to internal friction or radioactive decay are accounted for by the production term

$$P = \int_\omega \pi(\boldsymbol{x}, t)\,\mathrm{d}v = \int_\Omega \Pi(\boldsymbol{X}, t)\,\mathrm{d}V. \tag{3.56}$$

Effects from the exterior can take place either over the volume or the surface of the subbody. The supply or source

$$S = \int_\omega \sigma(\boldsymbol{x}, t)\,\mathrm{d}v = \int_\Omega \Sigma(\boldsymbol{X}, t)\,\mathrm{d}V \tag{3.57}$$

is exclusively supplied from outside the body, but the effect influences the whole domain. Examples are the effects of gravitation and heat radiation. In contrast to the supply S, the effect of the flux

$$F = -\int_{\partial\omega} \boldsymbol{\phi}(\boldsymbol{x}, t)\cdot\boldsymbol{n}\,\mathrm{d}a = -\int_{\partial\Omega} \boldsymbol{\Phi}(\boldsymbol{X}, t)\cdot\boldsymbol{n}_{\mathrm{R}}\,\mathrm{d}A \tag{3.58}$$

enters the body through the surface $\partial\omega$ or $\partial\Omega$; it is said to flow from outside into the body. In this representation the Cauchy-Lemma has already been incorporated and unit normal vectors of the current configuration $\boldsymbol{n}$ and the reference configuration $\boldsymbol{n}_{\mathrm{R}}$ have been introduced, see [Hutter and Jöhnk, 2004, p. 55].[7] Examples for the flux densities are surface stress and heat flux through a surface. The general balance equation (3.55) can now be written as

$$\frac{\mathrm{d}}{\mathrm{d}t}\int_\omega \gamma(\boldsymbol{x}, t)\,\mathrm{d}v = \int_\omega [\pi(\boldsymbol{x}, t) + \sigma(\boldsymbol{x}, t)]\,\mathrm{d}v - \int_{\partial\omega} \boldsymbol{\phi}(\boldsymbol{x}, t)\cdot\boldsymbol{n}\,\mathrm{d}a, \tag{3.59a}$$

$$\frac{\mathrm{d}}{\mathrm{d}t}\int_\Omega \Gamma(\boldsymbol{X}, t)\,\mathrm{d}V = \int_\Omega \left[\Pi(\boldsymbol{X}, t) + \Sigma(\boldsymbol{X}, t)\right]\,\mathrm{d}V - \int_{\partial\Omega} \boldsymbol{\Phi}(\boldsymbol{X}, t)\cdot\boldsymbol{n}_{\mathrm{R}}\,\mathrm{d}A. \tag{3.59b}$$

These are so-called global balance statements for the physical variable G. Under certain continuity requirements on the integrands of equations (3.59), the statements can be reformulated as local statements in the form of partial differential equations.

To this end, firstly the sequence of differentiation and integration of the left-hand side of equations (3.59) has to be interchanged and secondly the surface integral on the right-hand side has to be transformed to a volume integral. In the material formulation, i.e. in coordinates of the reference configuration, the interchange of variables can be carried out, provided Γ is differentiable

$$\frac{\mathrm{d}}{\mathrm{d}t}\int_\Omega \Gamma(\boldsymbol{X}, t)\,\mathrm{d}V = \int_\Omega \frac{\partial\Gamma(\boldsymbol{X}, t)}{\partial t}\,\mathrm{d}V. \tag{3.60a}$$

---

[7]The Cauchy Lemma states, that the surface densities depend linearly on the normal $\boldsymbol{n}$ or $\boldsymbol{n}_{\mathrm{R}}$ of the surface. The densities are given by a contraction.

In the spatial representation, i.e. in coordinates of the current configuration, the domain of integration ω also depends on time and this leads to *Reynolds* transport theorem

$$\frac{\mathrm{d}}{\mathrm{d}t} \int\limits_{\omega(t)} \gamma\left(\boldsymbol{x}, t\right) \mathrm{d}v = \int\limits_{\Omega} \left(\dot{\gamma}\det\mathbf{F} + \gamma(\det\mathbf{F})^{\boldsymbol{\cdot}}\right) \mathrm{d}V = \int\limits_{\omega} \left(\frac{\mathrm{d}\gamma}{\mathrm{d}t} + \gamma\mathrm{div}\,\boldsymbol{v}\right) \mathrm{d}v, \quad \text{(3.60b)}$$

see also [Hutter and Jöhnk, 2004]. Here, the relation for the rate of the volume element (3.45) has been made use of. Furthermore, if the continuity requirements of the divergence theorem are fulfilled by ϕ respectively Φ, then the application of the theorem leads to

$$\int\limits_{\partial\omega} \boldsymbol{\phi}(\boldsymbol{x}, t) \cdot \boldsymbol{n}\,\mathrm{d}a = \int\limits_{\omega} \mathrm{div}\,\boldsymbol{\phi}\,\mathrm{d}v \tag{3.61a}$$

and

$$\int\limits_{\partial\Omega} \boldsymbol{\Phi}(\boldsymbol{X}, t) \cdot \boldsymbol{n}_{\mathrm{R}}\,\mathrm{d}A = \int\limits_{\Omega} \mathrm{Div}\,\boldsymbol{\Phi}\,\mathrm{d}V. \tag{3.61b}$$

With equations (3.60) and (3.61) the balance equations (3.59) can be written as

$$\int\limits_{\omega} \left(\frac{\mathrm{d}\gamma}{\mathrm{d}t} + \gamma\mathrm{div}\,\boldsymbol{v} - \pi - \sigma + \mathrm{div}\,\boldsymbol{\phi}\right) \mathrm{d}v = 0 \tag{3.62a}$$

and

$$\int\limits_{\Omega} \left(\frac{\partial\Gamma}{\partial t} - \Pi - \Sigma + \mathrm{Div}\,\boldsymbol{\Phi}\right) \mathrm{d}V = 0. \tag{3.62b}$$

Due to the free body principle the global (integral) form of the balance equations hold for any partial volume of the material body $\mathcal{B}$. Assuming furthermore that the integrands of equations (3.62) are continuous with respect to $\boldsymbol{x}$ and $\boldsymbol{X}$, respectively, then it holds that the integrands vanish over the whole integration domain, [Haupt, 2000, p. 77]. This leads to the local balance of equations

$$\frac{\mathrm{d}\gamma}{\mathrm{d}t} + \gamma\mathrm{div}\,\boldsymbol{v} = -\mathrm{div}\,\boldsymbol{\phi} + \pi + \sigma, \tag{3.63a}$$

$$\frac{\partial\Gamma}{\partial t} = -\mathrm{Div}\,\boldsymbol{\Phi} + \Pi + \Sigma. \tag{3.63b}$$

The local balance equations are derived for scalar-valued equations. They have the same form also in the case of higher-dimensional tensors fields. In this case the divergence operates not on a vector but on a general tensor field, see e.g. [Helm, 2003, p. 111].

3.2.2. Balance of Mass

Mass is a characteristic property of a material body $\mathcal{B}$. It is a measure for the effect of inertia and gravity. The mass $m : (\mathcal{B}, t) \to \mathbb{R}^+$ is defined by the volume integral over the mass density distribution $\varrho(\boldsymbol{x}, t)$ as

$$(\mathcal{B}, t) \mapsto m(\mathcal{B}, t) = \int_\omega \varrho(\boldsymbol{x}, t) \, \mathrm{d}v = \int_\Omega \varrho_\mathrm{R}(\boldsymbol{X}, t) \, \mathrm{d}V. \tag{3.64}$$

The mass densities of the current and reference configuration are related by

$$\varrho_\mathrm{R} = \varrho \det \mathbf{F}. \tag{3.65}$$

The mass of any material body $\mathcal{B}$ is temporally constant

$$\frac{\mathrm{d}m}{\mathrm{d}t} = \frac{\mathrm{d}}{\mathrm{d}t} \int_\omega \varrho(\boldsymbol{x}, t) \, \mathrm{d}v = \frac{\mathrm{d}}{\mathrm{d}t} \int_\Omega \varrho_\mathrm{R}(\boldsymbol{X}, t) \, \mathrm{d}V = 0. \tag{3.66}$$

The local formulation of the mass balance in the material representation follows as

$$\frac{\partial}{\partial t} \varrho_\mathrm{R}(\boldsymbol{X}, t) = 0 \Longleftrightarrow \varrho_\mathrm{R} = \varrho_\mathrm{R}(\boldsymbol{X}). \tag{3.67}$$

According to the general equation (3.60b) it follows for the spatial representation

$$\frac{\mathrm{d}}{\mathrm{d}t} \varrho + \varrho \, \mathrm{div} \, \boldsymbol{v} = 0. \tag{3.68}$$

3.2.3. Balance of Linear Momentum

The linear momentum $\boldsymbol{p} : (\mathcal{B}, t) \to \mathbb{R}^3$ characterizes the kinetic state of a material body. It combines the velocity and mass distribution of the body and is defined as

$$\boldsymbol{p}(\mathcal{B}, t) = \int_\omega \boldsymbol{v}(\boldsymbol{x}, t) \, \varrho(\boldsymbol{x}, t) \, \mathrm{d}v = \int_\Omega \boldsymbol{v}(\boldsymbol{X}, t) \, \varrho_\mathrm{R}(\boldsymbol{X}) \, \mathrm{d}V. \tag{3.69}$$

The balance of linear momentum resembles *Newton*'s second law, according to which the sum of all forces acting on a body is equal to the time rate of change of its momentum. In the context of continuum mechanics, forces[8] appear as surface and volume forces leading to

$$\frac{\mathrm{d}\boldsymbol{p}}{\mathrm{d}t} = \frac{\mathrm{d}}{\mathrm{d}t} \int_\omega \boldsymbol{v}\varrho \, \mathrm{d}v = \int_{\partial\omega} \boldsymbol{t} \, \mathrm{d}a + \int_\omega \boldsymbol{k}\varrho \, \mathrm{d}v, \tag{3.70a}$$

$$\frac{\mathrm{d}\boldsymbol{p}}{\mathrm{d}t} = \frac{\mathrm{d}}{\mathrm{d}t} \int_\Omega \boldsymbol{v}\varrho_\mathrm{R} \, \mathrm{d}V = \int_{\partial\Omega} \boldsymbol{t}_\mathrm{R} \, \mathrm{d}A + \int_\Omega \boldsymbol{k}\varrho_\mathrm{R} \, \mathrm{d}V. \tag{3.70b}$$

---

[8]For a full discussion of force in the continuum context see [Truesdell, 1991].

The quantity $\boldsymbol{k}$ represents a force density per unit mass[9] such as acceleration or gravity. The surface force density $\boldsymbol{t}$ is called Cauchy stress vector. Due to Cauchy's lemma the stress vectors depend linearly on the unit normal vectors. In the spatial representation this leads to the Cauchy stress tensor

$$\boldsymbol{t} = \mathbf{T}\boldsymbol{n}. \tag{3.71}$$

The components of the Cauchy stress tensor describe the surface force acting on a material surface element in the current configuration

$$\mathrm{d}\boldsymbol{f} = \boldsymbol{t}\,\mathrm{d}a = \mathbf{T}\,\mathrm{d}\boldsymbol{a}. \tag{3.72}$$

Similar to strain tensors, also stress tensors can be expressed with respect to different configurations. In the material representation this leads to the first Piola-Kirchhoff stress tensor

$$\boldsymbol{t}_{\mathrm{R}} = \mathbf{T}_{\mathrm{R}}\boldsymbol{n}_{\mathrm{R}}. \tag{3.73}$$

It describes the force acting on the surface in the reference configuration and defines the Piola-Kirchhoff stress vector $\boldsymbol{t}_{\mathrm{R}}$. The physical action of the force still takes place in the current configuration[10] leading to the force vector

$$\mathrm{d}\boldsymbol{f} = \boldsymbol{t}_{\mathrm{R}}\,\mathrm{d}A = \mathbf{T}_{\mathrm{R}}\,\mathrm{d}\boldsymbol{A}. \tag{3.74}$$

The differential surface forces $\mathrm{d}\boldsymbol{f}$ given by equations (3.72) and (3.74) obviously have to be equal. Together with the transformation rule of material surface elements (3.17) this yields the relationship between the stress tensors

$$\mathbf{T}_{\mathrm{R}} = \mathbf{T}(\det \mathbf{F})\mathbf{F}^{-\mathrm{T}}. \tag{3.75}$$

With the help of the stress tensors, the surface integrals of equations (3.70a) and (3.70b) can be transformed into volume integrals. To this end, the stress vector is replaced by the corresponding stress tensor formulation (3.71) or (3.73) and then the divergence theorem is applied. In the current configuration this leads to

$$\frac{\mathrm{d}}{\mathrm{d}t}(\varrho\boldsymbol{v}) + \varrho\boldsymbol{v}\mathrm{div}\,\boldsymbol{v} = \mathrm{div}\,\mathbf{T} + \varrho\boldsymbol{k}, \tag{3.76}$$

which can be further simplified with the balance of mass (3.68) and gives

$$\varrho\frac{\mathrm{d}}{\mathrm{d}t}\boldsymbol{v} = \mathrm{div}\,\mathbf{T} + \varrho\boldsymbol{k}. \tag{3.77a}$$

The procedure is the same for the reference configuration and leads to

$$\varrho_{\mathrm{R}}\frac{\mathrm{d}}{\mathrm{d}t}\boldsymbol{v} = \mathrm{Div}\,\mathbf{T}_{\mathrm{R}} + \varrho_{\mathrm{R}}\boldsymbol{k}. \tag{3.77b}$$

---

[9]Some authors, see for example [Altenbach and Altenbach, 1994, p. 129], also define a body force density for the reference configuration. Due to the results of the balance of mass, both densities are equal and a different notation is therefore omitted in this text.

[10]Since $\mathrm{d}\boldsymbol{A}$ and $\mathrm{d}\boldsymbol{f}$ are associated with the reference and current configuration, respectively, the first Piola-Kirchhoff stress tensor is a two-point tensor.

3.2.4. Balance of Moment of Momentum

The rotational or moment of momentum is similar to the linear momentum a vector $\boldsymbol{m} : (\mathcal{B}, t) \rightarrow \mathbb{R}^3$ that characterizes the kinetic state of a material body. It is defined as

$$\boldsymbol{m}(\mathcal{B}, t) = \int_\omega (\boldsymbol{x} - \boldsymbol{c}) \times \boldsymbol{v}\varrho\, \mathrm{d}v = \int_\Omega (\boldsymbol{\chi}_\mathrm{R} - \boldsymbol{c}) \times \boldsymbol{v}\varrho_\mathrm{R}\, \mathrm{d}V, \tag{3.78}$$

where $\boldsymbol{c}$ is an arbitrary but fixed reference point in space. The balance of rotational momentum corresponds to the Euler equations of a rigid body, see for example [Szabó, 1996, p. 30]. It states, that the time rate of change of the rotational momentum is equal to the moment exerted by all forces acting on the body. The resulting moment of the external forces is given in terms of surface and volume integrals, which lead to

$$\frac{\mathrm{d}\boldsymbol{m}}{\mathrm{d}t} = \frac{\mathrm{d}}{\mathrm{d}t} (\boldsymbol{x} - \boldsymbol{c}) \times \boldsymbol{v}\varrho\, \mathrm{d}v = \int_{\partial\omega} (\boldsymbol{x} - \boldsymbol{c}) \times \boldsymbol{t}\, \mathrm{d}a + \int_\omega (\boldsymbol{x} - \boldsymbol{c}) \times \boldsymbol{k}\varrho\, \mathrm{d}v. \tag{3.79}$$

This statement can be expressed in local form with the relation of the Cauchy stress tensor (3.71) and the divergence theorem. This results in the symmetry of the Cauchy stress tensor

$$\mathbf{T} = \mathbf{T}^\mathrm{T}. \tag{3.80}$$

For details of the mathematical derivation with and without component representation compare [Haupt, 2000, p. 99] and [Ogden, 1997, p. 148] respectively.

From equation (3.75) follows that the first Piola-Kirchhoff stress tensor is unsymmetric and satisfies

$$\mathbf{T}_\mathrm{R}\mathbf{F}^\mathrm{T} = \mathbf{F}\mathbf{T}_\mathrm{R}^\mathrm{T} \Longleftrightarrow \mathbf{T}_\mathrm{R} = \mathbf{F}\mathbf{T}_\mathrm{R}^\mathrm{T}\mathbf{F}^{-\mathrm{T}}. \tag{3.81}$$

3.2.5. Balance of Energy - First Law of Thermodynamics

When surface and volume forces act on a body, work is done and energy is supplied to the body. In addition to this, energy can be supplied in the form of heat and further non-mechanical work. In the case of pure mechanical processes the balance of mechanical energy is a direct consequence of the balance equations for mass and momentum. The statement is just as universally valid as the basic balance equations themselves. In the general case the balance of energy establishes the equivalence of mechanical and non-mechanical work introduced e.g. by thermal, electro-magnetical, or chemical processes. The total energy of a body $\mathcal{B}$ consists[11] of kinetic K and internal energy E. The kinetic energy is defined by a volume integral as

$$K(\mathcal{B}, t) = \int_\omega \tfrac{1}{2}\boldsymbol{v} \cdot \boldsymbol{v}\varrho\, \mathrm{d}v. \tag{3.82}$$

---

[11]In general the total energy also includes potential energy. In many engineering applications this energy part plays only an insignificant role and is neglected in many contributions on continuum mechanics.

The internal energy is also an extensive quantity, thus given by the integration over the specific internal energy e as

$$E(\mathcal{B}, t) = \int_\omega e\varrho \, \mathrm{d}v. \tag{3.83}$$

It is the remainder of the total energy after subtracting the kinetic energy. Often it consists of strain energy, potential energy, thermal energy, or chemical energy. Of course further energy forms are conceivable.

Due to external loads and internal sources the total energy changes. The time rate of change is equal to the power of external forces L and the resultant heat supply Q leading to

$$\dot{K}(\mathcal{B}, t) + \dot{E}(\mathcal{B}, t) = L(\mathcal{B}, t) + Q(\mathcal{B}, t). \tag{3.84}$$

The power of external forces includes the action of surface and volume forces

$$L(\mathcal{B}, t) = \int_{\partial\omega} \boldsymbol{t} \cdot \boldsymbol{v} \, \mathrm{d}a + \int_\omega \boldsymbol{k} \cdot \boldsymbol{v}\varrho \, \mathrm{d}v. \tag{3.85}$$

Thermal energy can be supplied to a material body by heat conduction through its surface and heat radiation distributed over its volume

$$Q(\mathcal{B}, t) = -\int_{\partial\omega} \boldsymbol{q} \cdot \boldsymbol{n} \, \mathrm{d}a + \int_\omega r\varrho \, \mathrm{d}v. \tag{3.86}$$

Here the heat flow density is given by the scalar product of the normal vector $\boldsymbol{n}$ and the vector $\boldsymbol{q}$, which is called Cauchy heat flux vector. Its minus sign is due to the convention that the heat flow is positive if the material body absorbs energy. The scalar r denotes the specific thermal energy production, which can be due to radiation or internal processes.

Using the definitions of the individual physical quantities (3.82), (3.83), (3.85), and (3.86), the balance of energy reads in the current configuration

$$\frac{\mathrm{d}}{\mathrm{d}t} \int_\omega \left(\tfrac{1}{2} \boldsymbol{v} \cdot \boldsymbol{v} + e \right) \varrho \, \mathrm{d}v = \int_{\partial\omega} \mathbf{T}\boldsymbol{n} \cdot \boldsymbol{v} \, \mathrm{d}a + \int_\omega \boldsymbol{k} \cdot \boldsymbol{v}\varrho \, \mathrm{d}v - \int_{\partial\omega} \boldsymbol{q} \cdot \boldsymbol{n} \, \mathrm{d}a + \int_\omega r\varrho \, \mathrm{d}v. \tag{3.87}$$

Applying the divergence theorem yields

$$\int_\omega (\boldsymbol{v} \cdot \dot{\boldsymbol{v}} + \dot{e}) \, \varrho \, \mathrm{d}v = \int_\omega \left[\operatorname{div} \left(\mathbf{T}^\mathsf{T}\boldsymbol{v} \right) + \boldsymbol{k} \cdot \boldsymbol{v}\varrho - \operatorname{div} \boldsymbol{q} + r\varrho \right] \mathrm{d}v. \tag{3.88}$$

With the product rule $\operatorname{div} \left(\mathbf{T}^\mathsf{T}\boldsymbol{v} \right) = (\operatorname{div} \mathbf{T}) \cdot \boldsymbol{v} + \mathbf{T} \cdot \operatorname{grad} \boldsymbol{v}$, the symmetry of $\mathbf{T}$, and the definition of the strain rate tensor $\mathbf{D}$ according to equation (3.41) this can be written as

$$\int_\omega \left(\frac{\mathrm{d}e}{\mathrm{d}t} + \underline{\boldsymbol{v} \cdot \dot{\boldsymbol{v}}} \right) \varrho \, \mathrm{d}v = \int_\omega (\mathbf{T} \cdot \mathbf{D} - \operatorname{div} \boldsymbol{q} + r\varrho) \, \mathrm{d}v + \int_\omega \underline{(\operatorname{div} \mathbf{T} + \boldsymbol{k}\varrho)} \cdot \boldsymbol{v} \, \mathrm{d}v. \tag{3.89}$$

According to the balance of linear momentum (3.70a) the underlined terms are equal and the expression (3.89) further simplifies to

$$\int_{\omega} \left(\frac{\mathrm{d}e}{\mathrm{d}t} - \frac{1}{\varrho} \mathbf{T} \cdot \mathbf{D} + \mathrm{div}\, \boldsymbol{q} - r \right) \varrho\, \mathrm{d}v = 0. \tag{3.90}$$

Thus, the local balance of energy reads in the current configuration

$$\frac{\mathrm{d}e}{\mathrm{d}t} = \frac{1}{\varrho} \mathbf{T} \cdot \mathbf{D} - \frac{1}{\varrho} \mathrm{div}\, \boldsymbol{q} + r. \tag{3.91a}$$

For the material representation follows analogously

$$\frac{\mathrm{d}e}{\mathrm{d}t} = \frac{1}{\varrho_{\mathrm{R}}} \tilde{\mathbf{T}} \cdot \dot{\mathbf{E}} - \frac{1}{\varrho_{\mathrm{R}}} \mathrm{Div}\, \boldsymbol{q}_{\mathrm{R}} + r. \tag{3.91b}$$

In this formulation a further stress tensor and heat flux vector are introduced. The second Piola-Kirchhoff stress tensor is defined by

$$\tilde{\mathbf{T}} := (\det \mathbf{F})\, \mathbf{F}^{-1} \mathbf{T} \mathbf{F}^{-\mathrm{T}}. \tag{3.92}$$

The definition ensures the equality of the specific stress power expressed in terms of variables of the current and reference configuration

$$\frac{1}{\varrho} \mathbf{T} \cdot \mathbf{D} = \frac{\det \mathbf{F}}{\varrho_{\mathrm{R}}} \mathbf{T} \cdot \mathbf{F}^{-\mathrm{T}} \dot{\mathbf{E}} \mathbf{F}^{-1} = \frac{1}{\varrho_{\mathrm{R}}} \tilde{\mathbf{T}} \cdot \dot{\mathbf{E}}. \tag{3.93}$$

In this expression the relation (3.51) of the strain rate tensor $\mathbf{D}$ and the time rate of the Green strain tensor $\mathbf{E}$ are used. By equation (3.75) the first and the second Piola-Kirchhoff stress tensors are related by

$$\mathbf{T}_{\mathrm{R}} = \mathbf{F}\tilde{\mathbf{T}}. \tag{3.94}$$

In the energy balance in the material representation (3.91b) the Piola-Kirchhoff heat flux vector $\boldsymbol{q}_{\mathrm{R}}$, which operates on the reference configuration, is introduced. The vector is related to the Cauchy heat flux vector by

$$\boldsymbol{q}_{\mathrm{R}} = (\det \mathbf{F})\, \mathbf{F}^{-1} \boldsymbol{q}. \tag{3.95}$$

3.2.6. Principle of Irreversibility - Second Law of Thermodynamics

The first law of thermodynamics states, that the total energy of an isolated system is conserved and is only transformed from one energy form to another one. There is no information provided on the direction and kind of the transformation. Although it is

known from experience, that real processes are directional, i.e. they proceed in a certain chronological order and are irreversible. It is observed for example, that heat flows only from hot to cool regions and that gas flows from a high-pressure to low-pressure region. The (so far) missing information on the direction and kind of energy transformation is given by the second law of thermodynamics on the basis of the concepts of temperature and entropy. Both are considered to be primitive variables with the temperature θ being an intensive and the entropy S an extensive variable. The entropy can be viewed as a measure for the amount of energy, which has been transformed irreversibly, see [Altenbach and Altenbach, 1994].

In physical systems an entropy production corresponds to irreversible changes and a conservation of the entropy value is associated with reversible changes of the system. From experience it is known that reversible processes are mere ideal limit cases, which do not occur in nature, [Stephan et al., 2009]. Formally a balance statement for the entropy can be stated as

$$\frac{\mathrm{d}S}{\mathrm{d}t} = \frac{\mathrm{d}}{\mathrm{d}t} \int_\omega s\varrho \, \mathrm{d}v = \int_\omega (\pi + \sigma) \, \mathrm{d}v - \int_{\partial\omega} \boldsymbol{\phi} \cdot \boldsymbol{n} \, \mathrm{d}a. \tag{3.96}$$

According to the second law of thermodynamics, entropy can only be produced but never annihilated, i.e. for the production term holds

$$\int_\omega \pi \, \mathrm{d}v > 0. \tag{3.97}$$

In classical thermodynamics, which is concerned with thermodynamic states of equilibrium, the entropy supply σ and the entropy flux $\boldsymbol{\phi}$ are related to the supply and transport of thermal energy and temperature θ. Even though the temperature has a physical background in equilibrium thermodynamics, it is just defined formally in non-equilibrium thermodynamics: a positive scalar is assigned to each material point and all times

$$\theta \colon \begin{cases} \mathcal{B} \times \mathbb{R} & \to \mathbb{R}^+ \\ (\mathcal{P}, t) & \mapsto \theta(\mathcal{P}, t) = \bar{\theta}(\boldsymbol{x}, t) = \hat{\theta}(\boldsymbol{X}, t). \end{cases} \tag{3.98}$$

The scalar θ is called absolute temperature or thermodynamic temperature. Mathematically, it can be interpreted as an integrating denominator, see e.g. [Stephan et al., 2009].

The entropy flux is driven by the heat flux over the surface of the body and is given as the quotient of the heat flux vector and the absolute temperature

$$\boldsymbol{\phi} = \frac{1}{\theta} \boldsymbol{q}. \tag{3.99}$$

Accordingly, the volume distributed entropy supply is the quotient of the radiation (heat production) and absolute temperature

$$\sigma = \frac{1}{\theta} r. \tag{3.100}$$

The relations (3.99) and (3.100) hold strictly only for equilibrium states of single component systems. For example in mixtures, a more general form of the entropy flux has to be postulated, see [Haupt, 2000]. For non-equilibrium processes, there is still a controversy on the correct formulation of the entropy flux and supply, see e.g. [Muschik, 1998].

Nevertheless, for processes close to equilibrium the relations (3.99) and (3.100) are good approximations and are commonly used in continuum thermomechanics. Inserting equations (3.97), (3.99), and (3.100) into the balance of entropy (3.96) leads to the so-called Clausius-Duhem inequality

$$\frac{\mathrm{d}}{\mathrm{d}t} \int_\omega s\varrho \,\mathrm{d}v \geq \int_\omega \frac{1}{\theta} r\varrho \,\mathrm{d}v - \int_{\partial\omega} \frac{1}{\theta} \boldsymbol{q} \cdot \boldsymbol{n} \,\mathrm{d}a. \tag{3.101}$$

The local form of the Clausius-Duhem inequality is achieved under adequate continuity assumptions by the application of the divergence theorem. The standard procedure yields

$$\varrho \dot{s}\theta \geq \varrho r - \operatorname{div} \boldsymbol{q} + \frac{1}{\theta} \operatorname{grad} \theta \cdot \boldsymbol{q}. \tag{3.102}$$

In this representation, the first two terms on the right-hand side can be substituted with the help of the energy balance (3.91a)

$$\varrho r - \operatorname{div} \boldsymbol{q} = \varrho \dot{e} - \mathbf{T} \cdot \mathbf{D}. \tag{3.103}$$

The substitution leads to

$$\varrho \frac{\mathrm{d}}{\mathrm{d}t}(\theta s - e) - \varrho s \frac{\mathrm{d}\theta}{\mathrm{d}t} + \mathbf{T} \cdot \mathbf{D} - \frac{1}{\theta} \operatorname{grad} \theta \cdot \boldsymbol{q} \geq 0. \tag{3.104a}$$

In the material representation the Clausius-Duhem inequality takes on the form

$$\varrho_R \frac{\partial}{\partial t}(\theta s - e) - \varrho_R s \frac{\partial\theta}{\partial t} + \tilde{\mathbf{T}} \cdot \dot{\mathbf{E}} - \frac{1}{\theta} \operatorname{Grad} \theta \cdot \boldsymbol{q}_R \geq 0. \tag{3.104b}$$

The energy density

$$\psi := e - \theta s \tag{3.105}$$

is called the (specific) free energy, Helmholtz free energy, or just Helmholtz energy. It is used in the formulation of many material models (including the one of this work) and related to other thermodynamic potentials by Legendre transformations, refer to [Haupt, 2000, p. 488] for further details.

3.2.7. Coupling of Balance Equations

All balance equations have to be fulfilled simultaneously bearing in mind that these are coupled with each other. The change of one field has an effect on the other field. In this

work the balance of momentum (3.77a) and the balance of energy (3.91a) are coupled by their field quantities.

For the thermal field, the temperature θ is chosen as field variable. According to the principle of local action, see [Haupt, 2000, p. 257], the materials behavior of a local point is governed by its close neighborhood. Thus, the right Cauchy-Green tensor C is chosen as field variable for the mechanical field. Both fields are coupled via their material equations.

The interdependence in the case of thermomechanical coupling, as considered in this work, is depicted in Fig. 3.6.

heat production due to mechanical work
$w\left(\mathbf{C}, \dot{\mathbf{C}}, \theta, \dot{\theta}, \mathbf{q}\right)$

$$
\begin{aligned}
\mathbf{0} &= \operatorname{Div} \mathbf{T}_{\mathrm{R}} + \varrho_{\mathrm{R}} \boldsymbol{k} \\
\tilde{\mathbf{T}} &= \mathbf{h}\left(\mathbf{C}, \theta, \mathbf{q}\right) \\
\dot{\mathbf{q}} &= \boldsymbol{f}\left(\mathbf{C}, \theta, \mathbf{q}\right)
\end{aligned}
$$

Mechanical Field

Thermal Field

$$
c_{\mathrm{d}} \dot{\theta} = -\frac{1}{\varrho_{\mathrm{R}}} \operatorname{Div} \boldsymbol{q}_{\mathrm{R}} + r + w
$$

heat flux $\boldsymbol{q}_{\mathrm{R}}\left(\mathbf{C}, \theta\right)$

thermal expansion
$\check{\mathbf{F}}_{\theta} = \varphi(\theta)\mathbf{1}$
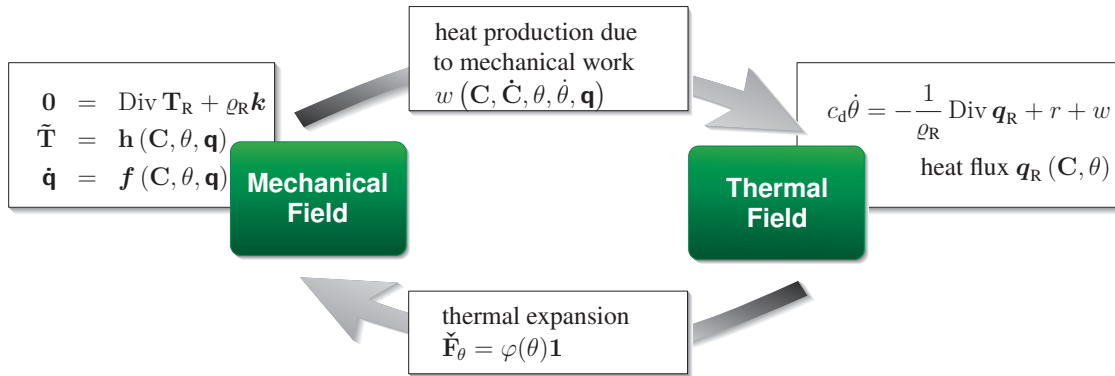
Figure 3.6.: Thermomechanical Coupling

On the one hand, when mechanical work is supplied to a material body the resulting deformation causes heat production. One can distinguish heat production due to thermoelastic coupling, internal energy storage and plastic dissipation. The heat production is described in detail in Sec. 4.2. It depends on the value of internal variables **q** (describing the materials state), the right Cauchy-Green tensor, the temperature, and their time derivatives. Furthermore, the heat flux $\boldsymbol{q}_{\mathrm{R}}$ is not only a function of temperature but also depends on the deformation.

On the other hand, a change of temperature influences the mechanical field. First of all, it causes thermal expansion or contraction (depending on the sign of the temperature change). In Sec. 4.1.1 the thermally induced change of volume is assumed to be isotropic. Moreover, for a given deformation the state of stress depends on the value of the temperature and the internal variables. The evolution of the internal variables in turn is strongly influenced by θ. Details on the material model and the temperature dependence are given in Sec. 4.1.

In general, a change of temperature or state of stress can also result in a change of the material phase. During the process of phase transformation latent heat is relased or absorbed by the material body without a change of temperature. In many cases the mechanical properties have strongly changed, after a phase transformation. Phase transformations are not included in the material model used in this work.

4. Material Model

Exposed to the same external loads, different materials can behave in entirely different ways. For the steel 51CrV4 and the intended application, the thermomechanical material behavior in monotonous loading processes is most important. With the relations that have been covered up to now, it is impossible to predict the response of a material body and thus to determine the thermomechanical behavior of the workpiece. The missing link is given by constitutive equations, also referred to as material models.

4.1. Large Strain Thermoviscoplasticity Model for 51CrV4

The following model captures the main thermomechanical behavior of steel 51CrV4 in processes dominated by monotonous loading. It uses the method of internal variables to account for inelastic behavior and fulfills the basic requirements on constitutive equations, in particular the principle of material frame indifference and thermomechanical consistency. According to Lion [2000] it is advantageous to base phenomenological equations on rheological models. These allow an easily accessible interpretation and in most cases automatically lead to a thermomechanically consistent formulation, see also [Altenbach and Altenbach, 1994, p. 226].

4.1.1. Rheological Model

The present constitutive model is motivated by the one-dimensional rheological model of Fig. 4.1. It consists of an elastic (reversible deformations) and an inelastic (irre-
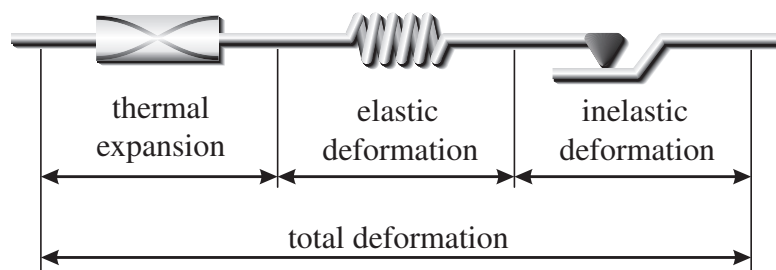
Figure 4.1.: Rheological model of constitutive equations

versible deformations) part. The reversible deformation can be split into a purely mechanical part, indicated by the spring in the middle, and a thermal expansion part, depicted by the element on the most left. Irreversible deformations arise after exceeding the yield stress, remain after removing external loads, and are usually associated with plasticity. According to the multiple splits, the model can be viewed as an extension of the model proposed in [Helm, 2006], where only inelastic and thermoelastic deformations are distinguished. This leads to different kinematical relations as discussed in the next section.

In the stress-strain diagram Fig. 2.4a of the steel 51CrV4 it is seen that the yield stress is significantly lower after it has been subjected to tensile stresses above the initial yield stress and is afterwards loaded in reverse direction. To capture this important phenomenon, referred to as the Bauschinger effect or kinematic hardening, the plastic deformation could be represented by a Kelvin-Voigt type model, as done in App. A.5.2. In general isotropic and kinematic hardening coexist, but experience shows that kinematic hardening is dominant in many cases, cf. [Haupt and Lion, 1995]. From Fig. 2.4 can be inferred that kinematic hardening is also dominant in the case of 51CrV4. However, in the present work monotonous loading processes are in the main focus. For these processes it is shown in [Hakansson et al., 2005] that both isotropic and kinematic hardening are suitable models and yield satisfactory results. Hence, isotropic hardening is chosen in the following to describe the hardening behavior due to its simplicity. Regarding cyclic processes, the two approaches admittedly lead to significant differences in the stress and temperature distributions.

The friction element in Fig. 4.1 resembles the total inelastic deformation, including hardening and viscous effects. Lion [2000] pointed out that rheological models including plasticity and hardening effects can be motivated by physical processes on the microscopic scale. Plasticity is attributed to local inelastic slip processes, while hardening can be interpreted as the spatial average of local elastic lattice deformations caused by dislocations. The inelastic deformations cause the stress power which is dissipated as heat and can be associated with a pronounced thermal influence. For metals a strong temperature-dependence of the inelastic material properties is often observed, cf. [Lubliner, 2008, p. 85]. Plastic deformations that take place at high temperatures do not produce any work-hardening. These deformations are known as hot-working, where the characteristic temperature is the so-called recrystallization temperature, which is typically between 35% to 50% of the melting temperature of the metal. These aspects have to be considered in the following.

4.1.2. Kinematical Relations and Measures of Stress

To decompose the deformation in the various parts induced by the rheological model the multiplicative split of the deformation gradient can be applied, cf. [Lubarda, 2004]. The procedure can be traced back to [Eckart, 1948], where a local relaxed state for inelastic deformations is introduced. In its present form it is originally developed in [Lee, 1969]

for elastoplastic and in [Lu and Pister, 1975] for thermoelastic deformations.[1] Here, following the proposals in [Lion, 2000] and [Meggyes, 2001], both splits are applied, resulting in a multiple multiplicative decomposition of the deformation gradient

$$\mathbf{F} = \check{\mathbf{F}}_r \mathbf{F}_i = \hat{\mathbf{F}}_e \check{\mathbf{F}}_\theta \mathbf{F}_i. \tag{4.1}$$

It consists of a multiplicative decomposition of the deformation gradient $\mathbf{F}$ into a reversible part $\check{\mathbf{F}}_r$ and an inelastic part $\mathbf{F}_i$. The latter includes viscous and plastic effects. The reversible part $\check{\mathbf{F}}_r$ is further decomposed into an elastic $\hat{\mathbf{F}}_e$ and a thermal $\check{\mathbf{F}}_\theta$ part, where $\hat{\mathbf{F}}_e$ is the stress-producing part of the deformation gradient.

Apparently, the proposed multiplicative decomposition of the deformation gradient is not unique. Arbitrary rotations of the intermediate configurations can be included as demonstrated by Haupt [2000, p. 435]. Thus, in addition to the assumption of frame-invariance all constitutive equations have to be invariant with respect to the free choice of $\bar{\mathbf{Q}}$. The decomposition induces two additional intermediate configurations denoted by $\check{\chi}_t$ and $\hat{\chi}_t$ which are illustrated in Fig. 4.2. The thermal intermediate configuration
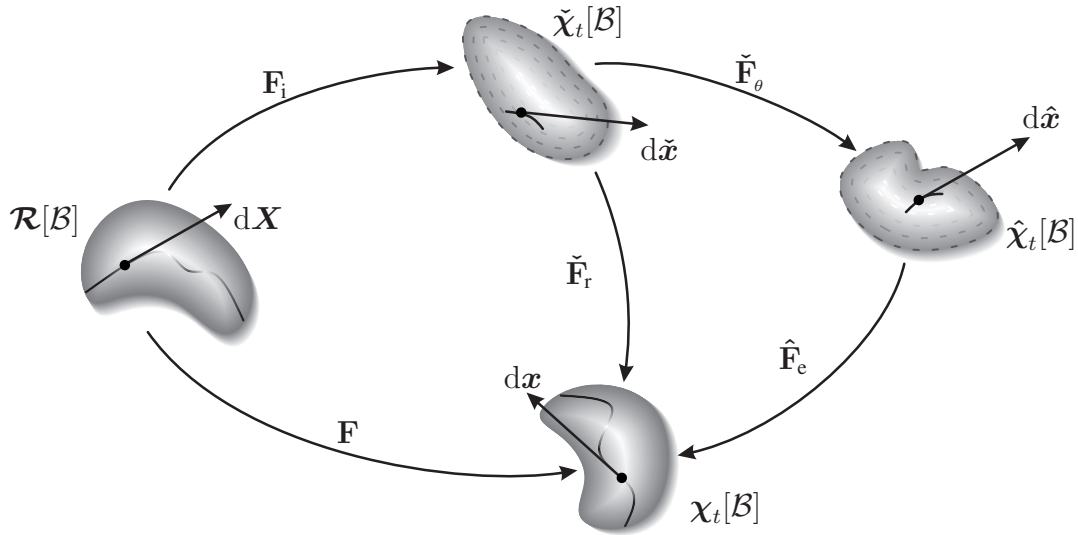
Figure 4.2.: Configurations implied by the multiplicative split of the deformation gradient

$\hat{\chi}_t$ is equal to the unloaded (stress-free) configuration in finite strain plasticity and is in the following the basis for the formulation of the stress-strain relation.

In addition to the kinematical relations introduced in Sec. 3.1, further relations are implied by the decomposition. Transferring the Green strain tensor to the inelastic in-

---

[1] Refer also to [Helm, 2006] for further references and remarks on the origin of the multiplicative split of the deformation gradient.

termediate configuration $\check{\chi}_t$ results in

$$\check{\Gamma} = \mathbf{F}_i^{-T}\mathbf{E}\mathbf{F}_i^{-1} = \tfrac{1}{2}\left(\check{\mathbf{F}}_r^T\check{\mathbf{F}}_r - \mathbf{1}\right) + \tfrac{1}{2}\left(\mathbf{1} - \mathbf{F}_i^{-T}\mathbf{F}_i^{-1}\right) = \check{\Gamma}_r + \check{\Gamma}_i. \tag{4.2}$$

In this configuration the total strain can be additively decomposed into a purely reversible part

$$\check{\Gamma}_r = \tfrac{1}{2}\left(\check{\mathbf{C}}_r - \mathbf{1}\right), \qquad \check{\mathbf{C}}_r := \check{\mathbf{F}}_r^T\check{\mathbf{F}}_r \tag{4.3}$$

and a purely inelastic part

$$\check{\Gamma}_i = \tfrac{1}{2}\left(\mathbf{1} - \mathbf{B}_i^{-1}\right), \qquad \mathbf{B}_i := \mathbf{F}_i\mathbf{F}_i^T. \tag{4.4}$$

The tensor $\check{\Gamma}_r$ has the structure of the Green strain tensor and consists only of reversible deformation components, i.e. deformations due to thermal expansion and stresses within the elastic range. According to the concept of dual variables (refer to [Haupt, 2000, p. 314ff.]), derivatives of Oldroyd type are introduced for the inelastic configuration. For the following only the covariant derivative

$$(\overset{\triangle}{\cdot}) = (\overset{\centerdot}{\cdot}) + \mathbf{L}_i^T(\,\cdot\,) + (\,\cdot\,)\mathbf{L}_i, \qquad \mathbf{L}_i := \dot{\mathbf{F}}_i\mathbf{F}_i^{-1}, \tag{4.5}$$

is needed. Consequently, the rate of the Green strain tensor can also be splitted additively in the intermediate configuration

$$\overset{\triangle}{\check{\Gamma}} = \mathbf{F}_i^{-T}\dot{\mathbf{E}}\mathbf{F}_i^{-1} = \dot{\check{\Gamma}} + \mathbf{L}_i^T\check{\Gamma} + \check{\Gamma}\mathbf{L}_i = \overset{\triangle}{\check{\Gamma}}_r + \overset{\triangle}{\check{\Gamma}}_i. \tag{4.6}$$

The rate of the inelastic part takes on a remarkably simple form. Transferring the purely inelastic part (4.4) to the reference configuration leads to the inelastic strain tensor $\mathbf{E}_i$. Computing the material time derivative of this tensor and transferring the result back to the inelastic intermediate configuration leads to the Oldroyd derivative

$$\overset{\triangle}{\check{\Gamma}}_i = \tfrac{1}{2}\left(\mathbf{L}_i^T + \mathbf{L}_i\right). \tag{4.7}$$

It is the symmetric part of the inelastic velocity gradient $\mathbf{L}_i$ and is sometimes called the inelastic strain rate tensor, as can been seen by comparison with equation (3.41).

Alternatively, the strain behavior can be expressed with respect to the thermal configuration $\hat{\chi}_t$. Transferring the Green strain tensor from the reference configuration to this configuration results in $\hat{\Gamma} = (\check{\mathbf{F}}_\theta\mathbf{F}_i)^{-T}\mathbf{E}(\check{\mathbf{F}}_\theta\mathbf{F}_i)^{-1} = \check{\mathbf{F}}_\theta^{-T}\check{\Gamma}\check{\mathbf{F}}_\theta^{-1}$. Regarding the reversible part of the strain tensor $\check{\Gamma}_r$ in the thermal configuration, one obtains

$$\hat{\Gamma}_r = \check{\mathbf{F}}_\theta^{-T}\check{\Gamma}_r\check{\mathbf{F}}_\theta^{-1} = \tfrac{1}{2}\left(\hat{\mathbf{F}}_e^T\hat{\mathbf{F}}_e - \mathbf{1}\right) + \tfrac{1}{2}\left(\mathbf{1} - \check{\mathbf{F}}_\theta^{-T}\check{\mathbf{F}}_\theta^{-1}\right) = \hat{\Gamma}_e + \hat{\Gamma}_\theta. \tag{4.8}$$

Again the strain tensor splits additively in two parts of Green and Almansi type. The purely elastic part of the deformation is given by

$$\hat{\boldsymbol{\Gamma}}_{\mathrm{e}} = \tfrac{1}{2}\left(\hat{\mathbf{C}}_{\mathrm{e}} - \mathbf{1}\right), \qquad \hat{\mathbf{C}}_{\mathrm{e}} := \hat{\mathbf{F}}_{\mathrm{e}}^{\mathrm{T}}\hat{\mathbf{F}}_{\mathrm{e}}. \tag{4.9}$$

It is this strain tensor that the stress-strain relation is based on in the following. The thermal part reads

$$\hat{\boldsymbol{\Gamma}}_{\theta} = \tfrac{1}{2}\left(\mathbf{1} - \check{\mathbf{B}}_{\theta}^{-1}\right), \qquad \check{\mathbf{B}}_{\theta} := \check{\mathbf{F}}_{\theta}\check{\mathbf{F}}_{\theta}^{\mathrm{T}}, \tag{4.10}$$

where a linear dependence of the thermal deformation gradient on the temperature is assumed. The gradient $\check{\mathbf{F}}_{\theta}$ is further assumed to represent isotropic expansion and is therefore given with the coefficient of linear thermal expansion α as

$$\check{\mathbf{F}}_{\theta} := (1 + \alpha\vartheta)\mathbf{1} = \varphi(\theta)\mathbf{1}, \qquad \vartheta := \theta - \theta_{\mathrm{i}}. \tag{4.11}$$

Additionally, the change of temperature ϑ is introduced here. Due to the special form of $\check{\mathbf{F}}_{\theta}$, the thermal gradient is symmetric and can be easily inverted. Thus, one obtains directly the relations

$$\check{\mathbf{C}}_{\theta} = \varphi^2\mathbf{1}, \quad \hat{\boldsymbol{\Gamma}}_{\theta} = \tfrac{1}{2}(1 - 1/\varphi^2)\mathbf{1}, \quad \check{\mathbf{F}}_{\theta}^{-1} = 1/\varphi\,\mathbf{1}, \quad \text{and} \quad \dot{\check{\mathbf{F}}}_{\theta} = \varphi'(\theta)\dot{\theta}\mathbf{1}, \tag{4.12}$$

where $\varphi'(\theta)$ denotes the derivative of φ with respect to θ. For the following investigation also the covariant derivative with respect to the thermal configuration is required. It is used to compute the stress power with respect to the thermal configuration and is given by

$$(\overset{\triangle}{\cdot}) = (\overset{\bullet}{\cdot}) + \mathbf{L}_{\theta\mathrm{i}}^{\mathrm{T}}(\,\cdot\,) + (\,\cdot\,)\mathbf{L}_{\theta\mathrm{i}}, \qquad \mathbf{L}_{\theta\mathrm{i}} := \dot{\mathbf{F}}_{\theta\mathrm{i}}\mathbf{F}_{\theta\mathrm{i}}^{-1} = (\dot{\check{\mathbf{F}}}_{\theta}\mathbf{F}_{\mathrm{i}} + \check{\mathbf{F}}_{\theta}\dot{\mathbf{F}}_{\mathrm{i}})(\mathbf{F}_{\mathrm{i}}^{-1}\check{\mathbf{F}}_{\theta}^{-1}). \tag{4.13}$$

Taking into account the special form of the thermal deformation gradient, the thermal-inelastic velocity gradient can be further simplified to

$$\mathbf{L}_{\theta\mathrm{i}} = \frac{\varphi'(\theta)}{\varphi}\dot{\theta}\mathbf{1} + \mathbf{L}_{\mathrm{i}}. \tag{4.14}$$

In addition to the kinematical relations, also the transformation behavior of stress tensors is important for the subsequent derivation. According to the results of Haupt [2000, p. 316], the various stress tensors transform as

$$\check{\mathbf{S}} = \mathbf{F}_{\mathrm{i}}\tilde{\mathbf{T}}\mathbf{F}_{\mathrm{i}}^{\mathrm{T}}, \quad \hat{\mathbf{S}} = \check{\mathbf{F}}_{\theta}\check{\mathbf{S}}\check{\mathbf{F}}_{\theta}^{\mathrm{T}}, \quad \mathbf{S} = \check{\mathbf{F}}_{\mathrm{r}}\check{\mathbf{S}}\check{\mathbf{F}}_{\mathrm{r}}^{\mathrm{T}}, \quad \text{and} \quad \mathbf{S} = \hat{\mathbf{F}}_{\mathrm{e}}\hat{\mathbf{S}}\hat{\mathbf{F}}_{\mathrm{e}}^{\mathrm{T}}. \tag{4.15}$$

Fig. 4.3 summarizes the transformations of the different strain, strain rate, and stress tensors. Using these relationships, the second law of thermodynamics can be evaluated in the various configurations. Doing so, additional restrictions on the constitutive equations are derived to further substantiate the model. Finally, these result in evolution equations for the internal variables introduced by the rheological model and further assumptions.

(a) Strain and strain rate transformations   (b) Stress and stress rate transformations
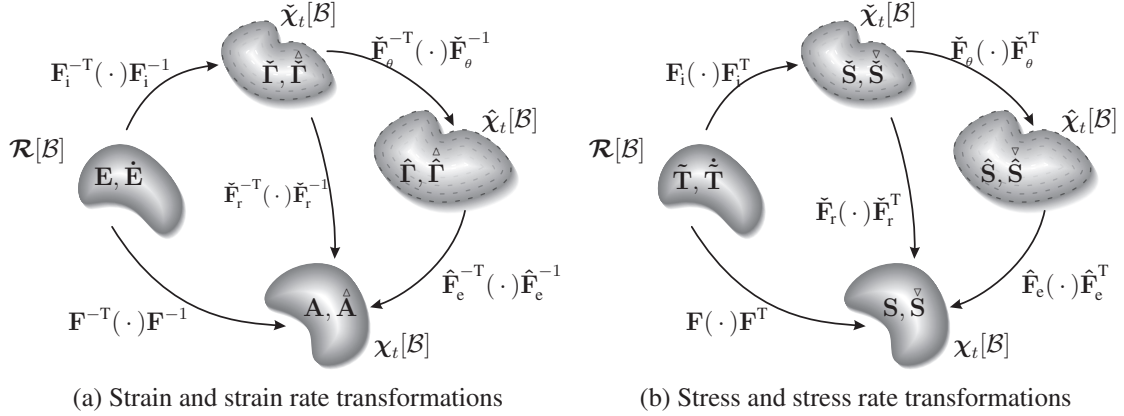
Figure 4.3.: Transformations induced by multiplicative split of the deformation gradient

4.1.3. Derivation of Evolution Equations

The kinematical relations are inserted into the second law of thermodynamics to guarantee the thermomechanical consistency of the model, cf. [Haupt, 2000, p. 491]. To this end, the second law in the form of the Clausius-Duhem inequality (3.104b) is applied and separated into the internal dissipation inequality

$$\delta = -\dot{\psi} - s\dot{\theta} + \frac{1}{\varrho_{\mathrm{R}}}\tilde{\mathbf{T}}\cdot\dot{\mathbf{E}} \geq 0 \tag{4.16a}$$

and the heat conduction inequality

$$-\frac{1}{\theta}\operatorname{Grad}\theta\cdot\boldsymbol{q}_{\mathrm{R}} \geq 0. \tag{4.16b}$$

This is in general a stronger requirement than the inequality (3.104b) itself which holds for many thermodynamical processes, cf. [Truesdell and Noll, 2004, p. 295], and is commonly assumed. The internal dissipation δ in inequality (4.16a) is connected to the entropy production due to thermomechanical processes. This is sometimes referred to as the local entropy production. The heat conduction inequality (4.16b) is used in Sec. 4.1.6 to propose a constitutive equation for the heat flux vector.

Along the lines of the rheological model in Fig. 4.1, the following structure of the free energy is assumed

$$\psi = \psi\big(\hat{\mathbf{\Gamma}}_{\mathrm{e}}, p, p_{\mathrm{s}}, \theta\big) = \psi_{\mathrm{e}}\big(\hat{\mathbf{\Gamma}}_{\mathrm{e}}, \theta\big) + \psi_{\mathrm{i}}\big(p, p_{\mathrm{s}}, \theta\big) + \psi_{\theta}(\theta). \tag{4.17}$$

It depends on the temperature θ, the elastic strain tensor $\hat{\mathbf{\Gamma}}_{\mathrm{e}}$, and two internal variables describing isotropic hardening, p and p_{s}. The rheological model also suggests an additive split in an elastic, a plastic, and a thermal part. The thermal and elastic parts are

associated with the energy stored by reversible thermomechanical processes. They correspond to the element on the left and the spring in the middle of the rheological model, which experience the deformations $\check{\mathbf{F}}_\theta$ and $\hat{\mathbf{F}}_e$, respectively.

The second part in equation (4.17) consists of the energy stored during plastic deformations. In the pioneering work of Taylor and Quinney [1934] it is found that up to 15% of the plastic work is stored in the material. The main part of the plastic work is dissipated in the form of heat. In subsequent works, see [Helm, 1998] and the literature cited therein, even higher amounts of stored energy are found for small plastic deformations. These can reach a maximum of 70% and decrease monotonously with increasing strains. Furthermore, this phenomenon can be related to hardening and thus, incorporated in the constitutive model by a hardening variable. During plastic deformations, dislocations are produced and move within the material. The energy dissipation in form of heat due to this movement can be accounted for by the scalar internal variable p_d. Further, the accumulated plastic strain p, also called equivalent or effective inelastic strain, is used for the description of isotropic hardening in the formulation of the free energy (4.17). The stored energy related to this effect is represented by the internal variable p_s, which is given by the difference $p_s = p - p_d$.

Taking the material time derivative of the free energy (4.17) and inserting the result in the internal dissipation inequality (4.16a) results in

$$
\delta = \left(\frac{1}{\varrho_R} \hat{\mathbf{S}} - \frac{\partial \psi_e}{\partial \hat{\mathbf{\Gamma}}_e} \right) \cdot \overset{\vartriangle}{\hat{\mathbf{\Gamma}}}_e - \left(s + \frac{\partial \psi}{\partial \theta} - \frac{2\varphi'}{\varphi} \hat{\mathbf{\Gamma}}_e \cdot \frac{\partial \psi_e}{\partial \hat{\mathbf{\Gamma}}_e} - \frac{1}{\varrho_R} \varphi \varphi' \operatorname{tr} \hat{\mathbf{S}} \right) \dot{\theta}
$$
$$
+ \left(2\hat{\mathbf{\Gamma}}_e \frac{\partial \psi_e}{\partial \hat{\mathbf{\Gamma}}_e} + \frac{1}{\varrho_R} \check{\mathbf{S}} + \frac{1}{\varrho_R} 2\check{\mathbf{\Gamma}}_\theta \check{\mathbf{S}} \right) \cdot \overset{\vartriangle}{\check{\mathbf{\Gamma}}}_i - \left(\frac{\partial \psi_i}{\partial p} + \frac{\partial \psi_i}{\partial p_s} \right) \dot{p} + \frac{\partial \psi_i}{\partial p_s} \dot{p}_d \geq 0. \quad (4.18)
$$

In this expression the stress power is evaluated in the thermal intermediate configuration $\hat{\chi}_t$ with the previously derived relations of stresses and strains. Additionally, ψ_e is assumed to be an isotropic tensor function of the elastic strain tensor, i.e. $\psi_e(\hat{\mathbf{\Gamma}}_e, \theta) = \psi_e(\mathbf{Q}\hat{\mathbf{\Gamma}}_e\mathbf{Q}^T, \theta)$. This implies that the derivative is coaxial with the strain argument and their product commutes, i.e. $(\partial \psi_e / \partial \hat{\mathbf{\Gamma}}_e)\hat{\mathbf{\Gamma}}_e = \hat{\mathbf{\Gamma}}_e(\partial \psi_e / \partial \hat{\mathbf{\Gamma}}_e)$. Consult [Ogden, 1997, p. 193] for further details.

In the first step, only purely reversible deformations are considered. In this case there is no plastic contribution and all internal variables related to plasticity remain constant. Thus, the rates of p, and p_s, as well as the Oldroyd-rate of $\check{\mathbf{\Gamma}}_i$ vanish identically and the internal dissipation is equal to zero. For arbitrary rates of $\hat{\mathbf{\Gamma}}_e$ and θ within the elastic range this implies potential relations for the stress tensor and the entropy

$$
\hat{\mathbf{S}} = \varrho_R \frac{\partial \psi_e}{\partial \hat{\mathbf{\Gamma}}_e} \quad \text{and} \quad s = -\frac{\partial \psi}{\partial \theta} + \frac{\varphi'}{\varrho_R} \left(\varphi \operatorname{tr} \check{\mathbf{S}} + \frac{2}{\varphi} \hat{\mathbf{\Gamma}}_e \cdot \hat{\mathbf{S}} \right). \quad (4.19)
$$

In the second step, arbitrary deformations, including viscoplastic contributions, are considered. It is assumed that relations (4.19) derived for the purely thermoelastic case are

also valid in the plastic range. For p_s a conjugate stress variable is introduced

$$R := \varrho_\mathrm{R} \frac{\partial \psi_\mathrm{i}}{\partial p_\mathrm{s}}, \tag{4.20}$$

which can be identified as a "back-stress" with a physical interpretation. As plastic deformation proceeds, dislocations multiply and eventually get stuck at obstacles within the metallic lattice. The dislocations pile up at the barriers and introduce local stress fields. These fields act as "back-stresses" which impede the mobility of other dislocations and make the creation of new dislocations more difficult. Even higher stresses are necessary to produce additional plastic deformations. A phenomenon known as work hardening, cf. [Lubliner, 2008, p. 101].

Inserting the definition (4.20) in the dissipation inequality and taking into account the potential relations (4.19) yields

$$\delta = \frac{1}{\varrho_\mathrm{R}} \left(\mathbf{1} + 2\check{\boldsymbol{\Gamma}}_\mathrm{r} \right) \check{\mathbf{S}} \cdot \overset{\triangle}{\check{\boldsymbol{\Gamma}}_\mathrm{i}} - \left(\frac{\partial \psi_\mathrm{i}}{\partial p} + \frac{1}{\varrho_\mathrm{R}} R \right) \dot{p} + \frac{1}{\varrho_\mathrm{R}} R \dot{p}_\mathrm{d} \geq 0. \tag{4.21}$$

This expression can be further simplified with the definition of the Mandel stress tensor

$$\check{\mathbf{P}} := \left(\mathbf{1} + 2\check{\boldsymbol{\Gamma}}_\mathrm{r} \right) \check{\mathbf{S}} = \check{\mathbf{C}}_\mathrm{r} \check{\mathbf{S}}, \tag{4.22}$$

which operates on the inelastic intermediate configuration. As pointed out by Tsakmakis and Willuweit [2004], stress tensors of this type arise in a natural way in the case of finite deformations.

The positiveness of the first term of the dissipation inequality (4.21) is guaranteed by an associated (normality) flow rule of the form

$$\overset{\triangle}{\check{\boldsymbol{\Gamma}}_\mathrm{i}} = \Lambda \frac{\check{\mathbf{P}}^\mathrm{D}}{\left\| \check{\mathbf{P}}^\mathrm{D} \right\|}, \tag{4.23}$$

where Λ is the so-called plastic multiplier and the superscript "D" denotes the deviator operator of a second order tensor $\mathbf{A}^\mathrm{D} = \mathbf{A} - \frac{1}{3}(\mathrm{tr}\,\mathbf{A})\mathbf{1}$. It is generally observed that plastic flow is independent of hydrostatic stress states and thus, solely driven by the deviatoric stress components, cf. [Rösler et al., 2008, p. 86]. The flow rule can be derived by computing the derivative of the yield function of von Mises-type

$$F\left(\check{\mathbf{P}}, R, \theta\right) = \left\| \check{\mathbf{P}}^\mathrm{D} \right\| - \sqrt{\tfrac{2}{3}}(k(\theta) + R). \tag{4.24}$$

It dissects the stress space into an elastic and an inelastic region. Elastic loading of the material occurs if the value of F is negative or equal to zero, i.e. the relative stress measure is below the yield stress $k(\theta) + R$. It is assumed to be temperature-dependent

since a strong temperature influence of the yield stress is reported for metals, cf. [Rösler et al., 2008, p. 195].

The plastic multiplier is assumed to be of Perzyna-type to incorporate viscous effects

$$\Lambda := \frac{1}{\eta} \left\langle \frac{F}{\sigma_0} \right\rangle^m . \tag{4.25}$$

In this expression η and m are parameters which control the viscous behavior and σ_0 is used to normalize the value of the yield function. The brackets $\langle \cdot \rangle$ denote the so called McCauley brackets with the property $\langle x \rangle^m = x^m$ if $x > 0$ and $\langle x \rangle^m = 0$ otherwise. A flow rule of the type (4.23) with the plastic multiplier of equation (4.25) has been originally proposed in [Perzyna, 1963]. It is an extension of the proposal of Hohenemser and Prager [1932], where the exponent is set to unity $m = 1$.

Similarly, the positiveness of the last term in inequality (4.21) (dissipation during hardening) is guaranteed by choosing the evolution of p_d to be proportional to the change of the yield stress

$$\dot{p}_d = \zeta R, \tag{4.26}$$

with the positive scalar valued function $\zeta(\theta)$. This temperature-dependent function is further specified in the following. The variable p_d is the dissipative part of the accumulated plastic strain p. For this, the rate is commonly defined as

$$\dot{p} := \sqrt{\tfrac{2}{3}} \left\| \overset{\triangle}{\check{\Gamma}}_i \right\| = \sqrt{\tfrac{2}{3}} \Lambda, \tag{4.27}$$

where the traditional factor $\sqrt{2/3}$ is chosen such that the model gives in an uniaxial tension test the same value as a one-dimensional model would, see [Lubliner, 2008, p. 69].

4.1.4. Choice of Free Energy

The free energy function given in equation (4.17) represents the different storage mechanisms occurring during thermomechanical deformations. It is additively composed of a purely elastic, a purely inelastic, and a thermal part. Since the temperature also influences the mechanical behavior, also the elastic and inelastic free energies are functions of the temperature θ. The elastic part consists of an isochoric and a dilatoric part, it is given by

$$\varrho_R \psi_e(\hat{\Gamma}_e, \theta) = U(J_e, \theta) + v(I_{\bar{e}}, \theta), \tag{4.28}$$

with the specific parts

$$U(J_e, \theta) = \frac{K(\theta)}{50} \left(J_e^5 + J_e^{-5} - 2 \right), \quad \text{and} \quad v(I_{\bar{e}}, \theta) = \frac{G(\theta)}{2} \left(I_{\bar{e}} - 3 \right), \tag{4.29}$$

where $I_{\bar{e}}$ is the first invariant of the isochoric part of the elastic right Cauchy-Green tensor

$$I_{\bar{e}} := \operatorname{tr} \overline{\mathbf{C}}_e, \qquad \overline{\mathbf{C}}_e := \left(\det \hat{\mathbf{C}}_e \right)^{-1/3} \hat{\mathbf{C}}_e. \tag{4.30}$$

Hence, the tensor $\overline{\hat{\mathbf{C}}}_{\mathrm{e}}$ is unimodular, i.e. the property $\det \overline{\hat{\mathbf{C}}}_{\mathrm{e}} = 1$ holds. This split into a volumetric and isochoric part is based on the suggestion of Flory [1961]. Only the unimodular part of the elastic right Cauchy-Green tensor influences the volume preserving part of the free energy $v(\mathrm{I}_{\bar{\mathrm{e}}}, \theta)$, which is of Neo-Hooke type. The dilatoric part $U(J_{\mathrm{e}}, \theta)$ follows the proposal in Hartmann and Neff [2003] and depends only on the determinant of the elastic deformation gradient $J_{\mathrm{e}} := \det \hat{\mathbf{F}}_{\mathrm{e}}$.

In addition to the elastic part of the free energy, the inelastic behavior of the body also contributes to its energy balance. The inelastic part of the free energy is specified as

$$\varrho_{\mathrm{R}} \psi_{\mathrm{i}}(p, p_{\mathrm{s}}, \theta) = \frac{\gamma(\theta)}{2} p_{\mathrm{s}}^2 + \phi k(\theta) p. \tag{4.31}$$

The first term is the standard assumption for nonlinear isotropic hardening, which has been successfully used for example by Fritsch [2004] for thermomechanical problems, and by Chaboche [1993a] and Hartmann et al. [1997] in an isothermal setting. The second term follows an original idea of Tsakmakis [1998]. It is linear in p and is added to take account of the aforementioned energy storage mechanisms during hardening. The amount of stored energy is specified by the value of ϕ. A higher value of ϕ results in an increased energy storage, while the value $\phi = 0$ is equal to a complete dissipation of the plastic stress power. The term has no effect on the hardening behavior but only influences the energy storage and thus the resulting temperature field in a thermomechanically coupled analysis. This approach is also used in [Jansohn, 1997], [Lämmer, 1998], [Helm, 1998], and [Helm, 2006]. Further remarks on the modeling of energy storage during plastic deformations and a comparison with experimental data are also given by Chaboche [1993b].

Inserting the intermediate results and the inelastic free energy according to equation (4.31) in the dissipation inequality (4.21) results in the compact form of the dissipation inequality

$$\varrho_{\mathrm{R}} \delta = \Lambda \left(F + \sqrt{\tfrac{2}{3}}(1 - \phi)k \right) + \zeta R^2 \geq 0, \tag{4.32}$$

which has to be satisfied for every thermomechanical process. During inelastic deformations, the value of the plastic multiplier Λ, the yield function F, and the temperature-dependent initial yield stress k are positive. For a thermomechanical consistent model, this inequality limits the range of the energy storage parameter ϕ to $0 \leq \phi \leq 1$. Furthermore, with the specific choice of the inelastic part of free energy, the back-stress (change of yield stress) can be given explicitly. Inserting equation (4.31) in the potential relation (4.20) leads to the back-stress

$$R = \gamma(\theta) \, p_{\mathrm{s}} = \gamma(\theta) \, (p - p_{\mathrm{d}}). \tag{4.33}$$

With this result, it is possible to express the rate of the dissipative part of the plastic arc length in terms of p and p_{d}. Inserting the back-stress in the evolution equation yields

$$\dot{p}_{\mathrm{d}} = \zeta R = \Lambda \sqrt{\tfrac{2}{3}} \beta(\theta) \, (p - p_{\mathrm{d}}), \tag{4.34}$$

where the definition $\zeta = \beta/\gamma\dot{p}$ is used. This implies the following rate of the back-stress

$$\dot{R} = \gamma\dot{p} - \left(\beta\dot{p} - \frac{1}{\gamma}\frac{\partial\gamma}{\partial\theta}\dot{\theta}\right) R. \tag{4.35}$$

For a constant temperature or temperature-independent material parameters this differential equation of first order is separable and can be integrated analytically (either by separation or variable substitution, cf. [Greenberg, 1998, p. 46]). For homogeneous initial conditions $R(0) = 0$ MPa, the solution is given in terms of the plastic arc length as

$$R(p) = \frac{\gamma}{\beta}\left(1 - \exp(-\beta p)\right). \tag{4.36}$$

Thus, the material parameters can be interpreted physically. The parameter $\gamma = R'(0)$ is equal to the initial slope of the back-stress, while the parameter β determines its saturation value $R_\infty = \lim_{p\to\infty} R = \gamma/\beta$. This value decreases with higher temperatures and typically tends to zero when the temperature reaches a value between 35% to 50% of the melting temperature of the metal. The qualitative development of the back-stress at constant temperature is depicted in Fig. 4.4, where the back-stress R is plotted versus the plastic arc length p. The nonlinear hardening and the saturation are clearly visible.
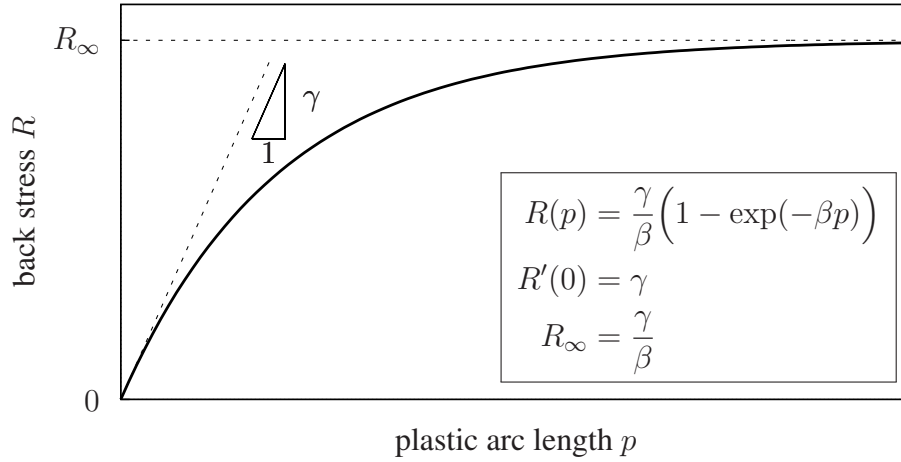
Figure 4.4.: Evolution of back-stress in nonlinear isotropic hardening

Having specified the elastic part of the free energy in equation (4.28) with the specific parts of equation (4.29), it is possible to evaluate the potential relation of the stress tensor. Equation (4.19) yields the stress tensor in the thermal intermediate configuration

$$\hat{\mathbf{S}} = 2\varrho_R\frac{\partial\psi_e}{\partial\hat{\mathbf{C}}_e} = J_e U'(J_e, \theta)\hat{\mathbf{C}}_e^{-1} + J_e^{-2/3}G\left(\mathbf{1} - \tfrac{1}{3}\left(\operatorname{tr}\overline{\hat{\mathbf{C}}}_e\right)\overline{\hat{\mathbf{C}}}_e^{-1}\right) \tag{4.37}$$

$$= \frac{K}{10}\left(J_e^5 - J_e^{-5}\right)\hat{\mathbf{C}}_e^{-1} + G J_e^{-2/3}\left(\mathbf{1} - \tfrac{1}{3}\left(\operatorname{tr}\hat{\mathbf{C}}_e\right)\hat{\mathbf{C}}_e^{-1}\right). \tag{4.38}$$

Further, the Mandel stress tensor given in equation (4.22) can be expressed with the elastic right Cauchy-Green tensor and the stress tensor in the thermal intermediate configuration. To this end, the specific form of the thermal deformation gradient (4.11) is taken into account and leads to

$$\check{\mathbf{P}} = \check{\mathbf{C}}_{\mathrm{r}}\check{\mathbf{S}} = \hat{\mathbf{C}}_{\mathrm{e}}\hat{\mathbf{S}} = \frac{K}{10}\left(J_{\mathrm{e}}^5 - J_{\mathrm{e}}^{-5}\right)\mathbf{1} + GJ_{\mathrm{e}}^{-2/3}\left(\hat{\mathbf{C}}_{\mathrm{e}} - \tfrac{1}{3}\left(\operatorname{tr}\hat{\mathbf{C}}_{\mathrm{e}}\right)\mathbf{1}\right). \qquad (4.39)$$

In the following, the constitutive relations and in particular the evolution equations have to be evaluated and integrated in time. This allows to predict the materials behavior and to make an overall simulation of the thermomechanical metal forming process. The time integration is done in the reference configuration.

4.1.5. Transformation into Reference Configuration

In principle, it is possible to evaluate and integrate the constitutive equations in any configuration. However, the reference configuration plays a special role in that it is constant. That is, arbitrary configurations deform during a general process, which has to be accounted for in the time integration and often leads to low order approximations, refer for example to [Simo and Hughes, 2000, p. 279].

Thus, to be able to apply general high-order time integration methods, all constitutive equations are transformed into the reference configuration. To this end, the relations derived in Sec. 4.1.2 are used. They yield the second Piola-Kirchhoff stress tensor

$$\tilde{\mathbf{T}} = \mathbf{F}_{\theta\mathrm{i}}^{-1}\hat{\mathbf{S}}\mathbf{F}_{\theta\mathrm{i}}^{-\mathrm{T}} = \frac{1}{\varphi^2}\mathbf{F}_{\mathrm{i}}^{-1}\hat{\mathbf{S}}\mathbf{F}_{\mathrm{i}}^{-\mathrm{T}} \qquad (4.40)$$

$$= \frac{K(\theta)}{10}\left(J_{\mathrm{e}}^5 - J_{\mathrm{e}}^{-5}\right)\mathbf{C}^{-1} + G(\theta)J_{\mathrm{e}}^{-2/3}\left(\frac{1}{\varphi^2}\mathbf{C}_{\mathrm{i}}^{-1} - \tfrac{1}{3}\left(\operatorname{tr}\hat{\mathbf{C}}_{\mathrm{e}}\right)\mathbf{C}^{-1}\right), \qquad (4.41)$$

where J_{e} and $\operatorname{tr}\hat{\mathbf{C}}_{\mathrm{e}}$ can be expressed as functions of the right Cauchy Green tensor $\mathbf{C}$ and the inelastic right Cauchy-Green tensor $\mathbf{C}_{\mathrm{i}}$ as

$$J_{\mathrm{e}} = \frac{1}{\varphi^3}\frac{J}{J_{\mathrm{i}}} \quad \text{and} \quad \operatorname{tr}\hat{\mathbf{C}}_{\mathrm{e}} = \frac{1}{\varphi^2}\operatorname{tr}\left(\mathbf{C}_{\mathrm{i}}^{-1}\mathbf{C}\right), \qquad (4.42)$$

where $J := \det\mathbf{F}$ and $J_{\mathrm{i}} := \det\mathbf{F}_{\mathrm{i}}$ are the determinants of the total and the inelastic deformation gradient. Concluding, the stress strain relation of the second Piola-Kirchhoff tensor is of the general form

$$\tilde{\mathbf{T}} = \mathbf{h}(\mathbf{C}, \theta, \mathbf{q}). \qquad (4.43)$$

For the present model, the internal variables $\mathbf{q}$ include the inelastic right Cauchy-Green tensor $\mathbf{C}_{\mathrm{i}}$, the accumulated plastic strain p and its dissipative part p_{d}. The stress itself depends only on the value of the inelastic right Cauchy-Green tensor. This tensor changes

if the yield limit is exceeded, which is given by the yield function (4.24). The evolution is given by

$$\dot{\mathbf{C}}_i = 2\dot{\mathbf{E}}_i = 2\mathbf{F}_i^{\mathrm{T}}\overset{\triangle}{\check{\boldsymbol{\Gamma}}}_i\mathbf{F}_i = 2\Lambda\left(\mathbf{F}_i^{\mathrm{T}}\check{\mathbf{P}}^{\mathrm{D}}\mathbf{F}_i\right)/\|\check{\mathbf{P}}^{\mathrm{D}}\|, \tag{4.44}$$

where the deviator of the Mandel stress tensor reads

$$\check{\mathbf{P}}^{\mathrm{D}} = GJ_{\mathrm{e}}^{-2/3}\hat{\mathbf{C}}_{\mathrm{e}}^{\mathrm{D}} \qquad \text{with} \qquad \mathbf{F}_i^{\mathrm{T}}\hat{\mathbf{C}}_{\mathrm{e}}^{\mathrm{D}}\mathbf{F}_i = \frac{1}{\varphi^2}\mathbf{C} - \tfrac{1}{3}\left(\mathrm{tr}\,\hat{\mathbf{C}}_{\mathrm{e}}\right)\mathbf{C}_i. \tag{4.45}$$

The evolution equations of the accumulated plastic strains (4.27), and (4.34) are independent of the configuration and do not require any transformation. Their values determine the backstress R and thereby the value of the yield function F and the plastic multiplier Λ.

Summarizing, the evolution equations are of the general form

$$\mathbf{A}\dot{\mathbf{q}} = \boldsymbol{r}(\mathbf{C}, \theta, \mathbf{q}), \qquad \mathbf{q}(\boldsymbol{X}, t_i) = \mathbf{q}_i(\boldsymbol{X}). \tag{4.46}$$

Depending on the coefficient matrix $\mathbf{A}$, the evolution equations form an ODE or a DAE. In the case of the currently investigated thermoviscoplastic material model, $\mathbf{A}$ is regular (here $\mathbf{A} = \mathbf{1}$) and (4.46) becomes an ordinary differential equation system.

In addition to the constitutive equations for the mechanical part of the material, relations for the thermal part are required. This regards the ability of the steel 51CrV4 to store and conduct thermal energy.

4.1.6. Constitutive Equation of Heat Flux Vector

For the derivation of the evolution equations, the Clausius-Duhem inequality (3.104b) has been separated into the internal dissipation inequality (4.16a) and a second inequality (4.16b), which describes the entropy production due to heat conduction within the body. Inequality (4.16a) is satisfied for every thermomechanical process, due to the construction of the evolution equations and it remains to find a constitutive relation for the heat flux vector. The most simple relation which satisfies the heat conduction inequality is the popular Fourier's law

$$\boldsymbol{q}_{\mathrm{R}} = -\boldsymbol{\lambda}_{\mathrm{R}}\,\mathrm{Grad}\,\theta, \tag{4.47}$$

which proposes a linear relation between the temperature gradient and the heat flux vector. Here, $\boldsymbol{\lambda}_{\mathrm{R}}$ is the heat conductivity of the material. It is in general a positive definite second order tensor to take account of directional dependencies. In many cases the conductivity tensor is defined with respect to the current configuration

$$\boldsymbol{q} = -\boldsymbol{\lambda}\,\mathrm{grad}\,\theta. \tag{4.48}$$

It can be easily shown (see also (3.95)) that both tensors are related by

$$\boldsymbol{\lambda}_{\mathrm{R}} = (\det\mathbf{F})\,\mathbf{F}^{-1}\boldsymbol{\lambda}\mathbf{F}^{-\mathrm{T}}. \tag{4.49}$$

For isotropic materials, such as the workpieces of 51CrV4, the tensor $\boldsymbol{\lambda}$ degenerates into a scalar λ.

Other, more complicated models for the heat flux have been proposed in the literature. The most frequently criticized shortcoming of Fourier's law is that it leads to a parabolic equation for the temperature field, which implies an instantaneous distribution of information throughout the entire medium. This behavior contradicts the principle of causality and is known as the 'paradox of heat conduction'. By adding a thermal inertia term the behavior can be corrected, as for example done in the Maxwell-Cattaneo model for heat conduction, cf. [Christov, 2009]. However, this model can lead to a contradiction of the second law of thermodynamics. This deficiency is in turn overcome by the relativistic heat conduction model, cf. [Ali and Zhang, 2005]. This model is known to be compatible with the theory of special relativity, the second law of thermodynamics, electrodynamics, and quantum mechanics, simultaneously. Nevertheless, there is also some criticism of this model and a number of conceptual issues are highly controversial.

The effect of finite heat propagation has a strong impact for small scales of time and length. However, for metallic materials of technically relevant dimensions, this effect can be neglected. See also the discussion in [Helm, 2001, p. 62]. Thus, the linear Fourier's law is used in the following to model the heat conduction and energy balance of the steel 51CrV4. This is further substantiated in the following.

4.2. Derivation of Heat Conduction Equation

The transfer of thermal energy within a body is referred to as heat conduction. It takes place from regions of higher temperatures to regions of lower temperatures, as given by the heat flux vector. Physically, heat flux is due to the combination of vibrations of the molecules in the metallic lattice of 51CrV4 and the energy transport by free electrons. In addition to this, heat can also be transferred by radiation and convection. Often several processes occur simultaneously and constitute a supply of thermal energy to a work piece (material body).

During thermomechanical processes mechanical energy is transformed into thermal energy. The local form of the balance of energy (3.91b) establishes the link between mechanical and non-mechanical work and also accounts for the transfer of thermal energy within a body.

In this work temperature θ is chosen as global variable to describe the thermal state of the body. For this quantity, a partial differential equation, describing the spatial and temporal evolution, can be derived from the balance of energy. To this end, the specific internal energy e is expressed in terms of the specific free energy ψ, the entropy s, and the temperature using equation (3.105). Inserting the time derivative in the balance of energy (3.91b) results in

$$\dot{\psi} + \dot{\theta}s + \theta\dot{s} = \frac{1}{\varrho_R}\tilde{\mathbf{T}} \cdot \dot{\mathbf{E}} - \frac{1}{\varrho_R}\operatorname{Div}\boldsymbol{q}_R + r. \tag{4.50}$$

With the internal dissipation δ, given by equation (4.16a), one arrives at the compact expression

$$\theta \dot{s} = \delta - \frac{1}{\varrho_R} \operatorname{Div} \boldsymbol{q}_R + r, \tag{4.51}$$

with the internal dissipation according to equation (4.21). The entropy is given by the potential relation (4.19) and thus, depends on the elastic right Cauchy-Green tensor $\hat{\mathbf{C}}_e$, the plastic arc length p, the energy storing part of the plastic arc length p_s, and the temperature θ. Substituting the total time derivative of the entropy yields

$$\theta \frac{\partial s}{\partial \theta} \dot{\theta} = \delta - \theta \left(\frac{\partial s}{\partial \hat{\mathbf{C}}_e} \cdot \dot{\hat{\mathbf{C}}}_e + \frac{\partial s}{\partial p_s} \dot{p}_s + \frac{\partial s}{\partial p} \dot{p} \right) - \frac{1}{\varrho_R} \operatorname{Div} \boldsymbol{q}_R + r. \tag{4.52}$$

In this expression,

$$c_d := \theta \frac{\partial s}{\partial \theta} \tag{4.53}$$

is referred to as the specific heat at constant deformation (see also [Haupt, 2000, p. 513]) and

$$w := \delta - \theta \left(\frac{\partial s}{\partial \hat{\mathbf{C}}_e} \cdot \dot{\hat{\mathbf{C}}}_e + \frac{\partial s}{\partial p_s} \dot{p}_s + \frac{\partial s}{\partial p} \dot{p} \right), \qquad w = -w_e + w_p - w_s \tag{4.54}$$

is the heat production due to internal dissipation. According to [Helm, 1998, p. 85], this term can be further split into three parts with a physical meaning. It consists of a thermoelastic coupling part

$$- w_e := -\theta \frac{\partial s}{\partial \hat{\mathbf{C}}_e} \cdot \dot{\hat{\mathbf{C}}}_e, \tag{4.55}$$

a plastic dissipation part due to the stress power of plastic strains

$$w_p := \frac{1}{\varrho_R} \check{\mathbf{P}} \cdot \overset{\triangle}{\dot{\boldsymbol{\Gamma}}}_i = \frac{1}{\varrho_R} \Lambda \left(F + \sqrt{\tfrac{2}{3}} (k + R) \right), \tag{4.56}$$

and an energy storing part which is given by the stress power due to a change of internal variables

$$- w_s := \frac{1}{\varrho_R} \zeta R^2 - \theta \left(\frac{\partial s}{\partial p_s} \dot{p}_s + \frac{\partial s}{\partial p} \dot{p} \right) - \frac{1}{\varrho_R} \Lambda \sqrt{\tfrac{2}{3}} k \phi. \tag{4.57}$$

With the definitions of the specific heat and the heat production, the heat conduction equation is given in the reference configuration as

$$c_d \dot{\theta} = -\frac{1}{\varrho_R} \operatorname{Div} \boldsymbol{q}_R + r + w. \tag{4.58}$$

Equivalently, it can be expressed in the current configuration

$$c_d \dot{\theta} = -\frac{1}{\varrho} \operatorname{div} \boldsymbol{q} + r + w. \tag{4.59}$$

The derived expressions are valid for arbitrary thermomechanical processes. In the case of metal plasticity small elastic strains are commonly assumed to simplify the equations and the numerical treatment, cf. [Helm, 2001; Jansohn, 1997; Lührs, 1997; Lührs et al., 1997]. The applicability and its implications are considered in the next chapter.

4.3. Assumption of Small Elastic Strains

Elastic strains in a plastically deformed metal (in metal forming applications) are only of the order 10^{-3}, while plastic strains of the order unity are not unusual, cf. [Lee, 1969].[2] Thus, elastic strains are often neglected in finite deformation plasticity equations, resulting in a simplified theory, cf. [Lubliner, 2008, p. 490]. In this case, the main implication is a simplified transformation between configurations, cf. [Haupt, 2000, p. 451]. Regarding the transformation, it is assumed that the elastic stretch tensor is approximately the unity tensor, $\hat{\mathbf{U}}_e \approx \mathbf{1}$, and thus the elastic deformation gradient equals the elastic rotation tensor, $\hat{\mathbf{F}}_e \approx \hat{\mathbf{R}}_e$. One speaks of small elastic strains and arbitrary rotations. The resulting form of the associated flow rule is then the same as in small-deformation theory. The stress-strain relation is, however, not modified and used in its original form.

In the following, it is also assumed that the elastic strains are small next to unity, $\|\hat{\mathbf{C}}_e - \mathbf{1}\| \ll 1$. Contrary to the aforementioned approach, all equations are treated equal and linearized with respect to the elastic right Cauchy-Green tensor.

4.3.1. Thermomechanical Relations

Under the assumption that the stress tensor in the thermal configuration is analytic, it can be expanded into an infinite series. Dropping all nonlinear terms of the Taylor series at the point $\hat{\mathbf{C}}_e = \mathbf{1}$ results in

$$\hat{\mathbf{S}}(\hat{\mathbf{C}}_e, \cdot) \approx \hat{\mathbf{S}}(\mathbf{1}, \cdot) + D\hat{\mathbf{S}}(\mathbf{1}, \cdot)\big[\hat{\mathbf{C}}_e - \mathbf{1}\big]. \tag{4.60}$$

Here, only the dependence on the elastic right Cauchy-Green tensor $\hat{\mathbf{C}}_e$ is regarded. The dependence on other variables is indicated by the centered dot. In the final formulation, the stress tensor is of course given as a function of the total right Cauchy-Green tensor $\mathbf{C}$, the temperature θ, the temperature gradient $\mathrm{Grad}\,\theta$, and internal variables $\mathbf{q}$, as stated in equation (4.43). The second summand represents the directional derivative of the stress tensor in the direction of the change of the elastic Cauchy-Green tensor $\hat{\mathbf{C}}_e - \mathbf{1}$. Forming the derivative of equation (4.38) and computing its value at $\hat{\mathbf{C}}_e = \mathbf{1}$ one arrives at

$$\hat{\mathbf{S}} = \frac{K}{2}\left(\mathrm{tr}\,\hat{\mathbf{C}}_e - 3\right)\mathbf{1} + G\hat{\mathbf{C}}_e^{\mathrm{D}}. \tag{4.61}$$

---

[2]Plastic deformations under high pressure, which occur for example in explosive forming, also produce finite elastic strains. In this case the assumption of small elastic strains and the implied simplifications can not be justified.

The Mandel stress tensor given by equation (4.39) is treated along the same lines. It can be easily shown that the linearized Mandel stress in the inelastic configuration is equal to the linearized stress tensor in the thermal configuration

$$\check{\mathbf{P}} \approx \hat{\mathbf{S}}. \tag{4.62}$$

For the application of high-order time integration methods, all quantities are needed in the reference configuration. To this end, the linearization is applied to the transformed (nonlinear) quantities.

4.3.2. Transformation into Reference Configuration

The nonlinear second Piola-Kirchhoff stress tensor (4.41) is linearized at $\hat{\mathbf{C}}_e = \mathbf{1}$, which yields

$$\tilde{\mathbf{T}} = \frac{K}{2\varphi^2} \left(\frac{\text{tr}(\mathbf{C}\mathbf{C}_i^{-1})}{\varphi^2} - 3 \right) \mathbf{C}_i^{-1} + \frac{G}{\varphi^4} \left(\mathbf{C}_i^{-1}\mathbf{C}\mathbf{C}_i^{-1} - \tfrac{1}{3} \text{tr}(\mathbf{C}\mathbf{C}_i^{-1})\mathbf{C}_i^{-1} \right). \tag{4.63}$$

The same result can be obtained by transforming the linearized stress tensor of the thermal configuration, given by equation (4.61), into the reference configuration. In addition to the stress tensor, the evolution equations of the internal variables are required. However, equation (4.44) can not be linearized, since it includes the normal direction given by the deviator of the Mandel stress tensor $\check{\mathbf{P}}$.[3] Instead, the already linearized Mandel stress tensor of equation (4.62) is inserted and leads to

$$\dot{\mathbf{C}}_i = 2\Lambda \frac{\frac{1}{\varphi^2}\mathbf{C} - \tfrac{1}{3}\left(\text{tr}\, \hat{\mathbf{C}}_e \right) \mathbf{C}_i}{\| \hat{\mathbf{C}}_e^{\mathrm{D}} \|} = 2\Lambda \frac{\mathbf{C} - \tfrac{1}{3} \text{tr}\left(\mathbf{C}\mathbf{C}_i^{-1} \right) \mathbf{C}_i}{\sqrt{\mathbf{C}_i^{-1}\mathbf{C} \cdot \mathbf{C}\mathbf{C}_i^{-1} - \tfrac{1}{3} \text{tr}\left(\mathbf{C}\mathbf{C}_i^{-1} \right)^2}}. \tag{4.64}$$

Accordingly, the linearized Mandel stress tensor is also used to compute the value of the yield function (4.24) and thus the plastic multiplier Λ of equation (4.25).

Consistent with the present approach, the quantities related to the energy balance are linearized with respect to the elastic right Cauchy-Green tensor.

4.3.3. Heat Conduction Equation

According to the definition of the heat capacity (4.53), c_d is given by the product of the absolute temperature θ and the temperature derivative of the entropy s. The entropy

---

[3]This is similar to the one-dimensional expression of the sign function $\text{sgn}\, x = x/|x|$, for which a meaningful linearization at $x = 0$ is not available either.

itself can be computed with the potential relation (4.19) and reads

$$s = -\frac{\partial \psi_\theta}{\partial \theta} - \frac{1}{\varrho_R} \left[\frac{K'(\theta)}{50} \left(J_e^5 + J_e^{-5} - 2 \right) + \frac{G'(\theta)}{2} \left(I_{\bar{e}} - 3 \right) \right.$$
$$\left. - \frac{3K\alpha}{10\varphi} \left(J_e^5 - J_e^{-5} \right) + \frac{\gamma'(\theta)}{2} p_s^2 + \phi k'(\theta) p \right]. \quad (4.65)$$

Computing its derivative with respect to temperature and linearizing the result yields

$$c_d = -\theta \left[\frac{\partial^2 \psi_\theta}{\partial \theta^2} + \frac{1}{\varrho_R} \frac{3\alpha}{2\varphi} \left(\frac{\alpha}{\varphi} K - K'(\theta) \right) \mathrm{tr} \left(\mathbf{CC}_i^{-1} - \mathbf{1} \right) \right.$$
$$\left. + \left(\frac{\gamma''(\theta)}{2} p_s^2 + \phi k''(\theta) p \right) \right]. \quad (4.66)$$

In accordance with the previous simplifications, the deformation-dependent part of the heat capacity can be neglected in the case of steel 51CrV4 and the intended range of application. Thus, the common approximation

$$c_d \approx -\theta \frac{\partial^2 \psi_\theta}{\partial \theta^2} \quad (4.67)$$

is even during thermomechanical processes a sufficient approximation of the heat capacity, see also [Jansohn, 1997, p. 33]. The thermal part of the free energy ψ_θ can be chosen to reflect the thermal behavior seen in the DSC-measurements in Sec. 2.2.1.

Furthermore, the heat production due to internal dissipation is needed for the complete definition of the heat conduction equation. The heat production due to thermoelastic coupling (4.55) converts under the assumption of small elastic strains to

$$- w_e = -\theta \frac{1}{\varrho_R} \frac{3K\alpha}{2\varphi} \mathrm{tr} \, \dot{\mathbf{C}}_e = -\theta \frac{1}{\varrho_R} \frac{3K\alpha}{2\varphi} \frac{\mathrm{d}}{\mathrm{d}t} \left(\frac{1}{\varphi^2} \mathrm{tr}(\mathbf{CC}_i^{-1}) \right). \quad (4.68)$$

Inserting the time derivatives of the plastic arc lengths in equation (4.57), the heat production due to energy storage can be written as

$$- w_s = \frac{1}{\varrho_R} \left(\frac{\beta}{\gamma} R^2 + \theta \gamma'(\theta) (p - p_d) \left(1 - \frac{\beta}{\gamma} R \right) + \theta \varphi k'(\theta) - k\varphi \right) \dot{p}. \quad (4.69)$$

The heat production due to internal dissipation is a function of the displacement, temperature, their velocities, and internal variables,

$$w = \hat{w} \big(\mathbf{C}, \dot{\mathbf{C}}, \theta, \dot{\theta}, \mathbf{q} \big). \quad (4.70)$$

The most significant amount of heat is produced during plastic deformations according to equation (4.56). The model is now completely defined for thermomechanical processes with small elastic deformations. It still remains to determine the material parameters.

4.4. Parameter Identification

The parameters of the proposed material model have to be identified according to the experimental results of Chp. 2. This identification has to be done for the thermomechanical as well as the thermophysical properties.

4.4.1. Thermomechanical Properties

First of all, the significance of the thermomechanical parameters and their influence on the stress-strain curve are regarded. To this end, the stress response of a uniaxial tension test with a constant strain rate of $\dot{\varepsilon}_{xx} = 0.002 \text{ s}^{-1}$ is computed. At $t = 20$ s, the axial strain is held at a constant level of $\varepsilon_{xx} = 0.04$. The described test is repeated several times where all parameters but one are fixed. The fixed parameters are set according to Tab. 4.1 and the varied parameter is indicated in the respective plot.

In the first test, the isotropic hardening parameter β is varied and the resulting stress evolution is shown in Fig. 4.5a. Increasing the value of β lowers the maximal back-stress R_∞, as implied by equation (4.36). The hardening parameter γ has a similar

(a) Isotropic hardening parameter β

(b) Isotropic hardening parameter γ
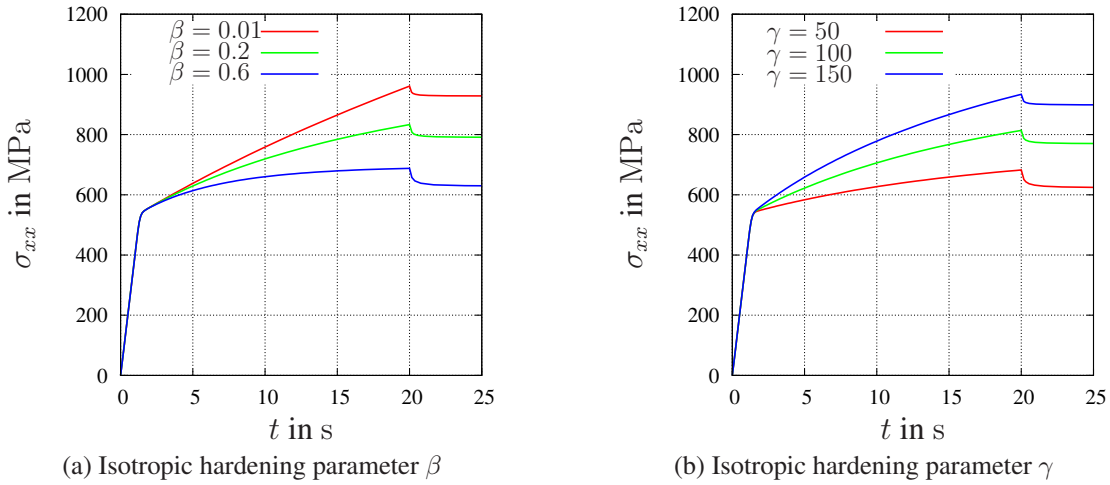
Figure 4.5.: Influence of hardening parameters on material behavior

effect on the resulting stress curve. Increasing γ increases the maximal back-stress R_∞, which scales linearly with the hardening parameter. Both parameters have a contrary effect and one or the other can be used to achieve a specified back-stress. Moreover, by simultaneously adjusting both parameters (keeping the quotient γ/β constant), the curvature of the stress curve can be fitted to given data.

Next, the initial yield stress k_0 and the viscosity η are varied. Changing k_0 in Fig. 4.6a moves the begin of yielding on the stress curve in vertical direction. The shape of the stress curve itself is not influenced. Even though, the material starts to yield at the

prescribed value of k_0, this point is not clearly visible in the curves. At the begin of plastic flow the internal variables grow at a moderate rate which increases with further developed plastic strains. This causes the yield limit to appear to be at a higher level. In contrast to the initial yield stress k_0, the viscosity η has a strong influence on the

(a) Initial yield stress k_0 (b) Viscosity η
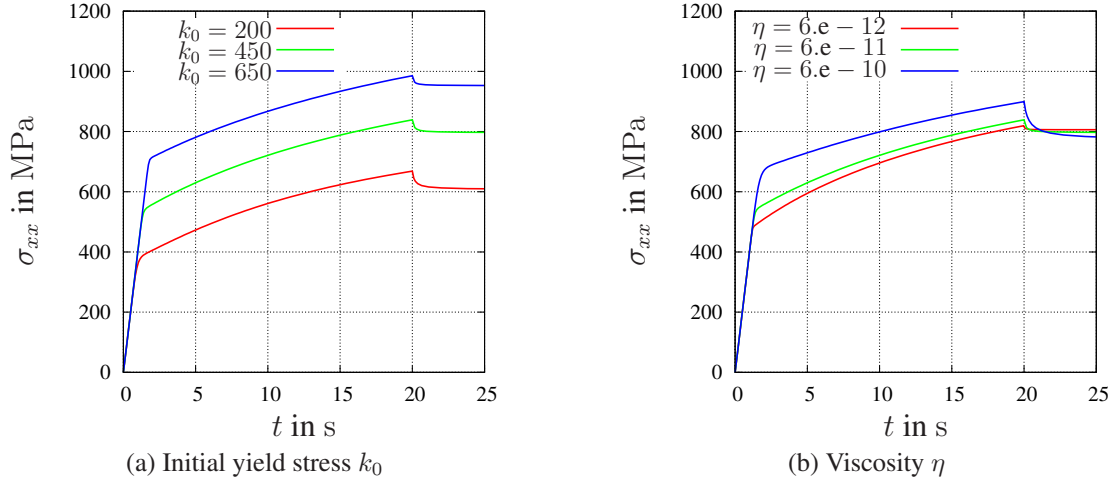
Figure 4.6.: Influence of parameters on material behavior

materials velocity dependence and the shape of the stress curve. Higher values of η produce higher over stresses, as seen in the relaxation phase for $t \geq 20$ s in Fig. 4.6b. Furthermore, the transition from the elastic to the plastic region is more smooth.

Now, that the influence of the material parameters is known, they can be easily fitted by hand. In the first step, the elastic parameters are determined. The elastic modulus E is given by the initial slope of the experimental stress-strain curve. Assuming a Poisson's number[4] of $\nu = 0.3$ results in the values for the bulk modulus K_0 and the shear modulus G_0 at room temperature as specified in Tab. 4.1. In the second step the inelastic parameters are fitted. The value of k_0 is given by the beginning of plastic flow and the hardening behavior determines the values of γ and β. The relaxation characteristic finally specifies the viscosity η. The additional parameters which define the plastic multiplier in equation (4.25) are set to $\sigma_0 = G_0$ and $m = 2$. With the material parameters of Tab. 4.1 the experimental and theoretical stress curves in Fig. 4.8a correspond to a sufficient degree.

Not only the isothermal properties are important. Of central interest is the thermomechanical behavior of the material. Unfortunately, experimental data is not available for 51CrV4. Due to this lack the values of these parameters have to be chosen on the grounds of theoretical considerations.

On the basis of the well known metallic bonding model, it can be argued that Young's elasticity modulus E varies approximately linearly with temperature, refer to Rösler

---

[4]The relations between elastic parameters are given for example in [Haupt, 2000, p. 186].

Table 4.1.: Material parameters

K_0	c_K	G_0	c_G	k_0	k_H	γ	η	β_0	β_H	b	α
GPa	MPa/°C	GPa	MPa/°C	MPa	MPa	MPa	-	-	-	1/°C	1/°C
167	-91	76.9	-42	450	100	110	6e-11	0.19	1	42e-4	1.2e-5

et al. [2008, p. 60]. A similar dependence is also seen in computations with the multi-phase alloy program JMatPro.[5] This program is based on thermodynamic modeling and calculations which are augmented by theoretical material models and properties databases. This approach allows a quantitative calculation of mechanical properties, and thermophysical and physical properties, cf. [Guo et al., 2010, 2009; Saunders et al., 2003]. Based on these considerations, a linear temperature dependence of the elastic moduli is assumed

$$K(\theta) = K_0 + c_K(\theta - \theta_0), \qquad G(\theta) = G_0 + c_G(\theta - \theta_0) \tag{4.71}$$

and depicted in Fig. 4.7a. Technically more relevant than the change of elastic proper-

(a) Bulk and shear modulus

(b) Initial yield stress k
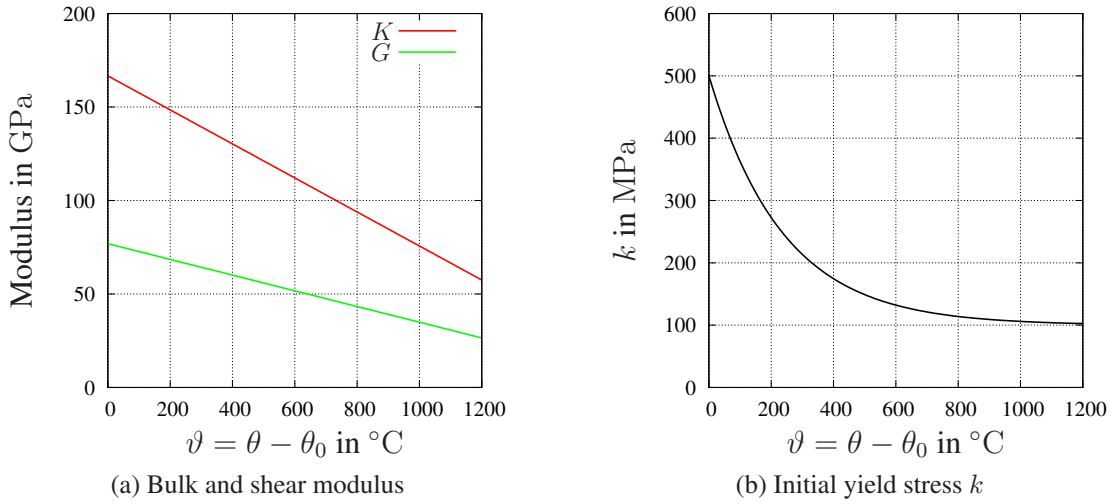
Figure 4.7.: Temperature influence on material parameters

ties is the change of the plastic behavior. In hot-working, i.e. at temperatures above the recrystallization temperature (typically 35 to 50% of the melting point in Kelvin), plastic deformations do not produce any work hardening, anisotropy, or the Bauschinger effect. Furthermore, it is well known that temperature has a significant influence on the yield strength. At higher temperatures steel shows softening, i.e. a decrease of the

---

[5]The computational results using JMatPro were provided by the work group of Prof. Maier from the University of Paderborn.

yield strength, and deforms plastically at lower stresses. This behavior can be explained by the Boltzmann-law of thermodynamics, which describes the probability of a process to take place. It is also the basis of the Arrhenius equation which governs many thermally activated physico-chemical processes, see [Rösler et al., 2008, p. 194] and [Lubliner, 2008, p. 85]. The equation states that the rate of the process is proportional to $\exp(-\Delta E/(k_\mathrm{B}\theta))$, where ΔE is the activation energy of the process, k_B is the Boltzmann's constant, and θ is the absolute temperature in K.

In the present model all evolution equations, such as the rate of the inelastic right Cauchy-Green tensor according to equation (4.44), are proportional to the plastic multiplier. The plastic multiplier Λ itself is according to equation (4.25) proportional to the value of the yield function (4.24). Motivated by the Arrhenius equation and the aforementioned effects, an exponential temperature dependence is assumed for the yield stress k and the hardening parameter β according to

$$k(\theta) = (k_0 - k_\mathrm{H})\mathrm{e}^{-b(\theta-\theta_0)} + k_\mathrm{H}, \qquad \beta(\theta) = (\beta_0 - \beta_\mathrm{H})\mathrm{e}^{-b(\theta-\theta_0)} + \beta_\mathrm{H}. \qquad (4.72)$$

This temperature dependence is depicted for the yield stress in Fig. 4.7b. Numerical values of the chosen parameters for the yield stress and the hardening parameter are also contained in Tab. 4.1. Using the full set of parameters, the material response is computed for different temperatures between room temperature and $\vartheta = 1200\,°\mathrm{C}$. The resulting stress curves are shown in Fig. 4.8a. For the time integration the implicit method of

(a) Flow curves at different temperatures

(b) Step size behavior, with refined time steps at yield point
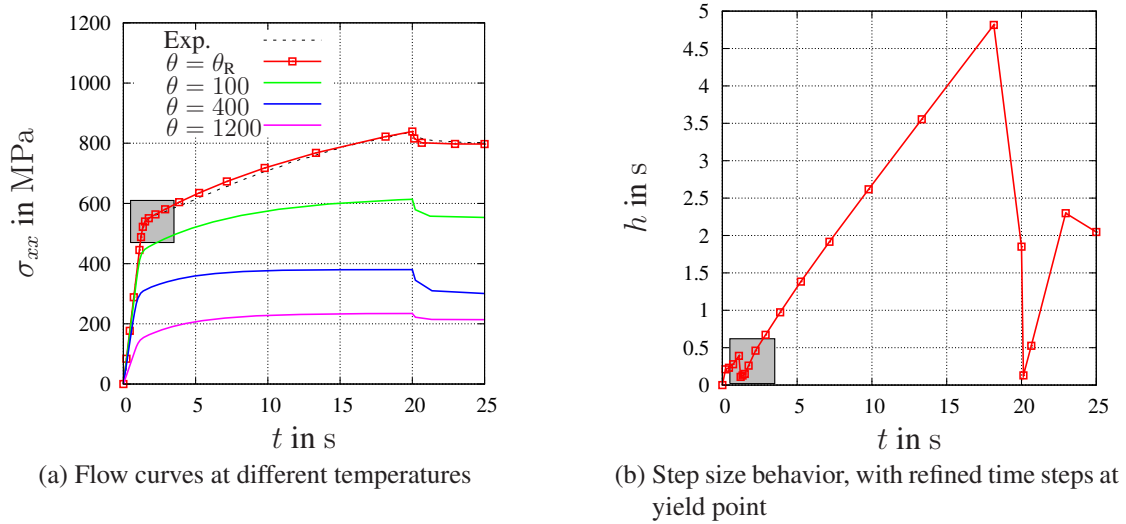
Figure 4.8.: Flow curves with fitted material parameters

Ellsiepen using adaptive step size control is applied. Refer to Sec. 5.5.4 for details on the applied time integration methods. The error estimator automatically resolves the transition from elastic to plastic behavior by choosing small time steps, indicated by the

small box in Fig. 4.8b. At the same time it is highly efficient by allowing large time steps in the smooth regions of pure elastic or plastic behavior.

4.4.2. Thermophysical Properties

The heat capacity and the emissivity are strongly influenced by the phase transformation of the material between $700\,°C$ and $800\,°C$ (see Figs. 2.9b and 2.11b). In order to obtain a reasonable temperature-dependent phenomenological constitutive model, the logarithmic interpolation concept of Kreisselmeier and Steinhauser [1979] is applied. According to the investigations in [Bier and Hartmann, 2006] the interpolation formula (weighted mean) of two scalar functions $y_1 = f_1(x)$ and $y_2 = f_2(x)$

$$f(x) = -c \ln \left(\frac{e^{-f_1(x)/c} + e^{-f_2(x)/c}}{2} \right) \tag{4.73}$$

has the property that $f(x)$ tends for $c > 0$ at fixed x to the value of the function with smaller value at that point. Furthermore, $f(x_0) = f_1(x_0) = f_2(x_0)$ holds at the intersection point x_0. The parameter c controls the closeness of $f(x)$ to the functions $f_1(x)$ for $x \leq x_0$ and $f_2(x)$ for $x \geq x_0$ and the sharpness at the intersection point x_0. In view of the experimental data in Fig. 2.9 and 2.11 the combination of exponential and linear functions seems appropriate. In [Hartmann et al., 2009b] the proposal

$$c_{\mathrm{d1}}(\theta) = a_1 e^{a_2 \theta} + a_3, \qquad c_{\mathrm{d2}}(\theta) = a_4 e^{-a_5(\theta - \theta_0)} + a_6 \theta, \tag{4.74}$$

$$\epsilon_1(\theta) = d_1 e^{d_2 \theta}, \qquad \epsilon_2(\theta) = d_3 e^{-d_4(\theta - \theta_0)} + d_5 \theta. \tag{4.75}$$

leads to the final form of the heat capacity and emissivity

$$c_{\mathrm{d}}(\theta) = -c \ln \left(\frac{e^{-c_{\mathrm{d1}}(\theta)/c} + e^{-c_{\mathrm{d2}}(\theta)/c}}{2} \right), \tag{4.76}$$

$$\epsilon(\theta) = -\hat{c} \ln \left(\frac{e^{-\epsilon_1(\theta)/\hat{c}} + e^{-\epsilon_2(\theta)/\hat{c}}}{2} \right). \tag{4.77}$$

For the heat conductivity a polynomial of order three within the temperature range of interest seems to be sufficient

$$\lambda(\theta) = b_0 + b_1 \theta + b_2 \theta^2 + b_3 \theta^3. \tag{4.78}$$

The identification process for c_{d} and ϵ is done as follows: first the functions $c_{\mathrm{d1}}(\theta)$ and $\epsilon_1(\theta)$ are identified within the increasing part of the experimental data. Afterwards, the functions $c_{\mathrm{d2}}(\theta)$ and $\epsilon_2(\theta)$ are calibrated to the data in the region with decreasing values. For each branch, the material parameters are obtained by using a Levenberg-Marquardt method yielding $a_1 = 34.2$, $a_2 = 0.0026$, $a_3 = 421.15$, $a_4 = 956.5$, $a_5 = 0.012$, $a_6 = 0.45$, $b_0 = 40.1$, $b_1 = 0.05$, $b_2 = -0.0001$, $b_3 = 4.9 \times 10^{-8}$, $d_1 = 0.16$,

$d_2 = 0.002$, $d_3 = 0.06$, $d_4 = 0.025$, $d_5 = 0.0002$, and $\theta_0 = 900$. Finally, the values c and $\hat{c}$ of the interpolation functions (4.76) and (4.77) are determined. The values control the sharpness of the change in the functions of heat capacity and emissivity, where $c = 10$ and $\hat{c} = 0.01$ are appropriate. In Figs. 2.9, 2.10, and 2.11 the result of the identification procedure is depicted. Obviously, the heat capacity drops down by approximately 50% and the emissivity increases by a maximum factor of four.

With the complete model at hand, predictions of the material's response to prescribed strains and heat fluxes can be computed. So far these predictions are restricted to a material point, or homogeneous states. However, in practice non-homogeneous states and workpieces of finite dimension are most relevant. For predictions in these cases the balance equations of Sec. 3.2 have to be fulfilled simultaneously and solved for the mechanical and thermal state, which form an initial boundary value problem. Closed solutions are known only for special cases and in general the solution has to be obtained numerically.

Table 4.2.: Summary of constitutive equations (small elastic strains)

Stress relation

$$\tilde{\mathbf{T}} = \frac{K(\theta)}{2}\left(\operatorname{tr}(\mathbf{C}\mathbf{C}_i^{-1}) - 3\right)\frac{\mathbf{C}_i^{-1}}{\varphi^2} + \tag{4.63}$$
$$G(\theta)\left(\frac{1}{\varphi^4}\mathbf{C}_i^{-1}\mathbf{C}\mathbf{C}_i^{-1} - \frac{1}{3}\operatorname{tr}(\mathbf{C}\mathbf{C}_i^{-1})\frac{\mathbf{C}_i^{-1}}{\varphi^2}\right) = \mathbf{h}(\mathbf{C}, \theta, \mathbf{C}_i)$$

Elastic moduli

$$K(\theta) = K_0 + c_K(\theta - \theta_0), \qquad G(\theta) = G_0 + c_G(\theta - \theta_0) \tag{4.71}$$

Flow rule

$$\dot{\mathbf{C}}_i = 2\Lambda\left(\mathbf{C}_i^{-1}\mathbf{C}\cdot\mathbf{C}\mathbf{C}_i^{-1} - \frac{1}{3}\operatorname{tr}\left(\mathbf{C}\mathbf{C}_i^{-1}\right)^2\right)^{-1/2}\left(\mathbf{C} - \frac{1}{3}\operatorname{tr}\left(\mathbf{C}\mathbf{C}_i^{-1}\right)\mathbf{C}_i\right) \tag{4.64}$$

$$\dot{p}_s = \dot{p} - \dot{p}_d = \Lambda\sqrt{\frac{2}{3}}\left(1 - \beta(\theta)\left(p - p_d\right)\right)$$

Plastic multiplier

$$\Lambda = \frac{1}{\eta}\left\langle\frac{F}{\sigma_0}\right\rangle^m \tag{4.25}$$

Yield function

$$F = \frac{G}{\varphi^2}\sqrt{\mathbf{C}_i^{-1}\mathbf{C}\cdot\mathbf{C}\mathbf{C}_i^{-1} - \frac{1}{3}\operatorname{tr}\left(\mathbf{C}\mathbf{C}_i^{-1}\right)^2} - \sqrt{\frac{2}{3}}(k(\theta) + R(p_s)) \tag{4.24}$$

Yield stress

$$k(\theta) = (k_0 - k_H)\mathrm{e}^{-b(\theta - \theta_0)} + k_0 \tag{4.72}$$

Back-stress

$$R = \gamma\, p_s \tag{4.33}$$

Hardening parameter

$$\beta(\theta) = (\beta_0 - \beta_H)\mathrm{e}^{-b(\theta - \theta_0)} + \beta_0 \tag{4.72}$$

Internal heat production $w = w_p - w_e - w_s$

$$w_p = \frac{1}{\varrho_R}\Lambda\left(F + \sqrt{\frac{2}{3}}(k + R)\right) \tag{4.56}$$

$$-w_e = -\theta\frac{1}{\varrho_R}\frac{3K\alpha}{2\varphi}\operatorname{tr}\dot{\mathbf{C}}_e = -\theta\frac{1}{\varrho_R}\frac{3K\alpha}{2\varphi}\frac{\mathrm{d}}{\mathrm{d}t}\left(\frac{1}{\varphi^2}\operatorname{tr}(\mathbf{C}\mathbf{C}_i^{-1})\right) \tag{4.68}$$

$$-w_s = \frac{1}{\varrho_R}\left(\frac{\beta}{\gamma}R^2 + \theta\gamma'(\theta)\left(p - p_d\right)\left(1 - \frac{\beta}{\gamma}R\right) + \theta\varphi k'(\theta) - k\varphi\right)\sqrt{\frac{2}{3}}\Lambda \tag{4.69}$$

Heat flux vector

$$\boldsymbol{q} = -\boldsymbol{\lambda}(\theta)\operatorname{grad}\theta \tag{4.48}$$

5. Numerical Solution of Initial Boundary Value Problems

The main task of this work is to help making predictions and through this assist the engineering process of differential thermomechanical production processes. To this end, continuum mechanics helps to determine the scalar density field $\varrho = \varrho(\boldsymbol{X}, t)$, the vector field of displacement $\boldsymbol{u}(\boldsymbol{X}, t) = \boldsymbol{\chi}_\mathrm{R}(\boldsymbol{X}, t) - \boldsymbol{X}$ (respectively motion $\boldsymbol{x}$), and the scalar field of temperature $\theta = \theta(\boldsymbol{X}, t)$. The balance equations by themselves are insufficient for determining the field variables. On the one hand, the balance equations give a total of 8 equations.[1] But on the other hand, there is a total of 19 unknown variables.[2] The fields $\boldsymbol{k}$ (body force density) and r (internal heat production, e.g. due to electromagnetic radiation) are part of the given data. This system of equations is under-determined. To uniquely determine all variables, the system has to be closed. To this end, the balance relations are combined with a constitutive model, comprising 11 constitutive equations, and lead to an initial boundary value problem (IBVP), the field equations.

The resulting system of equations can in general not be solved analytically; instead numerical methods have to be employed. In this regard the finite element method has proved itself as a powerful tool and is used in the following for the spatial discretization. The method is established on a variational formulation of the IBVP. This so-called weak form is derived for the fully coupled thermomechanical system. Further aspects, which require particular attention, are the integration in time, as well as robust and fast solution techniques for the underlying algebraic systems of equations (nonlinear and linear).

5.1. Local Form of Initial Boundary Value Problems

The thermomechanically coupled problem is governed by the balance of momentum (3.77b)

$$\boldsymbol{0} = \mathrm{Div}\,\mathbf{T}_\mathrm{R} + \varrho_\mathrm{R}\boldsymbol{k},$$

---

[1]The following numbers of equations are at hand: balance of mass (1), balance of linear moment (3), balance of energy (1), and balance of moment of momentum (3).

[2]The following variables are unknown: density (1), motion (3), stress tensor (9), energy (1), heat flux vector (3), entropy (1), and temperature (1).

the heat conduction equation (4.58)

$$c_{\mathrm{d}}\dot{\theta} = -\frac{1}{\varrho_{\mathrm{R}}}\operatorname{Div}\boldsymbol{q}_{\mathrm{R}} + r + w,$$

and the evolution of the internal variables (4.46)

$$\dot{\mathbf{q}} = \boldsymbol{f}\left(\mathbf{C},\theta,\mathbf{q}\right).$$

To complete the problem statement, initial and boundary conditions are needed. For the motion and the temperature initial conditions have to be specified in the complete domain, i.e. the material body $\mathcal{B}$.

In many engineering applications it is reasonable to neglect the influence of inertia, thus omitting the acceleration term in the balance of momentum. In this case, the prescription of the initial position and velocity are omitted, [Marsden and Hughes, 1994, p. 213]. As in the present study, the problem in hand may still depend on time due to transient boundary conditions and time-dependent internal processes, leading to a quasistatic problem, [Fritzen, 1997, p. 67].

Thus, initial conditions have to be prescribed in this case as well. They can either be given in the material or the spatial representation. Concerning the motion, the position and velocity distribution of matter at the initial time t_{i} are naturally given in the material configuration, cf. [Ogden, 1997, p. 230] and [Haupt, 2000, p. 101]. For the temperature distribution both descriptions are reasonable and read

$$\theta(\boldsymbol{X},t_{\mathrm{i}}) = \theta_{\mathrm{i}}(\boldsymbol{X}), \qquad\qquad \text{for all } \boldsymbol{X} \in \Omega, \qquad\qquad (5.1)$$

$$\theta(\boldsymbol{x},t_{\mathrm{i}}) = \theta_{\mathrm{i}}(\boldsymbol{x}), \qquad\qquad \text{for all } \boldsymbol{x} \in \omega, \qquad\qquad (5.2)$$

in the reference and current configuration, respectively. The initial state of the material is given by the values of the internal variables at the time t_{i} and is stated as

$$\mathbf{q}(\boldsymbol{X},t_{\mathrm{i}}) = \mathbf{q}_{\mathrm{i}}(\boldsymbol{X}), \qquad\qquad \text{for all } \boldsymbol{X} \in \Omega, \qquad\qquad (5.3)$$

$$\mathbf{q}(\boldsymbol{x},t_{\mathrm{i}}) = \mathbf{q}_{\mathrm{i}}(\boldsymbol{x}), \qquad\qquad \text{for all } \boldsymbol{x} \in \omega, \qquad\qquad (5.4)$$

for the reference and current configuration, respectively.

Furthermore, data for the mechanical and the thermal field has to be given at the boundary of the domain. Three different kinds of boundary conditions are distinguished. The boundary condition of first kind prescribes the field variable itself. It is also called Dirichlet, essential, or geometric boundary condition. The boundary condition of second kind prescribes the directional derivative of the field variable. It is often termed Neumann, natural, or dynamic boundary condition. A combination of the field variable and its derivative on the boundary is a boundary condition of third kind.[3] If the combination

---

[3]Even though omitted in many books on continuum mechanics, a combination of the primary variable and its directional derivative is a common boundary condition in engineering. A beam, which is at one end spring supported, see e.g. [Meirovitch, 2001, p. 386], is an example for such a mechanical system. Convective heating or cooling at the surface are common examples for thermal systems, cf.[Incropera et al., 2007, p. 78] and [Greenberg, 1998, p. 952].

is linear, then it is referred to as Robin boundary condition, [Greenberg, 1998].

To define boundary conditions, the material surface of the body $\mathcal{B}$ is split into disjoint (open) subsets.[4] For the mechanical field follows

$$\partial\Omega = \overline{\partial_{\mathrm{u}}\Omega \cup \partial_{\mathrm{s}}\Omega}, \qquad\qquad \partial_{\mathrm{u}}\Omega \cap \partial_{\mathrm{s}}\Omega = \varnothing,$$

in the material and

$$\partial\omega = \overline{\partial_{\mathrm{u}}\omega \cup \partial_{\mathrm{s}}\omega}, \qquad\qquad \partial_{\mathrm{u}}\omega \cap \partial_{\mathrm{s}}\omega = \varnothing,$$

in the spatial representation.[5] Refer also to Fig. 5.1. The Dirichlet boundary condi-

$$\partial\Omega = \overline{\partial_{\mathrm{u}}\Omega \cup \partial_{\mathrm{s}}\Omega},$$
$$\partial_{\mathrm{u}}\Omega \cap \partial_{\mathrm{s}}\Omega = \varnothing,$$

$$\partial\omega = \overline{\partial_{\mathrm{u}}\omega \cup \partial_{\mathrm{s}}\omega},$$
$$\partial_{\mathrm{u}}\omega \cap \partial_{\mathrm{s}}\omega = \varnothing.$$
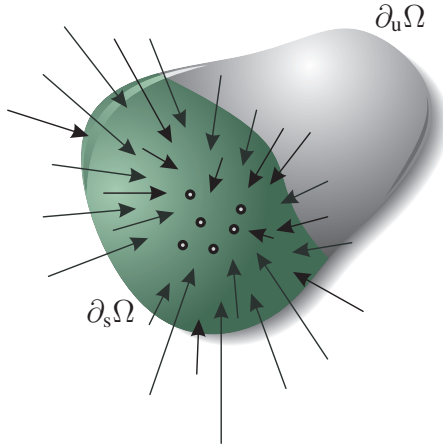
Figure 5.1.: Mechanical boundary conditions of Dirichlet and Neumann type

tion specifies the displacement over the finite open interval $]t_{\mathrm{i}}, t_{\mathrm{e}}[\subset \mathbb{R}$ and reads in the material representation

$$\boldsymbol{u} = \boldsymbol{\chi}_{\mathrm{R}}(\boldsymbol{X}, t) - \boldsymbol{X} = \boldsymbol{r}(\boldsymbol{X}, t) \qquad \text{for } \boldsymbol{X} \in \partial_{\mathrm{u}}\Omega \text{ and } t \in]t_{\mathrm{i}}, t_{\mathrm{e}}[. \qquad (5.5)$$

In the spatial representation the Dirichlet boundary condition refers to the velocity

$$\boldsymbol{v}(\boldsymbol{x}, t) = \boldsymbol{g}(\boldsymbol{x}, t) \qquad \text{for } \boldsymbol{x} \in \partial_{\mathrm{u}}\omega \text{ and } t \in]t_{\mathrm{i}}, t_{\mathrm{e}}[. \qquad (5.6)$$

---

[4]A bar above a set means set closure (the union of the set with its boundary), cf. [Hughes, 2000, p. 58].

[5]More general boundary conditions are possible, but are omitted for brevity. One possibility is to define a local basis $\boldsymbol{e}_i$ at every point of $\partial\Omega$ and to specify the ith component of either the stress or displacement vector for each $i \in \{1, 2, 3\}$, [Lubliner, 2008, p. 36]. A similar approach, following [Hughes, 2000, p. 77], is also implemented in the finite element code TASAFEM, [Hartmann, 2006a]. Other possibilities are to prescribe kinematic constraints, as shown in [Dhondt, 2004, p. 91 and p. 171], [Dhatt and Touzot, 1985, p. 232], and [Oñate, 2009, p. 309], and to take account of contact, see for example [Kloosterman, 2002] and [Rieger and Wriggers, 2004].

The Neumann boundary conditions naturally refer to the current configuration (forces and stress act on the current configuration). Here the Cauchy stress vector

$$\boldsymbol{t} = \mathbf{T}\boldsymbol{n} = \bar{\boldsymbol{s}}(\boldsymbol{x}, t) \qquad \text{for } \boldsymbol{x} \in \partial_\mathrm{s}\omega \text{ and } t \in \,]t_\mathrm{i}, t_\mathrm{e}[\tag{5.7}$$

is prescribed. By the constitutive equation of the Cauchy stress tensor, it depends on the strain and thus, on the derivative of the motion, i.e. the deformation gradient $\mathbf{F}$.

The Neumann boundary conditions can also be expressed with respect to the reference configuration. The equivalence of the force acting on the material surface elements according to the equations (3.73) and (3.75) leads to

$$\mathrm{d}\boldsymbol{f} = \mathbf{T}\boldsymbol{n}\,\mathrm{d}a = \mathbf{T}_\mathrm{R}\boldsymbol{n}_\mathrm{R}\,\mathrm{d}A \tag{5.8}$$

and thus,

$$\mathbf{T}\boldsymbol{n} = \mathbf{T}_\mathrm{R}\boldsymbol{n}_\mathrm{R}\frac{\mathrm{d}A}{\mathrm{d}a}. \tag{5.9}$$

The relation between the surface elements can be computed by considering equation (3.17). The norm of $\mathrm{d}\boldsymbol{a}$ is

$$\mathrm{d}a = \sqrt{\mathrm{d}\boldsymbol{a} \cdot \mathrm{d}\boldsymbol{a}} = (\det \mathbf{F}) \sqrt{\boldsymbol{n}_\mathrm{R} \cdot \mathbf{C}^{-1}\boldsymbol{n}_\mathrm{R}}\,\mathrm{d}A. \tag{5.10}$$

With the intermediate results (5.9) and (5.10) the boundary condition (5.7) is written as

$$\begin{aligned}
\boldsymbol{t} &= \frac{1}{(\det \mathbf{F}) \sqrt{\boldsymbol{n}_\mathrm{R} \cdot \mathbf{C}^{-1}\boldsymbol{n}_\mathrm{R}}}\mathbf{T}_\mathrm{R}\boldsymbol{n}_\mathrm{R} \\
&= \hat{\boldsymbol{s}}(\boldsymbol{X}, t) = \bar{\boldsymbol{s}}(\boldsymbol{\chi}_\mathrm{R}(\boldsymbol{X}, t), t) \qquad \text{for } \boldsymbol{X} \in \partial_\mathrm{s}\Omega \text{ and } t \in \,]t_\mathrm{i}, t_\mathrm{e}[.
\end{aligned} \tag{5.11}$$

In this representation, the stress vector also depends on the deformation. Another possibility (see [Haupt, 2000, p. 104]) is to omit the deformation dependence and to prescribe instead the Piola-Kirchhoff stress vector

$$\boldsymbol{t}_\mathrm{R} = \mathbf{T}_\mathrm{R}\boldsymbol{n}_\mathrm{R} = \boldsymbol{s}(\boldsymbol{X}, t) \qquad \text{for } \boldsymbol{X} \in \partial_\mathrm{s}\Omega \text{ and } t \in \,]t_\mathrm{i}, t_\mathrm{e}[. \tag{5.12}$$

This simplified boundary condition is referred to as dead loading and approximates expression (5.11) in the case of small deformations. In the case of large deformations the boundary condition (5.11) should be used.

In connection with the numerical solution using finite elements this kind of boundary condition is known under the names of follower, deformation-dependent, and path-following loads. The issue has been addressed for over three decades, see e.g. [Hibbit, 1979; Simo et al., 1991; Wriggers, 2009].

The specification of boundary conditions for the thermal field is done similarly to the mechanical ones. First the surface is split in the reference configuration into

$$\partial\Omega = \overline{\partial_\theta\Omega \cup \partial_\mathrm{q}\Omega \cup \partial_{\theta\mathrm{q}}\Omega}, \qquad\qquad \partial_\theta\Omega \cap \partial_\mathrm{q}\Omega \cap \partial_{\theta\mathrm{q}}\Omega = \varnothing,$$

and in the current configuration into

$$\partial\omega = \overline{\partial_\theta\omega \cup \partial_q\omega \cup \partial_{\theta q}\omega}, \qquad \partial_\theta\omega \cap \partial_q\omega \cap \partial_{\theta q}\omega = \varnothing.$$

The Dirichlet boundary condition reads

$$\theta(\boldsymbol{X}, t) = \hat{T}(\boldsymbol{X}, t) \qquad \text{for } \boldsymbol{X} \in \partial_\theta\Omega \text{ and } t \in \,]t_\mathrm{i}, t_\mathrm{e}[\tag{5.13}$$

in the reference configuration and

$$\theta(\boldsymbol{x}, t) = \bar{T}(\boldsymbol{x}, t) \qquad \text{for } \boldsymbol{x} \in \partial_\theta\omega \text{ and } t \in \,]t_\mathrm{i}, t_\mathrm{e}[. \tag{5.14}$$

in the current configuration. In the case of Neumann boundary conditions, the heat flux is prescribed. Similar to the stress vector for the mechanical field, this is done naturally in the current configuration. The condition is written as

$$q_\mathrm{n} = \boldsymbol{q} \cdot \boldsymbol{n} = \bar{f}_\mathrm{q}(\boldsymbol{x}, t) \qquad \text{for } \boldsymbol{x} \in \partial_q\omega \text{ and } t \in \,]t_\mathrm{i}, t_\mathrm{e}[. \tag{5.15}$$

An analogous argument as in equation (5.8) leads with the preliminary result (5.10) to the transformation into the reference configuration

$$\begin{aligned} q_\mathrm{n} &= \frac{1}{(\det \mathbf{F})\,\sqrt{\boldsymbol{n}_\mathrm{R} \cdot \mathbf{C}^{-1}\boldsymbol{n}_\mathrm{R}}} \boldsymbol{q}_\mathrm{R} \cdot \boldsymbol{n}_\mathrm{R} \\ &= \hat{f}_\mathrm{q}(\boldsymbol{X}, t) = \bar{f}_\mathrm{q}(\boldsymbol{\chi}_\mathrm{R}(\boldsymbol{X}, t), t) \qquad \text{for } \boldsymbol{X} \in \partial_q\Omega \text{ and } t \in \,]t_\mathrm{i}, t_\mathrm{e}[. \end{aligned} \tag{5.16}$$

See also equation (3.95) for the relation between the Cauchy and the Piola-Kirchhoff heat flux vectors.

The simplified condition

$$q_\mathrm{n} = \boldsymbol{q}_\mathrm{R} \cdot \boldsymbol{n}_\mathrm{R} = f_\mathrm{q}(\boldsymbol{X}, t) \qquad \text{for } \boldsymbol{X} \in \partial_q\Omega \text{ and } t \in \,]t_\mathrm{i}, t_\mathrm{e}[\tag{5.17}$$

neglects the deformation dependence of the heat flux and is a good approximation for small strains. In many situations the heat flux is not given as a function of time. Instead it depends on the surface temperature as in convective cooling and thermal radiation. This is expressed by a combined boundary condition of the form

$$\boldsymbol{q}_\mathrm{R} \cdot \boldsymbol{n}_\mathrm{R} = c(\boldsymbol{X}, \theta, t) \qquad \text{for } \boldsymbol{X} \in \partial_q\Omega \text{ and } t \in \,]t_\mathrm{i}, t_\mathrm{e}[, \tag{5.18}$$

which is in the following investigated for two important cases.

In the case of pure convection a linear dependence (Robin boundary condition) is often assumed

$$\bar{q}_\mathrm{con} = h_\mathrm{c}\,(\theta(\boldsymbol{x}) - \theta_\mathrm{f}), \qquad \text{for } \boldsymbol{x} \in \partial_{\theta q}\omega \text{ and } t \in \,]t_\mathrm{i}, t_\mathrm{e}[, \tag{5.19}$$

with the heat transfer coefficient h_c and the absolute temperature of the surrounding fluid θ_f (in K). The heat transfer coefficient reflects the mean heat transfer and can be determined experimentally or for special cases analytically, see for example [Incropera et al., 2007]. Another option is to additionally simulate the flow of the surrounding fluid and to determine the heat flux by fluid-structure interaction as done in [Birken et al., 2010; Hartmann et al., 2009c].

The net rate of heat transfer due to radiation per unit surface is given by

$$\overline{q}_{rad} = \epsilon\sigma\left(\theta^4(\boldsymbol{x}) - \theta_\infty^4\right), \qquad \text{for } \boldsymbol{x} \in \partial_{\theta q}\omega \text{ and } t \in \,]t_i, t_e[, \qquad (5.20)$$

where σ is the Stefan-Boltzmann constant ($\sigma = 5.67 \times 10^{-8}$ W/m^2 K^4), and θ_∞ is the absolute temperature (isothermal) of the surroundings. The emissivity ϵ depends on the surface material and condition (see Sec. 2.2.3); it takes on values between zero and one. Often the heat convection and radiation boundary conditions are linearly combined to $q_n = \overline{q}_{con} + \overline{q}_{rad}$.

The strong form of the initial boundary value problem formulated in the reference configuration is stated in Problem 1. The governing equations belong to different classes of differential equations. The evolution of the internal variables (4.46) is given (at a local point $\boldsymbol{X}$) by nonlinear ordinary differential equations, where the time dependent deformation $\mathbf{C}(\boldsymbol{X}, t)$ and temperature $\theta(\boldsymbol{X}, t)$ act as forcing functions. A further nonlinearity is introduced by the case distinction between the elastic and plastic region. The internal variables change only during plastic deformations.

For constant material parameters the heat conduction equation (4.58) is the prototypical example of a parabolic partial differential equation (PDE), see for example [Greenberg, 1998, p. 943]. In the case of temperature dependent material properties, i. e. heat capacity and heat conductivity, the PDE is said to be quasilinear, cf. [Greenberg, 1978, p. 523]. In [Rincon et al., 2005, 2006] existence, uniqueness, and asymptotic behavior of a one- and a two-dimensional nonlinear heat conduction equation are established. The diffusive character of the PDE has a regularizing effect, which contributes to the stability of numerical methods.

The balance of momentum (3.77b) represents in the case of small strain quasistatic elastic deformations an elliptic PDE. The mathematical theory for this class of problems is well developed and analytical solutions for many special cases are known, cf. [Sadd, 2005]. However, for nonlinear problems, a unique solution can in general not be expected, see also the comments of Ogden [1997, p. 234] for nonlinear elasticity. In the case of inelastic material behavior the situation is even more complicated, see for example [Alber, 1995; Fritzen, 1997, p. 64].

In the case of the fully coupled nonlinear thermomechanical Problem 1 studied here, the second Piola-Kirchhoff stress tensor depends on the temperature via the thermal expansion (given by $\varphi(\theta)$) and the elastic moduli. The bulk modulus K and shear modulus G vary linearly with θ. Furthermore, the initial yield stress $k(\theta)$ depends, according to (4.72), exponentially on the temperature. A similar dependence is chosen for the hardening parameter β which has a strong influence on the development of the back-stress

---

Problem 1 Strong form of the coupled problem

Given the initial conditions

$$\theta(\boldsymbol{X}, t_{\mathrm{i}}) = \theta_{\mathrm{i}}(\boldsymbol{X}) \qquad\qquad \boldsymbol{X} \in \Omega, \qquad\qquad (5.1)$$

$$\mathbf{q}(\boldsymbol{X}, t_{\mathrm{i}}) = \mathbf{q}_{\mathrm{i}}(\boldsymbol{X}) \qquad\qquad \boldsymbol{X} \in \Omega, \qquad\qquad (5.3)$$

and the boundary conditions

$$\boldsymbol{u}(\boldsymbol{X}, t) = \boldsymbol{r}(\boldsymbol{X}, t) \qquad\qquad \text{on } \partial_{\mathrm{u}}\Omega \times \,]t_{\mathrm{i}}, t_{\mathrm{e}}[, \qquad\qquad (5.5)$$

$$\mathbf{T}_{\mathrm{R}}\boldsymbol{n}_{\mathrm{R}} = \boldsymbol{s}(\boldsymbol{X}, t) \qquad\qquad \text{on } \partial_{\mathrm{s}}\Omega \times \,]t_{\mathrm{i}}, t_{\mathrm{e}}[, \qquad\qquad (5.12)$$

$$\theta(\boldsymbol{X}, t) = \hat{T}(\boldsymbol{X}, t) \qquad\qquad \text{on } \partial_{\theta}\Omega \times \,]t_{\mathrm{i}}, t_{\mathrm{e}}[, \qquad\qquad (5.13)$$

$$\boldsymbol{q}_{\mathrm{R}} \cdot \boldsymbol{n}_{\mathrm{R}} = f_{\mathrm{q}}(\boldsymbol{X}, t) \qquad\qquad \text{on } \partial_{\mathrm{q}}\Omega \times \,]t_{\mathrm{i}}, t_{\mathrm{e}}[, \qquad\qquad (5.17)$$

$$\boldsymbol{q}_{\mathrm{R}} \cdot \boldsymbol{n}_{\mathrm{R}} = c(\boldsymbol{X}, \theta, t) \qquad\qquad \text{on } \partial_{\theta\mathrm{q}}\Omega \times \,]t_{\mathrm{i}}, t_{\mathrm{e}}[, \qquad\qquad (5.18)$$

find $(\boldsymbol{u}, \theta) \colon \overline{\Omega} \times [t_{\mathrm{i}}, t_{\mathrm{e}}] \to \mathbb{R}^3 \times \mathbb{R}$ such that

$$\mathbf{0} = \operatorname{Div} \mathbf{T}_{\mathrm{R}} + \varrho_{\mathrm{R}}\boldsymbol{k} \qquad\qquad \text{on } \Omega \times \,]t_{\mathrm{i}}, t_{\mathrm{e}}[, \qquad\qquad (3.77\mathrm{b})$$

$$c_{\mathrm{d}}\dot{\theta} = -\frac{1}{\varrho_{\mathrm{R}}} \operatorname{Div} \boldsymbol{q}_{\mathrm{R}} + r + w \qquad\qquad \text{on } \Omega \times \,]t_{\mathrm{i}}, t_{\mathrm{e}}[, \qquad\qquad (4.58)$$

$$\dot{\mathbf{q}} = \boldsymbol{f}(\mathbf{C}, \theta, \mathbf{q}) \qquad\qquad \text{on } \Omega \times \,]t_{\mathrm{i}}, t_{\mathrm{e}}[, \qquad\qquad (4.46)$$

with the constitutive relations

$$\tilde{\mathbf{T}} = \mathbf{h}(\mathbf{C}, \theta, \mathbf{q}), \qquad\qquad (4.43)$$

$$w = \hat{w}(\mathbf{C}, \dot{\mathbf{C}}, \theta, \dot{\theta}, \mathbf{q}) \qquad\qquad (4.70)$$

$$\boldsymbol{q}_{\mathrm{R}} = -\boldsymbol{\lambda}_{\mathrm{R}} \operatorname{Grad} \theta. \qquad\qquad (4.47)$$

R. Both determine the value of the yield function (4.24). For higher temperatures the material starts to plastify at a lower value and experiences less hardening. See Fig. 4.8a for flow curves at different temperatures. The heat conduction equation is coupled with the displacement field by the internal heat production w and the heat conductivity $\boldsymbol{\lambda}_{\mathrm{R}}$, see Tab. 4.2 on p. 77 for a summary of the constitutive equations. Additional remarks on the thermomechanical coupling are given in Sec. 3.2.7.

For this coupled problem, neither a statement on the existence and uniqueness of a solution nor on the convergence behavior of numerical methods is known to the author. The existence of a solution to the nonlinear IBVP is assumed, but can be proved only for special cases. In particular the classical notion of a well-posed (correctly set) problem

according to Hadamard [2003] is inappropriate. This would imply the existence of a unique solution, which is continuously dependent on the given data.

5.2. Variational Form of Initial Boundary Value Problems

Some numerical methods such as the finite difference method begin the approximation directly from the strong statement of the problem. Many other numerical methods, including the finite element method, are based on a variational formulation of the IBVP, the so-called weak form.

The weak forms of the balance equations are in mathematical terms real functionals. A functional is a map from a vector space to the underlying field. In the present case, the field underlying the vector space of functions is the set of real numbers $\mathbb{R}$, i.e. a functional π is a function that takes a function as its argument and returns a scalar, as depicted in Fig. 5.2. Therefore, it is also referred to as a function of functions.
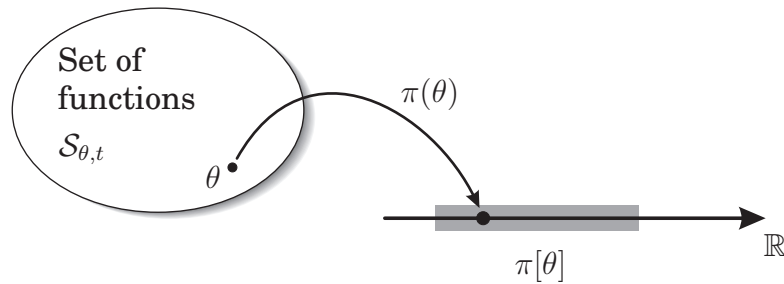
Figure 5.2.: Functional $\pi \colon \theta \mapsto \pi(\theta)$

The weak forms can be obtained from the strong forms. In the first step, the equations are multiplied by a variation, also called weighting function. Following, the product is integrated over the complete domain. To reduce the requirements of continuity (differentiability) on the solution, the divergence theorem is applied. By this procedure the highest derivatives are reduced by one order, thus enlarging the space of admissible functions. Accordingly, one speaks of the corresponding weak form. Under appropriate continuity assumptions it can be shown that the weak and the strong forms are equivalent, refer for example to [Hughes, 2000, p. 60]. As stated in [Zienkiewicz et al., 2005, p. 319] in the case of finite deformations, the derivation is most conveniently done in the reference configuration. Later on, the results can be easily transformed to the current configuration, if necessary. Details for the problems in hand are given in the following.

Two classes of functions for the motion and the temperature are introduced each. The first is composed of trial, or candidate solutions. These are required from the outset to satisfy the Dirichlet boundary conditions. The collections of all trial solutions are

written as

$$\boldsymbol{S}_{u,t} := \{ \, \boldsymbol{u}(\,\cdot\,,t) \mid \boldsymbol{u}\,(\boldsymbol{X},t) = \boldsymbol{r}(\boldsymbol{X},t) \text{ for } \boldsymbol{X} \in \partial_{\mathrm{u}}\Omega \, \} \tag{5.21}$$

and

$$\mathcal{S}_{\theta,t} := \left\{ \, \theta(\,\cdot\,,t) \, \middle| \, \theta(\boldsymbol{X},t) = \hat{T}(\boldsymbol{X},t) \text{ for } \boldsymbol{X} \in \partial_{\theta}\Omega \, \right\}. \tag{5.22}$$

Note, that these definitions vary as functions of time due to the time-dependent boundary conditions. Further, there are no assumptions on the function space. In contrast to the linear theory, which has a sound mathematical foundation (see for example [Strang and Fix, 1973]), such a tool is not at hand for the nonlinear case. The variational formulation of the equations of continuum mechanics is formal in the sense that up to today little is known about the appropriate mathematical structure for specific models, cf. [Simo and Hughes, 2000, p. 266]. Often $\mathcal{S} \subset \mathcal{H}^p(\Omega)$ are employed, where $\mathcal{H}^p(\Omega)$ denotes the Sobolev space of functions possessing square integrable derivatives up to order p.[6]

Similarly, associated with these trial functions, the sets of admissible test functions are defined as

$$\boldsymbol{\mathcal{V}}_u := \{ \, \delta\boldsymbol{u} \colon \Omega \to \mathbb{R}^3 \, \middle| \, \delta\boldsymbol{u}\,(\boldsymbol{X}) = \boldsymbol{0} \text{ for } \boldsymbol{X} \in \partial_{\mathrm{u}}\Omega \, \} \tag{5.23}$$

and

$$\mathcal{V}_\theta := \{ \, \delta\theta \colon \Omega \to \mathbb{R} \mid \delta\theta(\boldsymbol{X}) = 0 \text{ for } \boldsymbol{X} \in \partial_{\theta}\Omega \, \}. \tag{5.24}$$

The test functions are illustrated in Fig. 5.3 and can be interpreted as the difference between a fixed trial function, e.g. $\theta_0(x) \in \mathcal{S}_{\theta,t}$, and another arbitrary member $\theta(x)$ of the same set.[7] In contrast to the remarks in some engineering books on the finite element method, they do not have to be infinitesimal small. They only have to be admissible, i.e. functions from these sets vanish where Dirichlet boundary conditions are specified and form homogeneous counterparts to the trial functions. They are also referred to as weighting functions or variations.[8]

The Neumann boundary conditions are not explicitly enforced. They are satisfied automatically by the variational statement. This property simplifies the construction of approximate solutions, see [Jeltsch-Fricker, 2007, p. 209] and the literature cited therein.

---

[6]The necessary order $1 \le p < \infty$ has to be determined from the problem in hand, cf. [Zeidler, 1985, Sec. 42.7], and thus, depends on the constitutive equations. For hardening plasticity at small deformations holds $p = 1$, see [Simo and Hughes, 2000, p. 161].

[7]The dependence on the parameter t is not necessary in the mathematical derivation (due to the arbitrariness of the functions) and has been dropped.

[8]The variations can be formulated either with respect to the current or the reference configuration. In the first case the function spaces change with χ_{R} and their members are called spatial variations. The dependence on χ_{R} can be removed by a change of variables leading to material variations, as done here. Thus, $\delta\boldsymbol{u}$ and $\delta\theta$ span the fixed linear spaces $\boldsymbol{\mathcal{V}}_u$ and $\mathcal{V}_\theta$, respectively. For further details refer to [Simo and Hughes, 2000, p. 263].

(a) Variation of temperature with prescribed temperature at left and right end

(b) Spatial variation of motion
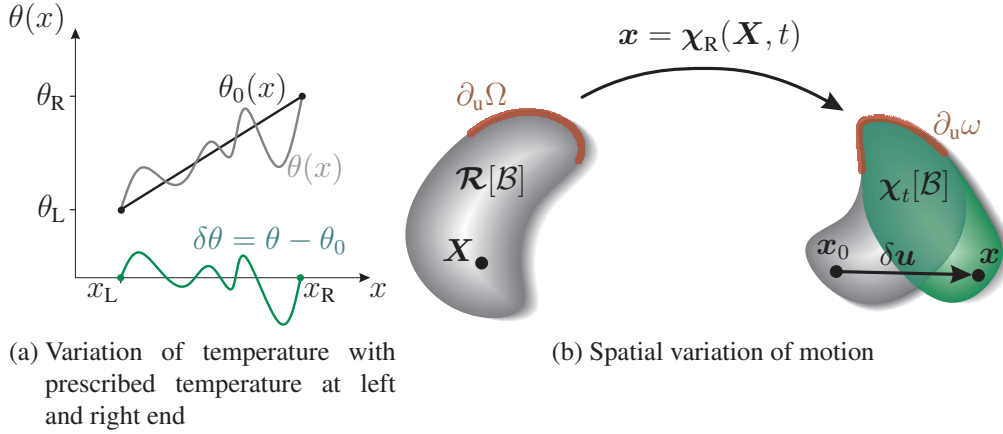
Figure 5.3.: Superposed variations

5.2.1. Weak Form of the Balance of Momentum

The derivation starts from the quasistatic balance of linear momentum given in equation (3.77b)

$$\mathbf{0} = \operatorname{Div} \mathbf{T_R} + \varrho_R \boldsymbol{k}.$$

In the first step the balance equation (3.77b) is multiplied by virtual displacements $\delta \boldsymbol{u}(\boldsymbol{X}) \in \boldsymbol{\mathcal{S}}_{u,t}$ and the product is integrated over the complete body

$$\int_\Omega \left(\operatorname{Div} \mathbf{T_R} + \varrho_R \boldsymbol{k} \right) \cdot \delta \boldsymbol{u} \, \mathrm{d}V = 0. \tag{5.25}$$

With the identity

$$\left(\operatorname{Div} \mathbf{T_R} \right) \cdot \delta \boldsymbol{u} = \operatorname{Div} \left(\mathbf{T_R}^T \delta \boldsymbol{u} \right) - \mathbf{T_R} \cdot \operatorname{Grad} \delta \boldsymbol{u} \tag{5.26}$$

follows

$$\int_\Omega \left(\operatorname{Div} \left(\mathbf{T_R}^T \delta \boldsymbol{u} \right) - \mathbf{T_R} \cdot \operatorname{Grad} \delta \boldsymbol{u} + \varrho_R \boldsymbol{k} \cdot \delta \boldsymbol{u} \right) \mathrm{d}V = 0. \tag{5.27}$$

In this form, the divergence theorem[9] can be applied to the first term of the integrand and leads to

$$\int_{\partial\Omega} \left(\mathbf{T_R}^T \delta \boldsymbol{u} \right) \cdot \boldsymbol{n_R} \, \mathrm{d}A - \int_\Omega \mathbf{T_R} \cdot \operatorname{Grad} \delta \boldsymbol{u} \, \mathrm{d}V + \int_\Omega \varrho_R \boldsymbol{k} \cdot \delta \boldsymbol{u} \, \mathrm{d}V = 0. \tag{5.28}$$

---

[9]See [Greenberg, 1998, p. 793] for the general idea of the divergence theorem and an outline of its proof.

With the aid of the Cauchy-theorem $\mathbf{T}_R \boldsymbol{n}_R = \boldsymbol{t}_R$ the integrand of the surface integral can be expressed in terms of the stress vector. Furthermore the relation between the first and the second Piola-Kirchhoff stress tensors $\mathbf{T}_R = \mathbf{F}\tilde{\mathbf{T}}$ can be utilized to yield

$$\int_{\partial\Omega} \boldsymbol{t}_R \cdot \delta\boldsymbol{u} \,\mathrm{d}A - \int_\Omega \tilde{\mathbf{T}} \cdot \mathbf{F}^\mathrm{T}\,\mathrm{Grad}\,\delta\boldsymbol{u} \,\mathrm{d}V + \int_\Omega \varrho_R \boldsymbol{k} \cdot \delta\boldsymbol{u} \,\mathrm{d}V = 0. \qquad (5.29)$$

Due to the symmetry of the second Piola-Kirchhoff stress tensor $\tilde{\mathbf{T}}$, the product in the second integral satisfies

$$\tilde{\mathbf{T}} \cdot \mathbf{F}^\mathrm{T}\,\mathrm{Grad}\,\delta\boldsymbol{u} = \tilde{\mathbf{T}} \cdot \tfrac{1}{2}\left(\mathbf{F}^\mathrm{T}\,\mathrm{Grad}\,\delta\boldsymbol{u} + \mathrm{Grad}^T \delta\boldsymbol{u}\,\mathbf{F}\right) = \tilde{\mathbf{T}} \cdot \delta\mathbf{E}. \qquad (5.30)$$

Where

$$\delta\mathbf{E} = \tfrac{1}{2}\left(\mathbf{F}^\mathrm{T}\,\mathrm{Grad}\,\delta\boldsymbol{u} + \mathrm{Grad}^T \delta\boldsymbol{u}\,\mathbf{F}\right) \qquad (5.31)$$

is the variation of the Green strain tensor

$$\delta\mathbf{E} = \frac{\mathrm{d}\mathbf{E}}{\mathrm{d}\boldsymbol{u}}\delta\boldsymbol{u} = \mathrm{D}\mathbf{E}[\delta\boldsymbol{u}]. \qquad (5.32)$$

The weak form of the balance of linear momentum in the reference configuration reads

$$\int_\Omega \tilde{\mathbf{T}} \cdot \delta\mathbf{E} \,\mathrm{d}V = \int_{\partial\Omega} \boldsymbol{t}_R \cdot \delta\boldsymbol{u} \,\mathrm{d}A + \int_\Omega \varrho_R \boldsymbol{k} \cdot \delta\boldsymbol{u} \,\mathrm{d}V. \qquad (5.33)$$

5.2.2. Weak Form of the Balance of Energy

The derivation of the weak form can be done either on the basis of the local balance of energy formulated in terms of the current configuration (3.91a), or in terms of the reference configuration (3.91b). Again, the balance equation in the reference configuration

$$\frac{\mathrm{d}e}{\mathrm{d}t} = \frac{1}{\varrho_R}\tilde{\mathbf{T}} \cdot \dot{\mathbf{E}} - \frac{1}{\varrho_R}\,\mathrm{Div}\,\boldsymbol{q}_R + r$$

serves as a point of departure. The equation is first multiplied by a virtual temperature $\delta\theta \in \mathcal{V}_\theta$ and subsequently integrated over the volume of the body

$$\int_\Omega \varrho_R \frac{\partial e}{\partial t}\delta\theta \,\mathrm{d}V = \int_\Omega \left(\tilde{\mathbf{T}} \cdot \dot{\mathbf{E}} - \mathrm{Div}\,\boldsymbol{q}_R + \varrho_R r\right) \delta\theta \,\mathrm{d}V. \qquad (5.34)$$

With the equivalence

$$\mathrm{Div}\left(\boldsymbol{q}_R \delta\theta\right) = \delta\theta\,\mathrm{Div}\,\boldsymbol{q}_R + \boldsymbol{q}_R \cdot \mathrm{Grad}\,\delta\theta \qquad (5.35)$$

the expression in equation (5.34) is converted into the weak form

$$-\int_{\Omega} \boldsymbol{q}_{\mathrm{R}} \cdot \mathrm{Grad}\, \delta\theta \,\mathrm{d}V =$$

$$\int_{\Omega} \tilde{\mathbf{T}} \cdot \dot{\mathbf{E}}\delta\theta \,\mathrm{d}V - \int_{\partial\Omega} \boldsymbol{q}_{\mathrm{R}} \cdot \boldsymbol{n}_{\mathrm{R}}\delta\theta \,\mathrm{d}A + \int_{\Omega} \varrho_{\mathrm{R}} \left(r - \frac{\partial e}{\partial t} \right) \delta\theta \,\mathrm{d}V. \quad (5.36)$$

The virtual temperatures fulfill the homogeneous Dirichlet boundary conditions, i.e. they vanish at those points where the temperature is prescribed. Thus, the surface integral has to be evaluated only over $\partial_{\mathrm{q}}\Omega$ and $\partial_{\theta\mathrm{q}}\Omega$, where the heat flux is given. The statement (5.36) is equal to the presentation in [Dhondt, 2004, p. 42] and [Miehe, 1988, p. 59]. However, in this form the time derivative of the temperature is not stated explicitly. Hence, the energy balance in the form of the heat conduction equation is commonly used, see for example [Dhondt, 2004, p. 307], [Heimes, 2003, p. 44], [Heimes, 2005, p. 94], [Fritsch, 2004], [Parisch, 2003, p. 263], and [Perić and Owen, 2004].

5.2.3. Weak Form of the Heat Conduction Equation

With constitutive assumptions (equations) the balance of energy is transformed into the heat conduction equation

$$c_{\mathrm{d}}\dot{\theta} = -\frac{1}{\varrho_{\mathrm{R}}} \mathrm{Div}\, \boldsymbol{q}_{\mathrm{R}} + r + w. \quad (4.58)$$

In general in this equation the heat capacity c_{d} and the production term w are temperature and deformation-dependent. The derivation of the weak form is analogous to the procedure for the balance of energy and leads to

$$\int_{\Omega} \varrho_{\mathrm{R}} c_{\mathrm{d}} \dot{\theta}\delta\theta \,\mathrm{d}V - \int_{\Omega} \boldsymbol{q}_{\mathrm{R}} \cdot \mathrm{Grad}\, \delta\theta \,\mathrm{d}V = -\int_{\partial\Omega} \boldsymbol{q}_{\mathrm{R}} \cdot \boldsymbol{n}_{\mathrm{R}}\delta\theta \,\mathrm{d}A + \int_{\Omega} \varrho_{\mathrm{R}}(r+w)\delta\theta \,\mathrm{d}V. \quad (5.37)$$

Starting from (4.59) and integrating over the current configuration yields to the weak form

$$\int_{\omega} \varrho c_{\mathrm{d}} \dot{\theta}\delta\theta \,\mathrm{d}v - \int_{\omega} \boldsymbol{q} \cdot \mathrm{grad}\, \delta\theta \,\mathrm{d}v = -\int_{\partial\omega} \boldsymbol{q} \cdot \boldsymbol{n}\delta\theta \,\mathrm{d}a + \int_{\omega} \varrho(r+w)\delta\theta \,\mathrm{d}v. \quad (5.38)$$

Formally, both weak expressions, in the reference and the current configuration, are of the same form.

5.2.4. Weak Form of the Coupled Problem

The equations (5.33) and (5.36), respectively (5.37), have to be fulfilled simultaneously. Multiplication by arbitrary scalars and subsequent addition leads to a single variational formulation for the coupled problem

$$
M \left\{ \int_\Omega \left(\tilde{\mathbf{T}} \cdot \delta \mathbf{E} - \varrho_{\mathrm{R}} \boldsymbol{k} \cdot \delta \boldsymbol{u} \right) \mathrm{d}V - \int_{\partial\Omega} \boldsymbol{t}_{\mathrm{R}} \cdot \delta \boldsymbol{u} \, \mathrm{d}A \right\}
$$
$$
+ T \left\{ \int_\Omega \left[\varrho_{\mathrm{R}} \left(c_{\mathrm{d}} \dot\theta - r - w \right) \delta\theta - \boldsymbol{q}_{\mathrm{R}} \cdot \operatorname{Grad} \delta\theta \right] \mathrm{d}V + \int_{\partial\Omega} \boldsymbol{q}_{\mathrm{R}} \cdot \boldsymbol{n}_{\mathrm{R}} \delta\theta \, \mathrm{d}A \right\} = 0. \quad (5.39)
$$

The constants M and T are arbitrary and can be used to lead to better conditioned systems of equations within the scope finite element analysis, as explored in [Miehe, 1988].

With the constitutive relation of the heat flux vector, i.e. Fourier's model (4.47), follows

$$
M \left\{ \int_\Omega \left(\tilde{\mathbf{T}} \cdot \delta \mathbf{E} - \varrho_{\mathrm{R}} \boldsymbol{k} \cdot \delta \boldsymbol{u} \right) \mathrm{d}V - \int_{\partial\Omega} \boldsymbol{t}_{\mathrm{R}} \cdot \delta \boldsymbol{u} \, \mathrm{d}A \right\}
$$
$$
+ T \left\{ \int_\Omega \left[\varrho_{\mathrm{R}} \left(c_{\mathrm{d}} \dot\theta - r - w \right) \delta\theta + \kappa \operatorname{Grad} \theta \cdot \operatorname{Grad} \delta\theta \right] \mathrm{d}V + \int_{\partial\Omega} \boldsymbol{q}_{\mathrm{R}} \cdot \boldsymbol{n}_{\mathrm{R}} \delta\theta \, \mathrm{d}A \right\} = 0.
$$
$$
(5.40)
$$

The transformation into a single variational form is often stated, see for example [Miehe, 1988] and [Heimes, 2003], but does not seem necessary. The proposition of a single equation is weaker as the one of two simultaneous equations. The arbitrariness of the virtual functions eventually leads to the same result as two simultaneous equations. Furthermore, the two constants M and T formally cancel during the solution process with finite elements. This might also be the reason why no effect on the condition, respectively solvability of the equation systems, is observed in [Miehe, 1988].

The weak form of the coupled initial boundary value problem formulated in the reference configuration is stated as Problem 2. For general domains and boundary conditions, this problem can only be solved numerically. The numerical solution with the method of lines is considered in the next section.

5.3. Method of Lines

The method of lines (MOL) is a technique for solving partial differential equations, where all variables but one are discretized, [Großmann and Roos, 2005; Schiesser,

Problem 2 Weak form of the coupled problem

Given the initial conditions θ_i, $\mathbf{q}_i$, the boundary conditions $\boldsymbol{r}$, $\boldsymbol{s}$, $\hat{T}$, f_q, and c, find $\boldsymbol{u} \in \boldsymbol{\mathcal{S}}_{u,t}$ and $\theta \in \mathcal{S}_{\theta,t}$ such that for any $t \in [t_i, t_e]$

$$\pi_u\big(\boldsymbol{u}, \theta, \mathbf{q}, \delta\boldsymbol{u}\big) = \int_\Omega \tilde{\mathbf{T}} \cdot \delta\mathbf{E}\,\mathrm{d}V - \int_{\partial_s\Omega} \boldsymbol{s} \cdot \delta\boldsymbol{u}\,\mathrm{d}A$$

$$- \int_\Omega \varrho_R \boldsymbol{k} \cdot \delta\boldsymbol{u}\,\mathrm{d}V = 0, \quad \text{for all } \delta\boldsymbol{u} \in \boldsymbol{\mathcal{V}}_u, \quad (5.33)$$

$$\pi_\theta(\boldsymbol{u}, \theta, \mathbf{q}, \delta\theta) = \int_\Omega \varrho_R \left(c_d\dot{\theta} - r - w\right)\delta\theta\,\mathrm{d}V - \int_\Omega \boldsymbol{q}_R \cdot \mathrm{Grad}\,\delta\theta\,\mathrm{d}V$$

$$+ \int_{\partial_q\Omega} f_q\delta\theta\,\mathrm{d}A + \int_{\partial_{\theta q}\Omega} c\delta\theta\,\mathrm{d}A = 0, \quad \text{for all } \delta\theta \in \mathcal{V}_\theta, \quad (5.37)$$

and

$$\dot{\mathbf{q}} = \boldsymbol{r}(\mathbf{C}, \theta, \mathbf{q}), \qquad \mathbf{q}(\boldsymbol{X}, t_i) = \mathbf{q}_i(\boldsymbol{X}), \qquad \text{for any } \boldsymbol{X} \in \Omega. \quad (4.46)$$

$$\tilde{\mathbf{T}} = \mathbf{h}(\mathbf{C}, \theta, \mathbf{q}), \quad (4.43)$$

$$\boldsymbol{q}_R = -\boldsymbol{\lambda}_R\,\mathrm{Grad}\,\theta. \quad (4.47)$$

1991].[10] In most cases, the time and spatial variables are treated differently, [Schiesser and Griffiths, 2009]. Owing to the principle of causality, the evolution of quantities in time possesses a certain directionality: current values can depend only on previous ones. In general, this property is in contrast to the spatial distribution and can be taken into account for the discretization of time, cf. [Schäfer, 2006, p. 152]. Another important requisite for the successful application of the MOL is the absence of sharp fronts in the solution that move rapidly as a function of both space and time. In other words the rapid moving fronts (if any) can be reasonably well decoupled in time and space. An important example where this condition is violated are hyperbolic PDEs with shocks, cf. [Ascher and Petzold, 1998, p. 15].

Most often, the spatial variables are discretized first, leaving the time variable continuous and leading to an ordinary differential equation in time, as shown for the heat

---

[10]Some authors use the name method of lines only in conjunction with a finite difference discretization of spatial variables and prefer the name semi-discrete method instead, [Cottrell et al., 2009, p. 186] and [Becker et al., 1981, p. 250].

conduction problem in [Becker et al., 1981, p. 246] and [Hughes, 2000].[11] The procedure is illustrated in Fig. 5.4 for a fixed two-dimensional domain.

(a) Semi-discrete system (continuous time)　　　(b) Fully discrete system
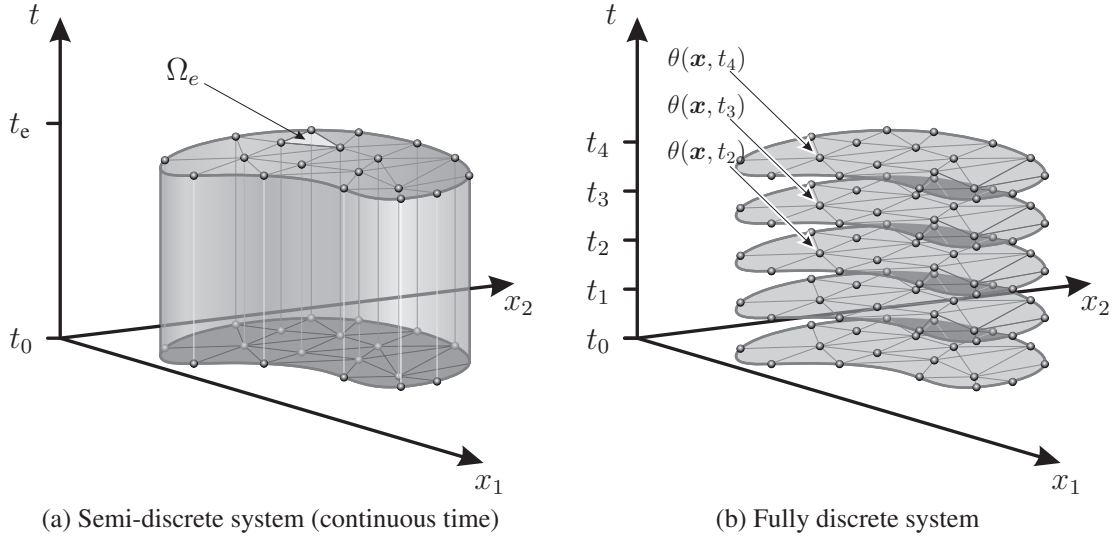
Figure 5.4.: Relation between spatial and temporal discretization for a two-dimensional domain

There are also discretization techniques, which do not distinguish between the spatial and temporal dimension. These are referred to as space-time finite elements, where a basis in space-time is created by taking a tensor product of the basis in the spatial and temporal dimension. Obviously, this approach greatly increases the total size of the problem. To minimize the problem size, a partitioning in the time direction is done. A single element in the time direction is solved one after another with the results of the previous elements weakly enforced as boundary conditions, as in a discontinuous Galerkin method, see [Cottrell et al., 2009, p. 191] and the literature cited therein.[12] Even though, this is an intellectually very satisfying approach and potentially very accurate, the semi-discrete (MOL) approach is chosen in this work. Due to the large anticipated problem size, performance issues play an important role and advocate the classical MOL approach.

In the following, finite elements with an isoparametric ansatz are chosen for the spatial discretization, as indicated in Fig. 5.4a. This approach has become widely accepted and is successfully applied in many engineering applications, see for example [Hughes, 2000; Wriggers, 2009].

---

[11]There is also a method of lines, where the first step consists of the discretization in time. The procedure leads to a boundary value problem and is better known under the name of *Rothe*-method, cf. [Großmann and Roos, 2005, p. 117 and p. 337].

[12]For the application of continuous and discontinous Galerkin time integration in different settings see for example [Carstens and Kuhl, 2005], [Kuhl, 2004a, p. 79], and [Kuhl and Meschke, 2007].

Isoparametric elements use the same shape functions for the approximation of the geometry and the physical quantities. This simplifies the formulation of the continuum problem and leads to well-conditioned algorithms, cf. [Strang and Fix, 1973]. Additionally, isoparametric elements allow a very good approximation of arbitrary geometries. The finite element method (FEM) which is used in this work is the subject of the next section.

5.4. Spatial Discretization using Finite Elements

The Ritz-Galerkin idea, which underlies most modern numerical solution techniques of partial differential equations, consists of two steps. In the first step finite-dimensional approximations of $\mathcal{S}_t$ and $\mathcal{V}$ are constructed. The finite-dimensional function spaces are assumed to be subspaces of $\mathcal{S}_t$ and $\mathcal{V}$, respectively, i.e.

$$\mathcal{S}_t^h \subset \mathcal{S}_t \quad \text{and} \quad \mathcal{V}^h \subset \mathcal{V}. \tag{5.41}$$

In this notation, the superscript h refers to the association of $\mathcal{S}_t^h$ and $\mathcal{V}^h$ with an underlying mesh (discretization) of characteristic length scale h. The superscript is used in the following for all approximate quantities associated with the mesh. Most modern finite element analysis are based on the Bubnov-Galerkin method, often just referred to as the Galerkin method.

The following illustration of Galerkin's method and isoparametric elements is based on the books [Hughes, 2000; Simo and Hughes, 2000; Wriggers, 2009]. The interpretation as differential-algebraic equations is motivated by the works of Ellsiepen and Hartmann [2001]; Fritzen [1997]; Hartmann [2003]; Wittekindt [1991], who investigated purely mechanical problems.

5.4.1. Galerkin's Method

In the Galerkin method, a special choice of $\mathcal{S}^h$ and $\mathcal{V}^h$ is made: Assuming the collection $\mathcal{V}_\theta^h$ is given. Then, to each member $\delta\theta^h \in \mathcal{V}_\theta^h$ a function $\theta^h \in \mathcal{S}_{\theta,t}^h$ is constructed by

$$\theta^h = \delta\theta^h + \hat{T}^h, \tag{5.42}$$

where $\hat{T}^h$ is a fixed function which approximates the Dirichlet boundary conditions, i.e.

$$\hat{T}^h(\boldsymbol{X}, t) \approx \hat{T}(\boldsymbol{X}, t) \quad \text{on } \partial_\theta \Omega. \tag{5.43}$$

In classical FEM typically $\hat{T}^h$ interpolates $\hat{T}$ at the nodes. Another option is to use a least-squares fit of the Dirichlet data. Thus, equation (5.42) defines the shifted subspace

$$\mathcal{S}_{\theta,t}^h := \hat{T}^h + \mathcal{V}_\theta^h = \left\{ \hat{T}^h + \delta\theta^h \,\middle|\, \delta\theta^h \in \mathcal{V}_\theta^h \right\}, \tag{5.44}$$

where the function $\hat{T}^h(\boldsymbol{X}, t)$ is called the lift or lifting of the subspace. Up to the lift, the collections $\mathcal{V}_\theta^h$ and $\mathcal{S}_{\theta,t}^h$ are composed of identical functions.[13] For the displacement, the finite-dimensional subspaces $\boldsymbol{\mathcal{S}}_{u,t}^h$ and $\boldsymbol{\mathcal{V}}_u^h$ are constructed in the same manner.

The second step of the Galerkin idea is to find among all linear combinations of the trial functions the one which satisfies the Galerkin form of the problem. The unknown coefficients of the linear combination are determined not by a partial differential equation, but by a differential-algebraic system of $n_{\mathrm{n}\theta} + 3n_{\mathrm{nu}}$ equations, where n_{n} is the dimension of the approximate function spaces.[14] In addition, ordinary differential equations for the evolution of the internal variables have to be solved simultaneously. The complete system is derived in the following.

Since the test spaces $\mathcal{V}^h$ are finite-dimensional, there exists a basis in $\mathcal{V}^h$, i.e. a finite number of linearly independent functions $\hat{N}_i \in \mathcal{V}^h, i = 1, \ldots, n_{\mathrm{n}}$, that span the subspace. Assuming a discretization with n_{nod} nodal points, $\boldsymbol{\eta} = \{\,1, 2, \ldots, n_{\mathrm{nod}}\,\}$ defines the nodal indexes of all basis functions. The sets containing all nodes with Dirichlet boundary conditions are denoted by $\boldsymbol{\eta}_\theta \subset \boldsymbol{\eta}$ and $\boldsymbol{\eta}_{\mathrm{u}} \subset \boldsymbol{\eta}$ for temperatures and displacements, respectively. With this numbering, the test spaces are given as

$$\mathcal{V}_\theta^h := \left\{\, \delta\theta^h \colon \delta\theta^h(\boldsymbol{X}) = \sum_{i \in \boldsymbol{\eta} - \boldsymbol{\eta}_\theta} \hat{N}_i(\boldsymbol{X})\, \delta\Theta_i \,\right\}, \tag{5.45}$$

and

$$\boldsymbol{\mathcal{V}}_u^h := \left\{\, \delta\boldsymbol{u}^h \colon \delta\boldsymbol{u}^h(\boldsymbol{X}) = \sum_{i \in \boldsymbol{\eta} - \boldsymbol{\eta}_{\mathrm{u}}} \hat{N}_i(\boldsymbol{X})\, \delta\mathbf{u}_i \,\right\}, \tag{5.46}$$

where $\boldsymbol{\eta} - \boldsymbol{\eta}_\theta$ denotes set subtraction. The cardinality of the sets (number of members) are $|\boldsymbol{\eta} - \boldsymbol{\eta}_\theta| = n_{\mathrm{n}\theta}$ and $|\boldsymbol{\eta} - \boldsymbol{\eta}_{\mathrm{u}}| = n_{\mathrm{nu}}$. The functions $\hat{N}_i$ are referred to as shape, basis, or interpolation functions. In general, different discretizations can be employed for the temperature and the displacement field (and even the displacements in different directions). However, to guarantee a monotone convergence, the basis functions can not be chosen completely independent from each other, refer to [Altenbach et al., 1991] and [Gabbert, 1987]. Using the same discretization for both fields fulfills the requirements.[15]

---

[13] In the Petrov-Galerkin method different weighting and test spaces are assumed. This changes the properties of the resulting discrete problem, which is advantageous for example in the cases of hyperbolic and singularly perturbed partial differential equations, cf. [Großmann and Roos, 2005, p. 367] and [Roos et al., 2008, p. 82].

[14] For the case of linear heat conduction, one arrives at a system of $n_{\mathrm{n}\theta}$ ordinary differential equations, cf. [Hughes, 2000, p. 421]. In the case of static (time-independent) partial differential equations, the coefficients are constant and can be determined from n_{n} ($n_{\mathrm{n}\theta}$ in the case of heat conduction and n_{nu} in the case of mechanical problems) discrete algebraic equations, cf. [Strang and Fix, 1973].

[15] In fluid flow problems, heterogeneous elements with functions of different nature are often used. In that case the velocity field is interpolated by a higher-order function than the pressure field. This choice is based on the nature of the governing equations, see [Dhatt and Touzot, 1985, p. 121].

To satisfy the homogeneous boundary conditions, it is required that the shape functions vanish where Dirichlet boundary conditions are prescribed

$$\hat{N}_i(\boldsymbol{X}) = 0 \quad \text{for } \boldsymbol{X} \in \partial_\theta\Omega, \quad i \in \boldsymbol{\eta} - \boldsymbol{\eta}_\theta, \tag{5.47}$$

$$\hat{N}_i(\boldsymbol{X}) = 0 \quad \text{for } \boldsymbol{X} \in \partial_\mathrm{u}\Omega, \quad i \in \boldsymbol{\eta} - \boldsymbol{\eta}_\mathrm{u}. \tag{5.48}$$

The members of $\mathcal{S}_{\theta,t}^h$ and $\boldsymbol{\mathcal{S}}_{u,t}^h$ are constructed according to equation (5.42) as

$$\theta^h(\boldsymbol{X},t) = \sum_{j\in\boldsymbol{\eta}-\boldsymbol{\eta}_\theta} \hat{N}_j(\boldsymbol{X})\,\Theta_j(t) + \hat{T}^h(\boldsymbol{X},t), \tag{5.49}$$

$$\boldsymbol{u}^h(\boldsymbol{X},t) = \sum_{j\in\boldsymbol{\eta}-\boldsymbol{\eta}_\mathrm{u}} \hat{N}_j(\boldsymbol{X})\,\mathbf{u}_j(t) + \boldsymbol{r}^h(\boldsymbol{X},t)\,. \tag{5.50}$$

The Dirichlet boundary conditions are approximated by

$$\hat{T}^h(\boldsymbol{X},t) = \sum_{j\in\boldsymbol{\eta}_\theta} \hat{N}_j(\boldsymbol{X})\,\overline{\Theta}_j(t), \tag{5.51}$$

$$\boldsymbol{r}^h(\boldsymbol{X},t) = \sum_{j\in\boldsymbol{\eta}_\mathrm{u}} \hat{N}_j(\boldsymbol{X})\,\overline{\mathbf{u}}_j(t). \tag{5.52}$$

For convenience, $\overline{\Theta}_j(t) = \hat{T}(\boldsymbol{X}_j,t)$ and $\overline{\mathbf{u}}_j(t) = \boldsymbol{r}(\boldsymbol{X}_j,t)$ are assumed, leading to the nodal interpolates of the prescribed functions. This is neither the only possibility, nor the best from the standpoint of accuracy. The effect is investigated for example in [Strang and Fix, 1973, p. 192]. Furthermore, the lift is not ambiguous, other constructions which include for example contributions from the nodes $\boldsymbol{\eta} - \boldsymbol{\eta}_\theta$ are possible. This choice however does not alter the final result.

Inserting the approximate primal variables θ^h, $\boldsymbol{u}^h$, and their variations into the weak forms (5.33) and (5.37) leads for an elastic material to a finite-dimensional problem. However, for non-elastic materials, the material's state is given by the evolution equations of the internal variables (4.46). These are still continuous with respect to the spatial location, rendering the complete problem infinite-dimensional. To obtain a finite-dimensional problem, a numerical quadrature has to be employed for all integrals depending on the internal variables.[16]

Independent of the specific choice of method, a quadrature rule transforms an integral into a sum of K terms. Each term is given by the integrand evaluated at a quadrature point $\boldsymbol{\zeta}_k$ and weighted by a factor γ_k. In the weak forms, the second Piola-Kirchhoff

---

[16]For the case of purely mechanical systems, this method results in a system of differential-algebraic equations as shown in [Wittekindt, 1991] and further investigated in [Fritzen, 1997], [Ellsiepen and Hartmann, 2001], and [Hartmann, 2003]. The algebraic part stems from the discrete balance of linear momentum and the differential part comes from the evolution equations of the internal variables.

stress tensor $\tilde{\mathbf{T}}$ and the production term due to internal dissipation w depend on the internal variables. Thus, the two integrals are approximated by

$$\int_{\Omega} \tilde{\mathbf{T}} \cdot \delta \mathbf{E} \, \mathrm{d}V \approx \sum_{k=1}^{K} \gamma_k \mathbf{h} \left(\mathbf{C}, \theta, \mathbf{q} \right) \cdot \delta \mathbf{E} \Big|_{\boldsymbol{X} = \boldsymbol{\zeta}_k}, \tag{5.53}$$

and

$$\int_{\Omega} \varrho_{\mathrm{R}} w \delta \theta \, \mathrm{d}V \approx \sum_{k=1}^{K} \gamma_k \varrho_{\mathrm{R}} w \delta \theta \Big|_{\boldsymbol{X} = \boldsymbol{\zeta}_k}, \tag{5.54}$$

turning the weak forms into their approximate counterparts π_{u}^h and π_{θ}^h. This does not pose a severe restriction on the method, since numerical integration has to be used in most cases anyway. Nevertheless, numerical quadrature is considered to be a variational crime, see for example [Strang and Fix, 1973, p. 181] and [Hughes, 2000, p. 191]. By the preceding construction, the internal variables $\mathbf{q}$ are only needed at the K quadrature points. The resulting Galerkin form of the coupled problem is given in Problem 3.

Problem 3 Galerkin form of the coupled problem

Given the initial conditions θ_{i}, $\mathbf{q}_{\mathrm{i}}$, the boundary conditions $\boldsymbol{r}$, $\boldsymbol{s}$, $\hat{T}$, w, and c, find $\boldsymbol{u}^h \in \boldsymbol{\mathcal{S}}_{u,t}^h$ and $\theta^h \in \mathcal{S}_{\theta,t}^h$ such that for any $t \in [t_{\mathrm{i}}, t_{\mathrm{e}}]$

$$\pi_{\mathrm{u}}^h \big(\boldsymbol{u}^h, \theta^h, \mathbf{q}_k, \delta \boldsymbol{u}^h \big) = 0, \quad \text{for all } \delta \boldsymbol{u}^h \in \boldsymbol{\mathcal{V}}_u^h, \tag{5.55}$$

$$\pi_{\theta}^h \big(\boldsymbol{u}^h, \theta^h, \mathbf{q}_k, \delta \theta^h \big) = 0, \quad \text{for all } \delta \theta^h \in \mathcal{V}_{\theta}^h, \tag{5.56}$$

and

$$\dot{\mathbf{q}} = \boldsymbol{r} \big(\mathbf{C}^h, \theta^h, \mathbf{q} \big) \Big|_{\boldsymbol{X} = \boldsymbol{\zeta}_k}, \quad \mathbf{q}(\boldsymbol{\zeta}_k, t_{\mathrm{i}}) = \mathbf{q}_{\mathrm{i}}(\boldsymbol{\zeta}_k), \quad k \in 1, \dots, K. \tag{5.57}$$

5.4.2. Nonlinear Differential-Algebraic Equations

The Galerkin form of Problem 3 is solved by evaluating the variational equations (5.55) and (5.56) with the finite-dimensional approximations of the temperature θ^h, the displacements $\boldsymbol{u}^h$, and their variations. Starting with the weak form of the heat conduction problem

$$\pi_{\theta}^h \big(\boldsymbol{u}^h, \theta^h, \mathbf{q}_k, \delta \theta^h \big) = \sum_{k=1}^{K} \gamma_k \varrho_{\mathrm{R}} \left(c_{\mathrm{d}} \dot{\theta} - r - w \right) \delta \theta \Big|_{\boldsymbol{X} = \boldsymbol{\zeta}_k}$$

$$- \int_{\Omega} \boldsymbol{q}_{\mathrm{R}} \cdot \mathrm{Grad} \, \delta \theta \, \mathrm{d}V + \int_{\partial_{\mathrm{q}} \Omega} f_{\mathrm{q}} \delta \theta \, \mathrm{d}A + \int_{\partial_{\theta \mathrm{q}} \Omega} c \delta \theta \, \mathrm{d}A = 0 \tag{5.58}$$

and inserting the temperature variation (5.45) leads to

$$
\sum_{i \in \boldsymbol{\eta} - \boldsymbol{\eta}_\theta} \delta \Theta_i \Bigg\{ \sum_{k=1}^{K} \gamma_k \varrho_{\mathrm{R}} \left(c_{\mathrm{d}} \dot{\theta} - r - w \right) \hat{N}_i \Big|_{\boldsymbol{X} = \boldsymbol{\zeta}_k}
$$

$$
- \int_{\Omega} \boldsymbol{q}_{\mathrm{R}} \cdot \operatorname{Grad} \hat{N}_i \, \mathrm{d}V + \int_{\partial_{\mathrm{q}}\Omega} f_{\mathrm{q}} \hat{N}_i \, \mathrm{d}A + \int_{\partial_{\theta \mathrm{q}}\Omega} c \hat{N}_i \, \mathrm{d}A \Bigg\} = 0. \quad (5.59)
$$

Since the coefficients $\delta \Theta_i$ are arbitrary, the terms in braces have to vanish for every $i \in \boldsymbol{\eta} - \boldsymbol{\eta}_\theta$. This is equivalent to the fundamental lemma of calculus of variations in the continuous case (or the du Bois-Reymond lemma in a more general setting), cf. [Jeltsch-Fricker, 2007, p. 20]. Further, inserting the ansatz of the approximate temperature (5.49) and approximate lift (5.51) results in

$$
\sum_{j \in \boldsymbol{\eta} - \boldsymbol{\eta}_\theta} \left(C_{ij} \dot{\Theta}_j + \Lambda_{ij} \Theta_j \right) = R_i - \sum_{j \in \boldsymbol{\eta}_\theta} \left(C_{ij} \dot{\overline{\Theta}}_j + \Lambda_{ij} \overline{\Theta}_j \right), \quad \text{for all } i \in \boldsymbol{\eta} - \boldsymbol{\eta}_\theta, \quad (5.60)
$$

an implicit system of $n_{\mathrm{n}\theta} - n_{\mathrm{p}\theta}$ ordinary differential equations of first order for the unknown coefficients Θ_j, $j \in \boldsymbol{\eta} - \boldsymbol{\eta}_\theta$. Here, $n_{\mathrm{p}\theta}$ is the number of prescribed temperature and the capacity matrix

$$
C_{ij} = \sum_{k=1}^{K} \gamma_k \varrho_{\mathrm{R}} c_{\mathrm{d}} \hat{N}_i \hat{N}_j \Big|_{\boldsymbol{X} = \boldsymbol{\zeta}_k}, \quad (5.61)
$$

the conductivity matrix (using Fourier's heat flux vector according to equation (4.47))

$$
\Lambda_{ij} = \int_{\Omega} \operatorname{Grad} \hat{N}_i \cdot \boldsymbol{\lambda}_{\mathrm{R}} \operatorname{Grad} \hat{N}_j \, \mathrm{d}V, \quad (5.62)
$$

and the right-hand side

$$
R_i = \sum_{k=1}^{K} \gamma_k \varrho_{\mathrm{R}} \left(r + w \right) \hat{N}_i \Big|_{\boldsymbol{X} = \boldsymbol{\zeta}_k} - \int_{\partial_{\mathrm{q}}\Omega} f_{\mathrm{q}} \hat{N}_i \, \mathrm{d}A - \int_{\partial_{\theta \mathrm{q}}\Omega} c \hat{N}_i \, \mathrm{d}A \quad (5.63)
$$

are introduced. In matrix notation equation (5.60) can be expressed as

$$
\boldsymbol{C}(\boldsymbol{\theta}) \, \dot{\boldsymbol{\theta}} + \boldsymbol{\Lambda}(\boldsymbol{\theta}) \, \boldsymbol{\theta} = \boldsymbol{R}(\boldsymbol{\theta}) - \overline{\boldsymbol{C}}(\boldsymbol{\theta}) \, \dot{\overline{\boldsymbol{\theta}}} - \overline{\boldsymbol{\Lambda}}(\boldsymbol{\theta}) \, \overline{\boldsymbol{\theta}}, \quad (5.64)
$$

where the vector $\boldsymbol{\theta}$ contains all unknown nodal temperatures Θ_j, the vector $\boldsymbol{u}$ consists of the unknown nodal displacements $\mathbf{u}_j$, and the vector $\boldsymbol{q}$ (with dimension n_{q}) is composed of all internal variables $\mathbf{q}_j$ of the complete domain. The overlined vectors contain the prescribed values of the corresponding vectors. In the most general case, the capacity matrices $\boldsymbol{C}, \overline{\boldsymbol{C}}$, the conductivity matrices $\boldsymbol{\Lambda}, \overline{\boldsymbol{\Lambda}}$, and the load vector $\boldsymbol{R}$ depend

on the nodal temperatures $\boldsymbol{\theta}$, internal variables $\boldsymbol{q}$, nodal displacements $\boldsymbol{u}$, and their velocities. The capacity matrix $\boldsymbol{C}$ is in general symmetric, positive-definite (cf. [Hughes, 2000, p. 422]) and thus invertible. Hence, equation (5.64) can be transformed to an explicit ODE. However, the capacity matrix often has a special structure (large, banded, and sparse). Computing its inverse results in general in a dense matrix and is time-consuming, as noted in [Ascher and Petzold, 1998, p. 237]. Instead, efficient numerical methods operate directly on the implicit ODE (5.64), see for example [Strehmel and Weiner, 1995, p. 270 and p. 363].

Next, the weak form of the balance of linear momentum

$$\pi_{\mathrm{u}}^h\left(\boldsymbol{u}^h, \theta^h, \mathbf{q}_k, \delta\theta^h\right) = \sum_{k=1}^{K} \gamma_k \mathbf{h}\left(\mathbf{C}, \theta, \mathbf{q}\right) \cdot \delta\mathbf{E}\Big|_{\boldsymbol{X}=\boldsymbol{\zeta}_k}$$
$$- \int_{\partial_{\mathrm{s}}\Omega} \boldsymbol{s} \cdot \delta\boldsymbol{u}\, \mathrm{d}A - \int_{\Omega} \varrho_{\mathrm{R}} \boldsymbol{k} \cdot \delta\boldsymbol{u}\, \mathrm{d}V = 0 \quad (5.65)$$

is treated in the same fashion as the heat equation. Expanding the approximate displacement variation yields

$$\sum_{i \in \boldsymbol{\eta} - \boldsymbol{\eta}_{\mathrm{u}}} \delta\boldsymbol{u}_i \cdot \left\{ \sum_{k=1}^{K} \gamma_k \mathbf{F}\tilde{\mathbf{T}}\operatorname{Grad}\hat{N}_i\Big|_{\boldsymbol{X}=\boldsymbol{\zeta}_k} - \int_{\partial_{\mathrm{s}}\Omega} \boldsymbol{s}\hat{N}_i\, \mathrm{d}A - \int_{\Omega} \varrho_{\mathrm{R}} \boldsymbol{k}\hat{N}_i\, \mathrm{d}V \right\} = 0, \quad (5.66)$$

which is linear in $\delta\boldsymbol{u}_i$. By the same argument as before, the term in braces is identically zero. Inserting further the ansatz of the displacement (5.50) in

$$\sum_{k=1}^{K} \gamma_k \mathbf{F}\tilde{\mathbf{T}}\operatorname{Grad}\hat{N}_i\Big|_{\boldsymbol{X}=\boldsymbol{\zeta}_k} - \int_{\partial_{\mathrm{s}}\Omega} \boldsymbol{s}\hat{N}_i\, \mathrm{d}A - \int_{\Omega} \varrho_{\mathrm{R}} \boldsymbol{k}\hat{N}_i\, \mathrm{d}V = \boldsymbol{0}, \qquad \text{for all } i \in \boldsymbol{\eta} - \boldsymbol{\eta}_{\mathrm{u}},$$
$$(5.67)$$

results in an algebraic system of $3n_{\mathrm{nu}} - n_{\mathrm{pu}}$ equations, where n_{pu} is the number of prescribed displacement values. It is written in matrix form as

$$\boldsymbol{g}(\boldsymbol{u}, \boldsymbol{\theta}, \boldsymbol{q}, t) = \boldsymbol{0}. \tag{5.68}$$

This system is nonlinear in the nodal displacements $\boldsymbol{u}$, the nodal temperatures $\boldsymbol{\theta}$, as well as the internal variables $\boldsymbol{q}$.

Formally, the entity of evolution equations of the internal variables at the quadrature points $\mathbf{q}_k$ can also be viewed as a global system of ordinary differential equations. This perspective leads to the semi-discrete Galerkin form of the coupled problem, Problem 4. It forms a system of nonlinear differential-algebraic equations (DAE). The algebraic part comes from the discretized balance of linear momentum (5.68), and the differential part is given by the evolution equations of the nodal temperatures (5.64) and the internal variables (5.70). Additionally, the evolution equations of the internal variables can also

---

Problem 4 Semi-discrete Galerkin form of the coupled problem

Given the initial conditions $\boldsymbol{\theta}_0$ and $\boldsymbol{q}_0$, find $\boldsymbol{u}$, $\boldsymbol{\theta}$, and $\boldsymbol{q}$ are such that for any $t \in [t_\mathrm{i}, t_\mathrm{e}]$

$$\boldsymbol{0} = \boldsymbol{g}(\boldsymbol{u}, \boldsymbol{\theta}, \boldsymbol{q}, t), \tag{5.68}$$

$$\boldsymbol{C}(\boldsymbol{\theta})\, \dot{\boldsymbol{\theta}} = \boldsymbol{r}_\theta(\boldsymbol{u}, \dot{\boldsymbol{u}}, \boldsymbol{\theta}, \dot{\boldsymbol{\theta}}, \boldsymbol{q}, t), \qquad\qquad \boldsymbol{\theta}(t_\mathrm{i}) = \boldsymbol{\theta}_0, \tag{5.69}$$

$$\dot{\boldsymbol{q}} = \boldsymbol{r}_q(\boldsymbol{u}, \boldsymbol{\theta}, \boldsymbol{q}), \qquad\qquad \boldsymbol{q}(t_\mathrm{i}) = \boldsymbol{q}_0. \tag{5.70}$$

---

contain an algebraic part. This is for example the case of a rate-independent plastic material, consult for example [Ellsiepen and Hartmann, 2001].

The DAE of Problem 4 has been set up without specifying the shape functions and without any regard to its computer implementation. The challenge of the Ritz-Galerkin method is to choose shape functions $\hat{N}_i$ that are on the one hand convenient to compute, i.e. can be easily processed by a computer, and on the other hand general enough to approximate closely the unknown solution. These goals are simultaneously achieved by what is today known as the finite element method (FEM), a Galerkin method with a special choice of shape functions. Furthermore, this choice of shape functions leads to advantageous numerical properties of the emerging equations.

5.4.3. Isoparametric Elements

The underlying idea of the finite element method is to subdivide a given structure into n_el smaller pieces with local domain Ω_e, i.e.

$$\overline{\Omega} \approx \overline{\Omega}^h = \bigcup_{e=1}^{n_\mathrm{el}} \overline{\Omega}_e, \qquad \Omega_i \cap \Omega_j = \varnothing, \text{ if } i \neq j, \tag{5.71}$$

as shown in Fig. 5.5a. Here, the domain is approximated by $\overline{\Omega} \approx \overline{\Omega}^h$ introducing an additional geometric approximation error (bar denotes closure, see fn. 4 on p. 81).

Within each subdomain, called finite element, the shape functions are given in an extremely simple form and are highly localized. Normally, polynomials are chosen which vanish outside the element domain Ω_e. Thus, the shape functions N_a are mostly orthogonal to each other, leading to band structured system matrices (such as $\boldsymbol{C}$ and $\boldsymbol{\Lambda}$) in the semi-discrete Galerkin form. Typical shapes of three-dimensional elements are tetrahedra and hexahedra as shown in Fig. 5.5b to 5.5e. Overlapping of elements and gaps are not allowed due to compatibility reasons.

To ensure convergence of the overall procedure, the shape functions have to satisfy certain requirements. According to Hughes [2000, p. 104], sufficient conditions on the shape functions for convergence are:

- Shape functions have to be smooth on each element interior Ω_e (at least C^1).

(a) Mesh of complete domain Ω consisting of elements with domain Ω_e

(b) Linear tetrahedron

(c) Quadratic tetrahedron

(d) Linear hexahedron

(e) Quadratic hexahedron
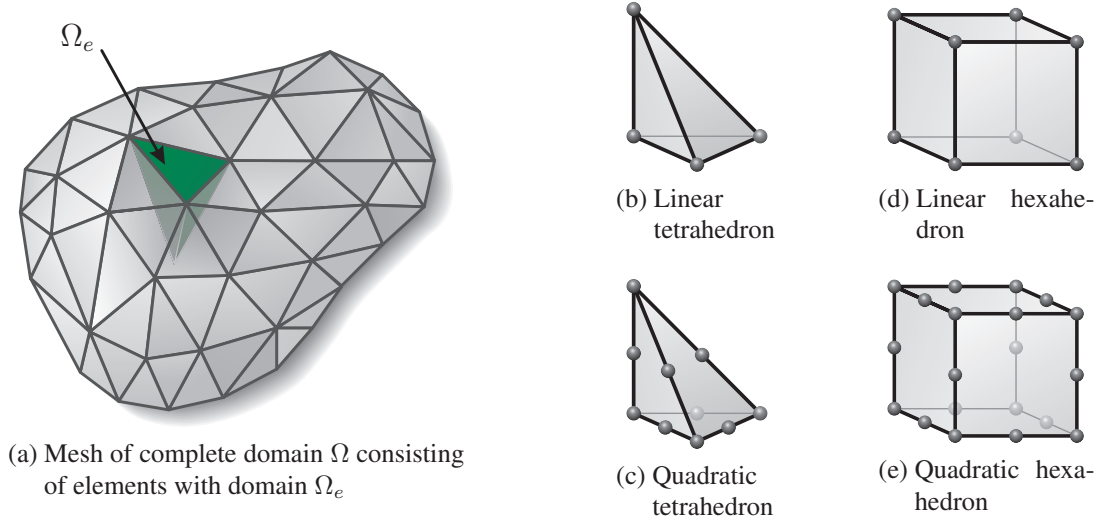
Figure 5.5.: Spatial discretization with finite elements

- Shape functions have to be continuous across each element boundary $\partial\Omega_e$.

- Shape functions have to be complete polynomials.

These conditions are only sufficient, i.e. there are elements constructed with shape functions that do not fulfill the conditions but the procedure still converges.

A special type of element class are isoparametric elements, which were first published in 1966 by Irons based on an original idea of Taig.[17] Due to their special construction, they automatically satisfy the basic convergence conditions, see [Hughes, 2000, p. 120]. They lend themselves to a concise computer implementation and can be designed to take on convenient shapes. As pointed out by Wriggers [2009, p. 105], they are in particular extremely well suited for nonlinear problems. A discretization of the spatial formulation is easily obtained and it makes no difference whether the weak form is evaluated in the initial or current configuration. Hence, the isoparametric element concept is used for the spatial discretization in the following.

In the construction of higher-order elements geometric difficulties due to complex boundary shapes are encountered. They can be dealt with by some form of coordinate mapping. For isoparamteric elements, the shape functions are formulated in a reference configuration denoted by $\Omega_\square$ in terms of natural coordinates $\boldsymbol{\xi}$. The element interpolation function is of the form

$$\theta^h : \Omega_\square \times \mathbb{R}^+ \to \mathbb{R}, \qquad \theta^h(\boldsymbol{\xi}, t) = \sum_{a=1}^{n_{\mathrm{en}}} N_a(\boldsymbol{\xi})\Theta_a^e(t), \tag{5.72}$$

which approximates in this case the temperature within the eth element. Here, n_{en} is the number of nodes per element. To relate the natural coordinates $\boldsymbol{\xi}$ with the geometrical

---

[17]A historical account of the development is given in [Zienkiewicz, 1995].

coordinates, a mapping of the same form as the interpolation function (5.72) is used, hence the name isoparametric element. The mapping reads for the reference configuration

$$\boldsymbol{X}^h \colon \Omega_\square \to \overline{\Omega}_e, \qquad \boldsymbol{X}^h(\boldsymbol{\xi}) = \sum_{a=1}^{n_{\mathrm{en}}} N_a(\boldsymbol{\xi})\boldsymbol{X}_a^e, \qquad (5.73)$$

and for the current configuration

$$\boldsymbol{x}^h \colon \Omega_\square \times \mathbb{R}^+ \to \overline{\omega}_e, \qquad \boldsymbol{x}^h(\boldsymbol{\xi}, t) = \sum_{a=1}^{n_{\mathrm{en}}} N_a(\boldsymbol{\xi})\boldsymbol{x}_a^e(t). \qquad (5.74)$$

These mappings are in most cases one-to-one, onto, $C^k, k \geq 1$ continuous, and have a positive Jacobian determinant $J^e = \det(\partial \boldsymbol{X}/\partial \boldsymbol{\xi}) > 0$ for all $\boldsymbol{\xi} \in \Omega_\square$.[18] Thus the inverse mapping $\boldsymbol{\xi} = \boldsymbol{X}^{-1} \colon \overline{\Omega}_e \to \Omega_\square$ exists and is C^k by the inverse function theorem, cf. [Burg et al., 2008, p. 507]. With these assumptions the mappings preserve the form of an element. The transformation of a linear hexahedral element from the normed parameter space $\Omega_\square$ to the reference configuration Ω_e and the current configuration ω_e is illustrated in Fig. 5.6. Stars in $\Omega_\square$ indicate the position of quadrature points which are used for the numerical evaluation of the weak forms and are considered in Sec. 5.4.4.

A basic and very popular element for three-dimensional analysis is the trilinear hexahedral element, see [Dhatt and Touzot, 1985, p. 114]. Its domain Ω_e is the image of the biunit cube in $\boldsymbol{\xi}$-space under a trilinear mapping. It is composed of eight nodes with the corresponding shape functions

$$N_a(\boldsymbol{\xi}) = \tfrac{1}{8}(1 + \xi_a\xi)(1 + \eta_a\eta)(1 + \zeta_a\zeta), \qquad (5.75)$$

where $\boldsymbol{\xi}_a$ denotes the coordinates of the nodes in $\boldsymbol{\xi}$-space. This element is in the FEM literature also referred to as cubic or brick element. It is the tensorial product of first order Lagrange polynomials, see for example [Schwarz and Köckler, 2004, p. 93]. Lagrange polynomials of order $n - 1$ are defined as

$$L_a \colon [-1, 1] \to \mathbb{R}, \quad L_a(\xi) = \prod_{\substack{b=1 \\ b \neq a}}^{n} \frac{(\xi - \xi_b)}{(\xi_a - \xi_b)}, \quad L_a(\xi_b) = \delta_{ab} = \begin{cases} 0 & \text{if } a \neq b \\ 1 & \text{if } a = b \end{cases}, \quad (5.76)$$

where δ_{ab} is the Kronecker delta as defined for example in [Kreyszig, 1989, p. 114]. A graphical representation of the three quadratic Lagrange polynomials with equidistant nodes is given in Fig. 5.7a. Each function takes on the value one at its node and is zero at the other nodes. This property can be used for the derivation of higher-order multidimensional (Lagrange) elements.

---

[18] An exception of practical relevance are elements with coalesced nodes, derived by element degeneration, such as wedge-shaped elements. See [Hughes, 2000, p. 120] for further remarks.
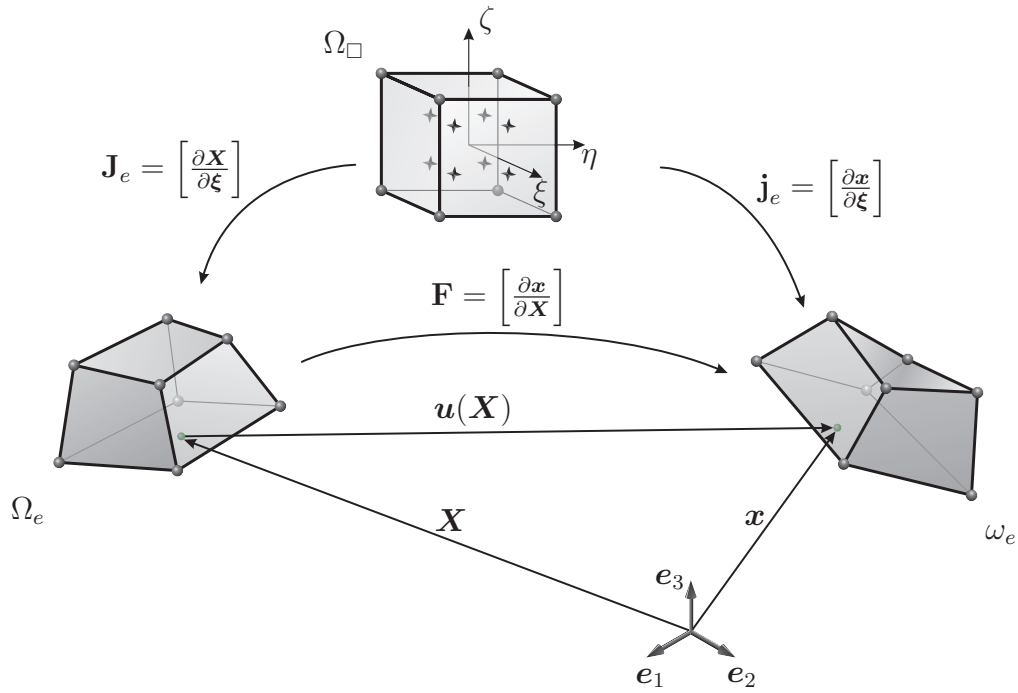
Figure 5.6.: Transformation of linear hexahedral element e from the normed parameter space $\Omega_\square$ into the reference Ω_e and the current ω_e configurations

(a) Quadratic Lagrange polynomials

(b) Tensorial product of Lagrange polynomials
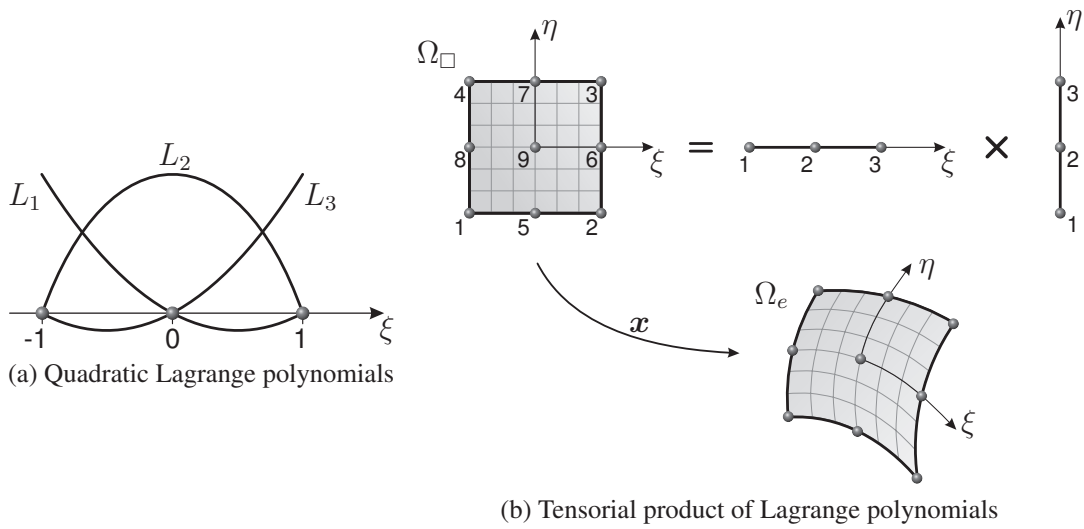
Figure 5.7.: Construction of Lagrange elements

For the construction of multidimensional elements, the tensorial product of Lagrange polynomials in the different coordinate directions of the $\boldsymbol{\xi}$-space can be employed,

$$N_a(\boldsymbol{\xi}) = L_i(\xi)L_j(\eta)L_k(\zeta). \tag{5.77}$$

This is illustrated in two dimensions in Fig. 5.7b, where the nine-node, quadratic hexahedron is composed of second order polynomials in ξ and η direction. Coordinate lines in $\boldsymbol{\xi}$-space are mapped (by the mapping (5.73) in the reference and (5.74) in the current configuration) into curvilinear lines in $\boldsymbol{x}$-space. Thus, curved boundaries may be approximated more closely with this element than with the linear element.

In three dimensions the generalization of the linear hexahedral element results in the 27-node Lagrange element. Its shape functions are depicted for fixed $\zeta = 1$ (top surface) in Fig. 5.8.

| (a) Corner Node | (b) Middle Node | (c) Midside Node |
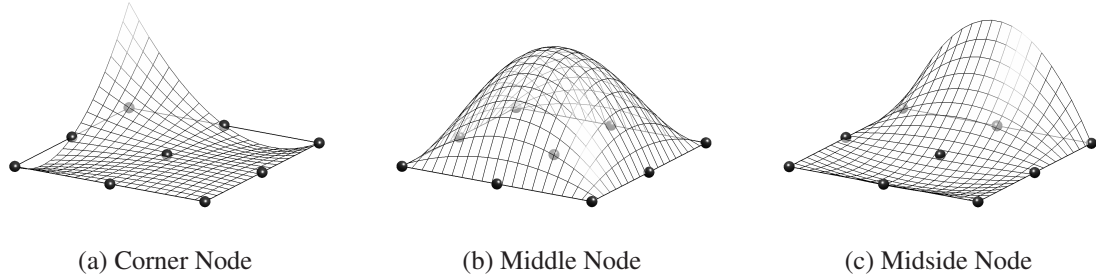
Figure 5.8.: Quadratic Lagrange shape functions at fixed $\zeta = 1$

Lagrange elements satisfy the completeness condition, but have a comparatively high number of element nodes n_{en} that results in a large global system of equations. Cost-effectiveness is often in dispute and the optimal choice of element is problem-dependent. In many cases similar results can be obtained by simplified elements with a reduced number of nodes. Elements that have nodeless interiors are referred to as Serendipity elements and are also used in the numerical examples. An example is the 20-node hexahedron of Fig. 5.5e, another one is the 8-node quadrilateral which is equal to the one displayed in Fig. 5.7b but with no internal node (node 9 is left out). The derivation of such an element and elements with a variable number of nodes is displayed in [Hughes, 2000, p. 132]. Various other element types, including elements with an increased interelement continuity are derived in [Dhatt and Touzot, 1985].

An advantage of the FEM is that the unknowns $\Theta_a^e(t)$ have a physical meaning in contrast to the weights produced by a general Ritz approximation. The unknowns $\Theta_a^e(t)$ resemble the function value at node a of element e. This property makes the computer output much easier to interpret. Another advantage is an easy improvement of the numerical solution, which can also be done locally. The accuracy of the approximation can be increased by refining the subdivision, i.e. increasing the number of finite ele-

ments.[19] In the classical Ritz-Galerkin method more and more complex trial functions are included for the same purpose.

A further advantage of the FEM is the computation of the weak forms. This is performed within a single element in the reference domain in identical manner each. To this end, the volume integral of an arbitrary integrand I are first approximated by the integral over the volume Ω^h. Subsequently, this integral can be split in a sum of integrals over element domains. These can, in turn, be computed in the $\boldsymbol{\xi}$-space by substitution, e.g. a change of variables (see for example [Burg et al., 2008, p. 569])

$$
\int_\Omega f(\boldsymbol{X})\,\mathrm{d}V \approx \int_{\Omega^h} f(\boldsymbol{X})\,\mathrm{d}V = \sum_{e=1}^{n_{\mathrm{el}}} \int_{\Omega_e} f(\boldsymbol{X})\,\mathrm{d}V
$$

$$
= \sum_{e=1}^{n_{\mathrm{el}}} \int_{\Omega_\square} f(\boldsymbol{\xi})\,\det \mathbf{J}^e(\boldsymbol{\xi})\,\mathrm{d}\Omega_\square = \sum_{e=1}^{n_{\mathrm{el}}} \int_{-1}^{+1}\int_{-1}^{+1}\int_{-1}^{+1} f(\boldsymbol{\xi})J^e(\boldsymbol{\xi})\,\mathrm{d}\xi\,\mathrm{d}\eta\,\mathrm{d}\zeta. \quad (5.78)
$$

Here $\mathbf{J}^e = [\partial \boldsymbol{X}/\partial\boldsymbol{\xi}]$ and $J^e = \det \mathbf{J}^e$ denote the Jacobian (functional) matrix and the Jacobian (functional) determinant of the transformation into the initial configuration, respectively. For the transformation into the current configuration, these values are denoted by $\mathbf{j}^e = [\partial\boldsymbol{x}/\partial\boldsymbol{\xi}]$ and j^e. Refer also to Fig. 5.6 for a graphical representation of the transformations and Fig. 5.7b for an illustration of curvilinear coordinates emanating from the transformation. Surface integrals, which are important with regard to boundary conditions, are treated in a similar manner. See the transformation (5.183) for details.

In the finite element method, the global system of equations is assembled not by looping through the basis functions, but by looping through the elements. At the element level, the local contributions are computed and in a second step assembled into the global system by means of connectivity arrays. This assembly process is described in minute detail in [Hughes, 2000], [Großmann and Roos, 2005, p. 205], [Dhatt and Touzot, 1985, p. 207], and [Becker et al., 1981, p. 107].

The integrand "$f(\boldsymbol{\xi})\det \mathbf{J}^e(\boldsymbol{\xi})$" in equation (5.78) is in general not a polynomial but a rational function of the new coordinates $\boldsymbol{\xi}$. Hence, one retreats to numerical integration in many cases.

5.4.4. Numerical Quadrature

Frequently, the integration can not be performed analytically or the exact computation would be too costly.[20] If so, the integral has to be approximated by a numerical in-

---

[19]This approach is commonly referred to as the h-version of FEM. There are also other possibilities to increase the accuracy. Uniformly increasing the polynomial degree of shape functions is called the p-FEM, while a combination of both approaches is known by the name hp-FEM, cf. [Szabó and Babuška, 1991].

[20]There are also attempts to obtain analytical integrals by symbolic computations. Videla et al. [2007] for example use the computer algebra system Maple to compute an analytical expression of the exact

tegration, also called numerical quadrature or cubature.[21] Numerical quadrature is so intimately related to the performance of the finite element method, that its selection is often part of the definition of a particular element formulation. However, doing so introduces further numerical errors which might affect the overall convergence behavior.

For this reason, numerical quadrature is listed under the heading of variational crimes by some authors. The effect of numerical quadrature on the solution is studied in [Strang and Fix, 1973, p. 191]. It is not necessary that every polynomial which appears is integrated exactly. Sufficient conditions to maintain full rate of convergence of the exactly integrated formulation are given. Full rate is attained if the quadrature rule is capable of exactly integrating all monomials through degree $\bar{k} + k - 2m$, where k is the order of the underlying Lagrange polynomial, $\bar{k}$ is the order of the highest-order monomial present in the element shape functions, and m is the order of the highest derivative.[22] First order convergence is obtained for quadrature rules that are exact for monomials through degree $\bar{k} - m$. When selecting a suitable quadrature rule, it is not sufficient to consider only accuracy requirements. Rank deficiency may also be an issue for low order quadrature rules and has to be considered separately. This effect leads to the famous spurious zero strain deformation patterns and hour-glass modes. In practice, a 8 point Gaussian quadrature is often used for the stiffness matrix (composed of derivatives of the shape functions) of trilinear brick elements, while a 27 point integration is used for elements with quadratic shape functions, cf. [Wriggers, 2009, p. 121]. For mass matrices a higher-order integration rule should be used. A more recent investigation on the effect of numerical integration in particular for higher-order elements, including the h- and the p-version of the FEM is done by Kim and Suri [1993].

Due to its accuracy and efficiency, the most popular quadrature rule in FEM is Gauss-Legendre quadrature. In fact, in one dimension it can be shown that Gauss-integration is optimal and integrates a polynomial of order $2n_{\text{ip}} - 1$ exactly, where n_{ip} is the number of integration points. See [Schwarz and Köckler, 2004, p. 321] for a proof and a derivation of parameters.

Starting with the one-dimensional case and assuming that the integrand f is smooth and integrable, the integral can be expressed as a finite sum and a remainder

$$\int_{-1}^{+1} f(\xi)\,\mathrm{d}\xi = \sum_{l=1}^{n_{\text{ip}}} \gamma_l f(\xi_l) + r[f] \approx \sum_{l=1}^{n_{\text{ip}}} \gamma_l f(\xi_l), \tag{5.79}$$

where ξ_l and γ_l denote the coordinate and the corresponding weight of the lth quadrature point of the Gaussian-rule. The remainder or error $r[f]$ generally depends on the

---

stiffness matrix of an 8-node plane elastic element. The authors found a reduction of CPU time of over 50% compared with the standard Gauss-Legendre quadrature.

[21]Some authors such as Überhuber [1997, p. 71] use the term quadrature for the numerical computation of a univariate integral and cubature for multiple integrals.

[22]Some examples on the computation of the necessary order of accuracy are given in [Hughes, 2000, p. 191]. See also [Zienkiewicz and Taylor, 2005, p. 169ff.].

function $f(\xi)$ and is dropped in the approximation.

It can be shown that the integration points ξ_l are the lth root of the Legendre polynomial of order n_{ip}.[23] The resulting quadrature coordinates and weights for up to 5 integration points are summarized in Tab. 5.1. Gaussian rules for integrals in several

Table 5.1.: Coordinates and weights of one-dimensional Gauss-Quadrature

n_{ip}	order of accuracy	ξ_l	γ_l
1	1	0.00000000000000	2.00000000000000
2	3	±0.57735026918963	1.00000000000000
3	5	±0.77459666924148	0.55555555555556
		0.00000000000000	0.88888888888889
4	7	±0.86113631159405	0.34785484513745
		±0.33998104358486	0.65214515486255
5	9	±0.90617984593866	0.23692688505619
		±0.53846931010568	0.47862867049937
		0.00000000000000	0.56888888888889

dimensions can be derived from the one-dimensional formula. For this purpose, the one-dimensional quadrature is employed on each coordinate separately

$$
\int_{-1}^{+1}\int_{-1}^{+1}\int_{-1}^{+1} f(\boldsymbol{\xi})\,\mathrm{d}\xi\,\mathrm{d}\eta\,\mathrm{d}\zeta = \int_{-1}^{+1}\int_{-1}^{+1}\left\{\sum_{i=1}^{n_{\mathrm{ip}}^{\xi}}\gamma_i f(\xi_i,\eta,\zeta)\right\}\mathrm{d}\eta\,\mathrm{d}\zeta =
$$

$$
\int_{-1}^{+1}\left\{\sum_{i,j=1}^{n_{\mathrm{ip}}^{\xi,\eta}}\gamma_i\gamma_j f(\xi_i,\eta_j,\zeta)\right\}\mathrm{d}\zeta = \sum_{i,j,k=1}^{n_{\mathrm{ip}}^{\xi,\eta,\zeta}}\gamma_i\gamma_j\gamma_k f(\xi_i,\eta_j,\zeta_k) = \sum_{l=1}^{n_{\mathrm{ip}}}\gamma_l f(\xi_l,\eta_l,\zeta_l). \quad (5.80)
$$

Unfortunately, in multidimensional cases these Gaussian quadrature rules are no longer optimal. In fact, the six-point (non-Gaussian) rule in Tab. A.1 (on p. 187) with quadrature points on the faces of the biunit cube attains the same accuracy as the $2 \times 2 \times 2 = 8$ point Gaussian quadrature. Even higher is the difference in the case of the 14-point rule, which is described in [Hammer and Stroud, 1958] and studied in the FEM context in [Irons, 1971]. In [Hellen, 1972] it is shown that this rule is of similar accuracy as the standard $3 \times 3 \times 3 = 27$ point rule for both very distorted and regular shaped serendipity elements with 20 nodes. The parameters of the integration formula are given in Tab. A.1.

For higher demands on the accuracy (in particular when using the p-version of FEM), these integration methods are ineffective. In that case vector quadrature methods as

---

[23]Refer to [Kreyszig, 1989, p. 176] for the definition and properties of Legendre polynomials.

developed in [Hinnant, 1994] yield more accurate solutions while having only a small fraction of the computational effort.

In the numerical examples of Chp. 6 either Gaussian integration rules or direct integration methods in several dimensions with the reduced computational effort of up 50% are employed. This is of particular importance when there a many time-consuming operations on integration-point level, as for example the time integration of complex material models. The origin of the local equations and the overall time integration is considered next.

5.5. Temporal Discretization using Runge-Kutta Methods

The nonlinear DAE of Problem 4 can only be solved numerically. For this purpose, different implicit time integration procedures of Runge-Kutta (RK) type are promising and described in the following.[24] The general procedure is developed on the basis of ordinary differential equations stemming from the heat conduction equation and later on extended to differential-algebraic equations.

5.5.1. Numerical Solution of Ordinary Differential Equations

A pure thermal problem is governed solely by the discretized heat conduction equation (5.64). The right-hand side can be summarized as a prescribed forcing function $\tilde{\boldsymbol{R}}(t)$, which might also depend on the nodal temperature vector $\boldsymbol{\theta}$, and leads to

$$\boldsymbol{C}\dot{\boldsymbol{\theta}} + \boldsymbol{\Lambda}\boldsymbol{\theta} = \tilde{\boldsymbol{R}}(t), \quad \boldsymbol{\theta}(t_{\mathrm{i}}) = \boldsymbol{\theta}_0. \tag{5.81}$$

It represents quasilinear differential equations as described in [Hairer and Wanner, 2002, p. 442]. Due to the properties of the capacity matrix $\boldsymbol{C}$ (see also the remarks on p. 99), the ODE (5.81) can be transformed into explicit form

$$\dot{\boldsymbol{\theta}} = \boldsymbol{C}^{-1}\left(\tilde{\boldsymbol{R}}(t) - \boldsymbol{\Lambda}\boldsymbol{\theta}\right).$$

Thus, the problem can be compactly stated as a general ODE system

$$\begin{aligned} \dot{\boldsymbol{\theta}}(t) &= \boldsymbol{f}(t, \boldsymbol{\theta}), \quad t \in [t_{\mathrm{i}}, t_{\mathrm{e}}] \\ \boldsymbol{\theta}(t_{\mathrm{i}}) &= \boldsymbol{\theta}_{\mathrm{i}}. \end{aligned} \tag{5.82}$$

---

[24]There are many different time integrations methods in the mathematical literature, among them the discontinous Galerkin (dG) methods and the Newmark algorithm. See also the footnote on p. 109. Refer for example to [Eriksson et al., 1985], [Johnson, 2009, p. 157], or the cited literature in Sec. 1.3.3 and 1.3.3 on the dG. The Newmark algorithm is a direct integration method for second order time problems, cf. [Hughes, 2000, p. 490ff.]. However, it can be adapted to first order problems by dropping all terms associated with the mass matrix M, see for example [Zienkiewicz and Taylor, 2005, p. 600ff.].

To construct an approximate solution of equation (5.82), the interval of integration is discretized by a mesh with strictly increasing finite numbers including the end points of the compact time interval

$$\mathcal{I}_h = \{t_0, t_1, \dots, t_N\} \quad \text{with} \quad t_i = t_0 < t_1 < \cdots < t_{N-1} < t_N = t_e.$$

The time step size is the difference between two consecutive points

$$h_n := t_{n+1} - t_n, \quad n = 0, \dots, N-1. \tag{5.83}$$

There are several possibilities to construct an approximate solution, i.e. a mesh function

$$\boldsymbol{\theta}^h(t) \colon \mathcal{I}_h \to \mathbb{R}^{n_{n\theta}}, \tag{5.84}$$

where $\boldsymbol{\theta}^h(t_n)$ is an approximation of the analytical solution $\boldsymbol{\theta}(t_n)$. In the case of an initial value problem (IVP), as the one at hand, one may proceed in time and use information from a previous step to compute the next time step.[25] This leads to one-step methods, which are of the general form

$$\boldsymbol{\theta}_{n+1} = \boldsymbol{\theta}_n + h\boldsymbol{\varphi}(t_n, \boldsymbol{\theta}_n; h), \quad n = 0, \dots, N-1 \tag{5.85}$$
$$\boldsymbol{\theta}_0 = \boldsymbol{\theta}_i. \tag{5.86}$$

Here, the increment function $\boldsymbol{\varphi}$ is only formally explicit and also includes implicit methods. Assuming sufficient differentiability of $\boldsymbol{\theta}(t)$, an implicit formulation can be derived from a Taylor series expansion of $\boldsymbol{\theta}(t)$ at the point t_{n+1}

$$\boldsymbol{\theta}(t_n) = \boldsymbol{\theta}(t_{n+1}) - h\dot{\boldsymbol{\theta}}(t_{n+1}) + \tfrac{1}{2}h^2\ddot{\boldsymbol{\theta}}(t_{n+1}) \mp \cdots,$$
$$\boldsymbol{\theta}(t_{n+1}) = \boldsymbol{\theta}(t_n) + h\dot{\boldsymbol{\theta}}(t_{n+1}) + \mathcal{O}(h^2). \tag{5.87}$$

Neglecting higher-order terms, this leads to the well known backward (implicit) Euler method

$$\boldsymbol{\theta}_{n+1} = \boldsymbol{\theta}_n + h_n \boldsymbol{f}(t_{n+1}, \boldsymbol{\theta}_{n+1}), \quad n = 0, \dots, N-1$$
$$\boldsymbol{\theta}_0 = \boldsymbol{\theta}_i. \tag{5.88}$$

The method uses the tangent $\boldsymbol{f}(t, \boldsymbol{\theta})$ at the future point $(t_{n+1}, \boldsymbol{\theta}_{n+1})$. This implies the solution of a system of algebraic equations which is in general nonlinear and requires

---

[25] Another important class of integration schemes are linear multistep methods. These exploit information from several preceding time steps, thus leading to efficient high-order methods. Details can be found in [Hairer et al., 2000, p. 356], [Hairer and Wanner, 2002, p. 261], [Ascher and Petzold, 1998, p. 123], and [Strehmel and Weiner, 1995, p. 325]. Kirchner and Simeon [1999] successfully apply a second order BDF integration scheme to a unified viscoplasticity model, whereas Eckert et al. [2004] treat an elasto-plasticity problem using a BDF2 method. However, according to Wittekindt [1991, p. 44] these methods have the drawback to require several restarts due to the elastic-plastic case distinction when applied to plasticity problems. Instead, he suggests to use one-step methods, in particular of Runge-Kutta type.

an iterative procedure. On the one hand the drawback is that the method becomes implicit but on the other hand this enhances the stability properties of the method (see for example [Ascher and Petzold, 1998, p. 51]).

Concerning the stability, one has to distinguish between the stability of the problem at hand and the stability of the numerical method. An ODE is said to be stable if small perturbations of the initial data remain bounded and possibly also decay with time (asymptotically stable).[26] This is an important requisite for any numerical solution. In the case of linear ODEs with constant coefficients this can be connected with the real part of eigenvalues of the underlying system matrix. For nonlinear ODEs the assessment is much more subtle and depends also on the particular solution path.

Another important characteristic of an initial value problem is its stiffness. Ideally, the choice of step size h is dictated only by accuracy demands. For many methods the step size is further restricted by stability requirements. An IVP is referred to as being stiff if the stability requirements dictate a much smaller step size than is needed to satisfy approximation demands. Stiffness depends on the differential equation itself, the accuracy requirements, the length of the interval of integration, and the region of absolute stability of the numerical method. A characteristic of stiff systems is that perturbations of a smooth solution decay very fast. This property leads to severe problems for explicit methods, cf. [Strehmel and Weiner, 1995, p. 238].

The concepts of stability and stiffness are illustrated by the one-dimensional example

$$\dot{\theta}(t) = \lambda(\theta(t) - g(t)), \tag{5.89}$$
$$\theta(t_\mathrm{i}) = \theta_\mathrm{i}, \tag{5.90}$$

where $g(t)$ is a bounded but otherwise arbitrary function.[27] For $\lambda < 0$, the problem is asymptotically stable. Choosing the function $g(t) = \sin(t)$, the analytical solution can be easily obtained

$$\theta(t) = \theta_\mathrm{h}(t) + \theta_\mathrm{p}(t) = \left(\theta_\mathrm{i} - \frac{\lambda}{1 + \lambda^2}\right)\exp(\lambda t) + \frac{\lambda}{1 + \lambda^2}\left(\lambda \sin(t) + \cos(t)\right). \tag{5.91}$$

The solution for $\lambda = -10$ and $\theta_\mathrm{i} = 1$ is displayed as the solid black curve in Fig. 5.9a. Perturbing the initial data, i.e. computing the solution for different θ_i as indicated by the gray curves, does not affect the solution path strongly. The perturbations decay fast and all curves eventually coincide. For a time step size of $h = \pi/20 \approx 0.16$, the numerical solution is computed with the forward and backward Euler method and plotted in Fig. 5.9b. The backward Euler method obtains a reasonable approximation but the forward Euler method shows spurious oscillations.[28] These become even more severe when the step size h or the factor $|\lambda|$ is enlarged.

---

[26]Refer to [Ascher and Petzold, 1998, p. 25] and [Strehmel and Weiner, 1995, p. 194] for a precise definition.

[27]See [Ascher and Petzold, 1998].

[28]The backward Euler method has the advantage of skipping fine-level solution details, due to its stability properties (denoted as L-stability or stiff decay). This is on the one hand a great potential for efficient use but on the other hand a great danger for misuse.

(a) Asymptotically stable solutions for different initial values θ_i

(b) Numerical stability of Euler methods
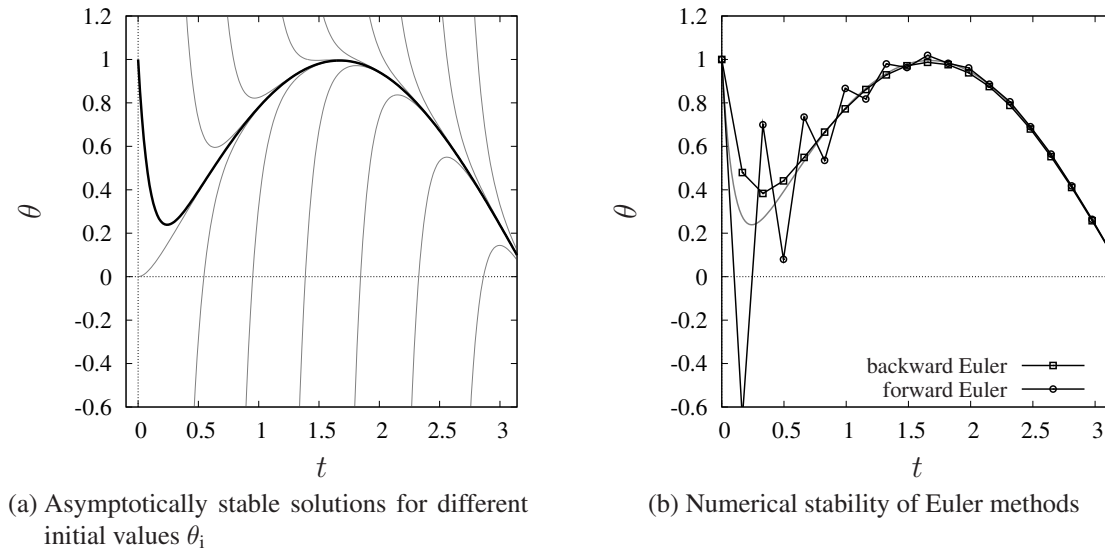
Figure 5.9.: Solution behavior

An improved numerical solution can be obtained by using an adapted mesh, which is very fine during the transient phase ($t < 0.3$) and coarse during the smooth phase. However, this does not resolve the problems of the explicit method. If the differential equation (5.89) is modified to read

$$\dot{\theta}(t) = \lambda(\theta(t) - g(t)) - \dot{g}(t),$$

then the analytical solution is simply $\theta(t) = g(t)$. Independent of the function $g(t)$, if $|\lambda| \gg 1$, this equation poses severe problems for methods with insufficient stability. This is studied in detail in [Strehmel and Weiner, 1995, p. 208]. In connection with the thermomechanical analysis, this property is important for two reasons. Firstly, the spatial discretization of the heat conduction equation leads for fine meshes to very stiff problems. This is studied analytically for the finite difference method in [Strehmel and Weiner, 1995, p. 207] and numerically for the finite element method in [Rothe, 2010]. Secondly, the behavior of many real materials leads to the construction of stiff evolution equations. These might even be of differential-algebraic type. Time integration methods for these problems have to comply with the stability requirements (often L-stable methods are chosen).

Low order methods, such as the backward Euler method, are appropriate for computing approximate solutions of a relatively low accuracy or if the problem being solved is rough. The construction of higher-order methods could in principle also be based on the Taylor polynom (5.87). This leads to so-called Taylor series methods, with the drawback that analytical expressions for higher-order derivatives are required. In practice, the derivation of these derivatives is cumbersome and prohibits a general application.[29]

---

[29]The ongoing development of compilers in particular of automatic differentiation (AD), cf. [Griewank

An alternative approach is based on the equivalent integral equation of the ODE (5.82). It allows to achieve a higher accuracy order just by using $\boldsymbol{f}(t, \boldsymbol{\theta})$, without forming symbolic derivatives of the Taylor series.

Integrating both sides of

$$\dot{\boldsymbol{\theta}}(t) = \boldsymbol{f}\big(t, \boldsymbol{\theta}(t)\big)$$

from t_n to t_{n+1} leads to

$$\int\limits_{t_n}^{t_{n+1}} \dot{\boldsymbol{\theta}}(t)\, \mathrm{d}t = \int\limits_{t_n}^{t_{n+1}} \boldsymbol{f}\big(t, \boldsymbol{\theta}(t)\big)\, \mathrm{d}t. \tag{5.92}$$

By the first fundamental theorem of calculus, see for example [Mattuck, 1999, p. 269], the left-hand side can be replaced by the difference of the temperature vector at the integration limits $\boldsymbol{\theta}(t_n) - \boldsymbol{\theta}(t_{n+1})$ and thus,

$$\boldsymbol{\theta}(t_{n+1}) = \boldsymbol{\theta}(t_n) + \int\limits_{t_n}^{t_{n+1}} \boldsymbol{f}\big(t, \boldsymbol{\theta}(t)\big)\, \mathrm{d}t$$

$$= \boldsymbol{\theta}(t_n) + h_n \int\limits_{0}^{1} \boldsymbol{f}\big(t_n + \tau h, \boldsymbol{\theta}(t_n + \tau h)\big)\, \mathrm{d}\tau \tag{5.93}$$

follows, where the substitution $t = t_n + \tau h_n$ scales the integral to unit length in the last statement. A prove of the reverse equality is given in [Mattuck, 1999, p. 454]. Hence, both statements, the ordinary differential equation and the integral equation, are equivalent.

The integral on the right-hand side of equation (5.93) can be approximated by a quadrature rule as outlined in Sec. 5.4.4. This leads to

$$\boldsymbol{\theta}(t_{n+1}) \approx \boldsymbol{\theta}(t_n) + h_n \sum_{i=1}^{s} b_i \boldsymbol{f}\big(t_n + c_i h, \boldsymbol{\theta}(t_n + c_i h)\big). \tag{5.94}$$

In this representation, s is the number of quadrature points with the quadrature weights b_i and the corresponding coordinates c_i, $i = 1, \ldots, s$. These quadrature points are called stages in connection with time integration. Many implicit Runge-Kutta methods use the same stages as classical quadrature rules, where Gauss methods obtain maximum order.

Unfortunately, the sum in equation (5.94) can not be computed yet, because $\boldsymbol{f}(t, \boldsymbol{\theta})$ has to be evaluated for the unknown temperatures $\boldsymbol{\theta}(t_n + c_i h)$. These stage temperatures can in turn be approximated by a similar quadrature formula. In order not to introduce

---

and Walther, 2008, p. 301] for higher-order derivative vectors with AD, might turn this into a more attractive method for realistic applications.

additional unknowns, the same stages (quadrature points) c_j but different weighting factors a_{ij} are chosen

$$\boldsymbol{\theta}(t_n + c_i h) = \boldsymbol{\theta}(t_n) + \int\limits_{t_n}^{t_n + c_i h_n} \boldsymbol{f}\big(t, \boldsymbol{\theta}(t)\big) \, \mathrm{d}t$$

$$\approx \boldsymbol{\theta}(t_n) + h_n \sum_{j=1}^{s} a_{ij} \boldsymbol{f}\big(t_n + c_j h, \boldsymbol{\theta}(t_n + c_j h)\big). \tag{5.95}$$

The latter approximation can be of lower order without degrading the accuracy order of the time step (5.94). It only has to be ensured that lower order errors cancel when finally summed up. To this end, the local discretization error has to be considered. It is defined as

$$\mathbf{e_l} = \boldsymbol{\theta}(t_{n+1}) - \boldsymbol{\theta}_{n+1}, \tag{5.96}$$

where $\boldsymbol{\theta}_{n+1}$ is the result of a single time step of any one-step method according to equation (5.85) with the starting vector $\boldsymbol{\theta}_n$ on the solution curve $\boldsymbol{\theta}(t)$.

A method with increment function $\boldsymbol{\varphi}(t_n, \boldsymbol{\theta}_n; h_n)$ is said to be consistent if for any given function $\boldsymbol{f}$ follows

$$\boldsymbol{\varphi}(t, \boldsymbol{\theta}(t); 0) = \boldsymbol{f}(t, \boldsymbol{\theta}), \tag{5.97}$$

i.e. the increment function $\boldsymbol{\varphi}$ tends to $\boldsymbol{f}$ as h approaches zero. In other words the rearranged calculation rule (5.85) of a single time step

$$\frac{\boldsymbol{\theta}_{n+1} - \boldsymbol{\theta}_n}{h} = \boldsymbol{\varphi}(t_n, \boldsymbol{\theta}_n; h) \tag{5.98}$$

is a local approximation of the differential operator given in equation (5.82). For practical considerations, the quality of this approximation is of importance. A measure for the degree of the approximation is the consistency (accuracy) order. A method is of consistency order p if

$$\max_{t \in \mathcal{I}_h \backslash t_N} \|\mathbf{e_l}(t + h)\| \leq C h^{p+1}. \tag{5.99}$$

The constant C and the order $p \in \mathbb{N}$ can be determined by comparison of the Taylor expansions of the true solution $\boldsymbol{\theta}(t)$ and the calculation rule.[30] Of course, this holds only under the assumption of sufficient differentiability of the differential operator $\boldsymbol{f}(t, \boldsymbol{\theta})$.

The real goal of the numerical time integration is not consistency, but convergence. Convergence means that (within exact arithmetic) the analytical solution can be approximated to an arbitrary accuracy by refining the mesh ($h_{\max} \to 0$). A method is convergent of order p^* if the global error

$$\mathbf{e_g}(t_n) = \boldsymbol{\theta}_n - \boldsymbol{\theta}(t_n), \quad n = 1, 2, \dots, N \tag{5.100}$$

---

[30] Although conceptually simple, this is a laborious task with an excess of terms to be matched. The task can be significantly eased by the introduction of a labeled tree. This graphical representation (described for example in [Hairer et al., 2000, p. 146] and [Strehmel and Weiner, 1995, p. 46]) however does not give a methodology for the construction of methods, only for checking their orders.

satisfies

$$\max_{t \in \mathcal{I}_h} \|\mathbf{e_g}(t)\| \leq C h_{\max}^{p^*}. \tag{5.101}$$

The order of convergence p^* has not to be the same as the order of consistency p. Nevertheless, it can be shown that under certain circumstances (refer to [Strehmel and Weiner, 1995, p. 36] and [Ascher and Petzold, 1998, p. 41] for technical details) consistency leads to convergence and that both, the order of consistency and the order of convergence are equal.

On a real (productive) computer system, all computations are done in a finite-dimensional environment (finite-dimensional number representation). This results in a second error contribution, the so called round-off error, as depicted in Fig. 5.10. The total error con-
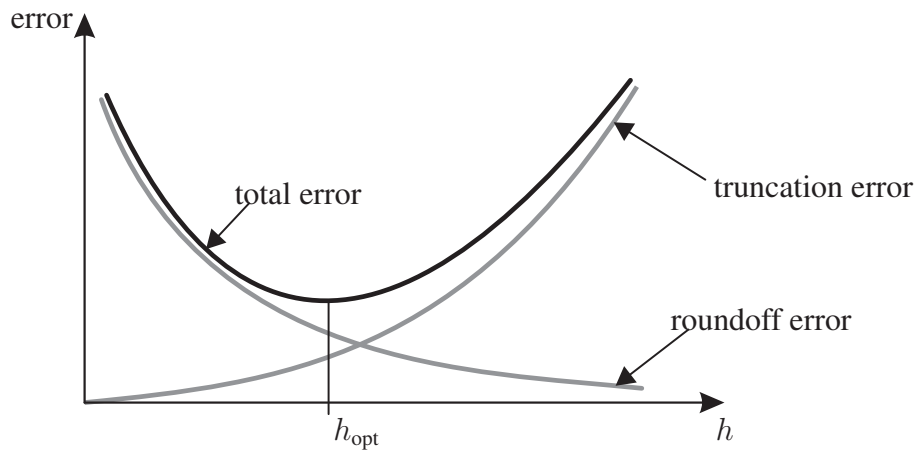
Figure 5.10.: Qualitative behavior of different error contributions

sists of the truncation error (governed by the order of convergence) and the inevitable round-off error.

A high order of convergence is preferable since it offers the potential of larger time steps with several accompanying advantages. A large time step h diminishes the round-off error of a single time step. The total number of time steps is reduced and at the same time the accumulation of round-off errors. Most of all, less time steps can speed up the computational scheme. A further and important gain in computational efficiency can be achieved by a special choice of algorithmic parameters.

A general implicit Runge-Kutta method is given by the parameter scheme termed Butcher tableau

$$
\begin{array}{c|cccc}
c_1 & a_{11} & a_{12} & \dots & a_{1s} \\
c_2 & a_{21} & a_{22} & \dots & a_{2s} \\
\vdots & \vdots & \vdots & \ddots & \vdots \\
c_s & a_{s1} & a_{s2} & \dots & a_{ss} \\
\hline
 & b_1 & b_2 & \dots & b_s
\end{array}
\quad , \quad
\text{which can be written compactly as}
\quad
\begin{array}{c|c}
\boldsymbol{c} & \mathbf{A} \\
\hline
 & \boldsymbol{b}^{\mathrm{T}}
\end{array}
\quad .
$$

Formulated with stage values $\boldsymbol{\Theta}_i$, the method reads

$$\boldsymbol{\theta}_{n+1} = \boldsymbol{\theta}(t_n) + h_n \sum_{i=1}^{s} b_i \boldsymbol{f}(t_n + c_i h, \boldsymbol{\Theta}_i) \tag{5.102}$$

$$\boldsymbol{\Theta}_i = \boldsymbol{\theta}(t_n) + h_n \sum_{j=1}^{s} a_{ij} \boldsymbol{f}(t_n + c_j h, \boldsymbol{\Theta}_j), \quad i = 1, \ldots, s, \tag{5.103}$$

or equivalently, formulated with stage derivatives $\dot{\boldsymbol{\Theta}}_i$, it is given by

$$\boldsymbol{\theta}_{n+1} = \boldsymbol{\theta}(t_n) + h_n \sum_{i=1}^{s} b_i \dot{\boldsymbol{\Theta}}_i \tag{5.104}$$

$$\dot{\boldsymbol{\Theta}}_i = \boldsymbol{f}\left(t_n + c_i h, \boldsymbol{\theta}(t_n) + h_n \sum_{j=1}^{s} a_{ij} \dot{\boldsymbol{\Theta}}_j\right), \quad i = 1, \ldots, s. \tag{5.105}$$

The stage values $\boldsymbol{\Theta}_i$ and stage derivatives $\dot{\boldsymbol{\Theta}}_i$ are intermediate approximations at times $t_n + c_i h$ to the solution and its derivative, respectively. Both quantities are local to the step from t_n to t_{n+1}. When such a method is applied to the ODE (5.82) then for each time step all stages values $\boldsymbol{\Theta}_i$ or alternatively all stage derivatives $\dot{\boldsymbol{\Theta}}_i$ are coupled and a nonlinear equation system of dimension $n_{\text{eq}} = n_{\text{n}\theta} \times s$ has to be solved. The computational expense of its solution is high and is a clear disadvantage in comparison with other methods.

The class of diagonally implicit Runge-Kutta (DIRK) methods avoids this burden. For efficiency reasons, the coefficient matrix $\mathbf{A}$ is chosen to be lower triangular

$$\begin{array}{c|cccc}
c_1 & a_{11} & & & \\
c_2 & a_{21} & a_{22} & & \\
\vdots & \vdots & \vdots & \ddots & \\
c_s & a_{s1} & a_{s2} & \ldots & a_{ss} \\
\hline
& b_1 & b_2 & \ldots & b_s
\end{array}.$$

Now, the ith stage value is defined as

$$\boldsymbol{\Theta}_i = \boldsymbol{\theta}(t_n) + h_n \sum_{j=1}^{i} a_{ij} \boldsymbol{f}(t_n + c_j h, \boldsymbol{\Theta}_j), \quad i = 1, \ldots, s. \tag{5.106}$$

$$= \boldsymbol{\Theta}_i^{\text{S}} + h_n a_{ii} \boldsymbol{f}(t_n + c_i h, \boldsymbol{\Theta}_i), \text{ with } \boldsymbol{\Theta}_i^{\text{S}} := \boldsymbol{\theta}(t_n) + h_n \sum_{j=1}^{i-1} a_{ij} \boldsymbol{f}(t_n + c_j h, \boldsymbol{\Theta}_j)$$

The choice $a_{ij} = 0, j > i$ decouples the single stages, which can in this case be solved one by one. Hence, a sequence of s nonlinear systems of the dimension $n_{\text{eq}} = n_{\text{n}\theta} - n_{\text{p}\theta}$

each has to be solved. This implies a significant reduction of computational costs, which becomes tremendous for large systems.

If in addition, the diagonal elements are all equal, i.e. $a_{ii} = \gamma, i = 1, \ldots, s$, one speaks of singly DIRK methods. Using a modified-Newton method (see Sec. 5.6, p. 146) only a single **LU** factorization has to be performed for the complete time integration. Of course, these advantages do not come for free and are at the expense of stability and accuracy. The maximum attainable order of a singly DIRK method is $p = s + 1$ and with $\gamma > 0$ these methods have only stage orders $q = 1$, cf. [Strehmel and Weiner, 1995, p. 265]. A Runge-Kutta method with a nonsingular coefficient matrix $\mathbf{A}$ which satisfies $a_{sj} = b_j, j = 1, \ldots, s$ is called stiffly accurate. This leads to the property of stiff decay, cf. [Ascher and Petzold, 1998, p. 101]. Additionally, the last stage value $\boldsymbol{\Theta}_s$ equals $\boldsymbol{\theta}_{n+1}$, as can be seen from equations (5.106) and (5.102). Thus, the evaluation of the latter equation can be omitted, saving additional computing time. Having said that, the attainable order is further restricted to $p = s$ in the case of stiffly accurate DIRK methods. The presented approach and its numerical features are studied in the next subsection.

5.5.2. Order Reduction Phenomenon

While the presented methods work very well and are known to achieve a high order of accuracy for general ODEs, this is not always the case when they are used in conjunction with the method of lines (MOL-RK approach). In the presence of Dirichlet boundary conditions, a convergence and order reduction can be seen when using the MOL-RK approach for parabolic and hyperbolic PDEs. This phenomenon is well known and reported in [Verwer, 1986] for implicit, as well as in [Sanz-Serna et al., 1986] for explicit Runge-Kutta methods. The temporal order of convergence can further be related to the spatial regularity and the type of boundary conditions as shown in [Lubich and Ostermann, 1993].

To study the effect in the present case, the heat conduction problem of Fig. 5.11 is treated with the MOL-RK approach using finite elements and DIRK methods. At the left and right side of the domain, the boundary temperatures are specified. A heat source term r is not specified, since the expected numerical difficulties are caused by the boundary conditions. The setup is such, that the problem degrades to a one-dimensional one. Its mathematical representation, the one-dimensional form of the heat equation (4.59), is also given in Fig. 5.11. In the formulation the one-dimensional Fourier's heat flux $q = -\lambda \partial \theta / \partial x$ according to equation (4.47) is used. Furthermore, the diffusivity $a = \lambda / (\varrho c_{\mathrm{d}})$ as introduced in equation (2.2) is used to summarize all material parameters. Using the same arguments as in the derivation of the weak form of the three-dimensional heat conduction equation (5.37), one arrives at its one-dimensional

$$\frac{\partial \theta}{\partial t} = a \frac{\partial^2 \theta}{\partial x^2}$$

$$\theta(x, t_{\mathrm{i}}) = \theta_{\mathrm{i}}(x)$$
$$\theta(0, t) = f(t)$$
$$\theta(L, t) = g(t)$$
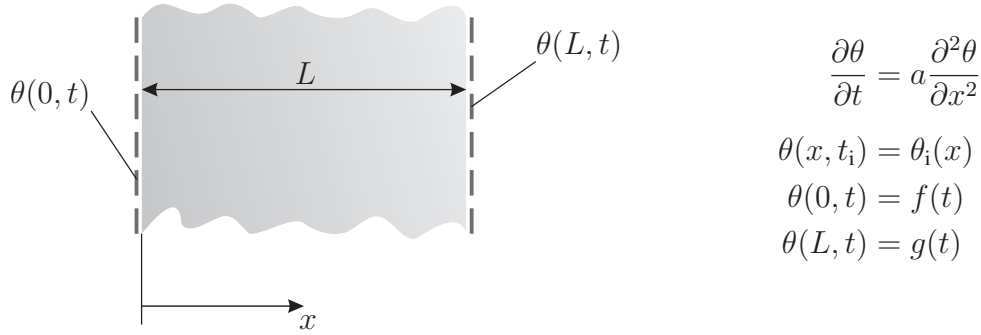
Figure 5.11.: Setup of one-dimensional heat conduction problem

counterpart

$$\int_0^L \dot{\theta} \delta\theta \, \mathrm{d}x + \int_0^L a\theta' \delta\theta' \, \mathrm{d}x = 0. \tag{5.107}$$

In this representation, the spatial derivative with respect to x is abbreviated by a prime. Along the MOL approach the weak form is first discretized in space and subsequently in time. The Galerkin ansatz using finite elements reads

$$\theta^h(x, t) = \sum_{j \in \boldsymbol{\eta} - \boldsymbol{\eta_\theta}} \hat{N}_j(x) \, \Theta(t) + \sum_{j \in \boldsymbol{\eta_\theta}} \hat{N}_j(x) \, \overline{\Theta}_j(t),$$

see equations (5.49) and (5.51). The most basic discretization uses linear shape functions and is depicted in Fig. 5.12. It leads to a piecewise linear approximation of the
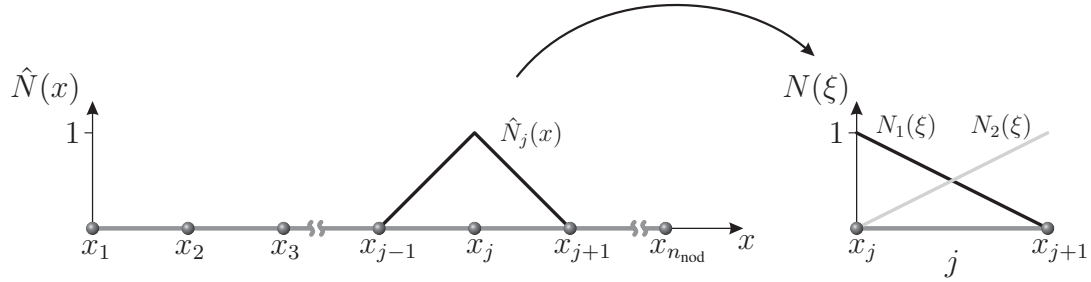
Figure 5.12.: Discretization of one-dimensional domain with linear finite elements

temperature distribution in space.

As outlined in Sec. 5.4.3, the shape functions and integrals are evaluated element wise. Thus, the temperature is given within the jth element $(x_j \leq x \leq x_{j+1})$ by

$$\theta^h(x, t) = N_1(\xi)\Theta_j(t) + N_2(\xi)\Theta_{j+1}(t), \qquad x(\xi) = N_1(\xi)x_j + N_2(\xi)x_{j+1}, \tag{5.108}$$

where $N_i(\xi)$, $i = 1, \ldots, n_{\mathrm{en}}$, is the shape function associated with the ith node of the element. A similar ansatz is chosen for the virtual temperatures. Using the same argument

as in equation (5.60), one arrives at the ODE

$$\boldsymbol{C}\dot{\boldsymbol{\theta}} + \boldsymbol{\Lambda}\boldsymbol{\theta} = -\overline{\boldsymbol{C}}\,\dot{\overline{\boldsymbol{\theta}}} - \overline{\boldsymbol{\Lambda}}\,\overline{\boldsymbol{\theta}}, \tag{5.109}$$

where $\boldsymbol{\theta}$ contains all unknown nodal temperature values. The vector $\overline{\boldsymbol{\theta}} = \{f(t), g(t)\}^{\mathrm{T}}$ consists of all prescribed values, here the boundary temperatures at nodes 1 and n_{nod}. The capacity matrices $\boldsymbol{C}$ and $\overline{\boldsymbol{C}}$ as well as the conductivity matrices $\boldsymbol{\Lambda}$ and $\overline{\boldsymbol{\Lambda}}$ are assembled from the element matrices $\boldsymbol{\mathsf{C}}$ and $\boldsymbol{\mathsf{\Lambda}}$. Due to the simplicity of the elements, all integrals can be evaluated analytically and a numerical quadrature is not needed. The conductivity matrix of the jth element is given by

$$\boldsymbol{\mathsf{\Lambda}}_j = \int\limits_{x_j}^{x_{j+1}} a \begin{bmatrix} N_1'N_1' & N_1'N_2' \\ N_2'N_1' & N_2'N_2' \end{bmatrix} \mathrm{d}x = \frac{a}{\Delta x} \begin{bmatrix} 1 & -1 \\ -1 & 1 \end{bmatrix}. \tag{5.110}$$

Similarly, the element capacity matrix can be computed analytically and reads

$$\boldsymbol{\mathsf{C}}_j = \int\limits_{x_j}^{x_{j+1}} \begin{bmatrix} N_1 N_1 & N_1 N_2 \\ N_2 N_1 & N_2 N_2 \end{bmatrix} \mathrm{d}x = \frac{\Delta x}{6} \begin{bmatrix} 2 & 1 \\ 1 & 2 \end{bmatrix}. \tag{5.111}$$

The capacity matrix $\boldsymbol{C}$ and the conductivity matrix $\boldsymbol{\Lambda}$ are of the dimension $n_{\mathrm{n}\theta} \times n_{\mathrm{n}\theta}$ and have the same structure (tridiagonal).

Applying a DIRK method, consisting of equations (5.102) and (5.106), results for the stage values $\boldsymbol{\Theta}_i$ in

$$\left[\frac{1}{h_n\, a_{ii}}\boldsymbol{C} + \boldsymbol{\Lambda}\right]\boldsymbol{\Theta}_i = \frac{1}{h_n\, a_{ii}}\boldsymbol{C}\boldsymbol{\Theta}_i^{\mathrm{S}} - \overline{\boldsymbol{C}}\dot{\overline{\boldsymbol{\theta}}}(t_n + c_i h_n) - \overline{\boldsymbol{\Lambda}}\,\overline{\boldsymbol{\theta}}(t_n + c_i h_n), \qquad i = 1,\dots,s, \tag{5.112}$$

where the starting vector

$$\boldsymbol{\Theta}_i^{\mathrm{S}} = \boldsymbol{\theta}_n + h_n \sum_{j=1}^{i-1} a_{ij}\, \dot{\boldsymbol{\Theta}}_j \tag{5.113}$$

is completely given by the previous stages. Formally, a single DIRK stage has the same structure and involves the same operations as one step of the classical backward Euler method. Thus, existing FEM codes with implicit time integration can be extended to high-order time integration with only minor changes. Stiffly accurate methods additionally have the advantage that the last stage value $\boldsymbol{\Theta}_s$ corresponds to the value at the next time step $\boldsymbol{\theta}_{n+1}$, as pointed out previously.

After the stage value $\boldsymbol{\Theta}_i$ is known, the stage derivative can be computed from equation (5.106), it is given by

$$\dot{\boldsymbol{\Theta}}_i = \frac{\boldsymbol{\Theta}_i - \boldsymbol{\Theta}_i^{\mathrm{S}}}{h_n\, a_{ii}}. \tag{5.114}$$

In the first example, homogeneous boundary conditions $f(t) = g(t) = 0$ are prescribed. A sinusoidal initial temperature distribution $\theta_i(x) = \sin(\pi x/L)$ is chosen, which is consistent with the boundary conditions. To minimize the influence of the spatial approximation, a very fine grid with $n_{nod} = 100000$ nodes is chosen. The parameters length and diffusivity are specified to be $L = 1$ and $a = 0.1$, respectively. Together with this fine discretization, this leads to a stiff ODE.

The temperature distribution can be computed analytically with the method of separation of variables as shown in [Greenberg, 1998, p. 954]. The solution is given by

$$\theta(x, t) = \sin\left(\frac{\pi x}{L}\right) \exp\left(-a\left(\frac{\pi}{L}\right)^2 t\right) \tag{5.115}$$

and slowly decays with time, tending towards the steady-state solution. It is depicted in Fig. 5.13a for different times. With the analytical solution at hand, the numerical

(a) Temperature distribution at $t = \{0, 0.2, \ldots, 1\}$ (b) Convergence behavior
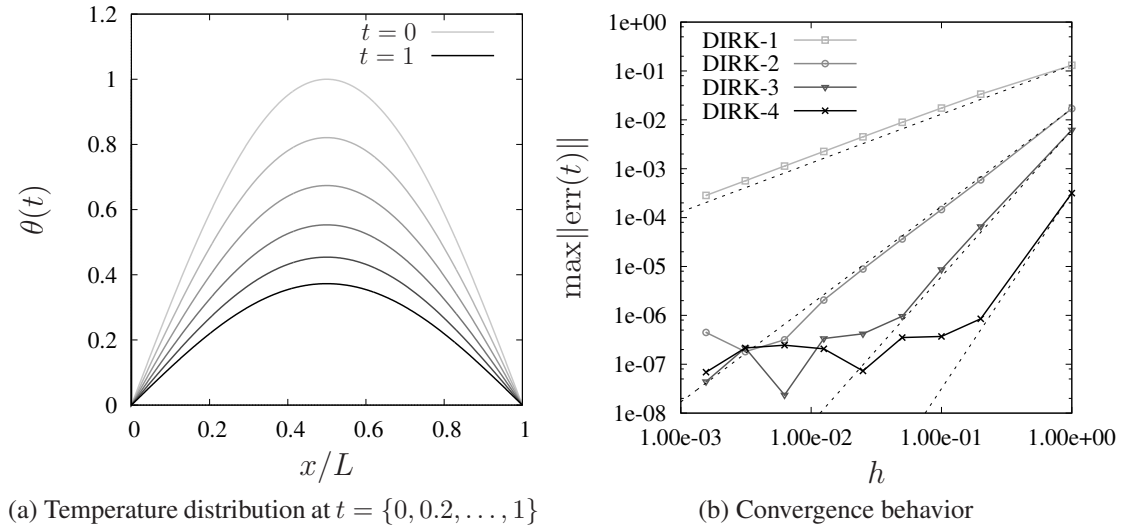
Figure 5.13.: Heat conduction problem with homogeneous boundary conditions

error can be computed for various time stepping methods. Here, the DIRK methods of App. A.2 are applied with different constant step sizes h. The results for the backward Euler method (DIRK-1), the second order method of Alexander [1977] (DIRK-2), the third order method of Alexander [1977] (DIRK-3), and the fourth order method of Hairer and Wanner [2002, p. 100] (DIRK-4) are shown in Fig. 5.13b. The order of convergence is given by the slope of the curves. For reference, the theoretical orders are indicated by dashed lines. As can be seen, the theoretical order are indeed achieved by the numerical methods. For small time steps h and high-order methods, the accuracy can not be improved due to round-off errors and the convergence degenerates after passing an optimal step size h_{opt}, refer also to Fig. 5.10. A similar behavior is often also observed for large time steps, where the error estimate (5.101) does not hold. Thus, an intermediate step size interval is typically chosen and of practical relevance.

Next, the problem is changed slightly by specifying a time-dependent boundary condition at the left side, $f(t) = \sin(\pi/2t)$. Its solution is displayed in Fig. 5.14a. The

(a) Temperature distribution at $t = \{0, 0.2, \dots, 1\}$

(b) Convergence behavior
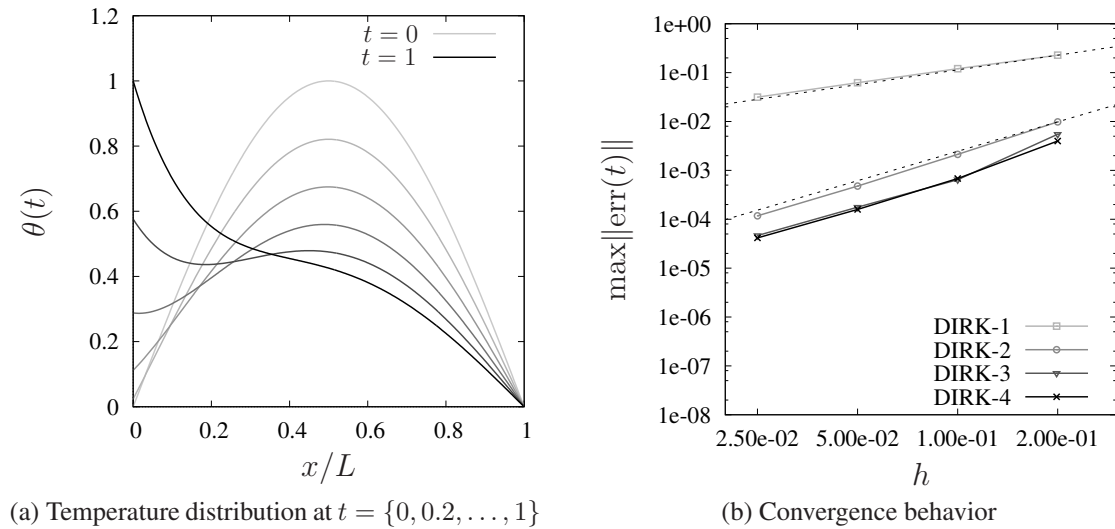
Figure 5.14.: Heat conduction problem with inhomogeneous boundary condition at left side

temperature distribution can still be derived analytically but is given in terms of an infinite series. This is demonstrated in [Al-Baldawi, 2008] along the lines of [Greenberg, 1998, p. 977]. Looking at the convergence behavior, it is seen in Fig. 5.14b that none of the methods exceeds second order rate of convergence. Spending a lot of computational effort does not pay off at all for the higher order methods. For explicit RK methods it is shown by Carpenter et al. [1995] that the conventional imposition of boundary conditions leads to a numerical scheme which is only first order accurate in the neighborhood of the boundary and globally only of second order accuracy, independent of the spatial operator.

There are several proposals to cope with the present problems. One approach is to reformulate the problem and move the "input" from the boundary conditions to the PDE, as done in the aforementioned analytical solution of this problem, see for example [Calvo and Palencia, 2001]. However, this approach is not suited for complicated boundary conditions in several dimensions and works only for linear problems. Another approach ignores the given boundary conditions during the intermediate stages and extends the inner values up to the boundary, possibly using one-sided approximations of the spatial derivatives. A drawback of this method is that the allowable step size is drastically reduced, rendering the RK method less attractive, cf. [Carpenter et al., 1995].

A remedy to this are corrections of the boundary terms for intermediate stages as described in [Pathria, 1997], [Alonso-Mallo, 2002], and [Alonso-Mallo and Cano, 2004]. The idea stems from the fact that the stage value Θ_i is according to equation (5.95) only

a lower order approximation of $\boldsymbol{\theta}(t_n + c_i h)$. In fact, the stage order of the considered methods is only $q = 1 \neq p$.

Instead of directly prescribing the stage values and derivatives at the boundary, the boundary conditions are cast in the form of an ODE $\dot{\bar{\boldsymbol{\theta}}}(t) = \{\dot{f}(t), \dot{g}(t)\}^\mathrm{T}$, which is added to the ODE (5.109). The time integration of this part is done in the usual way and boils down to a simple summation of weighted derivatives. For example for the function $f(t)$ the ith stage value is given as

$$ F_i = f(t_n) + h \sum_{j=1}^{i} a_{ij} \dot{f}(t_n + c_j h). \tag{5.116} $$

Its effect on the convergence behavior is shown for the sinusoidal boundary term in Fig. 5.15a. Remarkably, the order of convergence is completely restored in this case.

(a) Sinusoidal function   (b) Polynomial function
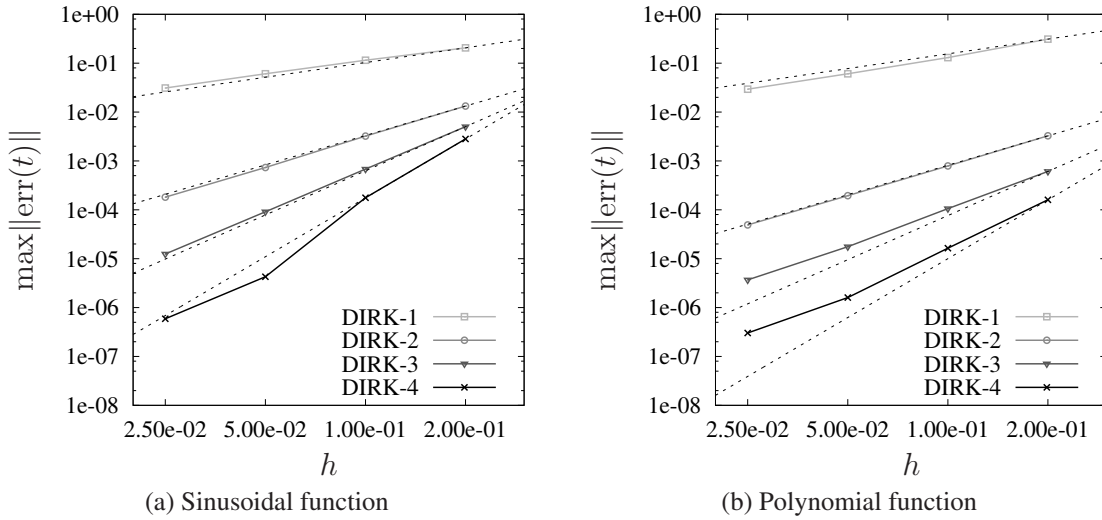
Figure 5.15.: Convergence behavior with modified internal stages

For a polynomial boundary function $f(t) = \frac{1}{2}(t^2 + t^3)$ the proposed method still works but the convergence order is slightly spoiled, as seen in Fig. 5.15b. In this case the more demanding iterative methods developed in [Alonso-Mallo, 2002] and [Alonso-Mallo and Cano, 2004] may overcome this deficiency.

Another demanding application, where order reductions are reported, are differential-algebraic equations. Their numerical treatment using DIRK methods is considered next.

5.5.3. Numerical Solution of Differential-Algebraic Equations

The semi-discrete Galerkin form of the thermomechanically coupled problem, Problem 4, constitutes a system of differential-algebraic equations (DAE). The class of DAEs

contains all ODEs, as well as mixed problems. Here, both differentiation and integration may be intertwined in a complex manner.

In the present case, the DAE is given in semi-explicit form and consists of a differential part and an algebraic part. Its differential part is composed of the afore-discussed ODE for the temperatures and the evolution equations of the internal variables. The algebraic part stems from the discretized balance of linear momentum.[31] The DAE

$$\mathbf{0} = \mathbf{g}(\mathbf{u}, \boldsymbol{\theta}, \mathbf{q}, t), \tag{5.117}$$

$$\mathbf{C}\dot{\boldsymbol{\theta}} = \hat{\mathbf{r}}_\theta(\mathbf{u}, \boldsymbol{\theta}, \mathbf{q}, t), \qquad \boldsymbol{\theta}(t_\mathrm{i}) = \boldsymbol{\theta}_0, \tag{5.118}$$

$$\dot{\mathbf{q}} = \mathbf{r}_q(\mathbf{u}, \boldsymbol{\theta}, \mathbf{q}), \qquad \mathbf{q}(t_\mathrm{i}) = \mathbf{q}_0, \tag{5.119}$$

with the consistent initial conditions $\mathbf{g}(\mathbf{u}_0, \boldsymbol{\theta}_0, \mathbf{q}_0, t_\mathrm{i}) = \mathbf{0}$ is of semi-explicit form. If the partial derivative of the algebraic part with respect to $\mathbf{u}$ is regular within the neighborhood of the solution, then it is a semi-explicit index-1 DAE. The index of a DAE is the number of differentiations needed to transform the DAE into an ODE. In the present case the algebraic equation can be differentiated with respect to time t, which first results in

$$\mathbf{0} = \frac{\partial \mathbf{g}}{\partial \mathbf{u}} \dot{\mathbf{u}} + \frac{\partial \mathbf{g}}{\partial \boldsymbol{\theta}} \dot{\boldsymbol{\theta}} + \frac{\partial \mathbf{g}}{\partial \mathbf{q}} \dot{\mathbf{q}} + \frac{\partial \mathbf{g}}{\partial t}, \tag{5.120}$$

and subsequently, yields the differential equation

$$\dot{\mathbf{u}} = - \left[\frac{\partial \mathbf{g}}{\partial \mathbf{u}} \right]^{-1} \left[\frac{\partial \mathbf{g}}{\partial \boldsymbol{\theta}} \dot{\boldsymbol{\theta}} + \frac{\partial \mathbf{g}}{\partial \mathbf{q}} \dot{\mathbf{q}} + \frac{\partial \mathbf{g}}{\partial t} \right]. \tag{5.121}$$

This procedure is called index reduction by differentiation. Afterwards, a standard solver can be applied to the resulting ODE. However, this is typically not a practical option for most large systems since it involves many operations and can deteriorate the numerical properties of the problem. E.g. the numerical solution does not exactly fulfill the algebraic constraint and may "drift off" from the manifold given by the constraint equations. Furthermore, due to internal heat production, the temperature evolution may also be coupled with the velocity and the rate of change of the internal variables

$$\mathbf{C}(\boldsymbol{\theta}) \dot{\boldsymbol{\theta}} = \mathbf{r}_\theta(\mathbf{u}, \dot{\mathbf{u}}, \boldsymbol{\theta}, \dot{\boldsymbol{\theta}}, \mathbf{q}, t). \tag{5.122}$$

Hence, the problem at hand is not an index-1 DAE and index reduction becomes even more involved and other methods are superior to it.[32] These methods can be classified

---

[31] For certain material models, the evolution equations of the internal variables themselves form DAEs, see for example [Hartmann, 2003] and the references therein.

[32] In general, the higher the index of a DAE, the more difficulties one can expect for its numerical solution. Note however, that the index by itself does not imply anything about the numerical difficulty of the solution. In fact, a higher-index DAE can often be simpler than an ODE or a lower-index DAE, refer for instance to the examples in [Ascher and Petzold, 1998, p. 242]. On the other hand, DIRK methods are known to experience a severe order reduction for semi-explicit index-2 DAEs and fully implicit index-1 problems, cf. [Ascher and Petzold, 1998, p. 271].

as direct or indirect discretization. The solution by indirect discretization is based on the regularity of $\partial \boldsymbol{g}/\partial \boldsymbol{u}$ and uses the implicit function theorem to obtain from the algebraic constraint (5.117) for all times t a unique solution $\boldsymbol{u}(t) = \tilde{\boldsymbol{g}}_\mathrm{u}(\boldsymbol{\theta}, \boldsymbol{q}, t)$. This relation can be substituted in the differential part of the DAE consisting of equations (5.118) and (5.119). The procedure results in an ODE which can be solved by a standard integration method.

On the other hand, in direct discretization the problem is first reformulated. The DAE is regularized by replacing the algebraic constraint equation by the ODE

$$\varepsilon \dot{\boldsymbol{u}} = \boldsymbol{g}(\boldsymbol{u}, \boldsymbol{\theta}, \boldsymbol{q}, t), \tag{5.123}$$

which depends on a small parameter $0 < \varepsilon \ll 1$. Together with the equations (5.118) and (5.119) a singularly perturbed initial problem emanates. For its numerical solution methods for stiff ODEs and in particular with stiff decay are promising, since the regularized ODE is very stiff. Applying a DIRK method leads to the equation system

$$\varepsilon \boldsymbol{U}_i = \varepsilon \boldsymbol{u}_n + h \sum_{j=1}^{i} a_{ij} \boldsymbol{g}(\boldsymbol{U}_j, \boldsymbol{\Theta}_j, \boldsymbol{Q}_j, t_n + h c_j) \tag{5.124}$$

$$\boldsymbol{C} \boldsymbol{\Theta}_i = \boldsymbol{C} \boldsymbol{\theta}_n + h \sum_{j=1}^{i} a_{ij} \boldsymbol{r}_\theta(\boldsymbol{U}_j, \dot{\boldsymbol{U}}_j, \boldsymbol{\Theta}_j, \dot{\boldsymbol{\Theta}}_j, \boldsymbol{Q}_j, t_n + h c_j), \tag{5.125}$$

$$\boldsymbol{Q}_i = \boldsymbol{q}_n + h \sum_{j=1}^{i} a_{ij} \boldsymbol{r}_q(\boldsymbol{U}_j, \boldsymbol{\Theta}_j, \boldsymbol{Q}_j), \tag{5.126}$$

which has to be solved at each stage $i = 1, \ldots, s$. Next, the limit $\varepsilon \to 0$ is considered. This leads to

$$\boldsymbol{0} = \boldsymbol{g}(\boldsymbol{U}_i, \boldsymbol{\Theta}_i, \boldsymbol{Q}_i, t_n + h c_i), \tag{5.127}$$

which replaces equation (5.124).

Introducing further starting vectors $\boldsymbol{Q}_i^\mathrm{S}$ and $\boldsymbol{U}_i^\mathrm{S}$ for the internal variables and nodal displacements (analogous to the definition (5.113)) simplifies the equation system to

$$\boldsymbol{0} = \boldsymbol{G}_u(\boldsymbol{U}_i, \boldsymbol{\Theta}_i, \boldsymbol{Q}_i) = \boldsymbol{g}(\boldsymbol{U}_i, \boldsymbol{\Theta}_i, \boldsymbol{Q}_i, t_n + h c_i), \tag{5.128}$$

$$\boldsymbol{0} = \boldsymbol{G}_\theta(\boldsymbol{U}_i, \boldsymbol{\Theta}_i, \boldsymbol{Q}_i) = \boldsymbol{C}\left(\boldsymbol{\Theta}_i - \boldsymbol{\Theta}_i^\mathrm{S}\right) - h a_{ii} \boldsymbol{r}_\theta(\boldsymbol{U}_i, \dot{\boldsymbol{U}}_i, \boldsymbol{\Theta}_i, \dot{\boldsymbol{\Theta}}_i, \boldsymbol{Q}_i, t_n + h c_i), \tag{5.129}$$

$$\boldsymbol{0} = \boldsymbol{L}(\boldsymbol{U}_i, \boldsymbol{\Theta}_i, \boldsymbol{Q}_i) \quad = \boldsymbol{Q}_i - \boldsymbol{Q}_i^\mathrm{S} - h a_{ii} \boldsymbol{r}_q(\boldsymbol{U}_i, \boldsymbol{\Theta}_i, \boldsymbol{Q}_i). \tag{5.130}$$

The stage derivatives depend on the stage values and are given by

$$\dot{\boldsymbol{U}}_i := \frac{\boldsymbol{U}_i - \boldsymbol{U}_i^\mathrm{S}}{h a_{ii}}, \quad \dot{\boldsymbol{\Theta}}_i := \frac{\boldsymbol{\Theta}_i - \boldsymbol{\Theta}_i^\mathrm{S}}{h a_{ii}}, \quad \text{and} \quad \dot{\boldsymbol{Q}}_i := \frac{\boldsymbol{Q}_i - \boldsymbol{Q}_i^\mathrm{S}}{h a_{ii}}. \tag{5.131}$$

Direct and indirect discretization of semi-explicit index-1 DAEs, as the one considered here, are equal if stiffly accurate RK methods are used, [Strehmel and Weiner, 1995,

p. 384]. For a DAE of index greater than two it is usually best to use index-reduction techniques to solve the problem in a lower-index form, cf. [Ascher and Petzold, 1998, p. 262].

The solution of the nonlinear equation system (5.128)-(5.130) has to be done iteratively and is considered in Sec. 5.6. Prior to that, another point related to the time integration deserves attention. The performance of any discretization method depends not only on the chosen method but to a large degree also on the time step size h and its control. For this purpose, different time step control techniques have been developed. The method used in this work is considered next.

5.5.4. Step Size Control

Methods with a constant step size perform poorly if the solution varies rapidly in some part of the integration interval and slowly in other parts. In these cases problem adapted meshes are required. The step size should be chosen in such a way that it is large in smooth parts and small in transient parts. Step sizes which are too small lead to a waste of computational resources and an accumulation of round-off errors.

The goal is to keep the entire integration process local and to only march forward in time. Hence, step size control relies on an estimation of the local error $\mathbf{e}_l(t_n + h)$. Using this estimation, the step size h is chosen in such a way that $\|\mathbf{e}_l(t_n + h)\|$ stays below a user-supplied error tolerance. Even though, some doubt on the quality of the error estimate is advisable, it is expected that by this procedure also the global error $\max_{t \in \mathcal{I}_h} \|\mathbf{e_g}(t)\|$ does not proliferate.[33]

A highly efficient method for local error control is based on an embedded Runge-Kutta method. For this purpose, two s-stage methods are constructed in such a way that they use the same stages c_i, have the same coefficient matrix $\mathbf{A}$, but use different weights b_i and $\hat{b}_i$, leading to different accuracy orders p and $\hat{p}$. The method reads in compact notation

$$\begin{array}{c|c} c & A \\ \hline & b^{\mathrm{T}} \end{array} \quad + \quad \begin{array}{c|c} c & A \\ \hline & \hat{b}^{\mathrm{T}} \end{array} \quad \Rightarrow \quad \begin{array}{c|c} c & A \\ \hline & b^{\mathrm{T}} \\ & \hat{b}^{\mathrm{T}} \end{array} .$$

To compute an estimate of the local error, the consistency orders of the two methods

---

[33] It is also possible to control the global error, which is closely related to goal-oriented adaptive control. One possibility is to use step doubling (also referred to as Richardson extrapolation), cf. [Ascher and Petzold, 1998, p. 93]. Another possibility is to solve an adjoint problem as described in [Lang and Verwer, 2007] and the literature cited therein. Certainly, these approaches are much more costly than local error control, since at least two full integrations over the complete time domain have to be done. Whether local error control is reliable or not, depends on the condition of the system. In general, this is no problem if the system is dissipative.

differ by one, i.e. $\hat{p} = p - 1$. Using both methods for a single step leads to

$$\boldsymbol{y}_{n+1} = \boldsymbol{y}(t_n + h) + \mathcal{O}\big(h^{p+1}\big), \tag{5.132}$$

$$\hat{\boldsymbol{y}}_{n+1} = \boldsymbol{y}(t_n + h) + \mathcal{O}\big(h^{\hat{p}+1}\big), \tag{5.133}$$

where the solution vector $\boldsymbol{y}^{\mathrm{T}} = \{\boldsymbol{u}^{\mathrm{T}}, \boldsymbol{\theta}^{\mathrm{T}}, \boldsymbol{q}^{\mathrm{T}}\}$ has been introduced. Consequently, the difference $\hat{\boldsymbol{y}}_{n+1} - \boldsymbol{y}_{n+1}$ estimates the main part of the local discretization error for the embedded method of consistency order $\hat{p} = p - 1$. Thus, the error estimation is done only for the "second best" approximation of $\boldsymbol{y}(t_n + h)$. On the other hand, this method uses in general much less computational resources than estimation methods. The pair of embedded Runge-Kutta methods share the stage computations, which have to be done only once. The local error is approximately given by

$$\mathbf{e}_{\mathrm{l}} \approx \boldsymbol{y}_{\mathrm{err}} = \hat{\boldsymbol{y}}_{n+1} - \boldsymbol{y}_{n+1} = h_n \sum_i^s \left(\hat{b}_i - b_i\right) \dot{\boldsymbol{Y}}_i, \tag{5.134}$$

with the stage derivatives

$$\dot{\boldsymbol{Y}}_i = \frac{\boldsymbol{Y}_i - \boldsymbol{Y}_i^{\mathrm{S}}}{h_n \, a_{ii}}. \tag{5.135}$$

These are computed at the end of each stage, once the stage vector $\boldsymbol{Y}_i$ is known. As before, the formula uses the starting vector $\boldsymbol{Y}_i^{\mathrm{S}}$, composed only of previously computed information

$$\boldsymbol{Y}_i^{\mathrm{S}} = \boldsymbol{y}_n + h_n \sum_{j=1}^{i-1} a_{ij} \dot{\boldsymbol{Y}}_j. \tag{5.136}$$

Hence, also for the algebraic variables, the displacements $\boldsymbol{u}$, stage derivatives and an error estimation can be obtained by the embedded method.

With the error estimate at hand, it can be checked whether the local error stays below a user-specified tolerance Etol. This is in general given as a combination of a user-prescribed absolute ε_{a} and relative tolerance ε_{r}. It is requested that the local error satisfies

$$\|\boldsymbol{y}_{\mathrm{err}}\| = \|\hat{\boldsymbol{y}}_{n+1} - \boldsymbol{y}_{n+1}\| \leq \varepsilon_{\mathrm{a}} + \varepsilon_{\mathrm{r}} \|\hat{\boldsymbol{y}}_{n+1}\| = \mathrm{Etol} \tag{5.137}$$

for each time step. If the components of the solution $\boldsymbol{y}$ are very different in magnitude, it is better to use an array of tolerances, as studied in conjunction with FEM computations in [Hartmann et al., 2008b]. For each component an individual absolute and a common relative error tolerance can be given.

In the case that the estimated error stays below the specified tolerance Etol, the integration can march forward, probably with a different step size. Otherwise the step is rejected and has to be repeated with a smaller step size. To find an appropriate size, the information from the error estimation can be used. Since the lower order method is of accuracy order $\hat{p}$, the local error behaves as $\|\mathbf{e}_{\mathrm{l}}(t_n + h_n)\| \approx C h_n^{\hat{p}+1}$. From this relationship

C can be approximately determined. An "optimal" step size is computed with the requirement, that the local error equals the specified tolerance, i.e. Etol $= \|\boldsymbol{y}_{\text{err}}\| \approx Ch_{\text{opt}}^{\hat{p}+1}$. This step size is given by

$$h_{\text{opt}} = h_n \left(\frac{\text{Etol}}{\|\boldsymbol{y}_{\text{err}}\|} \right)^{1/(\hat{p}+1)} = h_n \left(\frac{\varepsilon_{\text{a}} + \varepsilon_{\text{r}}\|\hat{\boldsymbol{y}}_{n+1}\|}{\|\hat{\boldsymbol{y}}_{n+1} - \boldsymbol{y}_{n+1}\|} \right)^{1/(\hat{p}+1)} \tag{5.138}$$

and the process is repeated until an acceptable step size if found. In this case the time integration can move forward. For successful time steps, the same formula can used to adapt the size for the next step.

In practice, safety factors have to be used to ensure a stable algorithm with neither too large nor too small time steps and to prevent too frequent changes of the step size. As pointed out before, different tolerances are used for quantities of different magnitude and physical meaning. Also the used norm has to be specified, its appropriate choice is crucial for the whole process. According to Deuflhard and Bornemann [2008, p. 170], it is advisable to use smooth norms, such as the euclidean norm. Following the proposal of Hairer et al. [2000, p. 168] and Hairer and Wanner [2002, p. 124], for the displacements and temperatures the weighted norms

$$\text{e}_u := \sqrt{\frac{1}{n_{\text{nu}}} \sum_{k=1}^{n_{\text{nu}}} \left(\frac{u_{\text{err},k}}{\varepsilon_{\text{a}}^u + \varepsilon_{\text{r}}^u |u_k|} \right)^2}, \qquad \text{e}_\theta := \sqrt{\frac{1}{n_{\text{n}\theta}} \sum_{k=1}^{n_{\text{n}\theta}} \left(\frac{\theta_{\text{err},k}}{\varepsilon_{\text{a}}^\theta + \varepsilon_{\text{r}}^\theta |\theta_k|} \right)^2}, \tag{5.139}$$

are employed, where u_k and θ_k are the kth components of $\boldsymbol{u}_{n+1}$ and $\boldsymbol{\theta}_{n+1}$, respectively. The respective error estimates $\boldsymbol{u}_{\text{err}}$ and $\boldsymbol{\theta}_{\text{err}}$ are given by equation (5.134). For the internal variables a maximum norm is used, since these are defined pointwise. Diebels et al. [1999] propose the usage of

$$\text{e}_q := \max_{1 \leq k \leq n_{\text{q}}} \left| \frac{q_{\text{err},k}}{\varepsilon_{\text{a}}^q + \varepsilon_{\text{r}}^q |q_k|} \right|. \tag{5.140}$$

After the error measures have been computed, the maximum $\text{e}_{\text{max}} = \max(\text{e}_u, \text{e}_\theta, \text{e}_q)$ is used to determine the new step size

$$h_{\text{new}} = h_n \times \begin{cases} \max\left(f_{\text{min}}, f_{\text{safety}} \times \text{e}_{\text{max}}^{-1/(\hat{p}+1)} \right) & \text{if } \text{e}_{\text{max}} > 1 \\ \min\left(f_{\text{max}}, f_{\text{safety}} \times \text{e}_{\text{max}}^{-1/(\hat{p}+1)} \right) & \text{if } \text{e}_{\text{max}} \leq 1 \end{cases}. \tag{5.141}$$

The safety factor $0 < f_{\text{safety}} < 1$ prevents oscillations of the step size while f_{min} and f_{max} keep the step size from increasing and decreasing too fast. Usually values around $0.8 < f_{\text{safety}} < 0.9$, $0.2 < f_{\text{min}} < 0.5$, and $2 < f_{\text{max}} < 3$ work best, but these can be highly problem-dependent.

If necessary, the step size control can be stabilized and further refined by methods developed in feedback control theory of mechanical and electrical systems. This approach was first studied by Gustafsson et al. [1988] and later on refined for explicit

Runge-Kutta methods in [Gustafsson, 1991] and for implicit Runge-Kutta methods in [Gustafsson, 1994]. A thorough review of the achievements in this area is given by Söderlind [2002]. In control theory commonly PI and PID control structures are used to improve robustness, where already the PI controller is satisfactory for many cases. It leads to a relatively simple modification of the elementary local error control

$$h_{\text{opt}} = h_n \left(\frac{\text{Etol}}{\|\boldsymbol{y}_{\text{err}}^{n+1}\|} \right)^{k_{\text{I}}} \left(\frac{\|\boldsymbol{y}_{\text{err}}^{n}\|}{\|\boldsymbol{y}_{\text{err}}^{n+1}\|} \right)^{k_{\text{P}}}, \tag{5.142}$$

where k_{I} and k_{P} are constant parameters that define the proportional and the integral gain, respectively. These parameters are somewhat problem-dependent and should be finetuned for a specific application. A generally reasonable choice for the parameters are $k_{\text{I}} = 0.3/(\hat{p} + 1)$ and $k_{\text{P}} = 0.4/(\hat{p} + 1)$.

In the course of the numerical solution of the DAE (5.117)-(5.119) with implicit time adaptive Runge-Kutta methods a sequence of nonlinear systems (5.128)-(5.130) emanates. Its solution has to be done iteratively and offers several aspects for performance gains compared to standard procedures. These aspects are considered in the following.

5.6. Solution of Nonlinear Systems

At each stage within a time step of the DIRK-methods, a nonlinear algebraic system

$$\boldsymbol{F} \colon \mathbb{R}^n \to \mathbb{R}^n, \qquad \boldsymbol{F}(\boldsymbol{y}) = \boldsymbol{0} \tag{5.143}$$

has to be solved. In the case of thermomechanically coupled problems, the vector of unknowns consists of the stage values $\boldsymbol{y}^{\text{T}} = \{\boldsymbol{U}^{\text{T}}, \boldsymbol{\Theta}^{\text{T}}, \boldsymbol{Q}^{\text{T}}\}$ and the system has the form

$$\boldsymbol{F}(\boldsymbol{y}) = \begin{Bmatrix} \boldsymbol{G}_u(\boldsymbol{U}, \boldsymbol{\Theta}, \boldsymbol{Q}) \\ \boldsymbol{G}_\theta(\boldsymbol{U}, \boldsymbol{\Theta}, \boldsymbol{Q}) \\ \boldsymbol{L}(\boldsymbol{U}, \boldsymbol{\Theta}, \boldsymbol{Q}) \end{Bmatrix} = \boldsymbol{0}, \tag{5.144}$$

with the dimension $n = n_{\text{nu}} + n_{\text{n}\theta} + n_{\text{q}}$ and the components of $\boldsymbol{F}$ given in equations (5.128)-(5.130). Of course, the function $\boldsymbol{F}$ and the variables depend on the current stage. The subscript i, denoting the ith stage, has been dropped for brevity, i.e. $\boldsymbol{U}$ stands for the unknown stage value $\boldsymbol{U}_i$ at the time $t = t_n + h_n\, c_i$. The discretized equilibrium condition $\boldsymbol{G}_u$ and the discretized heat equation $\boldsymbol{G}_\theta$ are assembled from element contributions and have to be solved on global level. In contrast to that, the internal variables were only formally assembled to a global vector $\boldsymbol{q}$. Thus, the discretized evolution equations of the internal variables are defined on local, i.e. quadrature point, level and are only coupled by the nodal temperatures $\boldsymbol{\theta}$ and the nodal displacements $\boldsymbol{u}$. This special structure of the equation system has to be considered when constructing efficient solution methods. The most popular method used in the context of nonlinear finite element analysis is the multilevel-Newton algorithm as pointed out by Hartmann [2005]. This a variant of the classical Newton-Raphson method.

5.6.1. Newton-Raphson Method

The numerical solution of the nonlinear system of equations (5.143) starts from the initial iterate (sometimes referred to as guess) $\boldsymbol{y}^{(0)}$ and uses an iteration of the form

$$\boldsymbol{y}^{(m+1)} = \boldsymbol{y}^{(m)} + \Delta\boldsymbol{y}^{(m)}. \tag{5.145}$$

To determine the Newton step $\Delta\boldsymbol{y}^{(m)}$, the system (5.143) is linearized at the point $\boldsymbol{y}^{(m)}$. To this end, the components of $\boldsymbol{F}$ are expanded in the form of a Taylor polynomial. Exemplarily, for the first component of $\boldsymbol{F}$ and $\boldsymbol{y}$ one obtains

$$F_1(y_1 + \Delta y_1, y_2, \ldots, y_n) = F_1(y_1, y_2, \ldots, y_n) + \Delta y_1 \left.\frac{\partial F_1}{\partial y_1}\right|_{\boldsymbol{y}^{(0)}} + \cdots .$$

The other components of $\boldsymbol{F}$ and $\boldsymbol{y}$ are treated in the same manner. Keeping only first order terms, this leads to a linear system of equations for the Newton step $\Delta\boldsymbol{y}^{(k)}$

$$\boldsymbol{F}\left(\boldsymbol{y}^{(m)}\right) + \left.\frac{\mathrm{d}\boldsymbol{F}}{\mathrm{d}\boldsymbol{y}}\right|_{\boldsymbol{y}^{(m)}} \Delta\boldsymbol{y}^{(m)} = \boldsymbol{0}$$

with the Jacobian matrix

$$\frac{\mathrm{d}\boldsymbol{F}}{\mathrm{d}\boldsymbol{y}} = \begin{bmatrix} F_{1,1} & \cdots & F_{1,n} \\ \vdots & \ddots & \vdots \\ F_{n,1} & \cdots & F_{n,n} \end{bmatrix}, \qquad F_{i,j} = \frac{\partial F_i}{\partial y_j}. \tag{5.146}$$

A solution exists under the assumption that the Jacobian matrix is regular. It is formally given by

$$\left.\frac{\mathrm{d}\boldsymbol{F}}{\mathrm{d}\boldsymbol{y}}\right|_{\boldsymbol{y}^{(m)}} \Delta\boldsymbol{y}^{(m)} = -\boldsymbol{F}\left(\boldsymbol{y}^{(m)}\right). \tag{5.147}$$

The iteration is finished, once a specified error tolerance is reached. Common are a tolerance for the Newton step vector $\|\Delta\boldsymbol{y}\| \leq \mathrm{tol}_y$, a tolerance for the residual $\|\boldsymbol{F}(\boldsymbol{y}^{(m)})\| \leq \mathrm{tol}_F$, and a combination of both.

When applied to the equations (5.144), the Newton-Raphson method has to be used with some caution. Two facets to keep in mind are related to the efficiency and the convergence properties of the method. The basic ideas of the solution scheme for the systems of nonlinear equations and the convergence theory for Newton's method are most often based on local considerations, see [Kelley, 1995]. The standard assumptions require that

- there is a solution $\boldsymbol{y}^*$ to the problem $\boldsymbol{F}(\boldsymbol{y}) = \boldsymbol{0}$

- the functional matrix of the function $\boldsymbol{F}(\boldsymbol{y})$, $\mathrm{d}\boldsymbol{F}(\boldsymbol{y})/\mathrm{d}\boldsymbol{y}$, is Lipschitz continuous near the solution $\boldsymbol{y}^*$

- $\mathrm{d}\boldsymbol{F}(\boldsymbol{y})/\mathrm{d}\boldsymbol{y}$ is non-singular.

Lipschitz continuity near $\boldsymbol{y}^*$ means that there is a constant $\kappa > 0$ such that $\|\boldsymbol{F}'(\boldsymbol{x}) - \boldsymbol{F}'(\boldsymbol{y})\| \leq \kappa\|\boldsymbol{x} - \boldsymbol{y}\|$. κ is called Lipschitz constant. These assumptions (in particular the requirement that $\boldsymbol{F}(\boldsymbol{y})$ is Lipschitz continuous differentiable) are rigorous and often violated in engineering problems. E.g. the existence of a yield surface with distinction in elastic and plastic region in material models of metal plasticity are non-differentiable functions.

Non-smooth functions and singular functional matrices can lead to order reduction and even the failure of convergence. There are many attempts to cope with these problems. Among these global methods are line search methods as the Armijo rule [Armijo, 1966], trust region methods [Dennis and Schnabel, 1996], homotopy [Watson et al., 1987] and pseudo-transient continuation [Kelley and Keyes, 1998]. Additionally, stability problems of the structure are frequently solved by means of the arc-length method on global level. Further problems might occur in constitutive equations with softening behavior. In this case, local integration steps have to be treated with the methods discussed above. A small viscosity is commonly applied to regularize the case distinctions in yield function based models, as discussed in [Simo and Hughes, 2000].

5.6.2. Multilevel-Newton Algorithm

The multilevel-Newton algorithm (MLNA) is the most commonly used algorithm in the context of nonlinear finite element analysis of quasistatic problems in solid mechanics. It was originally developed in the context of large-scale electrical networks in [Rabbat et al., 1979]. The algorithm is known to have local quadratic convergence provided that suitable conditions on the continuity and regularity of the Jacobian matrix of the equations are satisfied. Ellsiepen and Hartmann [2001] relate the MLNA to the consistent tangent operator developed by Simo and Taylor [1985] and the classical structure of local iteration of the "stress algorithm".

The MLNA, which has in this case two levels, is also based on a correction of the form (5.145). In contrast to the classical Newton-Raphson method, the system of equations is decomposed into a local and global part, which are treated separately. Combining on the one hand the global equations of the equilibrium condition and the heat equation in $\boldsymbol{G}^{\mathrm{T}} := \{\boldsymbol{G}_u^{\mathrm{T}}, \boldsymbol{G}_\theta^{\mathrm{T}}\}$ and on the other hand the nodal displacements and temperatures in $\boldsymbol{V}^{\mathrm{T}} := \{\boldsymbol{U}^{\mathrm{T}}, \boldsymbol{\Theta}^{\mathrm{T}}\}$ leads to the compact system

$$\boldsymbol{G}(\boldsymbol{V}, \boldsymbol{Q}) = \boldsymbol{0}, \tag{5.148}$$

$$\boldsymbol{L}(\boldsymbol{V}, \boldsymbol{Q}) = \boldsymbol{0}. \tag{5.149}$$

Assuming that the local equation (5.149) is satisfied at the point $(\boldsymbol{V}_0, \boldsymbol{Q}_0)$, and supposing that the function $\boldsymbol{L}$ is C^1 continuous in some neighborhood N of $(\boldsymbol{V}_0, \boldsymbol{Q}_0)$ with $\partial\boldsymbol{L}/\partial\boldsymbol{Q}$

regular. Then the function $\boldsymbol{L}$ uniquely implies a function $\hat{\boldsymbol{Q}}(\boldsymbol{V})$ in N by the implicit function theorem, cf. [Greenberg, 1998, p. 647].[34] This function can be inserted into the global equation (5.148) leading to an expression which only depends on the global variables

$$G\left(\boldsymbol{V}, \hat{\boldsymbol{Q}}(\boldsymbol{V})\right) = \boldsymbol{0}. \tag{5.150}$$

Applying the classical Newton-Raphson scheme to equation (5.150) yields for each iteration m the linear system

$$\left[\frac{\partial \boldsymbol{G}}{\partial \boldsymbol{V}} + \frac{\partial \boldsymbol{G}}{\partial \hat{\boldsymbol{Q}}}\frac{\mathrm{d}\hat{\boldsymbol{Q}}}{\mathrm{d}\boldsymbol{V}}\right]_{\boldsymbol{Y}^{(m)}} \Delta \boldsymbol{V}^{(m)} = -\boldsymbol{G}\left(\boldsymbol{V}^{(m)}, \hat{\boldsymbol{Q}}\left(\boldsymbol{V}^{(m)}\right)\right), \tag{5.151}$$

where the matrix on the left-hand side is the generalized "consistent tangent operator" of the fully coupled thermomechanical system. The functional matrices read in component form

$$\frac{\partial \boldsymbol{G}}{\partial \boldsymbol{V}} = \begin{bmatrix} \frac{\partial \boldsymbol{G}_u}{\partial \boldsymbol{U}} & \frac{\partial \boldsymbol{G}_u}{\partial \boldsymbol{\Theta}} \\ \frac{\partial \boldsymbol{G}_\theta}{\partial \boldsymbol{U}} & \frac{\partial \boldsymbol{G}_\theta}{\partial \boldsymbol{\Theta}} \end{bmatrix}, \text{ and } \frac{\partial \boldsymbol{G}}{\partial \boldsymbol{Q}} = \begin{bmatrix} \frac{\partial \boldsymbol{G}_u}{\partial \boldsymbol{Q}} \\ \frac{\partial \boldsymbol{G}_\theta}{\partial \boldsymbol{Q}} \end{bmatrix}. \tag{5.152}$$

Since the function $\hat{\boldsymbol{Q}}(\boldsymbol{V})$ is in general unknown, $\boldsymbol{Q}$ is determined from equation (5.149) for given global variables $\boldsymbol{V}$. This is done blockwise using a classical Newton-Raphson scheme on quadrature point level. Thus, only local systems of low dimension have to be treated.

On the global level, the derivative $\mathrm{d}\hat{\boldsymbol{Q}}/\mathrm{d}\boldsymbol{V}$ is needed to assemble the generalized stiffness matrix in equation (5.151). It can be determined by inserting the function $\hat{\boldsymbol{Q}}(\boldsymbol{V})$ into the local equation (5.149) and forming the total derivative with respect to the global variables $\boldsymbol{V}$. The derivative $\mathrm{d}\boldsymbol{L}/\mathrm{d}\boldsymbol{V}$ vanishes identically, since $\hat{\boldsymbol{Q}}$ is obtained from equation (5.149). Following the chain rule one obtains

$$\frac{\mathrm{d}\boldsymbol{L}}{\mathrm{d}\boldsymbol{V}} = \frac{\partial \boldsymbol{L}}{\partial \boldsymbol{V}} + \frac{\partial \boldsymbol{L}}{\partial \hat{\boldsymbol{Q}}}\frac{\mathrm{d}\hat{\boldsymbol{Q}}}{\mathrm{d}\boldsymbol{V}} = \boldsymbol{0}, \quad \text{with} \quad \frac{\mathrm{d}\hat{\boldsymbol{Q}}}{\mathrm{d}\boldsymbol{V}} = \begin{bmatrix} \frac{\partial \boldsymbol{Q}}{\partial \boldsymbol{U}} \\ \frac{\partial \boldsymbol{Q}}{\partial \boldsymbol{\Theta}} \end{bmatrix},$$

which constitutes a linear system with several right-hand sides

$$\frac{\partial \boldsymbol{L}}{\partial \hat{\boldsymbol{Q}}}\frac{\mathrm{d}\hat{\boldsymbol{Q}}}{\mathrm{d}\boldsymbol{V}} = -\frac{\partial \boldsymbol{L}}{\partial \boldsymbol{V}}. \tag{5.153}$$

The outlined iteration is repeated until a user-prescribed convergence criterion is fulfilled. Tab. 5.2 summarizes the complete procedure with distinction into local and global level. On the global level, from eight different convergence criteria can be chosen in the

---

[34]These conditions are in general fulfilled for problems using viscoelastic and thermoviscoelastic material models. For material models of plasticity with case distinction this is not necessarily true. For instance the continuity can be violated, which might result in an order reduction or even a failure of the MLNA.

Table 5.2.: Multilevel-Newton algorithm in the ith stage of time-step from t_n to t_{n+1}

Given: $\boldsymbol{V}^{(0)}$, $\boldsymbol{Q}^{(0)}$ from initial iterate, h_n, $t_n + c_i h_n$, a_{ii}, $\boldsymbol{S}$

Repeat $\quad m = 0, \dots$

> *local (quadrature point) level*
>
> given: $\boldsymbol{V}^{(m)}$, $\boldsymbol{y} := \left(\boldsymbol{U}^{(m)}, \boldsymbol{\Theta}^{(m)}, \boldsymbol{Q}^{(m)} \right)$
>
> local integration step
> $$\boldsymbol{L}(\boldsymbol{V}^{(m)}, \boldsymbol{Q}^{(m)}) = \boldsymbol{0} \qquad\qquad \rightsquigarrow \boldsymbol{Q}^{(m)}$$
>
> consistent linearization
> $$\left.\frac{\partial \boldsymbol{L}}{\partial \boldsymbol{Q}}\right|_{\boldsymbol{y}} \left.\frac{\mathrm{d}\boldsymbol{Q}}{\mathrm{d}\boldsymbol{V}}\right|_{\boldsymbol{y}} = - \left.\frac{\partial \boldsymbol{L}}{\partial \boldsymbol{V}}\right|_{\boldsymbol{y}} \qquad \rightsquigarrow \left.\frac{\mathrm{d}\boldsymbol{Q}}{\mathrm{d}\boldsymbol{V}}\right|_{\boldsymbol{y}}$$

> *global level*
>
> solve linear system of equations
> $$\left[\left.\frac{\partial \boldsymbol{G}}{\partial \boldsymbol{V}}\right|_{\boldsymbol{y}} + \left.\frac{\partial \boldsymbol{G}}{\partial \boldsymbol{Q}}\right|_{\boldsymbol{y}} \left.\frac{\mathrm{d}\boldsymbol{Q}}{\mathrm{d}\boldsymbol{V}}\right|_{\boldsymbol{y}} \right] \Delta\boldsymbol{V} = -\boldsymbol{G}(\boldsymbol{y}) \quad \rightsquigarrow \Delta\boldsymbol{V}$$
>
> update of global variables
> $$\boldsymbol{V}^{(m+1)} \leftarrow \boldsymbol{V}^{(m)} + \Delta\boldsymbol{V} \qquad\qquad \rightsquigarrow \boldsymbol{V}^{(m+1)}$$

---

until the convergence criterion is fulfilled

---

inhouse code TASAFEM. These are listed in App. A.3 and include the classical criteria of the norms of the Newton update, the residual, and the combination of both.

Depending on the complexity and the kind of the material model as well as the global number of unknowns, the local integration step can consume a major part of the total computation time.[35] An advantage of the MLNA is that the local Newton (local integration step, also called stress algorithm) can be easily executed in parallel. To this end, all elements are grouped into element sets, where elements belonging to the same set share the same properties, i.e. they have the same shape, the same shape functions, and "are made of" the same material. The loop over all elements is in this work parallelized using OpenMP directives as described for example in [Chapman et al., 2008]. In this regard, it is important to maintain the same partitioning throughout the complete pro-

---

[35]The study in [Hartmann et al., 2009a] showed that for moderately sized models (up to 100000 degrees of freedom) and a model of metal plasticity, more than 60% of the computation time is spend on the local level. When the problem size is decreased, the ratio becomes even more pronounced and the solution time of the global system becomes insignificant.

gram sequence. For instance, already during the initialization of variables the same set of directives should be used. This ensures that memory is allocated according to and in physical proximity of the processors, which access the variables, later on. A measure for the quality of the implementation is the speed-up gained by using several processors (or threads). It is defined as

$$S_{\mathrm{p}} := \frac{\text{computing time with 1 processor}}{\text{computing time with } n \text{ processors}} = \frac{T_1}{T_n}, \tag{5.154}$$

see for example [Wriggers, 2009, p. 199]. Ideal is a linear speed-up, i.e. $S_{\mathrm{p}} = n$. This theoretical value is usually not reached since there is an overhead due to communication and synchronization (idle times of processors). The speed-up of the current implementation is shown in Fig. 5.16a. Shown is the speed-up of the local work (includ-

(a) Speed-up   (b) Normalized computation times
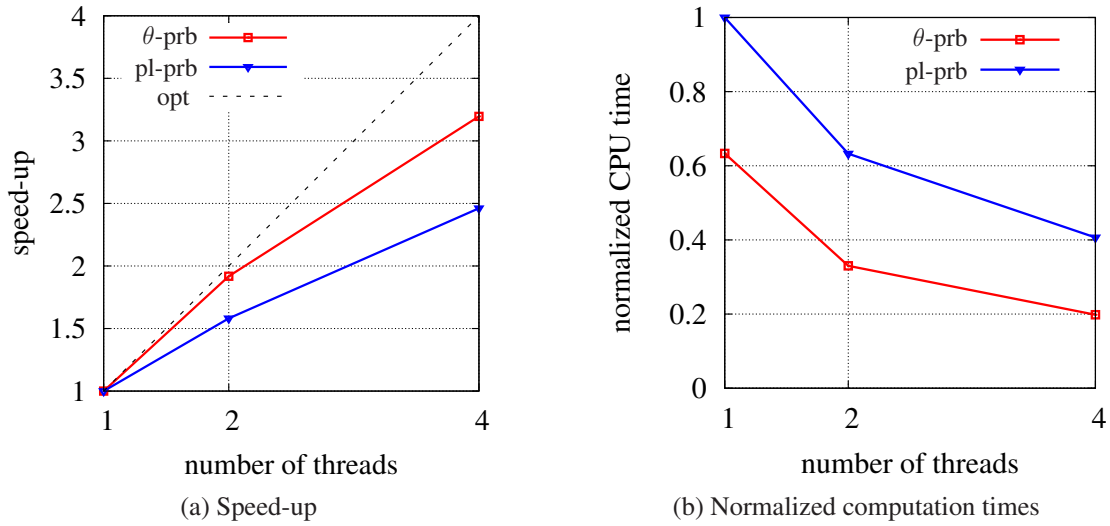
Figure 5.16.: Speed-up and computation times of element routines (θ-prb: mostly thermal problem, pl-prb: many plastic deformations)

ing element computation and assembly of elemental contributions) for a single MLNA iteration. The two curves represent two exemplary situations of a fully coupled thermomechanical problem involving large strains, see Sec. 6.3. The blue curve (pl-prb) corresponds to the case where the complete workpiece deforms plastically, while the red curve (θ-prb) corresponds to the mostly temperature driven case, see also Fig. 6.24 on p. 177. Even though, not all possibilities for parallelization are exploited and a comparatively simple parallelization is done here, the algorithm performs quite well for a small number of threads. In Fig. 5.16b the absolute gain of computational time is presented for the two cases. Here the computation time is normalized with respect to the maximum CPU time.

As mentioned above, the function values $\boldsymbol{G}$ and the global iteration matrix are computed within finite element routines. This process is described next.

5.6.3. Computation of Functions and Functional Matrices

At each iteration of the multilevel-Newton algorithm the linear system

$$\left[\frac{\partial \boldsymbol{G}}{\partial \boldsymbol{V}} + \frac{\partial \boldsymbol{G}}{\partial \hat{\boldsymbol{Q}}} \frac{\mathrm{d}\hat{\boldsymbol{Q}}}{\mathrm{d}\boldsymbol{V}}\right]_{\boldsymbol{y}^{(m)}} \Delta \boldsymbol{V}^{(m)} = -\boldsymbol{G}\left(\boldsymbol{V}^{(m)}, \hat{\boldsymbol{Q}}\left(\boldsymbol{V}^{(m)}\right)\right)$$

has to be set up and solved, where $\boldsymbol{G}^{\mathrm{T}} := \{\boldsymbol{G}_u^{\mathrm{T}}, \boldsymbol{G}_\theta^{\mathrm{T}}\}$ consists of the fully discretized balance of momentum and the discretized heat conduction equation, see also (5.152). The right-hand side and the functional matrix are assembled from element contributions. Analytical expressions for these contributions are most easily obtained by starting from the weak forms. Here, the spatial and temporal discretizations have to be taken into account. The spatial discretization is done using isoparametric finite elements, as described in Sec. 5.4. These have the following element interpolation functions

$$\theta(\boldsymbol{\xi}, t) = \sum_{a=1}^{n_{\mathrm{en}}} N_a(\boldsymbol{\xi})\Theta_a^e(t), \quad \boldsymbol{X}(\boldsymbol{\xi}) = \sum_{a=1}^{n_{\mathrm{en}}} N_a(\boldsymbol{\xi})\boldsymbol{X}_a^e, \quad \boldsymbol{x}(\boldsymbol{\xi}, t) = \sum_{a=1}^{n_{\mathrm{en}}} N_a(\boldsymbol{\xi})\boldsymbol{x}_a^e(t).$$

For the temporal discretization DIRK methods are applied. A single stage consists of determining the stage value

$$\boldsymbol{Y}_i = \boldsymbol{Y}_i^{\mathrm{S}} + h_n \, a_{ii} \dot{\boldsymbol{Y}}_i, \quad \text{with} \quad \boldsymbol{Y}_i^{\mathrm{S}} = \boldsymbol{y}_n + h_n \sum_{j=1}^{i-1} a_{ij} \dot{\boldsymbol{Y}}_j.$$

Thus, the stage derivative can be written as

$$\dot{\boldsymbol{Y}}_i = \frac{\boldsymbol{Y}_i - \boldsymbol{Y}_i^{\mathrm{S}}}{h_n \, a_{ii}}.$$

The complete method of time integration and further details are given in Sec. 5.5. In the following, the index of the ith stage of the DIRK-time integration and the mth MLNA-iteration are omitted for brevity. All values are to be understood as stage values within a MLNA iteration, if not stated otherwise.

Required derivatives of constitutive functions are computed numerically using finite differences according to [Press et al., 1992, p. 180, 381].

Balance of Momentum - Computation of Right-Hand Side

For purely mechanical problems with finite deformations the derivation is already given in the standard literature on nonlinear finite element methods, see e.g. [Bonet and Wood, 1997, p. 170ff.], [Wriggers, 2009, p. 123ff.], and [Zienkiewicz et al., 2005, p. 137ff.]. Following the standard procedure, the temporal discretization and the interpolation functions are inserted into the weak form of the balance of momentum (5.33)

$$\pi_{\mathrm{u}}\big(\boldsymbol{u}, \theta, \mathbf{q}, \delta\boldsymbol{u}\big) = \underbrace{\int_\Omega \tilde{\mathbf{T}} \cdot \delta\mathbf{E} \, \mathrm{d}V}_{R_{\mathrm{i}}} - \underbrace{\left(\int_{\partial_{\mathrm{s}}\Omega} \boldsymbol{s} \cdot \delta\boldsymbol{u} \, \mathrm{d}A + \int_\Omega \varrho_{\mathrm{R}}\boldsymbol{k} \cdot \delta\boldsymbol{u} \, \mathrm{d}V\right)}_{R_{\mathrm{e}}} = 0,$$

133

with the virtual work of internal R_i and external R_e forces. This leads to the global system

$$\delta \boldsymbol{U}^{\mathrm{T}} \boldsymbol{G}_u = \delta \boldsymbol{U}^{\mathrm{T}} (\boldsymbol{R}_i - \boldsymbol{R}_e) = 0, \qquad \boldsymbol{G}_u = \boldsymbol{G}_u(\boldsymbol{U}, \boldsymbol{\Theta}, \boldsymbol{Q}), \tag{5.155}$$

which is derived in the following. $\boldsymbol{R}_i$ and $\boldsymbol{R}_e$ are equivalent internal and external forces, which determine the function value of $\boldsymbol{G}_u$. The vectors $\boldsymbol{U}$ and $\boldsymbol{\Theta}$ consist of all nodal unknowns and $\boldsymbol{Q}$ is the assembly of the internal variables of all integration points of the complete structure. All quantities have to be evaluated at the ith stage of the nth time step and the mth MLNA iteration. Of course, the values of $\boldsymbol{R}_i$ and $\boldsymbol{R}_e$ also depend on the prescribed nodal values. However, these remain constant within each MLNA iteration. Thus, their dependence is not explicitly stated.

Within a single element e comprising n_{en} nodes, the displacement is approximated by using the shape functions N_a and nodal displacements $\mathbf{u}_a^e$,

$$\boldsymbol{u}(\boldsymbol{\xi}, t) = \boldsymbol{x}(\boldsymbol{\xi}, t) - \boldsymbol{X}(\boldsymbol{\xi}) = \sum_{a=1}^{n_{\mathrm{en}}} N_a(\boldsymbol{\xi}) \big(\boldsymbol{x}_a^e(t) - \boldsymbol{X}_a^e \big) = \sum_{a=1}^{n_{\mathrm{en}}} N_a(\boldsymbol{\xi}) \mathbf{u}_a^e(t).$$

A distinction in prescribed and unknown values is not done on this level. The nodal

$$\mathbf{u}^e(t) = \left\{ \begin{array}{c} \mathbf{u}_1^e \\ \mathbf{u}_2^e \\ \vdots \\ \mathbf{u}_{n_{\mathrm{el}}}^e \end{array} \right\}, \qquad \delta \mathbf{u}^e = \left\{ \begin{array}{c} \delta \mathbf{u}_1^e \\ \delta \mathbf{u}_2^e \\ \vdots \\ \delta \mathbf{u}_{n_{\mathrm{el}}}^e \end{array} \right\}.$$

$$\mathbf{u}_a^e = \left\{ \delta u_{a\,x}^e \;\; \delta u_{a\,y}^e \;\; \delta u_{a\,z}^e \right\}^{\mathrm{T}}$$
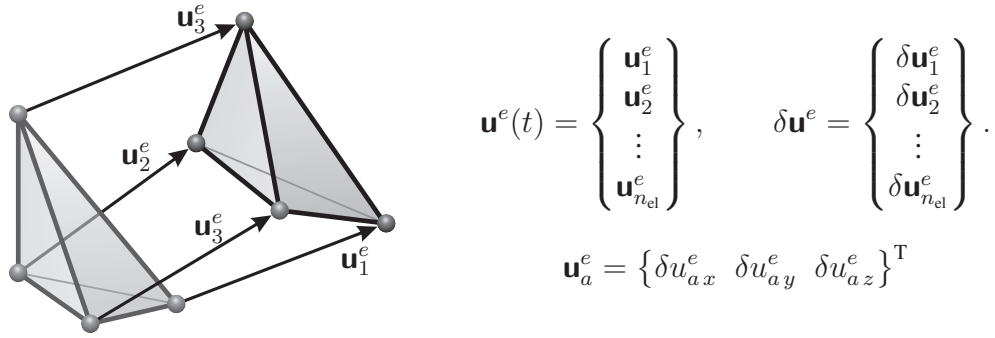
Figure 5.17.: Nodal displacements $\mathbf{u}_a^e$ and displacement vector $\mathbf{u}^e$ of volume element e

displacements are commonly arranged within an element displacement vector $\mathbf{u}^e$ of dimension $(3 n_{\mathrm{en}} \times 1)$, see also Fig. 5.17. Inserting the displacement approximation into the expression for the virtual Green strain tensor (5.31), one obtains the symmetric tensor expression

$$\delta \mathbf{E} = \frac{1}{2} \sum_{a=1}^{n_{\mathrm{en}}} \left(\mathrm{Grad}\, N_a \otimes \delta \mathbf{u}_a^e \right) \mathbf{F} + \mathbf{F}^{\mathrm{T}} \left(\delta \mathbf{u}_a^e \otimes \mathrm{Grad}\, N_a \right). \tag{5.156}$$

It is linear in the virtual displacements $\delta \mathbf{u}_a^e$ and its component form reads

$$\delta E_{\alpha\beta} = \frac{1}{2} \sum_{a=1}^{n_{\mathrm{en}}} \sum_{b=1}^{3} \left[F_{\alpha b} N_{a,\beta} + N_{a,\alpha} F_{b\beta} \right] \delta u_{a\,b}^e, \tag{5.157}$$

where $N_{a,\alpha}$ denotes the components of the gradient $\mathrm{Grad}\,N_a$, i.e. the partial derivative $\partial N_a / \partial X_\alpha$. Gradients with respect to different coordinates can be easily obtained within finite elements. The computation in the context of isoparametric interpolation functions is given in App. A.4.

The symmetry of the virtual Green strain tensor $\delta\mathbf{E}$ and the second Piola-Kirchhoff stress tensor $\tilde{\mathbf{T}}$ can be exploited. To this end, the tensors are mapped to column matrices (vectors), sometimes referred to as Voigt notation, see e.g. [Belytschko et al., 2004, p. 615], and [Wriggers, 2009, p.124]. The stress tensor reads in matrix notation

$$\tilde{\mathbf{T}} = \left\{ \tilde{T}_{11} \quad \tilde{T}_{22} \quad \tilde{T}_{33} \quad \tilde{T}_{12} \quad \tilde{T}_{23} \quad \tilde{T}_{31} \right\}^{\mathrm{T}}.$$

According to the expression (5.156), the virtual strain tensor is linear in $\delta\mathbf{u}_a^e$ and can thus be expressed as

$$\delta\mathbf{E} = \left\{ \begin{array}{c} \delta E_{11} \\ \delta E_{22} \\ \delta E_{33} \\ 2\delta E_{12} \\ 2\delta E_{23} \\ 2\delta E_{31} \end{array} \right\} = \sum_{a=1}^{n_{\mathrm{en}}} \tilde{\mathbf{B}}_a \delta\mathbf{u}_a^e. \tag{5.158}$$

It is defined similar to the common practice in small strain problems, where shearing components are doubled. This definition leads to the identity of the scalar products $\tilde{\mathbf{T}} \cdot \delta\mathbf{E} = \delta\mathbf{E}^{\mathrm{T}}\tilde{\mathbf{T}}$ and thus, permits an efficient evaluation. The matrix $\tilde{\mathbf{B}}_a$ is called strain-displacement matrix. It depends on the current value of the deformation gradient $\mathbf{F}$ and can be obtained from the component form (5.157),

$$\tilde{\mathbf{B}}_a = \begin{bmatrix} F_{11}N_{a,1} & F_{21}N_{a,1} & F_{31}N_{a,1} \\ F_{12}N_{a,2} & F_{22}N_{a,2} & F_{32}N_{a,2} \\ F_{13}N_{a,3} & F_{23}N_{a,3} & F_{33}N_{a,3} \\ F_{11}N_{a,2} + F_{12}N_{a,1} & F_{21}N_{a,2} + F_{22}N_{a,1} & F_{31}N_{a,2} + F_{32}N_{a,1} \\ F_{12}N_{a,3} + F_{13}N_{a,2} & F_{22}N_{a,3} + F_{23}N_{a,2} & F_{32}N_{a,3} + F_{33}N_{a,2} \\ F_{13}N_{a,1} + F_{11}N_{a,3} & F_{23}N_{a,1} + F_{21}N_{a,3} & F_{33}N_{a,1} + F_{31}N_{a,3} \end{bmatrix}. \tag{5.159}$$

With these preliminary results, the element contributions of the virtual work of internal forces are given by

$$R_{\mathrm{i}}^e = \int_{\Omega_e} \tilde{\mathbf{T}} \cdot \delta\mathbf{E} \,\mathrm{d}V = \sum_{a=1}^{n_{\mathrm{en}}} (\delta\mathbf{u}_a^e)^{\mathrm{T}} \int_{\Omega_e} \tilde{\mathbf{B}}_a^{\mathrm{T}} \tilde{\mathbf{T}} \,\mathrm{d}V =$$

$$\sum_{a=1}^{n_{\mathrm{en}}} (\delta\mathbf{u}_a^e)^{\mathrm{T}} \int_{\Omega_\square} \tilde{\mathbf{B}}_a^{\mathrm{T}} \tilde{\mathbf{T}} \det \mathbf{J}^e(\boldsymbol{\xi}) \,\mathrm{d}\Omega_\square = \sum_{a=1}^{n_{\mathrm{en}}} (\delta\mathbf{u}_a^e)^{\mathrm{T}} \boldsymbol{r}_{\mathrm{i}\,a}^e = (\delta\mathbf{u}^e)^{\mathrm{T}} \boldsymbol{r}_{\mathrm{i}}^e \tag{5.160}$$

The spatial integration is performed in the parametric space $\boldsymbol{\xi}$ using numerical quadrature, as explained in Sec. 5.4.4. See also the relation (5.78) and Fig. 5.6 for the transformation from the reference configuration to the parametric space. The nodal internal

force vectors $\boldsymbol{r}_{\mathrm{i}\,a}^{e}$ are collocated to the element internal force vector $\boldsymbol{r}_{\mathrm{i}}^{e}$, which is in turn assembled in the global internal force vector (A represents an assembly operator)

$$\boldsymbol{r}_{\mathrm{i}}^{e} = \left\{ \begin{array}{c} \boldsymbol{r}_{\mathrm{i}\,1}^{e} \\ \boldsymbol{r}_{\mathrm{i}\,2}^{e} \\ \vdots \\ \boldsymbol{r}_{\mathrm{i}\,n_{\mathrm{en}}}^{e} \end{array} \right\}, \qquad \boldsymbol{R}_{\mathrm{i}} = \mathop{\mathrm{A}}_{e=1}^{n_{\mathrm{el}}} \boldsymbol{r}_{\mathrm{i}}^{e}. \tag{5.161}$$

This is done in a similar manner as for the nodal displacements $\mathbf{u}_a^e$, see also Fig. 5.17. The assembly process is the same as in standard linear finite element procedures and not repeated here. Details can be found e.g. in the introductory works [Hughes, 2000, p. 42, 92ff.], [Reddy, 2004, p. 33], or [Zienkiewicz and Taylor, 2000, p. 8, 585ff.]. All other element vectors (also coming from the heat conduction equation) are assembled in an analogous manner. This is not explicitly noted in the following.

The virtual work of the external forces is treated in the same way. The contribution of the eth element is given by

$$R_{\mathrm{e}}^{e} = \int\limits_{\partial_{\mathrm{s}}\Omega_e} \boldsymbol{s} \cdot \delta\boldsymbol{u} \, \mathrm{d}A + \int\limits_{\Omega_e} \varrho_{\mathrm{R}} \boldsymbol{k} \cdot \delta\boldsymbol{u} \, \mathrm{d}V = \sum_{a=1}^{n_{\mathrm{en}}} (\delta\mathbf{u}_a^e)^{\mathrm{T}} \left(\int\limits_{\partial_{\mathrm{s}}\Omega_e} N_a \boldsymbol{s} \, \mathrm{d}A + \int\limits_{\Omega_e} \varrho_{\mathrm{R}} \boldsymbol{k} N_a \, \mathrm{d}V \right).$$

This results in the external nodal force vector

$$\boldsymbol{r}_{\mathrm{e}\,a}^{e} = \int\limits_{\partial_{\mathrm{s}}\Omega_e} N_a \boldsymbol{s} \, \mathrm{d}A + \int\limits_{\Omega_e} \varrho_{\mathrm{R}} \boldsymbol{k} N_a \, \mathrm{d}V, \tag{5.162}$$

which leads to the element external force vector $\boldsymbol{r}_{\mathrm{e}}^{e}$. These are again assembled to the global external force vector $\boldsymbol{R}_{\mathrm{e}}$. Now, the function value $\boldsymbol{G}_u$ (i.e. the right-hand side of the linear system) is determined. Next, the functional matrix $\partial\boldsymbol{G}_u/\partial\boldsymbol{V}$ has to be computed, see for example equation (5.151).

Balance of Momentum - Computation of Functional Matrix

The functional matrix can be obtained by forming the directional derivative of the weak form of the balance of momentum (5.155). The derivative in the direction $\Delta\boldsymbol{U}$ results in

$$\delta\boldsymbol{U}^{\mathrm{T}}\,\mathrm{D}\boldsymbol{G}_u[\Delta\boldsymbol{U}] = \delta\boldsymbol{U}^{\mathrm{T}} \left[\frac{\partial\boldsymbol{G}_u}{\partial\boldsymbol{U}} \right] \Delta\boldsymbol{U} = \delta\boldsymbol{U}^{\mathrm{T}}\boldsymbol{K}_{\mathrm{uu}}\Delta\boldsymbol{U}, \tag{5.163}$$

and the derivative in the direction $\Delta\boldsymbol{\Theta}$ is given by

$$\delta\boldsymbol{U}^{\mathrm{T}}\,\mathrm{D}\boldsymbol{G}_u[\Delta\boldsymbol{\Theta}] = \delta\boldsymbol{U}^{\mathrm{T}} \left[\frac{\partial\boldsymbol{G}_u}{\partial\boldsymbol{\Theta}} \right] \Delta\boldsymbol{\Theta} = \delta\boldsymbol{U}^{\mathrm{T}}\boldsymbol{K}_{\mathrm{u\theta}}\Delta\boldsymbol{\Theta}. \tag{5.164}$$

Assuming conservative external forces (i.e. displacement independent forces, no follower forces), R_e does not contribute to the tangent matrix. When looking at the derivative of R_i the displacement dependence of $\tilde{\mathbf{T}} = \mathbf{h}(\mathbf{C}, \theta, \mathbf{C}_\mathrm{i})$ as well as $\delta\mathbf{E}$ have to be considered. Using the equality $\tilde{\mathbf{T}} \cdot \delta\mathbf{E} = \mathbf{F}\tilde{\mathbf{T}} \cdot \mathrm{Grad}\,\delta\boldsymbol{u}$, one obtains

$$\mathrm{D}R_\mathrm{i}^e[\Delta\boldsymbol{u}] = \int_{\Omega_e} \big[\, \mathrm{Grad}\,\Delta\boldsymbol{u}\,\tilde{\mathbf{T}} + \mathbf{F}\,\mathrm{D}\mathbf{h}[\Delta\boldsymbol{u}] \,\big] \cdot \mathrm{Grad}\,\delta\boldsymbol{u}\,\mathrm{d}V. \qquad (5.165)$$

According to the stress relation (4.63), the second Piola-Kirchhoff stress tensor depends on the displacement (given by $\mathbf{C}$), the temperature θ, and internal variables $\mathbf{q}$. Its directional derivative with respect to the right Cauchy-Green tensor reads

$$\mathrm{D}\mathbf{h}[\Delta\mathbf{C}] = \left[\frac{\partial\mathbf{h}}{\partial\mathbf{C}} + \frac{\partial\mathbf{h}}{\partial\mathbf{q}}\frac{\partial\mathbf{q}}{\partial\mathbf{C}}\right]\Delta\mathbf{C} = \tfrac{1}{2}\overset{4}{\mathbf{C}}_\mathrm{u}\Delta\mathbf{C}, \qquad \Delta\mathbf{C} = \mathrm{D}\mathbf{C}[\Delta\boldsymbol{u}]. \qquad (5.166)$$

$\overset{4}{\mathbf{C}}_\mathrm{u}$ is a generalized (algorithmic) stiffness tensor of fourth order, that accounts for the assumed displacement dependence of the internal variables, refer also to the general equation of the MLNA (5.151). $\Delta\mathbf{C} = 2\Delta\mathbf{E}$ is the change of the right Cauchy-Green tensor due to a given displacement change. As elaborated in Sec. 5.6.2, it is assumed that the internal variables can be expressed as a function of the displacement and the temperature, due to the implicit function theorem. With this result two parts of the directional derivative (5.165) can be identified

$$\mathrm{D}R_\mathrm{i}^e[\Delta\boldsymbol{u}] = \int_{\Omega_e} \bigg(\underbrace{\mathrm{Grad}\,\Delta\boldsymbol{u}\,\tilde{\mathbf{T}} \cdot \mathrm{Grad}\,\delta\boldsymbol{u}}_{\text{geometric part}} + \underbrace{\delta\mathbf{E} \cdot \overset{4}{\mathbf{C}}_\mathrm{u}\Delta\mathbf{E}}_{\text{constitutive part}} \bigg)\,\mathrm{d}V. \qquad (5.167)$$

The first term, the geometric part, is often named initial stress term, since the stresses at a given state appear directly. It arises from the nonlinear form of the strain-displacement relation. The component form is constructed using indicial notation

$$\int_{\Omega_e} \big(\mathrm{Grad}\,\Delta\boldsymbol{u}\,\tilde{\mathbf{T}} \cdot \mathrm{Grad}\,\delta\boldsymbol{u}\big)\,\mathrm{d}V \qquad (5.168)$$

$$= \sum_{a=1}^{n_\mathrm{en}}\sum_{b=1}^{n_\mathrm{en}} \int_{\Omega_e} \big((\Delta\mathbf{u}_b^e \otimes \mathrm{Grad}\,N_b)\,\tilde{\mathbf{T}} \cdot (\delta\mathbf{u}_a^e \otimes \mathrm{Grad}\,N_a)\big)\,\mathrm{d}V \qquad (5.169)$$

$$= \sum_{a=1}^{n_\mathrm{en}}\sum_{b=1}^{n_\mathrm{en}} (\delta\mathbf{u}_a^e)^\mathrm{T} \int_{\Omega_e} (G_{ab}\mathbf{1})\,\mathrm{d}V\,\Delta\mathbf{u}_b^e, \quad G_{ab} = (\mathrm{Grad}\,N_a)^\mathrm{T}\,\tilde{\mathbf{T}}\,(\mathrm{Grad}\,N_b). \qquad (5.170)$$

This leads to the definition of the geometric stiffness submatrix of dimension (3×3)

$$\mathbf{k}_{\mathrm{uu,G}}^{e,ab} = \int_{\Omega_\square} (G_{ab}\mathbf{1})\,\det\mathbf{J}^e\,\mathrm{d}\Omega_\square, \qquad (5.171)$$

which links nodes a and b. It gives the geometric contribution to the change of the ath component of the internal element force vector due to a displacement change of the bth element node.

The second term of the directional derivative (5.167), the constitutive part, contains the algorithmic stiffness tensor $\overset{4}{\mathbf{C}}_{\mathrm{u}}$, also known as consistent tangent, and the increment of the Green strain tensor $\Delta\mathbf{E}$. Similar to the relation for the virtual Green strain tensor (5.158), one can express the symmetric increment of the strain tensor in matrix notation with the strain-displacement matrix (5.159)

$$\Delta\mathbf{E} = \sum_{b=1}^{n_{\mathrm{en}}} \tilde{\mathbf{B}}_b \Delta\mathbf{u}_b^e, \qquad \Delta\mathbf{C} = 2\sum_{b=1}^{n_{\mathrm{en}}} \tilde{\mathbf{B}}_b \Delta\mathbf{u}_b^e.$$

Also the (algorithmic) stiffness tensor has to be adopted to the matrix form. To this end, $\overset{4}{\mathbf{C}}_{\mathrm{u}}$ is transformed to a (6×6) matrix $\mathbf{C}_{\mathrm{u}}$. With these relations, the constitutive component of the linearized virtual work equation for element e is given by

$$\int_{\Omega_e} \left(\delta\mathbf{E} \cdot \overset{4}{\mathbf{C}}_{\mathrm{u}} \Delta\mathbf{E}\right) \mathrm{d}V = \sum_{a=1}^{n_{\mathrm{en}}}\sum_{b=1}^{n_{\mathrm{en}}} (\delta\mathbf{u}_a^e)^{\mathrm{T}} \int_{\Omega_e} \tilde{\mathbf{B}}_a^{\mathrm{T}} \mathbf{C}_{\mathrm{u}} \tilde{\mathbf{B}}_b \, \mathrm{d}V \Delta\mathbf{u}_b^e = \sum_{a=1}^{n_{\mathrm{en}}}\sum_{b=1}^{n_{\mathrm{en}}} (\delta\mathbf{u}_a^e)^{\mathrm{T}} \mathbf{k}_{\mathrm{uu,C}}^{e,ab} \Delta\mathbf{u}_b^e.$$

It yields the definition of the constitutive stiffness submatrix

$$\mathbf{k}_{\mathrm{uu,C}}^{e,ab} = \int_{\Omega_\square} \tilde{\mathbf{B}}_a^{\mathrm{T}} \mathbf{C}_{\mathrm{u}} \tilde{\mathbf{B}}_b \det \mathbf{J}^e \, \mathrm{d}\Omega_\square. \tag{5.172}$$

The sum of the geometric and constitutive stiffness matrices results in the nodal submatrix of dimension (3×3)

$$\mathbf{k}_{\mathrm{uu}}^{e,ab} = \mathbf{k}_{\mathrm{uu,G}}^{e,ab} + \mathbf{k}_{\mathrm{uu,C}}^{e,ab}. \tag{5.173}$$

It is often called tangent matrix and links element nodes a and b. Within one element the submatrices are arranged to form the element stiffness matrix

$$\mathbf{k}_{\mathrm{uu}}^e = \begin{bmatrix} \mathbf{k}_{\mathrm{uu}}^{e,11} & \mathbf{k}_{\mathrm{uu}}^{e,12} & \cdots & \mathbf{k}_{\mathrm{uu}}^{e,1n_{\mathrm{en}}} \\ \mathbf{k}_{\mathrm{uu}}^{e,21} & \mathbf{k}_{\mathrm{uu}}^{e,22} & \cdots & \mathbf{k}_{\mathrm{uu}}^{e,2n_{\mathrm{en}}} \\ \vdots & \vdots & \ddots & \vdots \\ \mathbf{k}_{\mathrm{uu}}^{e,1n_{\mathrm{en}}} & \mathbf{k}_{\mathrm{uu}}^{e,2n_{\mathrm{en}}} & \cdots & \mathbf{k}_{\mathrm{uu}}^{e,n_{\mathrm{en}}n_{\mathrm{en}}} \end{bmatrix}. \tag{5.174}$$

It has the dimension $(3n_{\mathrm{en}} \times 3n_{\mathrm{en}})$. The linear change of $\boldsymbol{r}_{\mathrm{i}}^e$ due to $\Delta\boldsymbol{u}^e$ is given by this matrix. On the global level, the element contributions are assembled to the global stiffness matrix

$$\boldsymbol{K}_{\mathrm{uu}} = \overset{n_{\mathrm{el}}}{\underset{e=1}{\mathbf{A}}} \mathbf{k}_{\mathrm{uu}}^e. \tag{5.175}$$

Here, also boundary conditions and concerning the computer implementation, the storage scheme have to be considered. Popular storage schemes for sparse matrices are the

compressed sparse row (CSR) and the *compressed sparse column* (CSC) format. See also the literature references given in Sec. 5.7 and after the assembly of nodal force vectors (5.161).

In the case of fully coupled thermomechanical problems, the weak form of the balance of momentum (5.33) also depends on the temperature θ. Thus, a linearization of the fully discretized equation (5.128) with respect to $\boldsymbol{\Theta}$ has to be computed. The external forces (i.e. stress vector $\boldsymbol{s}$ and body force density $\boldsymbol{k}$) are assumed to be independent of the temperature θ. Hence, the directional derivative of R_e vanishes. The directional derivative of the internal virtual work yields

$$\mathrm{D}R_\mathrm{i}^e[\Delta\theta] = \int_{\Omega_e} \mathrm{D}\tilde{\mathbf{T}}[\Delta\theta] \cdot \delta\mathbf{E} \,\mathrm{d}V. \tag{5.176}$$

Similar to the linearization of the stress tensor $\tilde{\mathbf{T}} = \mathbf{h}(\mathbf{C}, \theta, \mathbf{C}_\mathrm{i})$ with respect to a displacement change (5.166), a change of temperature leads to

$$\mathrm{D}\mathbf{h}[\Delta\theta] = \left[\frac{\partial\mathbf{h}}{\partial\theta} + \frac{\partial\mathbf{h}}{\partial\mathbf{q}}\frac{\partial\mathbf{q}}{\partial\theta}\right] \Delta\theta = \mathbf{C}_\mathrm{T}\Delta\theta.$$

The consistent linearization according to equation (5.150) implies that the internal variables depend on the displacement and the temperature. Instead of the material stiffness tensor $\overset{4}{\mathbf{C}}_\mathrm{u}$, a second order stiffness tensor $\mathbf{C}_\mathrm{T}$ arises. It resembles the change of the second Piola-Kirchhoff stress tensor due to a change of temperature $\Delta\theta$. Taking into account the matrix formulation, $\mathbf{C}_\mathrm{T}$ is transformed to the vector $\mathbf{C}_\mathrm{T}$. Inserting this relation in (5.176) leads to

$$\mathrm{D}R_\mathrm{i}^e[\Delta\theta] = \int_{\Omega_e} \delta\mathbf{E}^T\mathbf{C}_\mathrm{T}\Delta\theta \,\mathrm{d}V = \sum_{a=1}^{n_\mathrm{en}}\sum_{b=1}^{n_\mathrm{en}} (\delta\mathbf{u}_a^e)^\mathrm{T} \int_{\Omega_e} \left(\tilde{\mathbf{B}}_a^\mathrm{T}\mathbf{C}_\mathrm{T}N_b\right) \mathrm{d}V \Delta\Theta_b^e.$$

From this formulation the element stiffness submatrix of dimension (3×1) is identified as

$$\mathbf{k}_{\mathrm{u}\theta}^{e,ab} = \int_{\Omega_\square} \tilde{\mathbf{B}}_a^\mathrm{T}\mathbf{C}_\mathrm{T}N_b \det\mathbf{J}^e \,\mathrm{d}\Omega_\square. \tag{5.177}$$

So far, all required quantities related to the balance of momentum are determined. Still missing are the terms for the heat conduction equation. These are derived in the next subsection.

Heat Conduction Equation - Computation of Right-Hand Side

In many applications the heat conductivity $\boldsymbol{\lambda}$ is assumed to be constant with respect to the current configuration. Additionally, the heat transfer depends on the size of the

body's surface, which is influenced by the deformation. If these effects are to be included, it is advantageous to start from the weak form (5.37) formulated with respect to the current configuration. After all, the integrals are evaluated neither in the reference nor the current configuration, but the parametric space $\boldsymbol{\xi}$. In an analogous way to the balance of momentum, inserting the spatial and temporal discretization into the weak form of the heat conduction equation

$$
\pi_\theta(\boldsymbol{u}, \theta, \mathbf{q}, \delta\theta) = \\
\underbrace{\int_\omega \varrho c_\mathrm{d} \dot\theta \delta\theta \, \mathrm{d}v}_{H_\mathrm{c}} - \underbrace{\int_\omega \varrho \, (r - w) \, \delta\theta \, \mathrm{d}v}_{H_\mathrm{i}} - \underbrace{\int_\omega \boldsymbol{q} \cdot \mathrm{grad}\, \delta\theta \, \mathrm{d}v}_{H_\mathrm{q}} + \underbrace{\int_{\partial_\mathrm{q}\omega} f_\mathrm{q} \delta\theta \, \mathrm{d}a + \int_{\partial_{\theta\mathrm{q}}\omega} c\delta\theta \, \mathrm{d}a}_{H_\mathrm{e}} = 0.
$$

leads to the global system

$$
\delta\boldsymbol{\Theta}^\mathrm{T} \boldsymbol{G}_\theta = \delta\boldsymbol{\Theta}^\mathrm{T} \left(\boldsymbol{H}_\mathrm{c} - \boldsymbol{H}_\mathrm{i} - \boldsymbol{H}_\mathrm{q} + \boldsymbol{H}_\mathrm{e} \right) = 0, \qquad \boldsymbol{G}_\theta = \boldsymbol{G}_\theta(\boldsymbol{U}_i, \boldsymbol{\Theta}_i, \boldsymbol{Q}_i). \tag{5.178}
$$

Here, $\boldsymbol{H}_\mathrm{c}$, $\boldsymbol{H}_\mathrm{i}$, $\boldsymbol{H}_\mathrm{q}$, and $\boldsymbol{H}_\mathrm{e}$ are equivalent heat vectors related to heat storage, internal heat production, heat conduction, and external heat supply. Their values are again computed within one element and assembled on the global level. The derivation follows the same steps as for the nodal force vectors. Within an element these nodal values are arranged to the element vectors $\mathbf{h}_\mathrm{c}^e$, $\mathbf{h}_\mathrm{i}^e$, $\mathbf{h}_\mathrm{q}^e$, and $\mathbf{h}_\mathrm{e}^e$ of dimension $(n_\mathrm{en} \times 1)$. The ath components of the element heat vectors read

$$
h_{\mathrm{c}\,a}^e = \int_{\Omega_\square} \varrho_\mathrm{R} c_\mathrm{d} N_a \dot\theta \, J^e \, \mathrm{d}\Omega_\square, \tag{5.179}
$$

$$
h_{\mathrm{i}\,a}^e = \int_{\Omega_\square} \varrho_\mathrm{R} \, (r - w) \, N_a \, J^e \, \mathrm{d}\Omega_\square, \tag{5.180}
$$

$$
h_{\mathrm{q}\,a}^e = \int_{\Omega_\square} (\mathrm{grad}\, N_a)^\mathrm{T} \, \boldsymbol{q} \, j^e \, \mathrm{d}\Omega_\square, \tag{5.181}
$$

$$
h_{\mathrm{e}\,a}^e = \int_{\omega_e} f_\mathrm{q} N_a \, \mathrm{d}a + \int_{\partial_{\theta\mathrm{q}}\omega} c N_a \, \mathrm{d}a. \tag{5.182}
$$

As before, all quantities in these expressions have to be evaluated at the ith stage of the nth time step. This holds also for the stage derivatives, which are given by the relations (5.131). The temperature velocity $\dot\theta$ is computed using the starting value $\boldsymbol{\Theta}_i^\mathrm{S}$ and the stage value $\boldsymbol{\Theta}_i$ of the nodal temperature vector. It is given by the definition of the stage derivative $\dot{\boldsymbol{\Theta}}_i = \left(\boldsymbol{\Theta}_i - \boldsymbol{\Theta}_i^\mathrm{S} \right) / (ha_{ii})$. To guarantee the property of incremental objectivity (see [Simo and Hughes, 2000, p.278ff.]) the rate of the right Cauchy-Green tensor is defined as $\dot{\mathbf{C}}_i := \left[\mathbf{C}_i - \mathbf{C}_i^\mathrm{S} \right] / (ha_{ii})$. In (5.181) the Jacobian determinant of

the transformation from parametric space into the current configuration $j^e = \det \mathbf{j}^e = \det \left[\partial \boldsymbol{x} / \partial \boldsymbol{\xi} \right]$ is used for the coordinate transformation.

For the computation of the external heat supply (5.182), a coordinate transformation of surface integrals is needed. Surface integrals are evaluated in the reference element using the isoparametric parametrization. The computation follows the outline in [Greenberg, 1998, p.739ff.]. The surface element of the current configuration is given by

$$\mathrm{d}a = \left\| \boldsymbol{x}_{,\xi} \, \mathrm{d}\xi \times \boldsymbol{x}_{,\eta} \, \mathrm{d}\eta \right\| = \left\| \boldsymbol{x}_{,\xi} \times \boldsymbol{x}_{,\eta} \right\| \mathrm{d}\xi \, \mathrm{d}\eta = \left\| \frac{\partial \boldsymbol{x}}{\partial \xi} \times \frac{\partial \boldsymbol{x}}{\partial \eta} \right\| \mathrm{d}\xi \, \mathrm{d}\eta. \qquad (5.183)$$

The transformation of the surface element in the current configuration into the parametric space is shown in Fig. 5.18. As depicted, the differentials of the position vector $\boldsymbol{x}$,
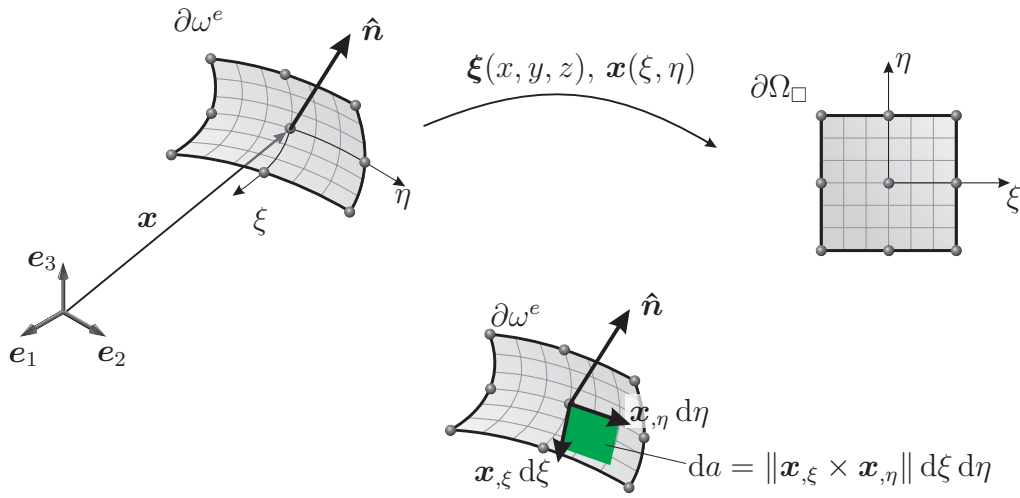

Figure 5.18.: Transformation of surface element e from the current configuration $\partial \omega^e$ into the normed parameter space $\partial \Omega_\square$ and illustration of $\mathrm{d}a$ and $\hat{\boldsymbol{n}}$

e.g. $\boldsymbol{x}_{,\xi} \, \mathrm{d}\eta$ and $\boldsymbol{x}_{,\eta} \, \mathrm{d}\eta$, form a parallelogram with area $\mathrm{d}a$. In the expression of the surface element, the cross product of the differentials is a non-unit normal vector $\hat{\boldsymbol{n}}$ on the surface of the element e. With $\hat{\boldsymbol{n}}$ the surface element can be expressed as

$$\mathrm{d}a = \left\| \hat{\boldsymbol{n}} \right\| \mathrm{d}\xi \, \mathrm{d}\eta, \qquad \hat{\boldsymbol{n}} = \begin{Bmatrix} x_{2,\xi} x_{3,\eta} - x_{2,\eta} x_{3,\xi} \\ x_{3,\xi} x_{1,\eta} - x_{3,\eta} x_{1,\xi} \\ x_{1,\xi} x_{2,\eta} - x_{1,\eta} x_{2,\xi} \end{Bmatrix}, \qquad (5.184)$$

where the differentials can be computed with the nodal position vector

$$\boldsymbol{x}_{,\xi} = \frac{\partial \boldsymbol{x}}{\partial \xi} = \sum_{a=1}^{n_{\mathrm{en}}} \frac{\partial N_a}{\partial \xi} \boldsymbol{x}_a^e(t), \qquad \text{and} \qquad \boldsymbol{x}_{,\eta} = \frac{\partial \boldsymbol{x}}{\partial \eta} = \sum_{a=1}^{n_{\mathrm{en}}} \frac{\partial N_a}{\partial \eta} \boldsymbol{x}_a^e(t).$$

The equivalent heat vectors, and thus the function value of $\boldsymbol{G}_\theta$ vary with displacement and temperature. The application of the MLNA therefore requires the linearization with respect to $\boldsymbol{U}$ and $\boldsymbol{\Theta}$.

Heat Conduction Equation - Computation of Functional Matrix

The linearization of the weak form of the heat conduction equation (5.178) leads to

$$\delta\boldsymbol{\Theta}^{\mathrm{T}}\,\mathrm{D}\boldsymbol{G}_\theta[\Delta\boldsymbol{U}] = \delta\boldsymbol{\Theta}^{\mathrm{T}}\left[\frac{\partial\boldsymbol{G}_\theta}{\partial\boldsymbol{U}}\right]\Delta\boldsymbol{U} = \delta\boldsymbol{\Theta}^{\mathrm{T}}\boldsymbol{K}_{\theta\mathrm{u}}\Delta\boldsymbol{U}, \tag{5.185}$$

and

$$\delta\boldsymbol{\Theta}^{\mathrm{T}}\,\mathrm{D}\boldsymbol{G}_\theta[\Delta\boldsymbol{\Theta}] = \delta\boldsymbol{\Theta}^{\mathrm{T}}\left[\frac{\partial\boldsymbol{G}_\theta}{\partial\boldsymbol{U}}\right]\Delta\boldsymbol{\Theta} = \delta\boldsymbol{\Theta}^{\mathrm{T}}\boldsymbol{K}_{\theta\theta}\Delta\boldsymbol{\Theta}. \tag{5.186}$$

Similar to the mechanical case, the components of the iteration matrices are computed on element level and determined by evaluating the directional derivative. For the heat storage term one obtains

$$\mathrm{D}H_{\mathrm{c}}^e[\Delta\theta] = \sum_{a=1}^{n_{\mathrm{en}}}\sum_{b=1}^{n_{\mathrm{en}}}\delta\Theta_a^e\int_{\omega_e}\varrho\left(\frac{\partial c_{\mathrm{d}}}{\partial\theta}\dot{\theta} + \frac{c_{\mathrm{d}}}{ha_{ii}}\right)N_aN_b\,\mathrm{d}v\Delta\Theta_b^e.$$

From this result one gets the components of a generalized heat capacity matrix

$$\mathrm{k}_{\theta\theta,\mathrm{c}}^{e,ab} = \int_{\Omega_\square}\varrho_{\mathrm{R}}\left(\frac{\partial c_{\mathrm{d}}}{\partial\theta}\dot{\theta} + \frac{c_{\mathrm{d}}}{ha_{ii}}\right)N_aN_b\det\mathbf{J}^e\,\mathrm{d}\Omega_\square. \tag{5.187}$$

Again the temperature velocity $\dot{\theta}$ (stage derivative) is computed from the stage value and the starting vector of nodal temperatures using relation (5.131).

In general the heat storage is also deformation dependent. However, in many cases only a temperature dependence of the heat capacity $c_{\mathrm{d}} = c_{\mathrm{d}}(\theta)$ is assumed. This is also the case for the material model derived in Sec. 4.1. Thus, the submatrix for nodes a and b becomes

$$\mathrm{D}H_{\mathrm{c}}^e[\Delta\boldsymbol{u}] = 0, \quad \mathbf{k}_{\theta\mathrm{u},\mathrm{c}}^{e,ab} = \mathbf{0}^{\mathrm{T}}.$$

It is a matrix (row vector) of dimension (1×3). The equivalent vector of internal heat production leads to

$$\mathrm{D}H_{\mathrm{i}}^e[\Delta\theta] = \sum_{a=1}^{n_{\mathrm{en}}}\sum_{b=1}^{n_{\mathrm{en}}}\delta\Theta_a^e\left(-\int_{\omega_e}\varrho\left(\frac{\mathrm{D}w}{\mathrm{D}\theta}\right)N_aN_b\,\mathrm{d}v\right)\Delta\Theta_b^e,$$

with the deformation dependent heat production $w = w\left(\mathbf{C}, \dot{\mathbf{C}}, \theta, \dot{\theta}, \mathbf{q}\right)$. Considering the DIRK-time integration (see relation (5.131) for the stage derivatives) and the implicit function theorem for $\mathbf{q}$, one obtains the algorithmic derivative

$$\frac{\mathrm{D}w}{\mathrm{D}\theta} = \frac{\partial w}{\partial\theta} + \frac{\partial w}{\partial\dot{\theta}}\frac{1}{ha_{ii}} + \left\{\frac{\partial w}{\partial\mathbf{q}}\right\}^{\mathrm{T}}\frac{\partial\mathbf{q}}{\partial\theta}. \tag{5.188}$$

The contribution to the components of the element iteration matrix is

$$k_{\theta\theta,i}^{e,ab} = - \int_{\Omega_\square} \varrho_R \left(\frac{\mathrm{D}w}{\mathrm{D}\theta} \right) N_a N_b \det \mathbf{J}^e \, \mathrm{d}\Omega_\square, \tag{5.189}$$

where $\mathrm{D}w/\mathrm{D}\theta$ is the algorithmic derivative (5.188). The directional derivative with respect to the displacement is computed similarly

$$\mathrm{D}H_i^e[\Delta\boldsymbol{u}] = \sum_{a=1}^{n_{\mathrm{en}}} \sum_{b=1}^{n_{\mathrm{en}}} \delta\Theta_a^e \left(- \int_{\omega_e} \varrho N_a \mathbf{w}_C^T \tilde{\mathbf{B}}_b \, \mathrm{d}v \right) \Delta\mathbf{u}_b^e, \tag{5.190}$$

with the matrix

$$\mathbf{w}_C = 2 \left\{ \frac{\partial w}{\partial \mathbf{C}} + \frac{1}{ha_{ii}} \frac{\partial w}{\partial \dot{\mathbf{C}}} + \left[\frac{\partial \mathbf{q}}{\partial \mathbf{C}} \right]^T \left\{ \frac{\partial w}{\partial \mathbf{q}} \right\} \right\}. \tag{5.191}$$

The terms in curly brackets in (5.190) form the algorithmic derivative of the heat production w with respect to a displacement change $\Delta\boldsymbol{u}$. In the formulation the spatial as well as the temporal discretization are included. The matrix $\mathbf{w}_C$ is of dimension (6×1). It is formed with $\mathbf{C}$, the matrix (column vector) representation of the right Cauchy-Green tensor $\mathbf{C}$. The stage derivative of the right Cauchy-Green tensor reads $\dot{\mathbf{C}}_i = \left[\mathbf{C}_i - \mathbf{C}_i^S \right]/(ha_{ii})$, where $\mathbf{C}_i$ and $\mathbf{C}_i^S$ are computed with the stage and starting value of the displacements $\boldsymbol{U}_i$ and $\boldsymbol{U}_i^S$, respectively. Accordingly, the nodal contribution to the iteration matrix reads

$$\mathbf{k}_{\theta u,i}^{e,ab} = - \int_{\Omega_\square} \varrho_R N_a \mathbf{w}_C^T \tilde{\mathbf{B}}_b \det \mathbf{J}^e \, \mathrm{d}\Omega_\square. \tag{5.192}$$

Looking at the term H_q, describing heat conduction within the body, the constitutive model of the heat flux specifies the starting point for the derivation of the iteration matrix. The heat flux vector used in this work is specified in the current configuration $\boldsymbol{q} = \boldsymbol{\lambda} \operatorname{grad} \theta$, where the conductivity tensor depends only on temperature $\boldsymbol{\lambda} = \boldsymbol{\lambda}(\theta)$.[36] Thus, H_q formulated in the current configuration is linearized in a first step with respect to the temperature change $\Delta\theta$. This results in

$$\mathrm{D}H_q^e[\Delta\theta] = \sum_{a=1}^{n_{\mathrm{en}}} \sum_{b=1}^{n_{\mathrm{en}}} \delta\Theta_a^e \left(- \int_{\omega_e} (\operatorname{grad} N_a)^T \left\{ \frac{\mathrm{d}\boldsymbol{\lambda}}{\mathrm{d}\theta} \operatorname{grad} \theta N_b + \boldsymbol{\lambda} \operatorname{grad} N_b \right\} \mathrm{d}v \right) \Delta\Theta_b^e,$$

which implies the nodal based iteration matrix

$$k_{\theta\theta,q}^{e,ab} = - \int_{\Omega_\square} (\operatorname{grad} N_a)^T \left\{ \frac{\mathrm{d}\boldsymbol{\lambda}}{\mathrm{d}\theta} \operatorname{grad} \theta N_b + \boldsymbol{\lambda} \operatorname{grad} N_b \right\} \det \mathbf{j}^e \, \mathrm{d}\Omega_\square. \tag{5.193}$$

---

[36]In the derivation given here, a symmetric tensor $\boldsymbol{\lambda}$ is considered, while in the examples of Chp. 6, the special case of an isotropic conductivity ($\boldsymbol{\lambda} = \lambda\mathbf{1}$) is used.

The effect of a displacement change is computed similarly. With the symmetry of the heat conductivity tensor $\boldsymbol{\lambda}$, the iteration submatrix is expressed in matrix formulation as

$$\mathbf{k}_{\theta u,q}^{e,ab} = \int\limits_{\Omega_\square}\Big\{ - \big[(\operatorname{grad} N_a)^{\mathrm{T}} \operatorname{grad} N_b\big] (\operatorname{grad} \theta)^{\mathrm{T}}\boldsymbol{\lambda} - \big[(\operatorname{grad} N_b)^{\mathrm{T}} \operatorname{grad} \theta\big] (\operatorname{grad} N_a)^{\mathrm{T}}\boldsymbol{\lambda}$$

$$+ \big[(\operatorname{grad} N_a)^{\mathrm{T}}\boldsymbol{\lambda} \operatorname{grad} \theta\big] (\operatorname{grad} N_b)^{\mathrm{T}}\Big\} \det \mathbf{j}^e \, \mathrm{d}\Omega_\square. \quad (5.194)$$

The last term that has to be linearized is the vector of external heat supply, $\mathbf{h}_{\mathrm{e}}^e$. The surface temperature of the body can determine the amount of heat transferred to the surroundings, as in the case of convective cooling. This is accounted for by the term c. The linear change of $\mathbf{h}_{\mathrm{e}}^e$ ath component due to bth nodal temperature change is given by

$$\mathrm{k}_{\theta\theta,\mathrm{e}}^{e,ab} = \int\limits_{\partial\Omega_\square} \frac{\partial c}{\partial \theta} N_a N_b \|\boldsymbol{x}_{,\xi} \times \boldsymbol{x}_{,\eta}\| \, \mathrm{d}\xi \, \mathrm{d}\eta. \quad (5.195)$$

Neither the prescribed surface heat flux f_{q}, nor the temperature dependent heat flux c (describing e.g. convective cooling or thermal radiation) vary with the displacement. However, both terms act on the current configuration. Thus, the effect of a changing surface has to be accounted for. This is done by linearizing the surface element in the current configuration $\mathrm{d}a = \|\boldsymbol{x}_{,\xi} \times \boldsymbol{x}_{,\eta}\| \, \mathrm{d}\xi \, \mathrm{d}\eta$. Doing so leads to

$$\mathrm{D}\,\mathrm{d}a[\Delta\boldsymbol{u}] = \left\{ \frac{\boldsymbol{x}_{,\xi} \times \boldsymbol{x}_{,\eta}}{\|\boldsymbol{x}_{,\xi} \times \boldsymbol{x}_{,\eta}\|} \right\}^{\mathrm{T}} \left\{ \Delta\boldsymbol{u}_{,\xi}\bar{\mathbf{N}}_{,\eta} - \Delta\boldsymbol{u}_{,\eta}\bar{\mathbf{N}}_{,\xi} \right\} \mathrm{d}\xi \, \mathrm{d}\eta$$

with

$$\bar{\mathbf{N}}_{,i} = \begin{bmatrix} 0 & x_{3,i} & -x_{2,i} \\ -x_{3,i} & 0 & x_{1,i} \\ x_{2,i} & -x_{1,i} & 0 \end{bmatrix},$$

where the comma indicates differentiation (e.g. $x_{1,\xi} = \partial x_1/\partial\xi$). See also [Wriggers, 2009, p. 144] and the literature cited therein. With this intermediate result the derivative of $\mathbf{h}_{\mathrm{e}}^e$ with respect to a nodal change of displacement yields the iteration matrix

$$\mathbf{k}_{\theta u,\mathrm{e}}^{e,ab} = \int\limits_{\partial\Omega_\square} (f_{\mathrm{q}} + c) N_a \left\{ \frac{\hat{\boldsymbol{n}}}{\|\hat{\boldsymbol{n}}\|} \right\}^{\mathrm{T}} \left\{ N_{b,\xi}\bar{\mathbf{N}}_{,\eta} - N_{b,\eta}\bar{\mathbf{N}}_{,\xi} \right\} \mathrm{d}\xi \, \mathrm{d}\eta, \quad (5.196)$$

where the non-unit normal vector $\hat{\boldsymbol{n}}$ is given in equation (5.184). The submatrix $\mathbf{k}_{\theta u,\mathrm{e}}^{e,ab}$ is a row vector of dimension (1×3). All nodal based contributions have to be added to account for the various effects due to a change of temperature and displacement

$$\mathrm{k}_{\theta\theta}^{e,ab} = \mathrm{k}_{\theta\theta,\mathrm{c}}^{e,ab} + \mathrm{k}_{\theta\theta,\mathrm{i}}^{e,ab} + \mathrm{k}_{\theta\theta,\mathrm{q}}^{e,ab} + \mathrm{k}_{\theta\theta,\mathrm{e}}^{e,ab}, \quad (5.197)$$

$$\mathbf{k}_{\theta u}^{e,ab} = \mathbf{k}_{\theta u,\mathrm{i}}^{e,ab} + \mathbf{k}_{\theta u,\mathrm{q}}^{e,ab} + \mathbf{k}_{\theta u,\mathrm{e}}^{e,ab}, \quad (5.198)$$

To form the element iteration matrices, the nodal contributions (submatrices) are arranged according to the node numbers. One obtains

$$
\mathbf{k}_{\theta\theta}^e =
\begin{bmatrix}
k_{\theta\theta}^{e,11} & k_{\theta\theta}^{e,12} & \cdots & k_{\theta\theta}^{e,1n_{en}} \\
k_{\theta\theta}^{e,21} & k_{\theta\theta}^{e,22} & \cdots & k_{\theta\theta}^{e,2n_{en}} \\
\vdots & \vdots & \ddots & \vdots \\
k_{\theta\theta}^{e,1n_{en}} & k_{\theta\theta}^{e,2n_{en}} & \cdots & k_{\theta\theta}^{e,n_{en}n_{en}}
\end{bmatrix},
\qquad
\mathbf{k}_{\theta u}^e =
\begin{bmatrix}
\mathbf{k}_{\theta u}^{e,11} & \mathbf{k}_{\theta u}^{e,12} & \cdots & \mathbf{k}_{\theta u}^{e,1n_{en}} \\
\mathbf{k}_{\theta u}^{e,21} & \mathbf{k}_{\theta u}^{e,22} & \cdots & \mathbf{k}_{\theta u}^{e,2n_{en}} \\
\vdots & \vdots & \ddots & \vdots \\
\mathbf{k}_{\theta u}^{e,1n_{en}} & \mathbf{k}_{\theta u}^{e,2n_{en}} & \cdots & \mathbf{k}_{\theta u}^{e,n_{en}n_{en}}
\end{bmatrix}.
$$

The element iteration matrices $\mathbf{k}_{\theta\theta}^e$ and $\mathbf{k}_{\theta u}^e$ account for the element contribution to a change of $\boldsymbol{G}_\theta$ due to a change of nodal temperature, and nodal displacement.

The assembly of the linear system (5.151) from the element contributions leads to a system with special structure. This can be solved efficiently using the solvers for sparse linear systems described in Sec. 5.7. Before this is done, another aspect deserves attention. In every finite element analysis, the solution of the nonlinear systems forms an integral part, which consumes a considerable part of the available computational resources. Different approaches for accelerating this iteration are considered next.

5.6.4. Accelerating the Newton Process

A very important efficiency hint is related to the initial iterate of the nonlinear solver. In standard textbooks on nonlinear finite elements such as [Bathe, 1996], [Belytschko et al., 2004], and [Wriggers, 2009], the authors suggest to use as initial iterate the value which was obtained from the previous time step t_n. The extension to the DIRK-method implies the starting vector of the last stage quantity (temperature, displacement, or both). Bathe [1996] further recommends to use the exact tangent stiffness matrix and to decrease the step size if convergence problems of the Newton-iteration occur. Belytschko et al. [2004] mention that the major restrictions on the size of the time-step in implicit methods arise (besides accuracy requirements) from the decreasing robustness of the Newton-procedure. They point out that large time-steps impair the convergence of the Newton-method and the starting iterate may be far from the solution.

To get in the range of quadratic convergence and to significantly reduce the number of iterations an approximation of the solution should be used. This approximation is often referred to as extrapolator or predictor and these initial guesses can be based on linear or quadratic extrapolation from the previous increments [Esche et al., 1997], [Stricklin et al., 1973], [Miller, 2005]. In the case of DIRK methods also a so-called stage extension extrapolation can be used. This was introduced in [Cameron, 1999] and studied in [Clemens et al., 2003] for the case of electro- and magneto-quasistatic field simulations.

In this work a linear extrapolation of the global variables from the last two computed

stages (time steps) is used

$$
\begin{aligned}
\boldsymbol{V}_{(i)}^{(0)} &= \boldsymbol{V}_{(i-1)} + \frac{t_{(i)} - t_{(i-1)}}{t_{(i-1)} - t_{(i-2)}} \left(\boldsymbol{V}_{(i-1)} - \boldsymbol{V}_{(i-2)} \right) \\
&= \frac{t_{(i)} - t_{(i-2)}}{t_{(i-1)} - t_{(i-2)}} \boldsymbol{V}_{(i-1)} + \frac{t_{(i-1)} - t_{(i)}}{t_{(i-1)} - t_{(i-2)}} \boldsymbol{V}_{(i-2)}.
\end{aligned}
\tag{5.199}
$$

The times $t_{(i)}$ define stage times, which can belong to the current or the previous time step.[37] This extrapolation can be done at almost no expense and yields great savings; in many examples the number of iterations is halved and the MLNA is stabilized essentially. In these cases the MLNA without extrapolator diverges and the time step has to be repeated with a smaller size. In the very first time step the prescribed step size is reduced to $h = 10^{-3}h_0$ to start the process when no information from previous stages is available. The proposed approach is only used to determine the starting vector of the global variables. Using the extrapolation technique for the internal variables did not result in any savings for the considered material model of metal plasticity. The reason for this might be related to the applied Multilevel-Newton algorithm in Tab. 5.2, where the local step (5.149) is mainly influenced by the known global variables $\boldsymbol{V}^{(m)}$. For a global block-Newton-method the conclusion might differ and these have to be studied separately.

At the heart of the Newton process and thus, the numerical process as a whole, is the solution of the global linear system (5.151). Its solution can consume over 80% of the total computation time, which poses the possibility for another way to accelerate the iteration process (when using a direct solver for the linear systems). In the chord method, also referred to as modified Newton method, one avoids the computation of the derivative and saves linear algebra work. The Jacobian matrix according to equation (5.146) is computed and factorized only once at the begin of the iteration. This leads to more iterations than the standard Newton method (convergence is only q-linear, see [Kelley, 2003, p. 33] and [Kelley, 1995, p. 76]) but the overall cost is usually significantly less. Another possibility is to compute the iteration matrix and its factorization every m iterations. This increases the rate of convergence (superlinear but less than 2) and is known as the Shamanskii method, cf. [Kelley, 1995, p. 78].

The success of the method depends also on the quality of the initial iterate, which is substantially imporved using the extrapolation described above. In view of the MLNA the global system is adapted

$$
\left[\frac{\partial \boldsymbol{G}}{\partial \boldsymbol{V}} + \frac{\partial \boldsymbol{G}}{\partial \hat{\boldsymbol{Q}}} \frac{\mathrm{d}\hat{\boldsymbol{Q}}}{\mathrm{d}\boldsymbol{V}} \right]_{\boldsymbol{Y}^{(0)}} \Delta \boldsymbol{V}^{(m)} = -\boldsymbol{G}\left(\boldsymbol{V}^{(m)}, \hat{\boldsymbol{Q}}\left(\boldsymbol{V}^{(m)} \right) \right),
\tag{5.200}
$$

---

[37] Of course, the stage times given by $c_i, i = 1, \ldots, s$ should be increasing for this simple extrapolation formula to work best. This property is also advantageous for the convergence behavior of the overall Newton process. However, this it is not the case for all considered DIRK methods.

where the iteration matrix (generalized consistent tangent operator) is kept constant

$$\left[\frac{\partial \boldsymbol{G}}{\partial \boldsymbol{V}} + \frac{\partial \boldsymbol{G}}{\partial \hat{\boldsymbol{Q}}} \frac{\mathrm{d}\hat{\boldsymbol{Q}}}{\mathrm{d}\boldsymbol{V}}\right]_{\boldsymbol{y}^{(0)}} = \frac{\mathrm{d}\boldsymbol{G}}{\mathrm{d}\boldsymbol{V}}\bigg|_0.$$

In this Chord-MLNA (CMLNA) the iteration matrix can be kept constant even for several time steps. Its recomputation is only necessary if the time step size changes (when singly DIRK methods are used, see p. 116)[38] or the rate of convergence degrades too much. The advantages are, that the factorization of the global system is kept constant and that only function evaluations are needed on element level. Derivatives do not have to be computed, i.e. on quadrature point level the consistent linearization (5.153) and on element level the computation of $\partial \boldsymbol{G}/\partial \boldsymbol{V}$ as well as $\partial \boldsymbol{G}/\partial \boldsymbol{Q}$ are not needed. Furthermore the assembly process of element matrices can be omitted.

To further improve the global convergence properties of the method a line search is added. Here, the Armijo rule (see [Kelley, 1995, p. 145]) is used to reduce the step length of the CMLNA if necessary. In a first step the search direction $\boldsymbol{d}$ is computed using

$$\left[\frac{\partial \boldsymbol{G}}{\partial \boldsymbol{V}} + \frac{\partial \boldsymbol{G}}{\partial \hat{\boldsymbol{Q}}} \frac{\mathrm{d}\hat{\boldsymbol{Q}}}{\mathrm{d}\boldsymbol{V}}\right]_{\boldsymbol{y}^{(0)}} \boldsymbol{d} = -\boldsymbol{G}\left(\boldsymbol{V}^{(m)}, \hat{\boldsymbol{Q}}\left(\boldsymbol{V}^{(m)}\right)\right). \tag{5.201}$$

To prevent overshoots and to keep the step from going to far it is required that

$$\left\|\boldsymbol{G}\left(\boldsymbol{V}^{(m)} + s\boldsymbol{d}, \hat{\boldsymbol{Q}}(\boldsymbol{V}^{(m)} + s\boldsymbol{d})\right)\right\| < \left\|\boldsymbol{G}\left(\boldsymbol{V}^{(m)}, \hat{\boldsymbol{Q}}(\boldsymbol{V}^{(m)})\right)\right\| \tag{5.202}$$

is fulfilled, with the step length s. Often one searches for the smallest integer n such that for $s = 2^{-n}$ the criterium (5.202) is satisfied. This corresponds to halving the step size each time. If the reduction is not sufficient after two steps a quadratic model can be build and used to determine s analytically. However, numerical experiments showed that this seems to be unnecessary for the intended application. Thus, this approach is not applied in the following (eventhough neither complicated nor computationally demanding). The global variables for the next iteration are given by

$$\boldsymbol{V}^{(m+1)} = \boldsymbol{V}^{(m)} + s\boldsymbol{d}. \tag{5.203}$$

As already mentioned before, the solution of the global linear system (5.151) can consume over 80% of the total computation time. Thus, its fast solution is compulsory. Different approaches and accelerating techniques are presented in the following.

---

[38]If general DIRK methods are applied a different Jacobian and factorization has to be stored for each stage with different diagonal element a_{ii}. This is supported by current solvers such as PARDISO, but of course significantly increases the amount of required memory. The feature of storing different factorizations could also be used for the staggered approach, where an iteration matrix for the thermal and one for the mechanical problem are needed.

5.7. Solution of Sparse Linear Systems

In the course of the numerical simulation, a sequence of linear systems emanates. These systems are similar to each other, i.e. the values of the coefficient matrices often change gradually during the simulation or changes are restricted to certain parts of the matrices. More importantly, the structure of the matrices is sparse, unstructured (e.g. not diagonal or block diagonal) and constant. There are only very few non-zero elements, whose locations (coordinates) do not change. Thus, special techniques can be utilized to take advantage of this structure.

Typical sparsity patterns are given in Fig. 5.19. The presented systems stem from

(a) Standard sparsity pattern as produced by GiD

(b) Sparsity pattern after reordering with the reverse Cuthill McKee algorithm
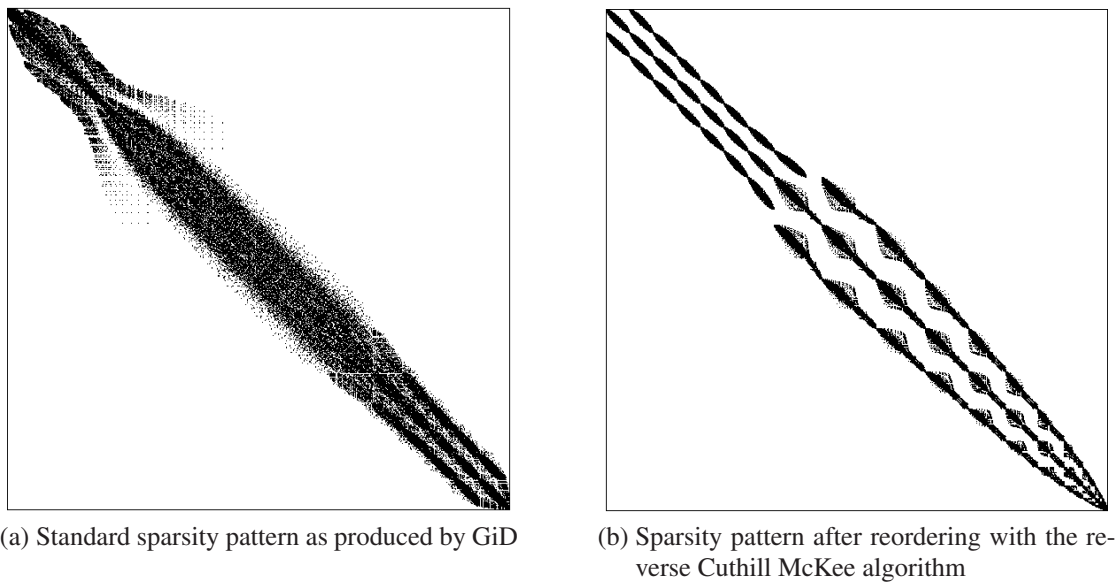
Figure 5.19.: Typical sparsity patterns of functional matrices, in this case from a tensile test with $n_{eq} = 6751$ unknowns and 462469 non-zero elements

a purely mechanical example, which is created using the GiD pre- and post-processor from the International Center for Numerical Methods in Engineering (CIMNE). The geometry is modeled using the CAD features of GiD, and subsequently meshed as described for example in [Oñate, 2009, p. 431]. Using the standard numeration leads to the pattern of Fig. 5.19a. The percentage of nonzero elements is only at the order of 1%. An improved matrix sparsity pattern can be obtained by an additional reordering, as shown in Fig. 5.19b. Here the reverse Cuthill-McKee ordering is applied, cf. [Saad, 2003, p. 81]. This algorithm uses a node at one corner of the structure as a starting point to produce matrices with small bandwidth and is known to be better for Gaussian elimination. However, in all tested examples this reordering does not result in any significant performance gain. This might be due to the preordering and pivoting, which is done anyway by advanced solver packages for linear systems.

All available solvers can be distinguished in direct and iterative solvers.[39] Commonly, direct solvers are used for small to medium sized problems (currently around 200000 unknowns) and iterative solvers for large scale problems, often with several million unknowns. Both approaches are briefly outlined and compared in the following.

5.7.1. Direct Solvers

During each iteration, the linear system of equations (5.151) has to be solved. It is of the general form

$$\boldsymbol{J}\boldsymbol{s} = \boldsymbol{r}, \quad \boldsymbol{s} \in \mathbb{R}^{n_{eq}} \tag{5.204}$$

where the coefficient matrix $\boldsymbol{J} := \mathrm{d}\boldsymbol{G}/\mathrm{d}\boldsymbol{V}|_{\boldsymbol{y}^{(m)}} \in \mathbb{R}^{n_{eq}\times n_{eq}}$ is the Jacobian, and the right-hand side $\boldsymbol{r} := \boldsymbol{G}(\boldsymbol{y}^{(m)}) \in \mathbb{R}^{n_{eq}}$ is the residual of the global equation system evaluated at the current approximation $\boldsymbol{y}^{(m)} = \left(\boldsymbol{U}^{(m)}, \boldsymbol{\Theta}^{(m)}, \boldsymbol{Q}^{(m)}\right)$. While the Jacobian matrix is often symmetric for the purely mechanical and the purely thermal subproblem, this is in general not the case for the fully coupled thermomechanical problem. Hence, in the following only methods for quadratic unsymmetric linear systems (but having a symmetric sparsity pattern; $\boldsymbol{J}$ is said to be structurally symmetric) are considered.

For the solution of general systems $\boldsymbol{L}\boldsymbol{U}$ decomposition is often applied, which is a modified form of the Gaussian elimination, cf. [Golub and van Loan, 1996, p. 94]. It is based on a decomposition of the coefficient matrix of the form

$$\boldsymbol{J} = \boldsymbol{L}\boldsymbol{U}, \tag{5.205}$$

where $\boldsymbol{L}$ is a unit lower triangular matrix and $\boldsymbol{U}$ is an upper triangular matrix having only zero entries below the main diagonal. For a 3×3 system, the factorization reads in component form

$$\begin{bmatrix} J_{11} & J_{12} & J_{13} \\ J_{21} & J_{22} & J_{23} \\ J_{31} & J_{32} & J_{33} \end{bmatrix} = \begin{bmatrix} 1 & 0 & 0 \\ L_{21} & 1 & 0 \\ L_{31} & L_{32} & 1 \end{bmatrix} \begin{bmatrix} U_{11} & U_{12} & U_{13} \\ 0 & U_{22} & U_{23} \\ 0 & 0 & U_{33} \end{bmatrix},$$

it also called triangular decomposition of the matrix $\boldsymbol{J}$. Once, the factors $\boldsymbol{L}$ and $\boldsymbol{U}$ are known, the solution to the original system is found by first, solving

$$\boldsymbol{L}\boldsymbol{t} = \boldsymbol{r}, \tag{5.206}$$

for $\boldsymbol{t}$ and second, solving

$$\boldsymbol{U}\boldsymbol{s} = \boldsymbol{t} \tag{5.207}$$

---

[39] An important class of iterative solvers, which is not considered here, are multilevel methods. These also provide an efficient way to solve large linear systems. Two different multilevel-method approaches are used, namely the geometric multigrid (GMG), refer for example to [Hackbusch, 1985], and more recently the algebraic multigrid (AMG), as illustrated in [Stüben, 1999]. Many information and references on both approaches can be found at `http://www.mgnet.org`.

for the unknown Newton direction **s**. Both equations are triangular and their solution is trivial, done recursively using only back-substitution. These require a computational effort of order $\mathcal{O}(n_{\text{eq}}^2)$, while computing the factorization requires the most floating-point operations (flop). In this case, the total number of flop is approximately $n_{\text{eq}}^3/3$ as shown in [Überhuber, 1997, p. 231]. This means, that once the *LU* decomposition has been computed, the solution of equation (5.204) can be obtained at a significantly lower cost for varying right-hand sides **r**. However, using the method directly as described would be unfeasible for large systems. The computational and memory requirements would even outrun the resources of current supercomputers.[40] Even though the coefficient matrix **J** is sparse, the factors **L** and **U** generally do not inherit this sparsity structure. One speaks of fill-in, which leads in the worst case to fully populated triangular matrices.

Fortunately, for sparse matrices the flop counts can be significantly lower, when the sparsity structure of the coefficient matrix **J** is exploited. Sparse direct methods generally employ graph models to minimize both the needed storage and the performed work. A typical solution process consists of four phases:

1. *Preordering Phase*
   Exploit matrix structure using for example minimum degree ordering or nested dissection ordering to reduce fill-in.

2. *Symbolic Factorization Phase*
   Analyze the matrix structure to determine a pivot sequence and data structures for efficient factorization.

3. *Numerical Factorization Phase*
   Compute actual factors **L** and **U** using the pivot sequence.

4. *Solve Phase*
   Compute forward and backward triangular sweeps for each different right-hand side **r** and iterative refinement.

Within this work, two popular modern LU-packages based on different factorization strategies, namely UMFPACK 5.0.3 [Davis and Duff, 1997] and PARDISO 3.2 [Schenk and Gärtner, 2004; Schenk et al., 1999], have been integrated in the inhouse FEM-code TASAFEM.[41] UMFPACK is a multifrontal solver, which builds the *LU* decomposition of a sparse matrix by working only on subsets of rows and columns at a time. Processing these subsets, which are called the fronts, involves dense matrix operations. These are highly optimized and use the computer architecture very efficiently.

---

[40] Another problem is the stability of the numerical method. The elimination process in its simplest form is numerically unstable as shown in a simple example in [Überhuber, 1997, p. 233]. Pivoting is used to overcome a loss of accuracy due to cancellation of leading digits.

[41] These two and nine other direct solvers for linear systems are also compared in [Gould et al., 2007]. PARDISO is shown to be among the fastest in different test scenarios.

The solution process using PARDISO starts with finding a symmetric fill-in reducing permutation matrix $\boldsymbol{P}$, see [Schenk and Gärtner, 2006] for details. Following, the factorization of the sparse matrix $\boldsymbol{P}\boldsymbol{J}\boldsymbol{P}^{\mathrm{T}} = \boldsymbol{Q}\boldsymbol{L}\boldsymbol{U}^{\mathrm{T}}$ is done in parallel, with the supernode pivoting matrix $\boldsymbol{Q}$ in order to balance numerical stability and scalability during the factorization process. Though, the result of the pivoting approach is that the factorization is, in general, not exact. This makes iterative refinement necessary, which might seem unfamiliar when using direct methods.

PARDISO is a high-performance, robust, and memory-efficient parallel solver. It is optimized for shared memory multiprocessor architectures and takes advantage of the memory hierarchy on modern microprocessors to achieve a high floating-point performance. It turns out to be even in its serial version faster than UMFPACK for the solution of many systems coming from a FEM discretization as shown in [Hartmann et al., 2009a]. In the following, only PARDISO is used as a direct solver.

Since the structure of the coefficient matrix $\boldsymbol{J}$ is constant during the complete simulation, it is sufficient to execute phase 1 and phase 2 (preordering and symbolic factorization) only once. Certainly, the numerical factorization and the back-substitution still have to be done. In PARDISO phase 1 and 2 are combined in a single phase (thus, there are only three phases) and the single phases can be executed separately. For three different medium sized models, the run times of the different phases and the total run time are recorded in Tab. 5.3. Furthermore, the influence of different numbers of threads

Table 5.3.: Measured runtimes of different phases of PARDISO

$n_{\mathrm{eq}}/1000$	Number of threads	CPU time Phase 1-1	CPU time Phase 2-3	CPU time total
21	1	0.3	1.6	1.9
46	1	0.7	6.6	7.3
100	1	1.8	28.0	29.8
21	2	0.3	0.9	1.2
46	2	0.7	3.6	4.3
100	2	1.8	15.0	16.8
21	4	0.3	0.5	0.8
46	4	0.7	2.0	2.7
100	4	1.8	8.3	10.1
21	8	0.3	0.4	0.7
46	8	0.8	1.6	2.4
100	8	1.7	7.4	9.2

is studied. The most time consuming part of PARDISO, the numerical factorization and back-substitution, scales nicely up to four threads. For eight threads there is only a small speed-up on the present hardware. Remarkably, phase 1 (the preordering and symbolic

factorization) does not profit from a higher number of threads and its CPU time can not be neglected. Thus, executing this phase just once safes a lot of computational time in transient nonlinear computations and becomes mandatory when using the parallel version of PARDISO.

A different approach for the solution of linear systems are iterative solvers. These solvers are in particular suitable for large systems and can be conveniently combined with the Newton process.

5.7.2. Iterative Solvers

All iterative solution methods for the linear system $\boldsymbol{J}\boldsymbol{s} = \boldsymbol{r}$ start with an initial approximation

$$\boldsymbol{s}_0 \in \mathbb{R}^{n_{eq}}$$

and construct a sequence $\{\, \boldsymbol{s}_k \colon k = 1, 2, 3, \dots \,\}$. The iteration is stopped when a user-specified tolerance is reached. Iterative methods can be classified as stationary and non-stationary. Stationary methods are older, simpler to understand and implement. Among them are the Jacobi, the Gauss-Seidel, and the Successive Overrelaxation (SOR) method.

Non-stationary methods, on the other hand, are a relatively recent development. Currently Krylov subspace methods are considered to be among the most important iterative techniques available for solving large linear systems. They are based on projection processes (both orthogonal and oblique) onto Krylov subspaces. In favorable cases this reveals dominant properties of the system at an early stage and one may expect rapid convergence. Krylov subspaces are subspaces spanned by vectors of the form $p(\boldsymbol{J})\boldsymbol{v}$, where p is a polynomial in $\boldsymbol{J}$ of degree $k - 1$, i.e.

$$\mathcal{K}_k(\boldsymbol{J}, \boldsymbol{v}) := \left\{\, \boldsymbol{v}, \boldsymbol{J}\boldsymbol{v}, \boldsymbol{J}^2\boldsymbol{v}, \dots, \boldsymbol{J}^{k-1}\boldsymbol{v} \,\middle|\, \boldsymbol{v} \in \mathbb{R}^{n_{eq}} \,\right\}. \tag{5.208}$$

A general projection method for solving $\boldsymbol{J}\boldsymbol{s} = \boldsymbol{r}$ is given by the projection onto $\mathcal{K}$ and orthogonal to $\mathcal{L}$:

$$\text{Find} \quad \boldsymbol{s}_k \in \boldsymbol{s}_0 + \mathcal{K}_k(\boldsymbol{J}, \boldsymbol{v}_0) \quad \text{such that} \quad \boldsymbol{r} - \boldsymbol{J}\boldsymbol{s}_k \perp \mathcal{L}_k,$$

with $\boldsymbol{v}_0 = \boldsymbol{r} - \boldsymbol{J}\boldsymbol{r}_0$. Different versions of Krylov subspace methods arise from different choices of the subspace $\mathcal{L}_k$ and from the ways in which the system is preconditioned. For example, in the Generalized Minimal Residual method (GMRES) $\mathcal{L}_k = \boldsymbol{J}\mathcal{K}_k$ is chosen, cf. [Saad and Schultz, 1986]. All previously computed vectors in the orthogonal sequence have to be stored and slow down the computation of a single iteration step. These steps become increasingly expensive. For this reason, in practice the iteration sequence is restarted with a new initial vector $\boldsymbol{s}_0$. This is referred to as the restarted GMRES and is used in the numerical examples. Another popular solver, which is also used in the following, is the biconjugate gradient stabilized method (BiCGSTAB), which is described in [van der Vorst, 1992]. The iterative solvers used in this work are modified

versions from Youcef Saad's Sparskit 2.0, [Saad, 1994b]. A nice overview with many hints on the implementation of iterative solvers is given in [Barrett et al., 1994]. The authors supply general templates, which allow ports to different machines and computer languages.

The selection of a suitable stopping tolerance of the iterative solver can be important for the overall computational efficiency. This is similar to choice in the Newton process (see App. A.3). In connection with the Newton iteration this allows a further efficiency gain, which can not be achieved by direct solvers.

5.7.3. Stopping Criteria for Iterative Solvers

As mentioned above, an important advantage of iterative methods is that they can be stopped as soon as the approximation is sufficient for the purpose of the overall computational process. For instance the accuracy of Newton step $\boldsymbol{s}$ (the solution of the linear system) should be related to the discretization error resulting from the approximations in space and time and stability considerations.

In the context of the Newton process in Tab. 5.2 this means that the accuracy to which the (large) global system is solved can be adjusted to achieve satisfactory convergence of the nonlinear residual. This is the main idea of inexact Newton methods as introduced in [Dembot et al., 1982]. Finding stopping criteria for the iterative solvers of linear systems in an inexact Newton method asks for balancing between moderately accurate solution of the linear problems and reasonably fast convergence of the nonlinear process. The standard paper containing useful stopping criteria (called forcing terms) for inexact Newton processes is [Eisenstat and Walker, 1996]. The tolerances which are used here are inspired by Kelley [1995, Chapter 6].

The residual norm of an approximation of an exact Newton step $\boldsymbol{s}$ is $\|\boldsymbol{J}\boldsymbol{s} - \boldsymbol{r}\|$. The coefficient matrix $\boldsymbol{J} = \mathrm{d}\boldsymbol{G}/\mathrm{d}\boldsymbol{V}|_{\boldsymbol{y}^{(m)}}$ is the Jacobian, and the right-hand side vector, given by $\boldsymbol{r} = \boldsymbol{G}(\boldsymbol{y}^{(m)})$, is the residual of the global equation system evaluated for the variables at the mth Newton iteration $\boldsymbol{y}^{(m)}$. A stopping criterion for the relative residual norm of the linear system can be written as

$$\|\boldsymbol{J}\boldsymbol{s} - \boldsymbol{r}\| \leq \varepsilon^{(m)}\|\boldsymbol{G}(\boldsymbol{y}^{(m)})\|.$$

In [Kelley, 1995, Chapter 6] the values $\varepsilon^{(m)}$ are obtained with

$$\varepsilon_A^{(m)} = \gamma\|\boldsymbol{G}(\boldsymbol{y}^{(m)})\|^2/\|\boldsymbol{G}(\boldsymbol{y}^{(m-1)})\|^2$$

for a parameter $\gamma \in (0, 1]$ as

$$\varepsilon^{(m)} = \begin{cases} \varepsilon_{\max}, & m = 0 \\ \min\left(\varepsilon_{\max}, \varepsilon_A^{(m)}\right), & m > 0, \gamma\varepsilon^{(m-1)^2} \leq 0.1 \\ \min\left(\varepsilon_{\max}, \max\left(\varepsilon_A^{(m)}, \gamma\varepsilon^{(m-1)^2}\right)\right), & m > 0, \gamma\varepsilon^{(m-1)^2} > 0.1 \end{cases} \quad (5.209)$$

for a value $\varepsilon_{\max}$ that bounds away the sequence $\varepsilon^{(m)}$ from 1, e.g. $\varepsilon_{\max} = 0.9$. See [Kelley, 1995, Chapter 6] for more details on these choices.

For the last linear system of the nonlinear process one may avoid over-solving with equation (6.20) in [Kelley, 1995, Chapter 6] or one may simply monitor the magnitude of $\|\boldsymbol{G}(\boldsymbol{y}^{(m)})\|$ and switch to a stopping criterion for this absolute residual norm as soon as it comes close to the desired accuracy.

5.7.4. Preconditioners for Iterative Solvers

The rate at which an iterative method converges depends on spectral properties of the coefficient matrix $\boldsymbol{J}$. In many real applications, iterative methods suffer from slow convergence. Thus, one transforms the linear system into an equivalent one, i.e. a system which has the same solution but posses favorable properties. This is usually done with a second matrix $\boldsymbol{M}$, the preconditioning matrix or just preconditioner. An example is left preconditioning as given by

$$\boldsymbol{M}^{-1}\boldsymbol{J}\boldsymbol{s} = \boldsymbol{M}^{-1}\boldsymbol{r}. \tag{5.210}$$

This system has the same solution as the original system and is called the preconditioned system. A good preconditioner improves the convergence rate of the iterative method and its construction and application is inexpensive. Most important, the solution of $\boldsymbol{M}\boldsymbol{s} = \boldsymbol{r}$ has to be cheap, since it is required at each step of the iterative solution. Preconditioning is a key ingredient for the success of Krylov subspace methods. There are three ways to apply a preconditioner: from left, right, or both sides.

Preconditioners can be algebraic or physics-based, i.e. derived by considering a simpler problem, which allows an inexpensive solution. Here, only algebraic preconditioners are considered. One way of defining a preconditioner is to perform an incomplete factorization of the original matrix $\boldsymbol{J}$ of the form

$$\boldsymbol{J} = \boldsymbol{L}\boldsymbol{U} - \boldsymbol{R},$$

where $\boldsymbol{L}$ and $\boldsymbol{U}$ have the same sparsity pattern as $\boldsymbol{J}$ and $\boldsymbol{R}$ is the residual or error of the factorization. This is often referred to as ILU(0) and is relatively inexpensive to compute. Admittedly, in many circumstances, this is a rather crude approximation and results in a low convergence rate of the Krylov subspace method. Several alternatives have been proposed to alleviate this situation by allowing more fill-in in the factors $\boldsymbol{L}$ and $\boldsymbol{U}$. In ILU(p) all fill-in elements whose level of fill does not exceed p are kept.[42] An approach that takes into account the numerical values of the matrix elements is incomplete factorization with threshold ILUT(p, τ). It drops elements according to their magnitude rather than their location.

Simple preconditioners, based on additively splitting the matrix $\boldsymbol{J}$ (such as Symmetric Successive Overrelaxation), proved to be too inaccurate. They perform poorly for the present systems and are not further considered. In this context, see also the remarks in [Hartmann et al., 2009a].

---

[42]Fill levels are basically path lengths in the graph of the matrix $\boldsymbol{J}$. A precise definition is given in [Saad, 2003, p. 297].

6. Numerical Examples

The purpose of computational engineering and science (CES) is to provide predictions of physical events and to assist in the design process, [Oden, 2002]. Its promise is to replace the standard engineering process of iterated empirical design-build-test cycles with an iterated design-mesh-analyze paradigm, [Post, 2009].

In order to fulfill these promises the CES approach has to be first of all reliable and in addition to that sufficiently fast. The first aspect is the subject of validation and verification as described by Babuška and Oden [2004] in the context of CES. The second aspect can be related to the performance of the underlying numerical methods. Both aspects are considered in the following examples.

6.1. Cooling Experiment of a Locally Heated Steel Specimen

The main purpose of this experiment is to provide data for the validation of the entire model consisting of material data, mathematical model, and its numerical solution.[1]

6.1.1. Experimental Setup and Results

A cylindrical steel specimen made of 51CrV4 with a diameter of 30 mm and a length of 200 mm undergoes the same heating process as the demonstrator flange described in Chp. 1.1. To record the temporal and spatial temperature distribution, the specimen is equipped with eight thermocouples. Their positions are indicated in Fig. 6.1.

no.	r	z	no.	r	z
-	mm	mm	-	mm	mm
1	0	0	5	15	75
2	15	0	6	0	100
3	13	50	7	7.5	100
4	7.5	75	8	15	100
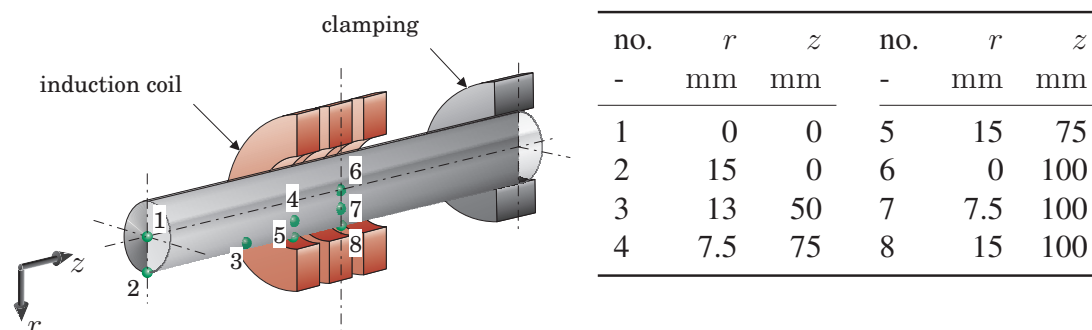
Figure 6.1.: Position of thermocouples (indicated by ●)

---

[1]The experiment has been carried out according to the specifications of the author in the laboratory of the Institute for Production Technology and Logistics, Chair of Metal Forming Technology, University of Kassel.

155

The specimen is inserted by hand in a transfer unit and clamped pneumatically, as shown in Fig. 6.2a. From that point on a test program is started and the complete process runs automatically. The process control of the system is based on a CAN-Bus-IO-module, which allows accurate time-dependent control of the machine functions. For the control and data acquisition of the process a program is used, which is based on LabView, see [Weidig et al., 2008] and [Sumathi and Surekha, 2007] for details. The clamping moves downward such that the centers of the specimen and the induction coil are aligned.

Next, the specimen is heated by induction, Fig. 6.2b. The induction facility al-

(a) Specimen with thermocouples

(b) Induction heating

(c) Cooling due to convection and radiation
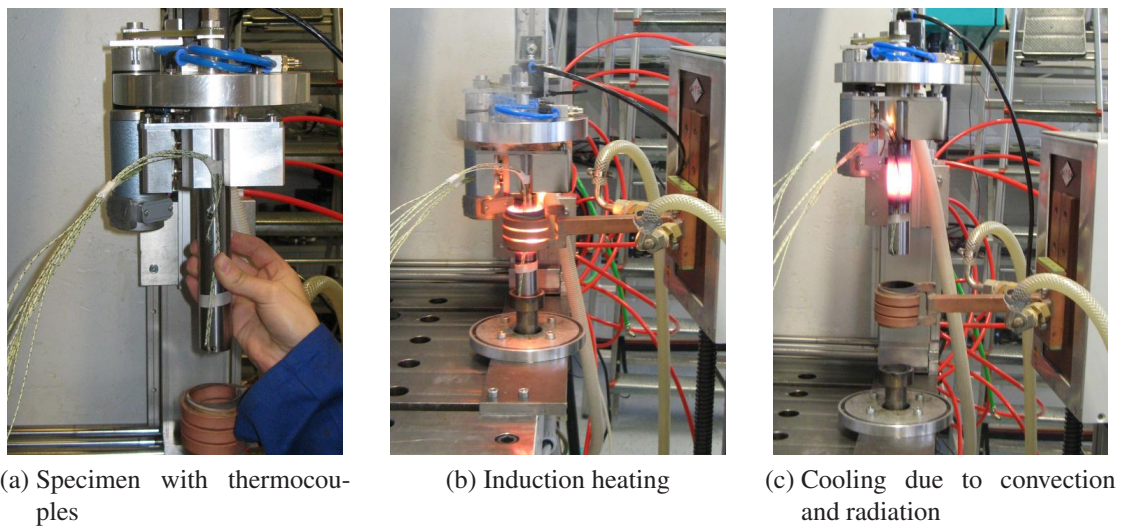
Figure 6.2.: Cooling experiment of locally heated specimen

lows the generation of three dimensional thermal profiles in workpieces. It consists of a high-capacity power supply and three independent medium-frequency transformers $(10 - 70 \text{ kHz})$ and an additional high-frequency transformer. In general, the resulting temperature profile depends on the heating time, heating power, heating frequency, and induction coil geometry. Here, a single three-turn coil with an inner diameter of 44 mm and a height of approximately 60 mm is used. The heating is done at two subsequent power levels. In the first stage the specimen is subjected for $t_1 = 12 \text{ s}$ to an inductive heating with a power of $P_1 = 42 \text{ kW}$. In the second stage this power is reduced to $P_2 = 15 \text{ kW}$. This stage lasts for $t_2 = 5 \text{ s}$ and is added to obtain a homogeneous temperature profile over the radius. In both stages a frequency of $f = 15 \text{ kHz}$ is used. At the end of the inductive heating process a maximum temperature of approximately 1200 °C is locally reached.

After finishing the heating process, the specimen is moved upward into its initial position and the temperature evolution is recorded, Fig. 6.2c. The resulting mean temperature evolution of ten independent experiments at various locations until $t_e = 180 \text{ s}$ is

shown in Fig. 6.3. During the measurement single thermocouples recorded completely

(a) Mean values at $z = 0$ mm

(b) Mean values at $z = 50$ mm and $z = 75.5$ mm

(c) Mean values at $z = 100$ mm

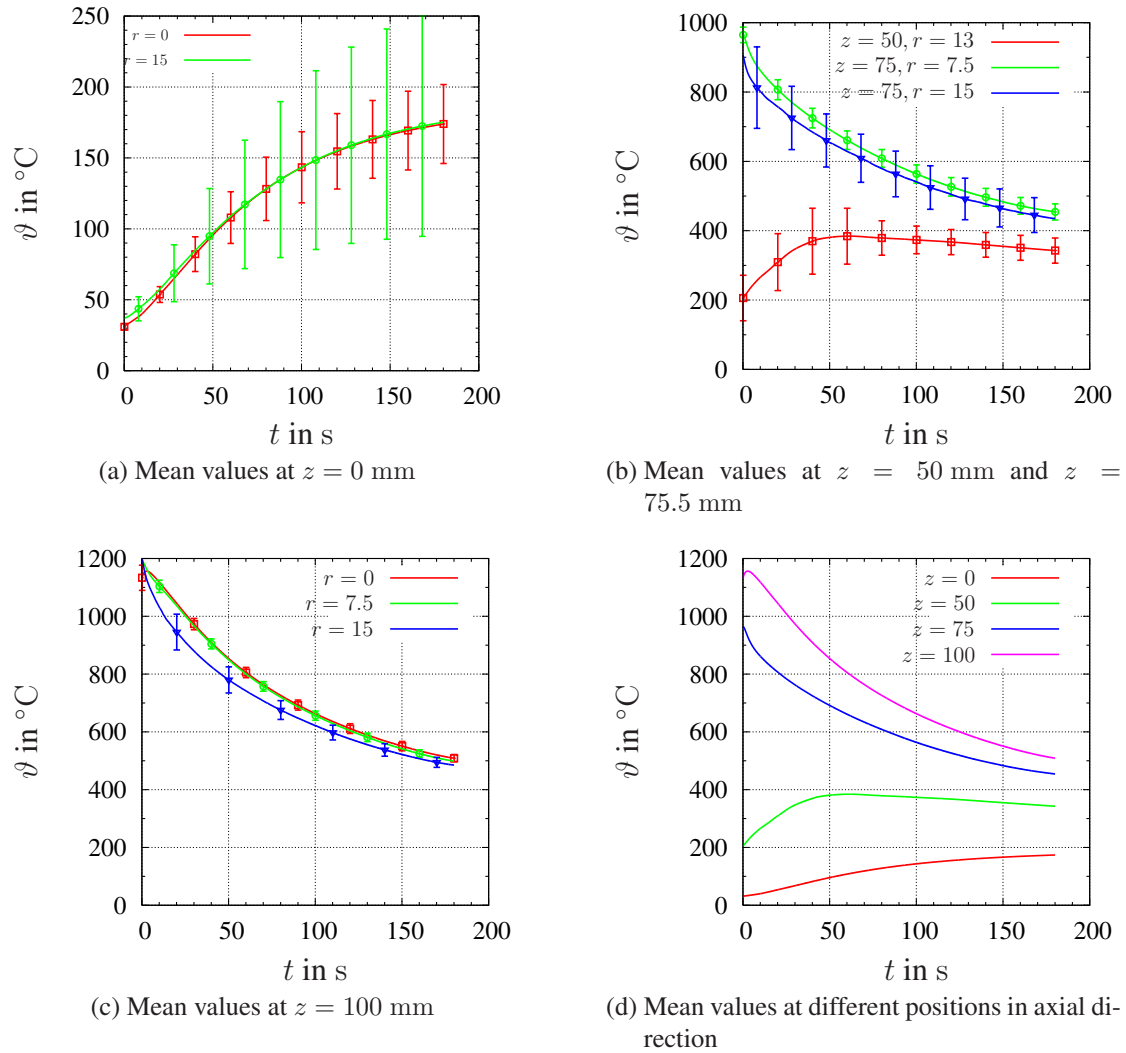(d) Mean values at different positions in axial direction

Figure 6.3.: Experimental results of cooling experiment

out of range data (zero signal, high frequency), which can not be explained by usual deviations. These thermocouples apparently lost contact (possibly due to broken or cold soldering joints) and broke down during the process. Their data is excluded from the evaluation. Concerning the rejection of experimental data, cf. [Taylor, 1997, p. 169]. The application of Chauvenet's criterion is controversial, because it operates merely on statistical data and is not applied here.

In Fig. 6.3a the mean temperature at the bottom of the specimen is depicted for the center 1: ($r = 0$ mm) and the circumference 2: ($r = 15$ mm). There is only a small temperature difference in radial direction, which is within the mean deviation of the recorded signal. The dispersion about the mean is larger at the surface of the specimen

than at its center. This phenomenon is seen in all measurements and might be due to a high sensitivity of the surface temperature on the surrounding environment. For the computation of the mean values four and seven data sets are used for the center and the circumference, respectively.

Fig. 6.3b shows the mean of eight values at the positions 3: ($z = 50\,\text{mm}, r = 13\,\text{mm}$), 4: ($z = 75\,\text{mm}, r = 7.5\,\text{mm}$), and 5: ($z = 75\,\text{mm}, r = 15\,\text{mm}$). Again the mean deviation at the surface is about four times as large as at an internal measuring point. A similar result is seen at the center of the specimen (positions 6, 7, and 8), Fig. 6.3c. There is only a small temperature difference in radial direction (in particular between $r = 7.5\,\text{mm}$ and $r = 15\,\text{mm}$) and there are significant deviations at the surface temperature between different measurements.

The temperature in axial direction varies strongly due to the local heating process. During the free cooling this imbalance is compensated by heat diffusion within the specimen and heat exchange with its surroundings. The mean temperature evolution at the four different locations in axial direction is plotted in Fig. 6.3d.

In addition to the measurement with thermocouples, the temperature field of the surface is recorded with thermal imaging, Fig. 6.4. The images show a pronounced temper-

(a) 0 s (b) 10 s (c) 20 s (d) 60 s (e) 120 s (f) 180 s
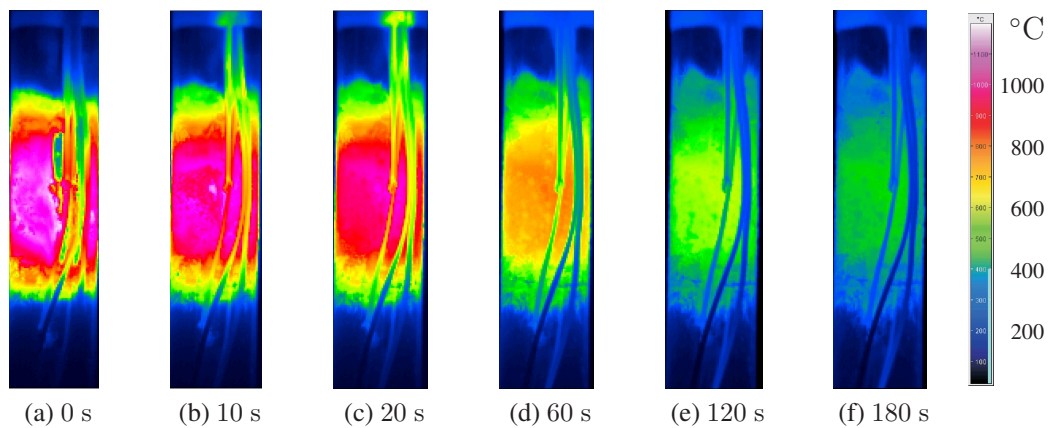
Figure 6.4.: Thermal images

ature gradient at the beginning of the cooling process ($t = 0$ s). This gradient is reduced quickly during the first seconds. Already at $t = 60$ s a smooth temperature distribution is seen. At large times ($t > 180$ s) this temperature distribution tends to a homogeneous state.

6.1.2. Numerical Simulation

For the numerical simulation a finite element model is set up. The model in Fig. 6.5a consists of the steel specimen, the clamping, and some part of the transfer unit. The dimensions of the geometry are given in Fig. 6.5a and Fig. 6.5b. Due to the symmetry
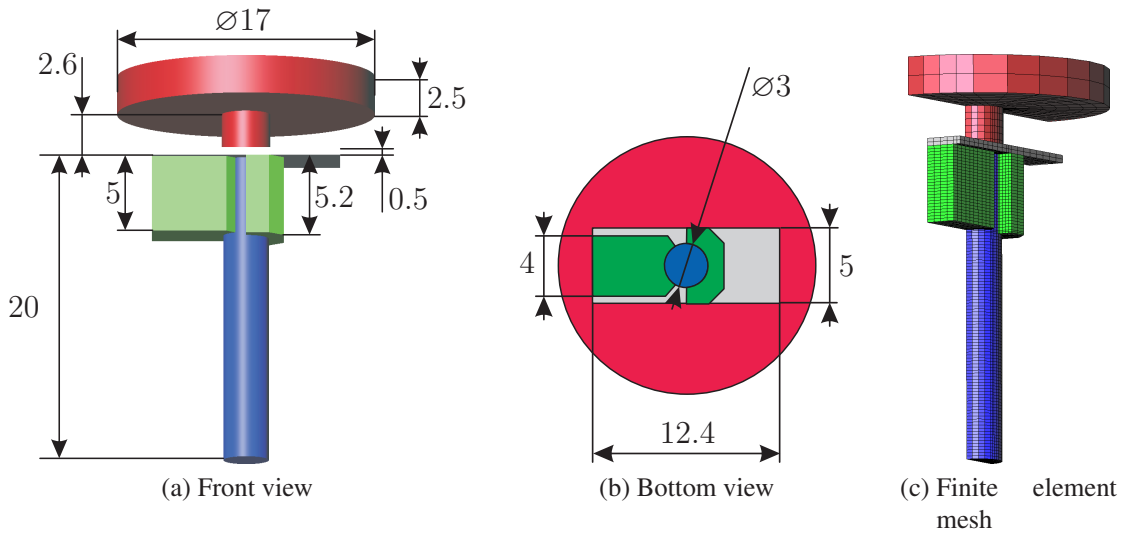
Figure 6.5.: Model of cooling experiment (dimensions in cm), the heat flux q is specified throughout the surface

of the geometry, the initial conditions, and the boundary conditions, it is sufficient to use only half of the setup in the computation, Fig. 6.5c. The geometry is approximated with finite elements. For the volume a total of 24102 eight-noded (linear) hexahedral elements are used. At the outer surface, the specimen can exchange thermal energy with its surrounding by free convection and heat radiation. This heat flow is taken account of by surface elements.[2] Here 3592 four-noded quadrilateral elements, which coincide with the surfaces of the corresponding hexahedral elements, are used. The complete model has a total of 27809 nodes which equals the number of unknown temperatures (no temperatures are prescribed at the boundary).

The problem setup is completed by an initial temperature distribution. To this end, the experimental data (see Fig. 6.3) at $t = 0$ s are used. In supplemental heating experiments the initial temperature is measured at two additional positions, 9: ($z = 62.5$ mm, $r = 15$ mm) and 10: ($z = 87.5$ mm, $r = 15$ mm). All points are fitted using biharmonic spline interpolation, [Sandwell, 1987]. The resulting initial temperature distribution is depicted in Fig. 6.6, where black spheres indicate the measured data points. To keep the temperature at the ends of the specimen at a constant level (and to prevent an unphysical temperature decrease) additional data points are specified at the ends. These points are indicated by gray spheres in Fig. 6.6a. Furthermore a symmetric temperature distribution with respect to reflection is assumed, the plane of symmetry being the cross section at the center of the specimen. Since the high temperature is concentrated at the center of the specimen this assumption holds at the beginning of the process. At later stages an asymmetry is suspected due to the clamping. The symmetric temperature profile at $r = 0$ mm is visualized in the Fig. 6.6b, where the measured data points (at several

---

[2]All surface integrals are evaluated within special elements. This has the advantage that within the volume elements no check for boundary conditions is necessary, which speeds up the computation. Of course, this does not change the result nor the number of unknowns.

(a) Temperature distribution over radius and axial direction
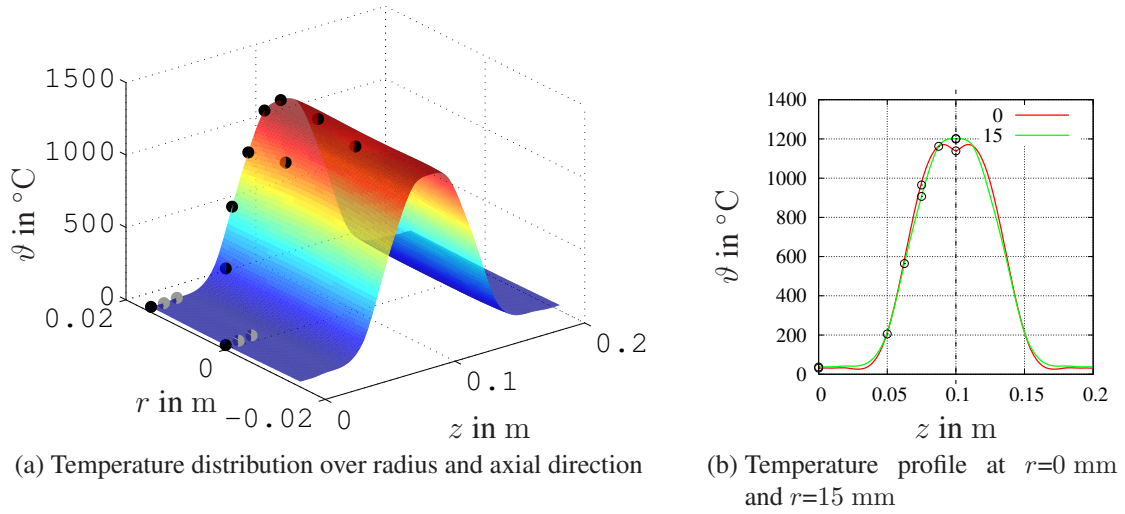
(b) Temperature profile at r=0 mm and r=15 mm

Figure 6.6.: Initial temperature distribution

different radii) are given by circles.

Neumann boundary conditions are specified throughout the surface. At the outer boundary the same conditions are specified for the transfer unit, the clamping and the specimen. Different combinations of heat transfer due to free convection and heat radiation are studied in the following. At the symmetry plane (internal boundary) a zero heat flux is prescribed.

In every technical solid surface microscopic and macroscopic irregularities are present which influence the thermal contact conductance. This phenomenon also occurs at the clamping, where a perfect contact is assumed in the model. The actual area of contact for most metallic surfaces is only about 1 to 2%, even at relatively high contact pressures of the order of 10 MPa, cf. [Madhusudana, 1996]. To accurately model the resistance induced by the imperfect contact additional experiments according to the lines in [Madhusudana, 1996, p. 67] are required.

6.1.3. Simulation Results using Different Models

First of all the validity of the proposed numerical procedure and the influence of model parameters are of interest. For this task, a series of four models, cf. Tab. 6.1, is set up and the resulting temperature evolutions are compared with the experimental data. In particular the influence of the thermophysical material parameters is studied. In the investigations the model predictions using a constant heat conductivity $\lambda_0 = 35$ W/(m K) and a constant heat capacity $c_{d0} = 600$ J/(kg K) are compared with the predictions using the temperature-dependent relations (4.78) and (4.76). For the mass density a value of $\varrho = 7815$ kg/m^3 is used throughout. Additionally, the effect of heat exchange with the surroundings is important. In this case, the value of the emissivity ϵ and the heat transfer coefficient h_c are varied. For the emissivity the temperature-dependent function (4.77) is used.

Table 6.1.: Sets of model parameters

set no.	λ W/(m K)	c_{d} J/(kg K)	h W/(m^2 K)	ϵ 1
1	λ_0	$c_{\mathrm{d}0}$	0	0
2	λ_0	$c_{\mathrm{d}0}$	$h_{\mathrm{c}0}$	0
3	$\lambda(\theta)$	$c_{\mathrm{d}}(\theta)$	$h_{\mathrm{c}0}$	0
4	$\lambda(\theta)$	$c_{\mathrm{d}}(\theta)$	$h_{\mathrm{c}0}$	$\epsilon(\theta)$

The heat transfer coefficient h_{c} is the only parameter for which there is no experimental data at hand. In the case of free convection h_{c} is typically in the range of 2 to 25 W/(m^2 K), cf. [Incropera et al., 2007, p. 8]. For special cases the heat transfer coefficient can be determined analytically using boundary layer theory, see for example [Schlichting and Gersten, 2006] and [Kays et al., 2005]. Assuming a constant temperature in axial direction the relations yield a value of $h_{\mathrm{c}} \approx 12$ W/(m^2 K), see App. A.6.

The analytical relations were experimentally investigated in [Popiel and Wojtkowiak, 2004] and [Popiel et al., 2007]. On the one hand the analytical relations could be confirmed by the experiments, but on the other hand a high sensitivity of the results was observed. In fact the experimenters had to close and seal all windows, doors, and ventilation ducts of the laboratory and additionally encase the specimen in a mosquito net housing. Such precautions are not taken in the present experiments. Thus, an increased heat transfer coefficient is expected. Small unpredictable air movements, which can not be avoided in an open production environment, are furthermore likely to be the reason for the large temperature deviations seen at the circumference ($r = 15$ mm) in Fig. 6.3. In the computations a constant value $h_{\mathrm{c}0} = 35$ W/(m^2 K) is compared with absent convective heat transfer ($h_{\mathrm{c}} = 0$ W/(m^2 K)).

Fig. 6.7 shows the resulting temperature evolutions for the models of Tab. 6.1 at different positions in axial direction. Simulation results are given by solid lines, while the mean of the measurements are indicated by crosses and the deviation from the mean is given by the gray surfaces. Values underneath the surface are chosen, if available, due to the higher accuracy of the measurements and to reduce the influence of the surface conditions. All models (set 1 through 4) are capable of capturing the qualitative behavior of the temperature evolution. Only the temperature at the free end of the specimen ($z = 0$ mm) is not well predicted by any model. The reason for this deviation might be the complex flow field and the resulting cooling condition at that point.

Neglecting the convective heat transfer (set 1) results in an overestimation of the temperatures. The temperature dependence of the material properties has only a minor influence on the result (compare set 2 and set 3). Using both, temperature-dependent material properties as well as convective heat and radiative heat transfer (set 4) leads to the best correlation between the experimental and numerical data.
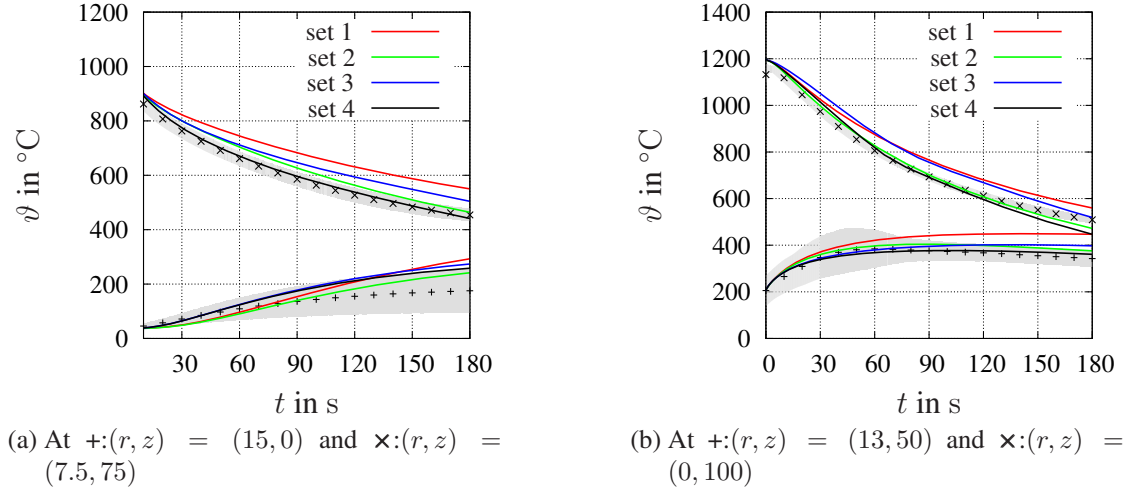
(a) At $+$:$(r, z) = (15, 0)$ and $\times$:$(r, z) = (7.5, 75)$

(b) At $+$:$(r, z) = (13, 50)$ and $\times$:$(r, z) = (0, 100)$

Figure 6.7.: Measured and computed temperature evolution for different models

6.1.4. Properties of Numerical Methods

The subject of this investigation are the actual rate of convergence and the computation time of high-order time integration methods. Here, the DIRK methods of Chp. 5.5 with an order between one and four are applied to the model, which includes convective heat transfer and nonlinear heat conductivity, heat capacity, and emissivity (set 4 of Tab. 6.1). The numerical solution is compared with a reference solution, thus defining the relative error

$$\text{rel err}_{\Theta} := \max_{n} \frac{\|\boldsymbol{\theta}_n - \boldsymbol{\theta}_n^{\text{ref}}\|}{\|\boldsymbol{\theta}_n^{\text{ref}}\|}. \tag{6.1}$$

It is the maximum of the relative deviation over all time steps $t_n \in [0\,\text{s}, 160\,\text{s}]$. Due to the lack of an analytical solution, the reference solution has to be computed numerically as well. For this purpose the fourth order method of Hairer et al. [2000] with a time step size of $h = 0.1\,\text{s}$ is used.

In Fig. 6.8a the relative error is plotted versus the constant time step size h. The slope of the curves represent the rate of convergence. The dashed lines indicate the theoretical orders one through four. Given are the results of the classical backward Euler method (BE, $p = 1$), the second order method of Ellsiepen [1999] (El), the third order method of Alexander [1977] (Alex), and the fourth order method of Hairer et al. [2000] (Hairer). All methods achieve their theoretical orders, only the fourth order method of Hairer stays below its expected order.

Of practical importance is not only the rate of convergence, but above all the computational costs of the methods. Fig. 6.8b shows the relative error in relation to the computation time. In this plot the third order method of Alexander shows the highest slope and is for high accuracy requirements most efficient. On the other hand the method

(a) Order of convergence
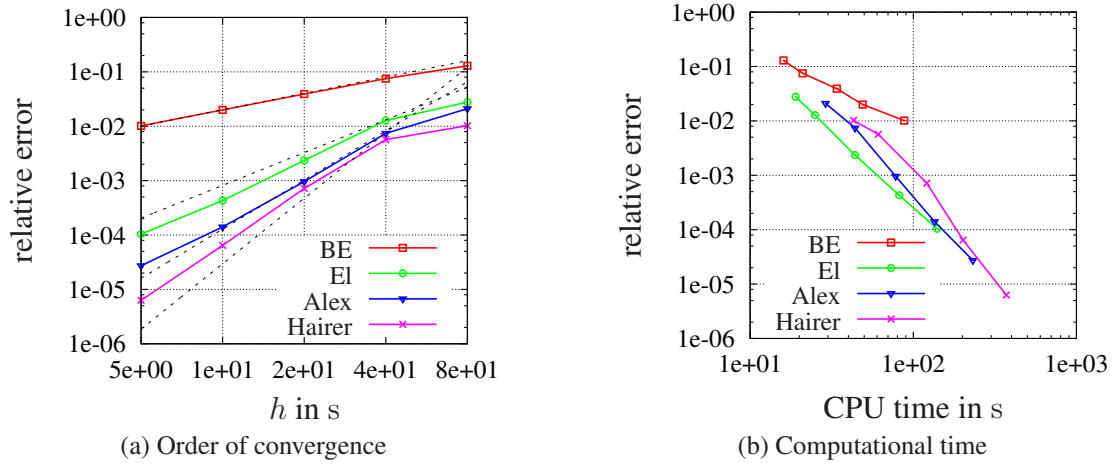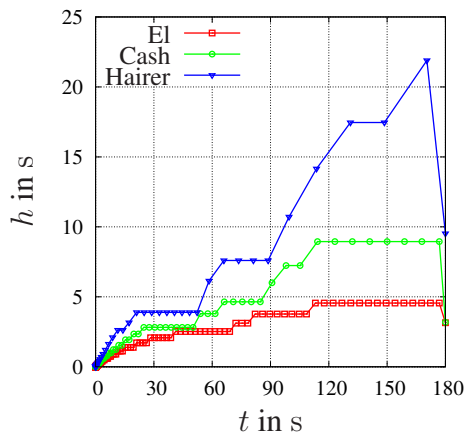

(b) Computational time

Figure 6.8.: Rate of convergence

of Ellsiepen is for a given error tolerance the fastest method in a large and practical important range. The backward Euler method gives even for high computation times only comparatively rough results.

A further gain of accuracy and a speed up of the computation can be achieved by using an adaptive time step. The error of the current time step is estimated by an embedded method as described in Chp. 5.5. This information is used to compute the size of the next time step.

The outlined procedure is applied to the complete cooling process with a duration of 180 s. Specified are a relative error tolerance $\varepsilon_r = 10^{-5}$ and an absolute error tolerance of $\varepsilon_a = 0.01$ °C. Fig. 6.9 shows the time step size versus the time for the three high-order methods of order $p = \{2, 3, 4\}$. The embedded method is one order smaller $(p-1)$ each,

Method	number of time steps	CPU time
Ellsiepen	107	242 s
Cash	78	277 s
Hairer	47	296 s

Figure 6.9.: Time step size behavior and computational costs

where the extension of Alexander's method to an embedded method is given in [Cash,

1979]. All tested methods perform a series of small time steps at the beginning of the process and increase the size gradually, while keeping the local error approximately constant.

6.2. Impact of Global System Solver on Overall Performance

At the center of all studied computations is the solution of a large sequence of linear systems. The size of the systems grows starting with the heat conduction problem, where each node has a single degree of freedom, and is biggest in the fully coupled problem. Here each node has four degrees of freedom, which leads to much larger systems with a more dense structure.

In the following, the application of direct and iterative solvers for the solution of the global system is studied in isothermal simulations. To also take into account the computational effort spend on local level different complexity levels of material models are considered. Two material models are used which span the room of realistic (practicable) complexity, for which the details are given in App. A.5.2. The first model describes finite strain viscoplasticity of metals and has been formulated for isothermal predictions of the steel 51CrV4, see [Hartmann et al., 2008a; Quint and Hartmann, 2007] and the literature cited therein. It is a fairly complex model with a relatively high local effort. The second model describes viscoplastic behavior in the small strain regime and has been developed for Polyoxymethylene (POM), according to [Hartmann, 2006b]. Its local solution can be obtained very efficiently.

6.2.1. Global and Local Computation Time

In the first example the influence of the discretization and the material model on the local, global, and total computation time is studied. See Tab. 5.2 in reference to operations performed on local and global level. This information is crucial because many algorithms, as e.g. the CMLNA, reduce the global computational cost at the expense of the local computational cost and vice versa.

A monotonous loading, Fig. 6.10a, of a plate with hole, Fig. 6.10b, is considered. Due to multiple symmetries only one eighth of the body needs to be considered. Note that the body and the boundary conditions are also symmetric in the thickness-direction. This setting serves as a benchmark problem to study various strategies in the following examples. Four different meshes with varying sizes are investigated, Fig. 6.11. The number of unknown displacements ranges from $n_{\mathrm{nu}} = 5006$ up to $n_{\mathrm{nu}} = 100520$ and the corresponding number of internal variables ranges from $n_{\mathrm{q}} = 126720$ up to $n_{\mathrm{q}} = 2965248$. For the time integration the method of Ellsiepen is used throughout (see Tab. A.5 on p. 190), which is of second order and has two stages.
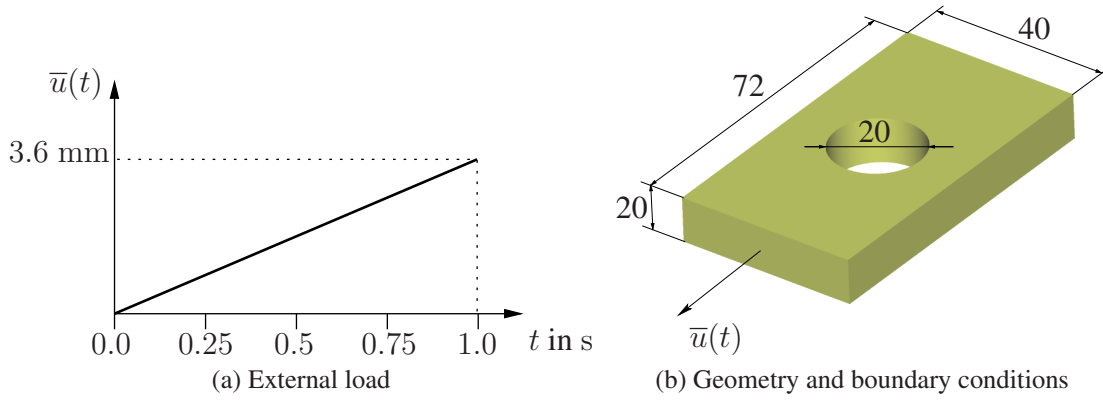
164

(a) External load

(b) Geometry and boundary conditions

Figure 6.10.: Boundary conditions of the plate with hole

(a) $n_{el} = 1320$, $n_{nu} = 5006$, $n_q = 126720$

(b) $n_{el} = 6144$, $n_{nu} = 21055$, $n_q = 589824$

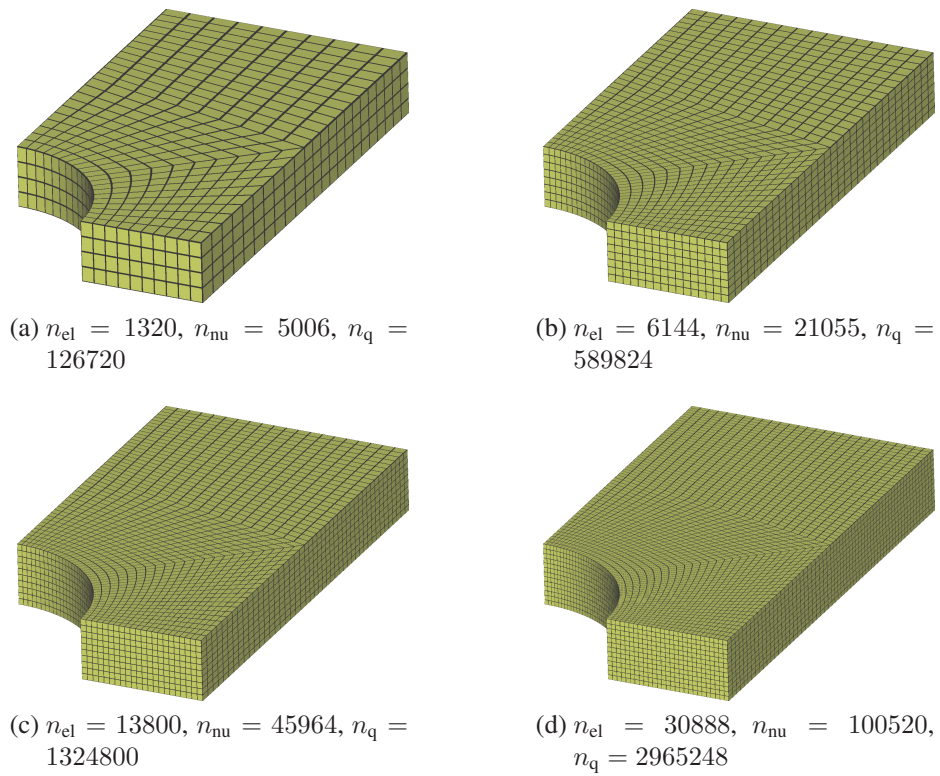(c) $n_{el} = 13800$, $n_{nu} = 45964$, $n_q = 1324800$

(d) $n_{el} = 30888$, $n_{nu} = 100520$, $n_q = 2965248$

Figure 6.11.: 3D meshes of plate with a hole

The local integration step (5.130) is very cheap for the POM-model (only function evaluations, see [Hartmann, 2006b]) and expensive in the case of the metal plasticity model, where local iterations have to be performed (see [Hartmann et al., 2008a]). The corresponding computation times are given in Fig. 6.12. Displayed is the normalized CPU time over the number of unknown displacements n_{nu}. For the polymer POM the local computation time, see equations (5.149) and (5.153), increases linearly with the number of unknowns but the global computation time grows more rapidly and outweights the local computation time, Fig. 6.12a. For the large strain metal plasticity model the local computation time increases also linearly. But in this case it is larger than the global computation time of equation (5.148) and dominates the total effort, Fig. 6.12b. Reducing the global computation cost has only a minor effect in this case. In a fully coupled scenario with a simplified and efficiently solved material model (such as the one developed in Chp. 4.3) the portion of the global system of the total computation cost is relatively high. Thus, the computational time distribution of the POM model resembles this situation more closely than that of the complex model.
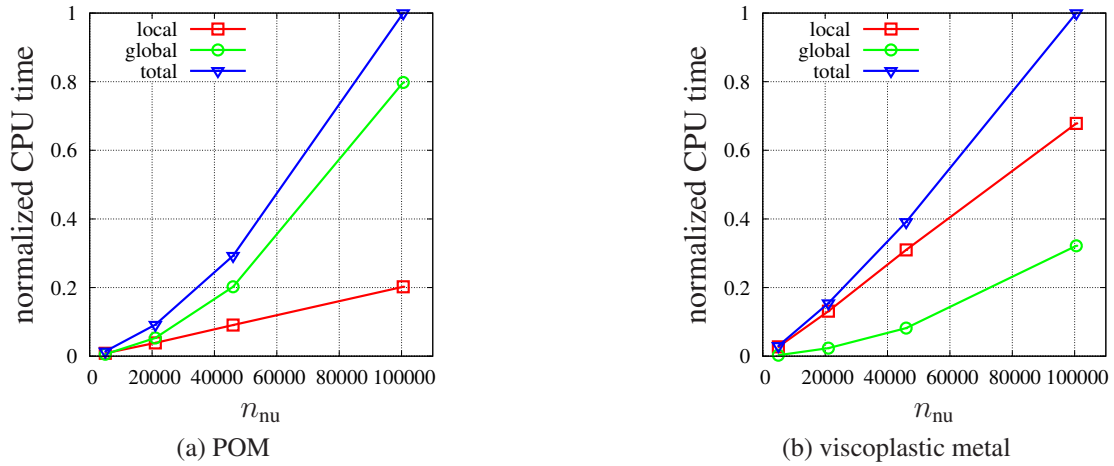
Figure 6.12.: Global/ Local computation times

6.2.2. Adaptive Stopping Tolerance for Iterative Solvers

In this subsection the usage of the adaptive stopping tolerance for the iterative solver is investigated (here ILUT-preconditioning for each linear system is used). As mentioned in Chp. 5.7.3, at the beginning of the Multilevel-Newton iteration the solution of the linear system of equations is not required to be very accurate, but the accuracy has to increase when coming closer to the sought-after solution. Here, the viscoplasticity model of POM is used, see App. A.5.1. The total time is decomposed into eleven time steps consisting of two time stages each (integration with the method of Ellsiepen).

As initial value for the stopping tolerance, $\varepsilon_{\text{max}} = 10^{-3}$ in equation (5.209) proved its worth. Using the value $\varepsilon_{\text{max}} = 0.25$ or even $\varepsilon_{\text{max}} = 0.5$ as suggested in [Kelley, 1995] led to more global iterations at the beginning of the Newton process and thus spoiled the savings of the iterative solver. The second parameter, which serves to compute a measure of the degree to which the nonlinear iteration approximates the solution, is set to $\gamma = 0.9$.

Again monotonous loading, Fig. 6.10a, is applied to the plate with a hole, Fig. 6.11d, having $n_{\text{nu}} = 100520$ unknown displacement degrees of freedom. In Fig. 6.13a the stopping tolerance ε is given over the Newton-iteration number. In the standard method the

(a) Stopping tolerance
    (b) Iterations to solve linear system
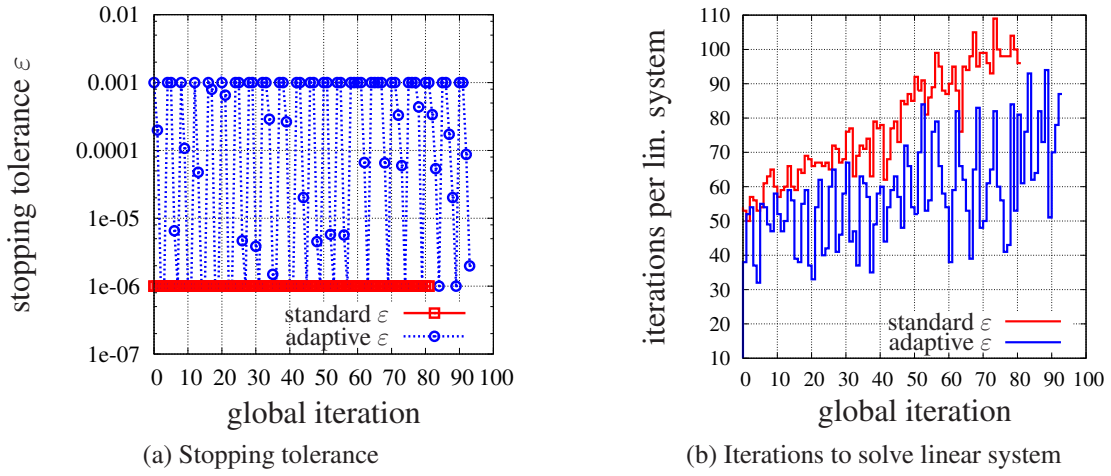
Figure 6.13.: Use of adaptive stopping tolerance for iterative solver for linear system of equations

stopping tolerance is fixed to $\varepsilon = 10^{-6}$. When using the adaptive stopping tolerance the initial value is $\varepsilon = 10^{-3}$. This value is used for the first Newton iteration. Then the stopping tolerance is reduced reaching eventually $\varepsilon = 10^{-6}$. After the fourth MLNA-iteration the solution of the nonlinear system is found and time is advanced to the next time stage yielding a new nonlinear system of equations. The stopping tolerance is reset to $\varepsilon = 10^{-3}$ and the process starts again. The reason for using an adaptive stopping tolerance is to reduce the number of iterations of the Krylov solver per Newton iteration. This number is displayed over the Newton-iteration number in Fig. 6.13b. Using the adaptive stopping tolerance reduces the number of iterations of the linear solver, particularly, at the beginning of each Newton-process. It can also be seen from the graph that the total number of Newton-iterations increases slightly when the adaptive stopping tolerance is used. Here, the standard (constant) stopping tolerance led to a total of 82 Newton iterations while the adaptive stopping tolerance needed 94 iterations. On the other hand the number of iterations of the BiCGSTAB solver was reduced from 6350 (standard) to 5384 (adaptive), even though more linear systems had to be solved. Comparing the computation times, the total saving when using the adaptive stopping tolerance is in this

example about 14%. The application of the adaptive stopping tolerance in the case of the finite strain viscoplasticity model of Appendix A.5.2 does not show any advantages, because the increase of global Newton-iteration steps is computational very costly due to the expensive computation of the tangential stiffness matrix (coefficient matrix) in equation (5.148).

6.2.3. Preconditioning Strategies

The computation of the preconditioner for the iterative solver can consume a significant amount of the total solution time of the linear system. As pointed out in Chp. 5.7.4 it is not necessary to recompute the preconditioner for every system but the preconditioner can be kept constant during the Newton-process or even over some time interval of the time integration.

In all computations the ILUT (incomplete LU-decomposition with dual-threshold strategy, see [Saad, 1994a]) is used as preconditioner. Gauss-Seidel and SSOR preconditioners (see e.g. [Großmann and Roos, 2005, p. 505ff.]) have proved too weak for the problems at hand in terms of convergence (they led to ten respectively five times more BiCGSTAB-iterations than using the ILUT preconditioner). Therefore, despite the negligible costs to compute these preconditioners, they were not considered in the following. To determine the parameters lfil (level of fill-in) and droptol (dropping tolerance) a pretest is performed with the BiCGSTAB solver on an example linear system. This system comes from the first Newton-step within the solution of the monotonous loading of the plate with hole (material model POM and $n_{\text{nu}} = 100520$ unknown displacement degrees of freedom). In Fig. 6.14 the computation time is given over the dropping tolerance for four different numbers of fill-in. The total computation time to solve the linear
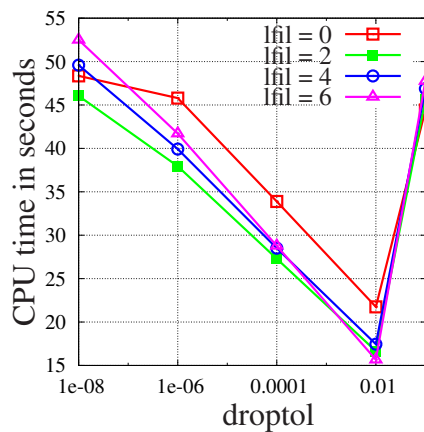
(a) Total computation time (ILUT & BiCGSTAB)
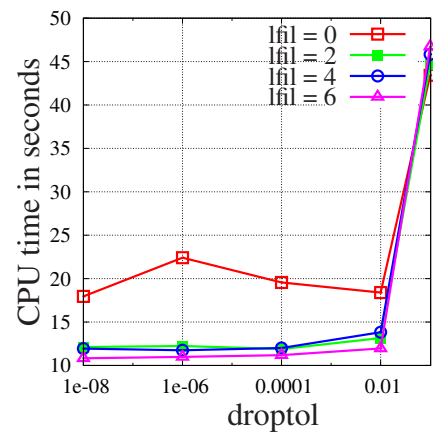
(b) Computation time of iterative solver

Figure 6.14.: Influence of droptol and lfil on computation times

system, consisting of a preconditioner computation plus a BiCGSTAB run, is plotted in Fig. 6.14a. The plot indicates that the level of fill-in has a minor influence and suggests using a rather rough dropping tolerance. In Fig. 6.14b only the computation time of the iterative solver is considered. This plot shows that the computation time decreases with smaller drop tolerances and reaches a minimum at about droptol $= 10^{-4}$. On the other hand the computation time rises quickly for a drop tolerance greater than 10^{-2}. Since the preconditioner is to be reused and to stay away from the large increase of computation time, the parameters lfil=6 and droptol=10^{-4} are chosen. Note that Figures 6.14a and 6.14b indicate that the „classical" ILU(0) decomposition, with parameters lfil=0 and droptol=0, is not efficient and that it is necessary to consider more sophisticated ILU-decompositions for satisfactory convergence speed. For completeness, the computational costs of the preconditioner and the iterative solver in dependence of the number of unknowns are given in Fig. 6.15a. Again the computation time of a single system coming from a Newton-step as described above is considered (now for the four different meshes of Fig. 6.11).

Next, results with periodic preconditioner recomputation with two different periods are presented: recomputation for every system, and utilizing a constant preconditioner. The number of iterations needed to solve each linear system ($n_{\mathrm{nu}} = 100520$) within the Multilevel-Newton iteration is displayed for two different periods in Fig. 6.15b. When

(a) Computational costs of iterative solver and preconditioner
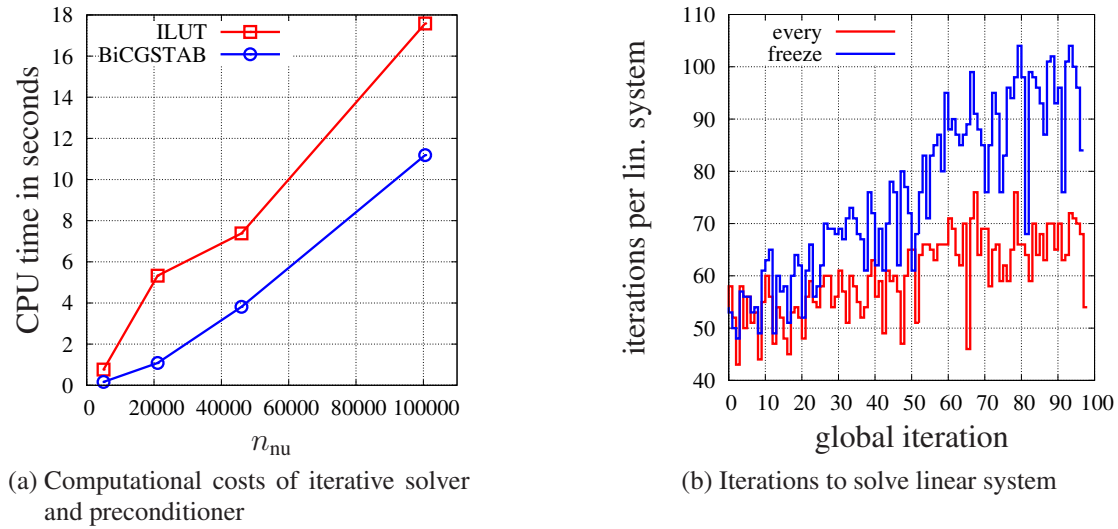
(b) Iterations to solve linear system

Figure 6.15.: Comparison of recomputation strategies of the preconditioner

working with the constant preconditioner, i.e. computing the preconditioner only once at the beginning of the simulation, the number of Krylov subspace iterations increases with time and the algorithm can even break down. Nevertheless more than half of the total computation time is saved. Recomputing the preconditioner every fortieth system yields a comparable number of iterations as when recomputing the preconditioner for

every system. This strategy saves 58% of the total computation time. In other words, the recycled preconditioner is as powerful as the preconditioner from scratch during the MLNA iterations and is insensitive to several time-steps. This makes additional updating of the recycled preconditioner, using additional techniques, unnecessary. The application of the preconditioner periodic recycling technique is possible for the finite strain viscoplasticity model as well. However, in this case, where on Gauss-point level 12 equations with 12 unknowns have to be computed, the reduction of the computational costs does not lead to an essential improvement since the local computation dominates the problem.

6.2.4. Comparison of Direct and Iterative Solver

Finally, the performances of direct and iterative solvers for sparse linear systems are compared for the plate with hole of Fig. 6.10b described with the material model of POM and subjected to the loading of Fig. 6.10a. The computation times are given for two direct solvers, UMFPACK 5.03 and PARDISO 3.2, and for the iterative solvers BiCGSTAB and restarted GMRES (both are modified versions from Youcef Saad's Sparskit2). For the BiCGSTAB and the GMRES solvers the incomplete LU factorization with threshold and parameters as described in Sect. 6.2.3 are used. The restart parameter of the GMRES solver is set to ten. To obtain high performance for the iterative solvers the preconditioner is computed periodically with a period of 40 linear systems and the adaptive stopping criteria is used with the parameters $\gamma = 0.9$, $\varepsilon_{\max} = 10^{-3}$, and $\varepsilon_{\min} = 10^{-6}$. Similarly, the user-specific parameters in the direct solver packages where tuned to obtain optimal performance. As can be seen from the graphs of Fig. 6.16, the

(a) Computation time to solve linear systems
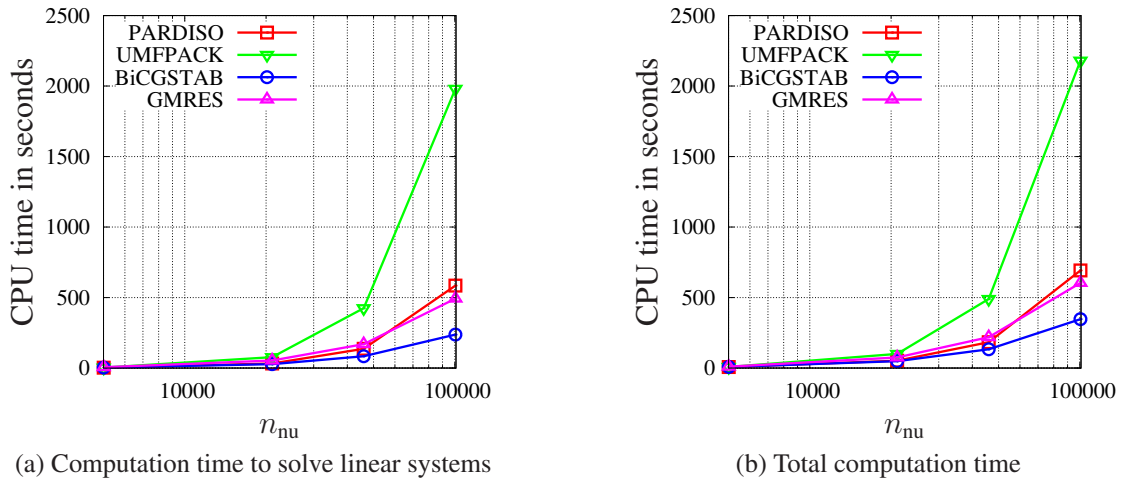
(b) Total computation time

Figure 6.16.: Comparison of direct and iterative solvers

iterative solvers outperform the direct ones when solving large systems. In particular,

the BiCGSTAB solver performs very well and is superior as soon as systems have more than about 20000 unknowns. For GMRES the superiority comes somewhat later, but still the slope of the curve for GMRES is clearly less steep than for the LU-packages. Note that the condition numbers (in the 1-norm) of the initial linear systems of the considered sequences are already of the order 10^5; this does not seem to have a negative influence on the performance of the iterative solvers.

6.2.5. Chord-MLNA

Another way to speed up the computation with direct solvers is to use the CMLNA, see p. 146 for details. In this case the global iteration matrix is assembled only once and kept constant during the iteration. Thus, a single LU-decomposition according to equation (5.205) at the beginning of the iteration is sufficient. This dramatically reduces the cost of a single iteration but is usually at the expense of the rate of convergence. Again the largest system of the plate with hole (material model POM and $n_{nu} = 100520$ unknown displacement degrees of freedom) is considered. According to Fig. 6.17a the rate of convergence drops to first order for the CMLNA. Hence, the CMLNA needs

(a) Convergence of MLNAs
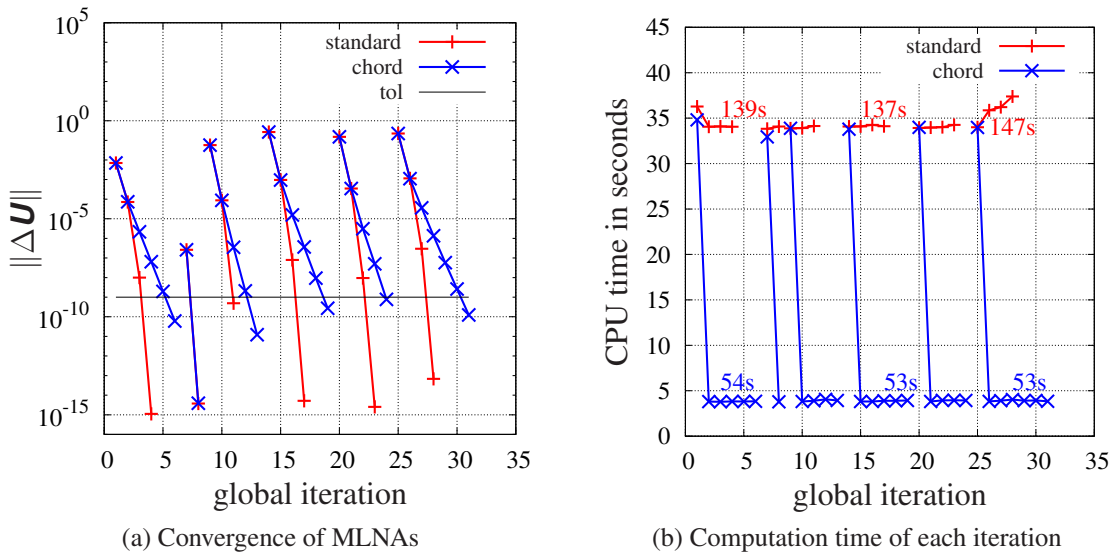
(b) Computation time of each iteration

Figure 6.17.: MLNA and CMLNA

more iterations. At the first stage it needs six instead of four global iterations, where the largest differences are at the end of the iteration process. At the second stage there is no difference because the initial value is so close to the solution that both methods converge with only a single global step. Looking at the computation time of the global iterations in Fig. 6.17b one can see that a single global iteration of the chord method (including the local iterations at each integration point) takes only about one seventh of the exact MLNA. Even though the CMLNA has only first order convergence rate and needs more

iterations, it computes the solution faster. The total computation times of the single time step are indicated in Fig. 6.17b as well. In the studied example a time step with the exact MLNA takes about two and a half times as much computation time as the CMLNA. In the case of the fully coupled setting the influence can be expected to be even higher due to the increased computational effort of the global solver.

6.3. Thermomechanical Forming Process

Finally, the first part of the new thermomechanical metal forming process of Chp. 1.1 is considered. The fully coupled process starts with inductive heating as shown in Fig. 1.1a. Subsequent to the electro-pneumatic transfer to the forming die, the workpiece is compressed in axial direction. The final step of closed die forming is not considered in the following.

6.3.1. Induction Heating

Induction or electromagnetic heating is based on energy absorption from an alternating magnetic field generated by an inductor. Variations of the magnetic field with time cause

(a) Current distribution $I(x)$
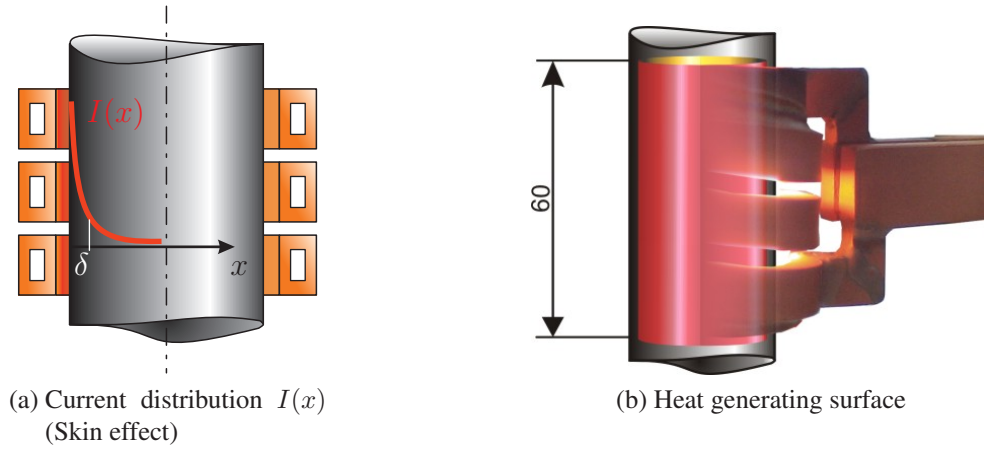   (Skin effect)

(b) Heat generating surface

Figure 6.18.: Modeling of heat generation due to induction heating

eddy currents within the workpiece which result in a heat up. The process is determined by a characteristic length δ, sometimes referred to as penetration depth of the eddy currents, which is given by

$$\delta = \sqrt{\frac{\rho}{\pi f \mu_r \mu_0}}. \tag{6.2}$$

Here ρ is the electrical resistivity of the material, f the frequency of the induction facility, $\mu_0 = 4\pi \times 10^{-7}$ N/A^2 the permeability of vacuum (magnetic constant), and μ_r is

the relative permeability of the material. The characteristic length on the one hand describes the current distribution in the workpiece and on the other hand gives a measure to distinguish between low and high frequency induction. In the case of planar bodies the induced current and power density depend exponentially on δ. A similar relation (involving Bessel's functions) can be found for cylinders, cf. [Nemkov, 2009, p. 436]. If the characteristic dimensions (e.g. cylinder diameter) of the workpiece are larger than 4δ, one speaks of high frequency induction. This is also the case for the considered workpiece and the applied frequency $f = 15$ kHz, which is used in the following. In the case of high frequencies, all electromagnetic processes take place in a thin skin layer of the part. In Fig. 6.18a a schematic plot of the distribution of the eddy current $I(x)$ versus the depth x is shown. At room temperature the relative permeability and electric resistivity of the material are $\mu_r(20\,^\circ\text{C}) \approx 600$ and $\rho(20\,^\circ\text{C}) \approx 0.2 \times 10^{-6}$ Ωm, respectively. This results in a penetration depth of $\delta(20\,^\circ\text{C}) \approx 0.075$ mm. With rising temperature the penetration depth increases and reaches at the maximum temperature a value of $\delta(1200\,^\circ\text{C}) \approx 5.2$ mm. To model this heat supply, the heat flux is prescribed at an imaginary surface, see Fig. 6.18b and 6.19a.[3] This heat generation surface is lo-

(a) Heat generation surface   (b) Heat transfer surface   (c) Mesh   (d) Mechanical BC
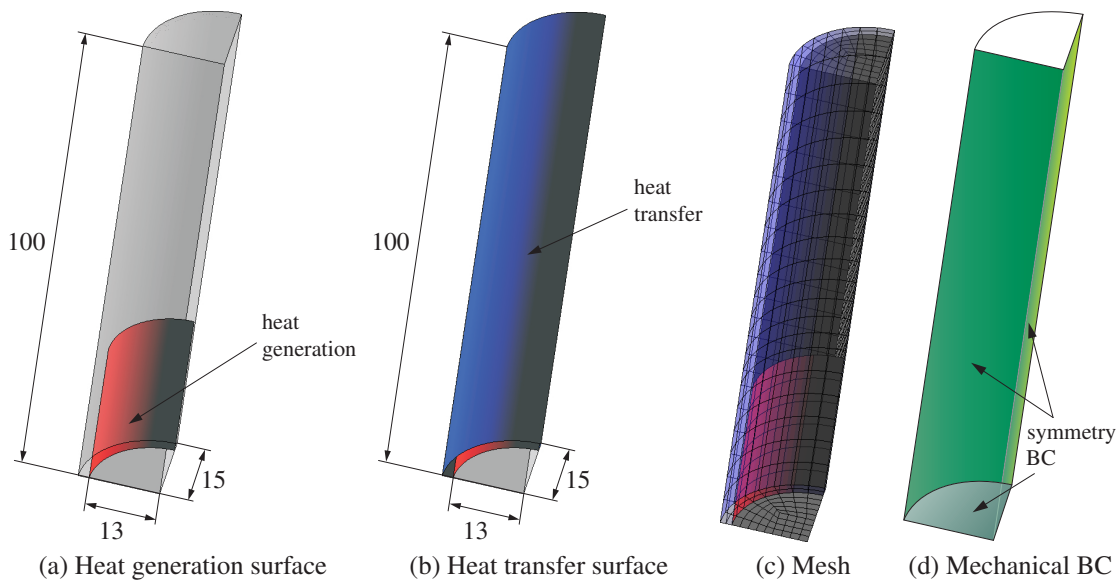
Figure 6.19.: Model of one eighth of the workpiece

cated 2 mm beneath the surface of the workpiece. To further account for heat transfer with the surrounding, a heat transfer boundary condition is specified at the outer surface, Fig. 6.19b. Due to the multiple symmetries it is sufficient to model only on eight of the workpiece to reduce the amount of computational effort.

---

[3]Another, even more realistic, approach to model the heat supply is to specify a volumetrically distributed heat source with depth-dependent magnitude. Of course, simulating the complete electromagnetic field and its influence on the workpiece would be most accurate.

The same induction facility as in Chp. 6.1.1 is used and the induction heating is applied in two stages, as already described. In the first stage (main heating) the workpiece is heated with a power of $P_1 = 42$ kW for $t_1 = 12$ s. In the second stage (homogenization) the power is reduced to $P_2 = 15$ kW and applied for $t_2 = 5$ s. Using these values directly and taking account of the size of the heat generation surface would result in too high temperatures. Consequently, the prescribed heat flux of the model has been reduced

(a) Prescribed heat flux
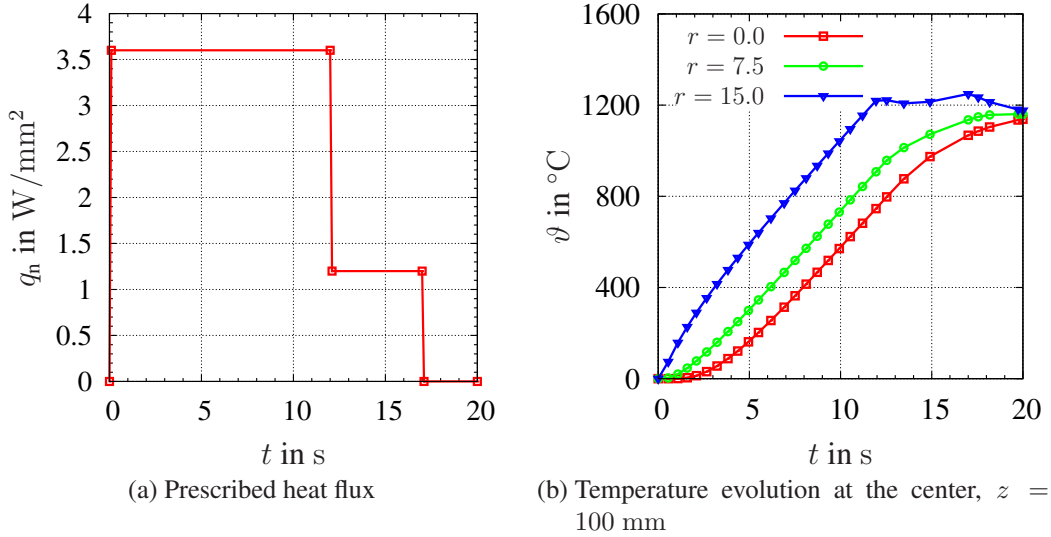
(b) Temperature evolution at the center, $z = 100$ mm

Figure 6.20.: Prescribed heat flux and resulting temperature evolution

to approximately 50% of the theoretical value to incorporate various power losses of the induction facility and the power transfer to the workpiece. The prescribed heat flux is shown in Fig. 6.20a, where both heating stages and the abrupt change between them are clearly visible. At $t = 17$ s the induction heating is finished and the workpiece is transported to and positioned in a forging die for the subsequent mechanical treatment. The transport is accounted by a cooling simulation without external heat supply, similar to Sec. 6.1.2.

The temperature evolution caused by the electrical heat induction is shown for three different points in Fig. 6.20b. All three points are located at the center of the workpiece and distributed over the radius. The temperature rises fastest at the surface ($r = 15$) and reaches a maximum temperature of $\theta = 1249$ °C at $t = 17$ s. Following this trend are the temperature evolutions of the other two points. Their temperature rises are slightly delayed, not as rapid as the one at the surface, and smoothed due to the parabolic character of the underlying differential equation.

The temperature field is obtained by a finite element computation with the mesh of Fig. 6.19c. The mesh consists of $n_{el} = 1584$ twenty-seven-noded (quadratic) hexaderal elements and $n_{el} = 240$ nine-noded (quadratic) quadrilateral surface elements which account for the heat transfer with the surrounding and the heat supply due to the heating.

The complete model has a total of $n_{\mathrm{nod}} = 7617$ nodes with up to four unknowns each (depending on the prescribed boundary condition of the specific node). This results in a total number of $n_{\mathrm{n}} = 28388$ unknown primary variables and $n_{\mathrm{q}} = 228096$ internal variables.

The preliminary investigations of the pure cooling problem (refer to Chp. 6.1.3) show that the temperature dependence of the thermal material parameters has only a negligible influence on the temperature evolution and distribution. Thus, the parameters of set number 2 of Tab. 6.1 on p. 161 (which result in a good correlation with experimental results) are chosen for simplicity.

Fig. 6.21 shows the complete temperature distribution at different times. The heat is induced at the outer surface of the middle section and flows in radial and axial direction. There is a strong temperature gradient in radial direction at early times of the first heat-

(a) Middle of first heating, $t = 5$ s (b) End of first heating, $t = 12$ s (c) End of second heating, $t = 17$ s (d) Begin of compression, $t = 20$ s
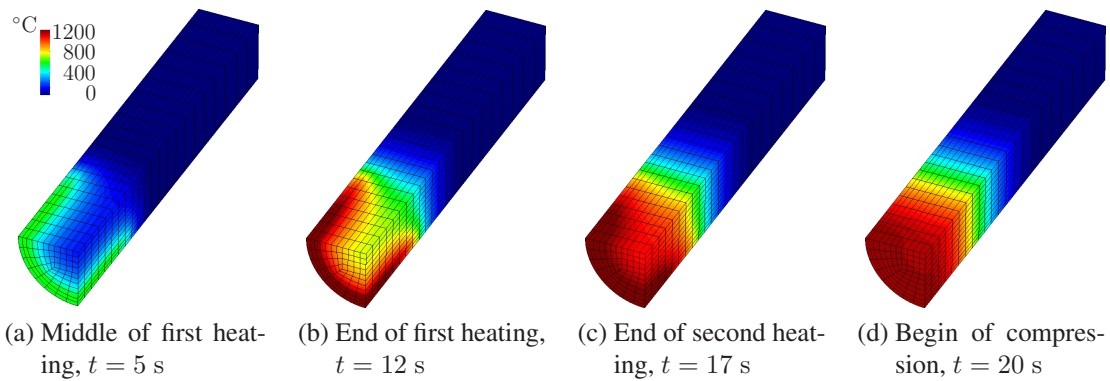
Figure 6.21.: Temperature distribution at different times during heating stages

ing stage. This strong imbalance alleviates with time. At the end of the second heating stage (homogenization stage) and in particular after the transport only a small temperature variation over the radius remains. Nevertheless, in axial direction the temperature gradient is still clearly visible and plays a crucial role in the following compression.

Induced by the temperature field, a displacement field emanates from the thermomechanical coupling. The resulting displacement field at the end of the transport is depicted in Fig. 6.22a. At the center of the workpiece there is no displacement due to the symmetry of the setup. Additionally, the displacement in axial and radial direction of two points are plotted in Fig. 6.22b. The coordinates of points 2 and 8 correspond to the positions of thermocouples in Fig. 6.1 on p. 155. Point 8 moves only in radial direction (which corresponds to the x-direction) and the main movement of point 2 is in axial direction (z-direction). Again, the effect of the two heating stages and the transport is visible. At the top surface (point 2) there is hardly any change, while point 8 contracts slightly. The heat flows from the middle region of high temperature to the cooler regions of the workpiece. Consequently, the middle of the workpiece cools down a little which causes thermal contraction. The heat distribution does not, however, have any influence

175

(a) Displacement field at begin of compression, $t = 20$ s

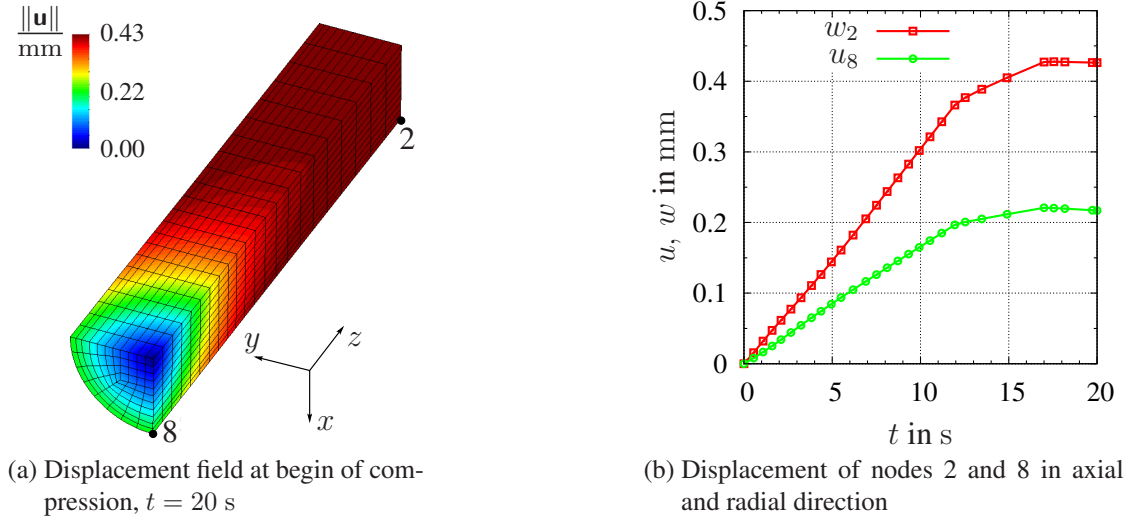(b) Displacement of nodes 2 and 8 in axial and radial direction

Figure 6.22.: Displacement field during heating and homogenization stages

on the axial displacement of the top surface, since for the material the coefficient of linear thermal expansion $\alpha = 1.2 \times 10^{-5}$ $1/°C$ is assumed to be constant.

6.3.2. Axial Compression

Following the heating process and transport, the workpiece is compressed in axial direction. To model this forming process, the same finite element model as already in the previous section is used. At the cross-sectional areas symmetry boundary conditions are prescribed. These boundary conditions and the mesh are illustrated in Fig. 6.23. For the

(a) Mechanical symmetry boundary conditions and prescribed compression of top surface

(b) Thermal symmetry boundary conditions and heat transfer of outer surfaces
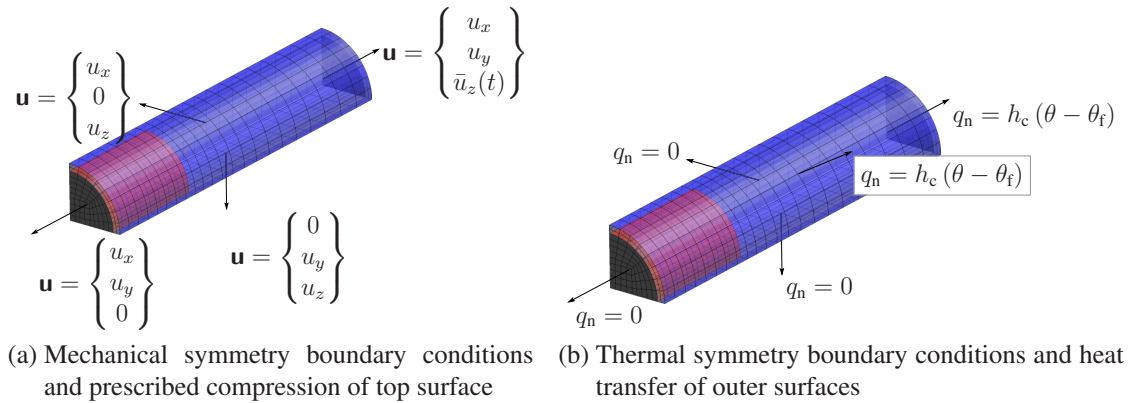
Figure 6.23.: Mechanical and thermal boundary conditions during compression

top surface the displacement in axial direction $\bar{u}_z(t)$ is prescribed. At $t = 20$ s the axial displacement is positive ($\bar{u}_z(20\text{ s}) \approx 0.4457$ mm) due to the thermal expansion during

the previous heating process, see also Fig. 6.22b. Within the following two seconds, the top surface is compressed up to a value of $\bar{u}_z(22\,\mathrm{s}) = -10\,\mathrm{mm}$, which corresponds to a compression of about 10% of the initial length.[4] The movement of the top surface in radial direction is not constrained at all. The material parameters describing the mechanical behavior correspond to the identified values in Tab. 4.1 on page p. 73.

The mechanical stresses caused by thermal expansion and external displacement loads lead to plastic deformations of the material. The zones of plastic behavior are shown in red in Fig. 6.24. Interestingly, already at the beginning of the heating process ($t =$
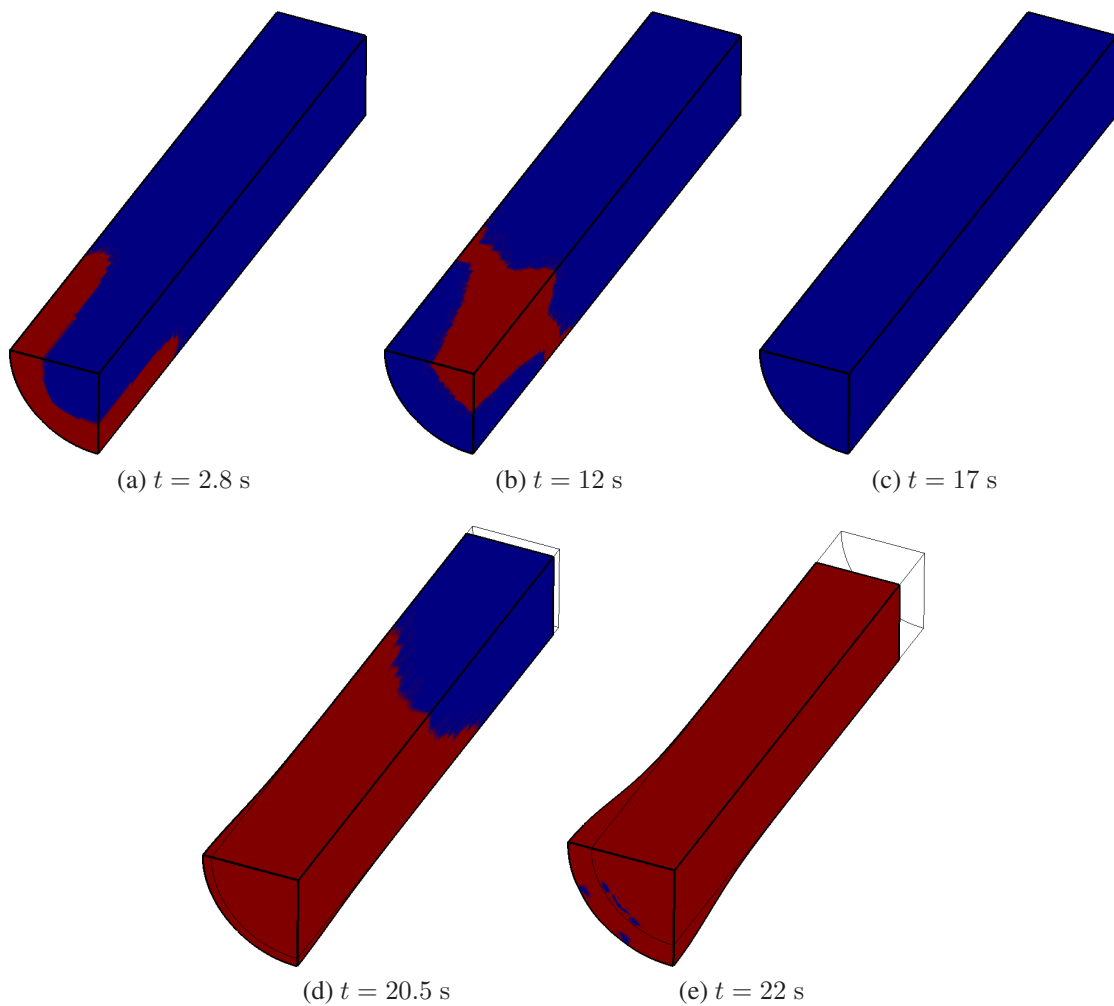

(a) $t = 2.8$ s (b) $t = 12$ s (c) $t = 17$ s

(d) $t = 20.5$ s (e) $t = 22$ s

Figure 6.24.: Evolution of plastic zones (red) during heating and compression

$2.8\,\mathrm{s}$), the metal reacts plastically in the hollow cylinder of heated material. The elevated

---

[4]The closed die forming stage, where the workpiece comes into contact with the forming die and is given its final shape, is not considered here.

temperature lowers the yield stress according to equation (4.72) and leads to thermal expansion and distortion within that region. See also Fig. 4.7b on p. 73, which shows the temperature dependence of the initial yield stress. At later times of the heating stage ($t = 12$ s), the thermal expansion of the outer material leads to higher stress in the center of the workpiece and causes there plastic yielding. However, the plastic strains caused during the induction heating are only of the scale $\|\mathbf{C}_i - \mathbf{1}\| \approx 0.01$. This is small compared to the values $\|\mathbf{C}_i - \mathbf{1}\| \approx 0.45$ which are reached at the center during the compression phase. During the second heating stage (homogenization) and the transport ($t = 17$ s), the thermal imbalance levels out. Even though there are still relatively large thermal displacements there is no distortion of the material and thus no plastic deformation. Of course this changes drastically in the following compression. In the compression phase ($t = 20.5$ s) the stress is initially homogeneously distributed, but the material at the center of the workpiece is at the highest temperature. Thus plastic yielding starts in this region and causes the workpiece to buckle. The plastic region gradually advances to the top of the workpiece until all material deforms plastically ($t = 22$ s), while the largest plastic deformations occur at the center of the workpiece.

The complete process including inductive heat up and mechanical compression is computed using the second order accurate method of Ellsiepen, see Chp. 5.5.3 and App. A.2 for details. The time integration is done in combination with the adaptive time step size control of Chp. 5.5.4. For each time step the errors of the primary and internal variables are estimated, where different tolerances are specified for each quantity. For the nodal displacements the absolute error $\varepsilon_a^u = 0.1$ mm and the relative error tolerance $\varepsilon_r^u = 10^{-3}$ are used. For the nodal temperatures and the internal variables the tolerances $\varepsilon_a^\theta = 1\ ^\circ\mathrm{C}$, $\varepsilon_r^\theta = 10^{-3}$, $\varepsilon_a^q = 10^{-4}$, and $\varepsilon_r^q = 10^{-2}$ are employed, respectively. Fig. 6.25 shows the time step size, which is computed by the controller, versus time. Additionally, rejected time steps are indicated by a cross. The specified initial step size
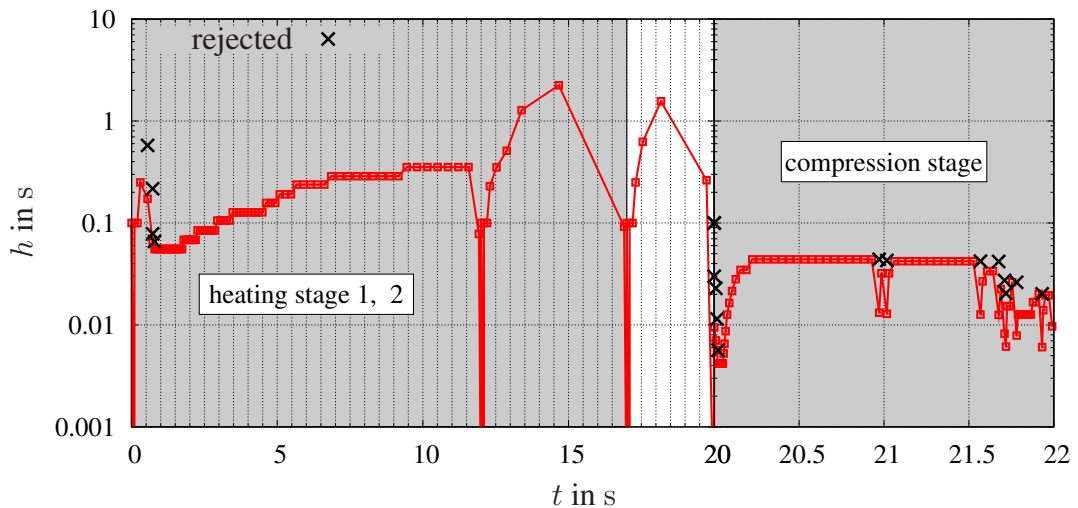

Figure 6.25.: Time step size behavior - rejected time step sizes indicated by ×

is $h = 0.1$ s. This step size is reduced to $h = 0.001$ s for the very first time step of each interval (to initialize the Newton extrapolator, as will be explained in the following) and then restored to its initial value for the second step. At the beginning of the first heating process the integration error is governed by the error of the nodal temperatures. This error is relatively small. Thus, the time integration could proceed with rather large steps. However, the heating leads to plastic behavior of the metal, as seen in Fig. 6.24a. This leads to high integration errors of the internal variables and results in rejected time steps at $t = 0.55$ s and $t \approx 0.72$ s. Thus, the step size is reduced and gradually increases during the heating process due to a more evenly distributed temperature field. At the begin of the second heating stage and the transport phase the time step size is reduced to its initial value by default. During these two phases there are none or only small plastic deformations. Hence, the time step size is rapidly increased up to a maximum of $h \approx 2.24$ s leading to very fast computations. With the start of the compression the behavior changes dramatically. The external loads lead to increased stresses, large deformations, and high plastic rates. This causes in particular at the interval start several time step rejections and small time steps. Over the course of the last integration interval there are only small variations of the step size. This has to do with the chosen factors of the step size controller ($f_{\min} = 0.3$, $f_{\max} = 2.5$, $f_{\text{safety}} = 0.85$, refer to p. 126) and is absolutely intended since it is advantageous for the Newton process.

The computational efficiency of the overall scheme is not only determined by the feasible time step size, but to a large degree also by the solution of the nonlinear systems, which arise during the integration process. To this end, the Multilevel-Newton algorithm (see Chp. 5.6.2) is employed. On local level, i.e. integration point level, a classical damped Newton-Raphson method is used. The functional matrix is recomputed and factorized for each iteration, since the local system is of low dimension. In the present case seven simultaneous equations have to be solved at each point. The iterative process requires in most cases only three to five iterations to reach the prescribed convergence criterion $\|\Delta\mathbf{q}\| \leq 1 \times 10^{-10}$. Here, the tolerance is fixed and stricter than the one used on the global level.[5]

On the global level a combination of relative and absolute tolerances based on the initial iterates are used in the previous simulations. Both, the norm of the residual $\|\boldsymbol{G}(\boldsymbol{V}, \boldsymbol{Q})\|$ and the correction of the primary variables $\|\Delta\boldsymbol{V}\|$ with $\boldsymbol{V}^{\mathrm{T}} = \{\boldsymbol{U}^{\mathrm{T}}, \boldsymbol{\Theta}^{\mathrm{T}}\}$ are monitored. Details are given in criterion 7 on p. 191 in App. A.3.

To study the performance of different versions of the solver for the linear system, the simple criterion $\|\Delta\boldsymbol{V}\| \leq \text{tol}_{\boldsymbol{V}}$ is used, with $\text{tol}_{\boldsymbol{V}} = 1 \times 10^{-7}$. The results of the direct solver PARDISO are given in Fig. 6.26. Displayed is the global correction $\|\Delta\boldsymbol{V}\|$ versus the iteration number for three successive time steps, which consist of two stages each (method of Ellsiepen). Thus, the solution sequence of totally six global nonlinear

---

[5] Another possibility is to use an adaptive tolerance for the local Newton method, which is based on the global iteration state, see criterion 4 on p. 191. However, the investigations in [Quint, 2004] show that this can have a negative effect on the global iteration and thus, increase the total effort. The adaptive criterion is not further considered here.
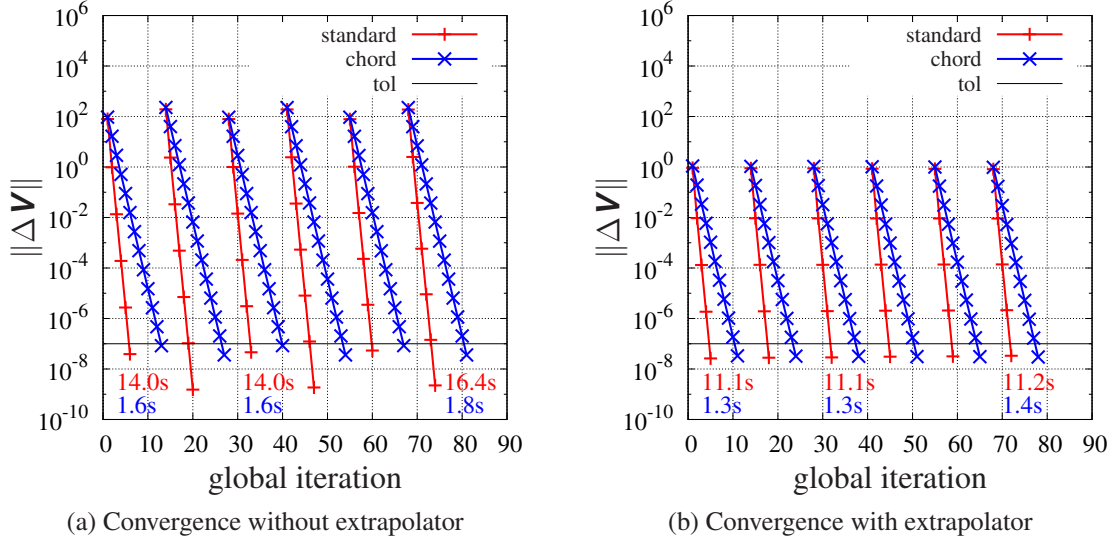
(a) Convergence without extrapolator

(b) Convergence with extrapolator

Figure 6.26.: Convergence and efficiency of different versions of MLNA

systems is considered. The tolerance of the convergence criterion tol_V is indicated by a horizontal line and the total computation times for the nonlinear system are indicated.

In Fig. 6.26a the second order rate of convergence of the standard-MLNA (red curve) is clearly visible. The algorithm reaches the prescribed tolerance within six to seven iterations. For each iteration, the global functional matrix according to equation (5.151) has to be evaluated and factorized. The chord-MLNA tries to avoid this burden as much as possible, at the expense of its rate of convergence. Here, the functional matrix is kept constant and set up only if the time step size changes or the rate of convergence degrades too much. In the considered example there is a total of 3327 iterations but only 148 LU factorizations are done by the CMLNA. Consequently, the rate of convergence drops to first order and the CMLNA (blue curve) needs more iterations. In the exemplary interval 13 to 14 iterations are typical. However, each single iteration is a lot cheaper than a single iteration of the standard-method. The gain is twofold, on the one hand the contributions to the functional matrix (element matrices) are not needed and on the other hand only back-substitutions have to be performed instead of a full LU factorization. Looking at the local effort, the chord method needs 15.7% (in the case of mostly elastic deformations) to 48.8% (mostly plastic deformations) of the CPU time of the standard-method. The gain related to the solution of the linear system has the largest impact and is approximately independent of the underlying system. Here, only 4% to 5% of the CPU time of the standard-method are consumed.

An additional acceleration can be achieved by the Newton extrapolator as described in Chp. 5.6.4. Its effect for the standard- and CMLNA is depicted in Fig. 6.26b. Both methods profit largely from the extrapolator, which improves the quality of the initial iterate. Thereby, it reduces the number of iterations by one to two for the standard-

method and two to three for the chord-method. Furthermore, it stabilizes the iteration process and allows larger time steps (which would be limited by the Newton process instead of the time integration, otherwise).

For large systems the difference between the chord- and standard-MLNA becomes even more pronounced. While the local effort grows linearly with the number of integration points (i.e. the number of elements), the solution effort of the linear system grows much faster. This is demonstrated using a very fine discretization of the workpiece, as shown in Fig. 6.27. In this case linear elements are used, which lead to a

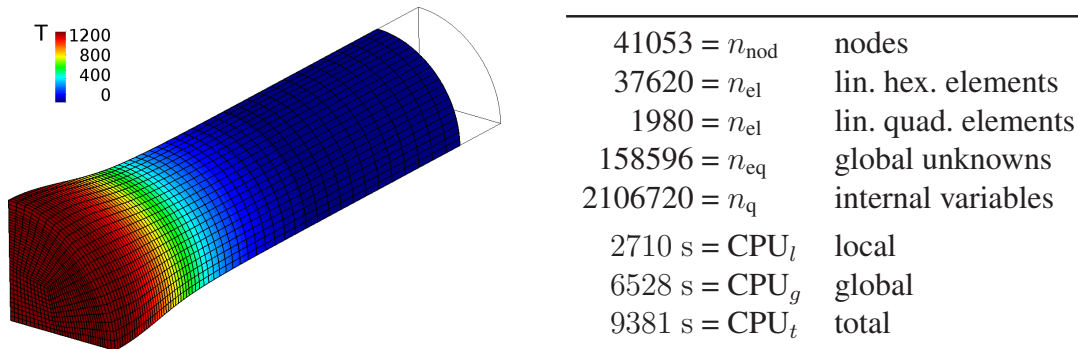|	
$41053 = n_{\mathrm{nod}}$	nodes
$37620 = n_{\mathrm{el}}$	lin. hex. elements
$1980 = n_{\mathrm{el}}$	lin. quad. elements
$158596 = n_{\mathrm{eq}}$	global unknowns
$2106720 = n_{\mathrm{q}}$	internal variables
$2710 \text{ s} = \mathrm{CPU}_l$	local
$6528 \text{ s} = \mathrm{CPU}_g$	global
$9381 \text{ s} = \mathrm{CPU}_t$	total

Figure 6.27.: Workpiece discretized with a fine mesh using linear elements and corresponding computation times of combined Ellsiepen-CMLNA approach

smaller bandwidth of the iteration matrix (see Fig. 5.19 on p. 148 and the remarks there) in comparison to higher order elements. The smaller bandwidth is accompanied by a lower number of nonzero entries in the sparsity pattern, thus consuming less memory, and allowing the solution of more global unknowns. For $n_{\mathrm{eq}} = 158596$ unknowns, back-substitutions need only about 1% of the computation time of the complete LU factorization. The combined approach of Newton extrapolator and CMLNA seems mandatory in this case.

Finally, all proposed acceleration techniques are compared to the standard approach. The comparison is done for the setup shown in Fig. 6.23 with two different prescribed displacements. In the first case a compression of $\bar{u}_z(22\,\text{s}) = -10$ mm is considered, which is also investigated in Fig. 6.24 and Fig. 6.25. In the second case a compression of $\bar{u}_z(22\,\text{s}) = -30$ mm is prescribed. The corresponding deformed configuration and temperature distribution is shown in Fig. 6.28a.

In the standard approach (Std.) the backward Euler method is used for time integration. It is combined with the standard-MLNA without extrapolator, Sec. 5.6.2. The time step is adjusted according to the number of Newton iterations. If the number exceeds a value of 15 or the algorithm does not find a solution the time step is reduced (multiplied by 0.3). If the number of Newton iterations is less than or equal to four the time step size is increased (multiplied by 1.2). In all other cases the time step size is kept constant. Parallelization is not exploited, thus only one processor is used.

(a) Compression of workpiece by prescribed $\bar{u}_z(22\,\mathrm{s}) = 30\,\mathrm{mm}$

(b) Comparison of CPU times (Opt. 1: CMLNA with Ellsiepen, Opt. 2: same as Opt. 1 but using efficient quadrature rule)
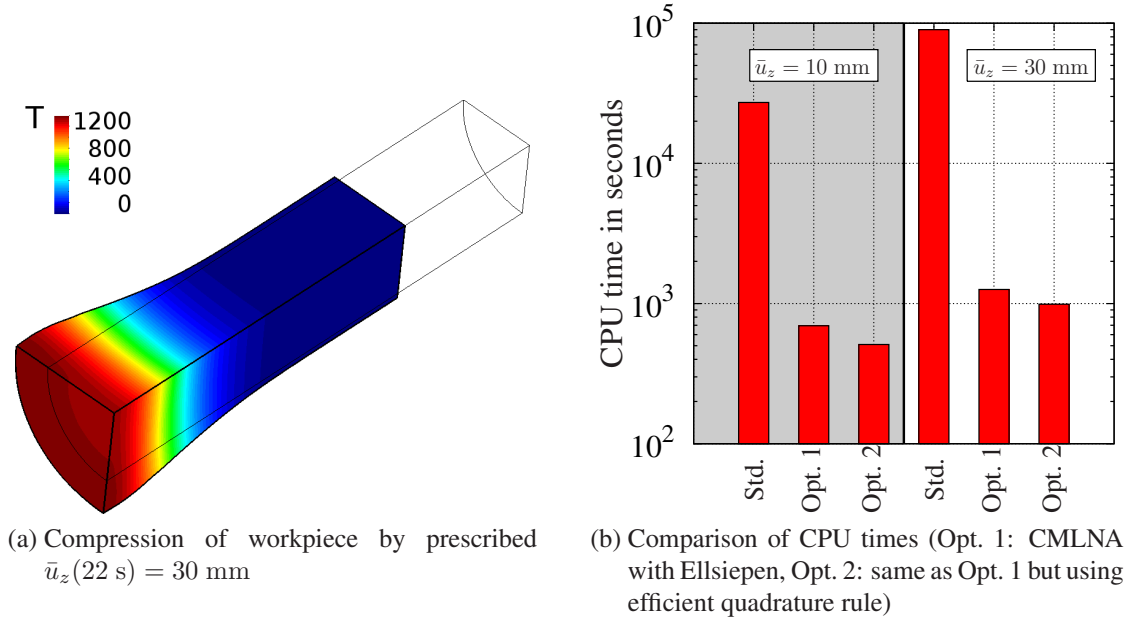
Figure 6.28.: Overall efficiency of the standard procedure in contrast to the optimized (adaptive) algorithms

The standard approach is contrasted with the optimized (adaptive) algorithms. Here, the second order accurate method of Ellsiepen is used for time integration in combination with the embedded adaptive step size control, see Sec. 5.5 and App. A.2. It is used with the CMLNA and uses the extrapolator for the global variables, both explained in Sec. 5.6.4 (Opt. 1). Furthermore, the influence of efficient quadrature rules is investigated (Opt. 2). Here the fourteen point rule of Stroud, given in Tab. A.1 on p. 187. Both optimized algorithms exploit parallelization and use four threads.

In Fig. 6.28b a large difference is seen between the standard and the optimized algorithms. The factor is for the smaller deformation ($\bar{u}_z(22\,\mathrm{s}) = -10\,\mathrm{mm}$) about 39.2 for Opt. 1 and 53.4 for Opt. 2, i.e. Opt. 1 needs about 2.5% of the CPU time of the standard procedure and Opt. 2 only 1.9%. In the case of the larger deformation ($\bar{u}_z(22\,\mathrm{s}) = -30\,\mathrm{mm}$) the difference is even more pronounced. Here Opt. 1 uses 1.9% and Opt. 2 uses 1.4% of the CPU time of the standard procedure. Computing a solution on a fine mesh such as the one depicted in Fig. 6.27 would not be feasible using the standard procedure.

7. Conclusions and Outlook

The purpose of this thesis is to further the understanding and prediction of advanced thermomechanically coupled forming processes. The project, which is the basis of this thesis is part of a twelve year joint research effort and has been developed during the first four years. Thus, it is not intended to answer all open questions yet.[1] The complexity and the strong interdependency of the studied processes demand an approach on the basis of computational science and engineering. Such a CSE-approach comprises a broad spectrum ranging from physical models to numerical algorithms and their implementation on current computer hardware. In this regard several open issues, which are relevant for the studied process, are identified and covered.

For the low alloy steel 51CrV4 the mechanical and thermal properties were not available. Thus, basic experiments are conducted that characterize some principle features. The mechanical behavior at room temperature is captured by various tensile tests in the small strain regime. The steel behaves symmetric in tension and compression and shows already at room temperature a small rate dependence. The specific heat capacity is determined by differential scanning calorimetry. The measurements show a strong jump around $700\,^\circ\mathrm{C}$ due to the Curie transition and metallic phase transformations. Additionally, the thermal conductivity and the emissivity of the steel are determined. The emissivity shows a similar irregularity around $800\,^\circ\mathrm{C}$. Additional experiments reveal that the abrupt change of the emissivity is permanent.

Material models with only a small number of temperature-dependent parameters are still considered to be state of the art in finite element analysis of engineering problems. However, it is known that in principle all parameters depend on temperature and that this dependence can be strongly nonlinear as seen in the presented experiments. In this work the temperature distribution within the workpiece and consequently the balance of energy play a crucial role. Accordingly, a material model for 51CrV4 based on the thermodynamic framework and the multiplicative decomposition of the deformation gradient is developed. It is an extension of the model proposed by Helm [2006], where a special focus is put on the mechanical heat dissipation in monotonous processes. Here, an alternative multiplicative decomposition of the deformation gradient into an elastic, a thermal, and a plastic part is chosen. The volumetric part of the free energy is of Neo-Hookean type and the dilatoric part follows the proposal in Hartmann and Neff [2003]. Furthermore, relevant material properties are modeled as temperature-dependent quantities. To allow a highly efficient computer implementation, the material equations are

---

[1]The author worked on the C1-project of the Transregional Collaborative Research Center SFB/TR
    TRR30 in Kassel.

simplified with the assumption of small elastic strains.

To investigate the thermo-physical behavior, the material model is used in cooling tests. The best correlation of the simulation and experimental data is achieved using temperature-dependent parameters. However, a fairly good agreement can also be obtained with constant material parameters and properly set boundary conditions. This can be of practical interest when no experimental data of thermo-physical properties is at hand and further leads to a linear model with considerably reduced computational effort.

An accurate prediction of the temperature distribution in time and space plays an important role in the studied processes. The local temperature evolution within the workpiece governs micro-structural solid state phase transformations and is therefore studied in detail. For the simulation of the temperature field a semi-discrete approach is used, consisting of a finite element approximation in space and a high-order Runge-Kutta integration in time. The proposed procedure has the main advantage that higher order rates of convergence in time can be achieved independently of the spatial approximation. The rate of convergence and the computational costs are investigated in an example and show that on the one hand the theoretical rates are indeed achieved. On the other hand the second order accurate method of Ellsiepen with time-adaptive step size control proves to be most efficient. The methods are in particular superior to the backward Euler method, which is widely used and recommended. Moreover, the embedded step size control of the high-order methods allows moreover to maintain a defined level of error at each time step.

Concerning the fully coupled thermomechanical problem, the vertical method of lines (semi-discrete approach) is applied using isoparametric finite elements for the spatial discretization. It is shown that this approach leads to a nonlinear differential-algebraic equation system, where the differential part stems from the evolution of the internal variables (describing viscous and plastic material effects) and the time-dependent temperature field. The algebraic part of the system comes from the quasistatic balance of linear momentum. The new point of view allows the consistent application of higher order time integration methods. To this end, adaptive high-order time integration is investigated, which is already known to be efficient for purely mechanical problems. Stiffly accurate diagonally implicit Runge-Kutta methods (SDIRK-methods) with step size control are applied, which also yield good results in the considered thermal problem. To account for the yield condition and to ensure objectivity, the time integration is performed in the reference configuration in combination with a return mapping consisting of an elastic predictor and a plastic corrector. In accordance with the results of quasistatic plasticity problems, an order reduction is seen for DIRK-methods. This prevents the achievement of higher orders than two. On the other hand, the method of Ellsiepen again proves to be most efficient and allows the application of an embedded error control. Contrary to popular myth (see for example [Jansohn, 1997, p. 2]), the results show that high-order methods are suitable for thermomechanically coupled problems, are more efficient than standard procedures, and allow an error control, respectively a time step adaptivity.

184

Due to the strong coupling of the intended application and to exploit the advantages of high-order accuracy and time-adaptivity a monolithic scheme is employed. This results in a large global system of equations, with an unsymmetric iteration matrix when Newton-type solution schemes are applied. To accelerate the solution process, several properties are taken advantage of. First of all, the convergence behavior (and thus, the required computational effort) of Newton-type iteration schemes depends on the quality of the initial iterate. In standard textbooks on nonlinear finite elements such as [Bathe, 1996], [Belytschko et al., 2004], and [Wriggers, 2009], the authors suggest to use the solution from the previous time step as starting point. They further point out that the lack of robustness of the Newton-procedure is the cause for major restrictions on the time-step size of implicit methods. To enhance the quality of the initial iterate a linear extrapolator is proposed. It uses the information from previous time stages of the DIRK-method to compute the new initial iterate. The extra effort is negligible since it requires only a fused multiply-add operation.[2] On the other hand it significantly improves the robustness of the Newton process allowing larger time steps (only limited by accuracy considerations of the time integration) and accelerates the iteration process. Doing so, the number of required iterations can be reduced by one third.

At the heart of the Newton process and thus, the numerical process as a whole, is the solution of the global linear system. Its solution can consume over 80% of the total computation time and its fast solution is compulsory. Looking at the complete sequence of linear systems emanating within implicit finite element analysis further aspects for an acceleration can be identified. When using iterative solvers a user-prescribed stopping tolerance has to be specified. Taking an adaptive tolerance (according to the state of the Newton convergence, i.e. low at the beginning and high at the end) can lead to savings of more than 14%. The main improvement is given by reducing the costs of the preconditioner. Although it is common to compute the preconditioner each time before the iterative solver is started, one can freeze the preconditioner for a large number of solution calls. It turns out that in some problems it is sufficient to compute the preconditioner only once at the very first time-step. Even if the preconditioner is computed for every fortieth call of the solver one can save an overall computational time of more than 50% in many applications.

When direct solvers are used for the linear system, a similar approach can be pursued. Bathe [1996] recommends to use the exact tangent stiffness matrix in order to profit from second order rate of convergence. However, this property is restricted to the vicinity of the exact solution, i.e. when the iterate is already sufficiently close to it. This is in particular not given at the beginning of the iteration process when using large time steps. Using instead the multilevel-Newton algorithm (MLNA) in combination with the chord-method, the exact tangent is computed only once. This spoils the second order rate of convergence, thus leading to more iterations, but reduces the total CPU time. In fact

---

[2]A fused multiply-add is a floating-point multiply-add operation performed in one step, with a single rounding. This is implemented inside many current microprocessors such as the Intel Itanium.

the exact MLNA takes two and a half times as much computation time as the Chord-MLNA. In the case of thermomechanically coupled simulations the difference is even bigger and for medium sized problems a factor of six to seven is not unusual. Of course, best would be to combine the advantages from both approaches. This could probably be done using Krylov-subspace recycling as described in [Parks et al., 2006]. Another interesting approach are matrix-free iterative methods along a similar line of thought. However, the determination of the necessary preconditioner is in this context still an open question and subject of current research.

To capture all important phenomena during the thermomechanical production process other issues should be considered in future work. First of all, thermomechanical experiments have to be conducted to determine the material properties at high temperatures. Most suitable for this purpose are compression tests with large deformations similar to the experiments done in [Brown et al., 1989]. With the experimental results at hand, the parameters of the presented material model can be determined without resorting to theoretical considerations. Furthermore, the material model has to be extended by phase transformations. This can be done along the lines of [Wolff et al., 2008], where phase fractions are proposed as additional internal variables with further evolution equations. This extension fits well with the overall structure of the proposed DIRK-MLNA approach. Preliminary studies in this direction have already been conducted with encouraging results.[3] Regarding the interaction of the workpiece and the work tool, thermomechanical contact has to be considered. The treatment of thermomechanical contact using finite elements is described for example in [Pantuso et al., 2000; Perić and Owen, 2004; Rieger and Wriggers, 2004], but has not been studied in connection with high-order time integration. Research in the fields of material testing, material modeling, and simulation is on going in various projects of the SFB/TR TRR30.

The scope of the thesis is restricted to the solid body and interactions with other bodies are included as boundary conditions. An exact determination of the thermal energy exchange of the workpiece with its surrounding environment by convection and radiation is still difficult and requires also further investigations. A promising approach is to use thermal fluid-structure interaction simulations. In this context, the author and collaborators extended the presented DIRK-approach to a two-dimensional coupled simulation of the workpiece and the surrounding air. Heat conduction within the workpiece is computed with the presented finite element approach using the in-house code Tasafem. The fluid flow around the workpiece is simulated with the finite volume program τ-code, see for example [Gerhold et al., 1997]. Both programs run on different machines and are coupled via the Component Template Library (CTL), refer to [Matthies et al., 2006]. It turns out, that the advantages already seen in the thermomechanical solid simulations are carried over to the thermally coupled FSI-problem. In future research, this approach should be validated in experiments and extended to complex three-dimensional settings.

---

[3]See the student reserach projects of Büchling [2010] and Rothe [2010], which were supervised by the author.

A. Appendix

A.1. Numerical Integration Formulas

In multidimensional cases Gaussian quadrature rules, obtained by applying the one-dimensional rule to each coordinate, are no longer optimal. So-called direct methods, constructed on the basis of three-dimensional monomials $\xi^a \eta^b \zeta^c$, are often more effective. In fact, the six-point (non-Gaussian) rule in Tab. A.1 with quadrature points on the faces of the biunit cube attains the same accuracy as the $2 \times 2 \times 2 = 8$ point Gaussian quadrature. Even higher is the difference in the case of the 13 and 14 point rules, which are developed in [Hammer and Stroud, 1958] and described in the FEM context in [Irons, 1971]. The 14 point rule is also given in Tab. A.1. In [Hellen, 1972] it is shown that these rules are of similar accuracy as the standard $3 \times 3 \times 3 = 27$ point rule for both very distorted and regular shaped serendipity elements with 20 nodes. A slightly less

Table A.1.: Coordinates and weights for integration on biunit cube

n_{ip}	order of accuracy	ξ_l	η_l	ζ_l	γ_l
4	2	0	$\pm\sqrt{2/3}$	$-1/\sqrt{3}$	2
		$\pm\sqrt{2/3}$	0	$1/\sqrt{3}$	2
6	3	± 1	0	0	$4/3$
		0	± 1	0	$4/3$
		0	0	± 1	$4/3$
6	3	$\sqrt{1/6}$	$\pm\sqrt{1/2}$	$-\sqrt{1/3}$	$4/3$
		$-\sqrt{1/6}$	$\pm\sqrt{1/2}$	$\sqrt{1/3}$	$4/3$
		$-\sqrt{2/3}$	0	$-\sqrt{1/3}$	$4/3$
		$\sqrt{2/3}$	0	$\sqrt{1/3}$	$4/3$
14	5	$\pm\sqrt{19/30}$	0	0	$320/361$
		0	$\pm\sqrt{19/30}$	0	$320/361$
		0	0	$\pm\sqrt{19/30}$	$320/361$
		$\pm\sqrt{19/33}$	$\pm\sqrt{19/33}$	$\pm\sqrt{19/33}$	$121/361$

accurate rule is derived in [Stroud, 1967] and given in Tab. A.2. Analytical expressions for the computation of more accurate representations are derived in [Peterson, 2009].

Table A.2.: Coordinates and weights for integration on biunit cube

n_{ip}	order of accuracy	ξ_l	η_l	ζ_l	γ_l
13	5	0	0	0	A
		$\pm\begin{pmatrix} a & b & b \end{pmatrix}$			B
		$\pm\begin{pmatrix} b & a & b \end{pmatrix}$			B
		$\pm\begin{pmatrix} b & b & a \end{pmatrix}$			B
		$\pm\begin{pmatrix} c & c & a \end{pmatrix}$			C
		$\pm\begin{pmatrix} c & d & c \end{pmatrix}$			C
		$\pm\begin{pmatrix} d & c & c \end{pmatrix}$			C

$$a = 8.80304406993097804773781820 98603\mathrm{E}{-}01$$
$$b = -4.95848171425711152814212423 642879\mathrm{E}{-}01$$
$$c = 7.95621422164095415429824825 675787\mathrm{E}{-}01$$
$$d = 2.52937117448425813473892559 293236\mathrm{E}{-}02$$
$$A = 1.68421052631578947368421052 631579\mathrm{E}{+}00$$
$$B = 5.44987351277567716846907821 808944\mathrm{E}{-}01$$
$$C = 5.07644227669791704205723757 138424\mathrm{E}{-}01$$

An overview on state of the art quadrature and cubature rules is given in [Cools, 2003]. The parameters of the methods can be retrieved as download from the authors website.

For the computation of mass matrices, the application of Lobatto integration, given in Tab. A.3, and their corresponding extension to the multidimensional case is sometimes advantageous. The formulas automatically lead to diagonal matrices and satisfy

Table A.3.: Coordinates and weights for Lobatto integration

n_{ip}	order of accuracy	ξ_l	γ_l
2	2	± 1	1
3	4	± 1	$1/3$
		0	$4/3$
4	6	± 1	$1/6$
		$\pm\sqrt{5}/5$	$5/6$

the discrete maximum dissipation principle, as shown in [Rank et al., 1983]. Thus, they are interesting for time dependent diffusion problems such as heat conduction. Another application is the solution of dynamic problems using the FEM in combination with explicit time integration methods. A (sparse) band structured mass matrix would prohibit the advantage of the explicit method.

There are also many integration rules for triangles and tetrahedra, see for example [Dhatt and Touzot, 1985, p. 258], [Hughes, 2000, p. 173], [Wriggers, 2009, p. 118 and p. 122] and the literature cited therein.

A.2. Butcher Tableaus of Runge-Kutta Methods

Implicit Runge-Kutta methods are given by the stages c_i, the weighting factors b_i, $i = 1, \ldots, s$, and the coefficient matrix a_{ij}. These parameters are written compactly in the form of Butcher arrays. In particular the structure (population) of the coefficient matrix $\mathbf{A} = [a_{ij}]$ has a strong influence on the methods stability characteristics and its computational effort. It can take on any of the forms given in Tab. A.4.

Table A.4.: General form of Butcher arrays

$$
\begin{array}{c|cccc}
c_1 & a_{11} & a_{12} & \ldots & a_{1s} \\
c_2 & a_{21} & a_{22} & \ldots & a_{2s} \\
\vdots & \vdots & \vdots & \ddots & \vdots \\
c_s & a_{s1} & a_{s2} & \ldots & a_{ss} \\
\hline
 & b_1 & b_2 & \ldots & b_s
\end{array}
\qquad
\begin{array}{c|cccc}
c_1 & a_{11} & & & \\
c_2 & a_{21} & a_{22} & & \\
\vdots & \vdots & \vdots & \ddots & \\
c_s & a_{s1} & a_{s2} & \ldots & a_{ss} \\
\hline
 & b_1 & b_2 & \ldots & b_s
\end{array}
\qquad
\begin{array}{c|cccc}
c_1 & \gamma & & & \\
c_2 & a_{21} & \gamma & & \\
\vdots & \vdots & \vdots & \ddots & \\
c_s & a_{s1} & a_{s2} & \ldots & \gamma \\
\hline
 & b_1 & b_2 & \ldots & b_s
\end{array}
$$

(a) Fully implicit Runge-Kutta methods (b) Diagonally implicit Runge-Kutta methods (c) Singly diagonally implicit Runge-Kutta methods

The most simple method within this class is the popular backward Euler method with the Butcher array

$$
\begin{array}{c|c}
1 & 1 \\
\hline
 & 1
\end{array}
\qquad
\boldsymbol{y}_{n+1} = \boldsymbol{y}_n + h_n \, \boldsymbol{f}\big(t_{n+1}, \boldsymbol{y}_{n+1}\big). \tag{A.1}
$$

In the literature, Runge-Kutta methods are often denoted by different names. The well known θ-method is given by

$$
\begin{array}{c|c}
\theta & \theta \\
\hline
 & 1
\end{array}
\qquad
\boldsymbol{y}_{n+1} = \boldsymbol{y}_n + h_n \, \boldsymbol{f}\big(t_n + \theta h_n \,, (1-\theta)\boldsymbol{y}_n + \theta \boldsymbol{y}_{n+1}\big). \tag{A.2}
$$

It includes the explicit Euler method ($\theta = 0$), the midpoint rule ($\theta = \frac{1}{2}$), and the backward Euler method ($\theta = 1$). Another example is the α-method, which is given by

$$
\begin{array}{c|cc}
0 & 0 & \\
1 & 1-\alpha & \alpha \\
\hline
 & 1-\alpha & \alpha
\end{array}
\qquad
\boldsymbol{y}_{n+1} = \boldsymbol{y}_n + h_n \big((1-\alpha)\boldsymbol{f}(t_n, \boldsymbol{y}_n) + \alpha \boldsymbol{f}(t_{n+1}, \boldsymbol{y}_{n+1})\big). \tag{A.3}
$$

Using the parameter $\alpha = 0$ and $\alpha = 1$, again leads to the forward and backward Euler method, respectively. The trapezoidal rule is attained for $\alpha = \frac{1}{2}$.

As pointed out in Chp. 5.5, diagonally implicit Runge-Kutta methods (DIRK) form a good compromise between stability and computational costs. The efficiency is further improved by using an embedded Runge-Kutta method of lower order to obtain an error estimate. Butcher arrays of the embedded DIRK methods, which are used in this work, are given in Tab. A.5. For each method, the number of stages s, the order of the main

Table A.5.: Butcher-arrays of embedded DIRK-methods

(a) Ellsiepen's method [Ellsiepen, 1999, p. 89] ($s = 2, p = 2, \hat{p} = 1$)

$$
\begin{array}{c|cc}
\alpha & \alpha & \\
1 & 1-\alpha & \alpha \\
\hline
 & 1-\alpha & \alpha \\
 & 1-\hat{\alpha} & \hat{\alpha}
\end{array}
\qquad \alpha = 1 - \tfrac{1}{2}\sqrt{2}, \qquad \hat{\alpha} = 2 - \tfrac{5}{4}\sqrt{2}
$$

(b) Combination of trapezoidal and backward Euler method ($s = 3, p = 2, \hat{p} = 1$)

$$
\begin{array}{c|ccc}
0 & 0 & & \\
1 & 0 & 1 & \\
1 & 0.5 & 0 & 0.5 \\
\hline
 & 0.5 & 0 & 0.5 \\
 & 0 & 1 & 0
\end{array}
$$

(c) Cash's method [Cash, 1979] ($s = 3, p = 3, \hat{p} = 2$)

$$
\begin{array}{c|ccc}
\gamma & \gamma & & \\
\delta & \tau - \gamma & \gamma & \\
1 & \alpha & \beta & \gamma \\
\hline
 & \alpha & \beta & \gamma \\
 & \hat{\alpha} & \hat{\beta} & 0
\end{array}
$$

$$
\begin{aligned}
\gamma &= 0.4358665215084580 \\
\tau - \gamma &= 0.2820667392457705 \\
\alpha &= 1.2084966491760101 \\
\beta &= -0.6443631706844691 \\
\delta &= 0.7179332607542295 \\
\hat{\alpha} &= 0.7726301276675511 \\
\hat{\beta} &= 0.2273698723324489
\end{aligned}
$$

(d) Hairer & Wanner's method [Hairer and Wanner, 2002] ($s = 5, p = 4, \hat{p} = 3$)

$$
\begin{array}{c|ccccc}
\frac{1}{4} & \frac{1}{4} & & & & \\
\frac{3}{4} & \frac{1}{2} & \frac{1}{4} & & & \\
\frac{11}{20} & \frac{17}{50} & -\frac{1}{25} & \frac{1}{4} & & \\
\frac{1}{2} & \frac{371}{1360} & -\frac{137}{2720} & \frac{15}{544} & \frac{1}{4} & \\
1 & \frac{25}{24} & -\frac{49}{48} & \frac{125}{16} & -\frac{85}{12} & \frac{1}{4} \\
\hline
 & \frac{25}{24} & -\frac{49}{48} & \frac{125}{16} & -\frac{85}{12} & \frac{1}{4} \\
 & \frac{59}{48} & -\frac{17}{96} & \frac{225}{32} & -\frac{85}{12} & 0
\end{array}
$$

method p, and the order of the embedded method $\hat{p}$ are specified.

A.3. Convergence Criteria of Global Newton Method

On the global level, the algebraic equation system (5.148) has to be solved, which reads in component form

$$G(V, Q) = \begin{Bmatrix} G_u(U, \Theta, Q) \\ G_\theta(U, \Theta, Q) \end{Bmatrix} = 0, \tag{A.4}$$

where the vector $V^{\mathrm{T}} := \{U^{\mathrm{T}}, \Theta^{\mathrm{T}}\}$ contains all global variables. In the special cases of purely mechanical and purely thermal problems, it is equal to the vector nodal displacements and nodal temperatures, respectively. To terminated the global Newton method, an appropriate convergence criterion has to be specified. Here, the user can choose from eight different criteria. These are listed in the following and include the classical criteria of the correction 1, the residual 2, and the combination of both 3.

1. Global correction based tolerance:
   $\|\Delta V\| \leq \mathrm{tol}_V$

2. Residual based tolerance:
   $\|G(V, Q)\| \leq \mathrm{tol}_G$

3. Combination of global correction and residual based tolerances:
   $\|\Delta V\| \leq \mathrm{tol}_V$, and $\|G(V, Q)\| \leq \mathrm{tol}_G$

4. Variable local tolerance, depending on the global convergence:
   $\|\Delta V\| \leq \mathrm{tol}_V$,
   set tolerance of local Newton iterations to
   $\mathrm{tol}_Q = \max\left(\min\left(\|\Delta V\|^2, \mathrm{tol}_Q^{(0)}\right), \mathrm{tol}_Q^{\min}\right)$

5. Combination of relative and absolute tolerance, based on the norm of the converged global variables at the previous stage
   $\|\Delta V\| \leq \mathrm{tol}_V^{\mathrm{rel}} \|V_{i-1}\| + \mathrm{tol}_V^{\mathrm{abs}} \sqrt{n_{\mathrm{eq}}}$

6. Combination of relative and absolute tolerance, based on the initial residual
   $\|G(V, Q)\| \leq \mathrm{tol}_G^{\mathrm{rel}} \|G\left(V^{(0)}, Q^{(0)}\right)\| + \mathrm{tol}_G^{\mathrm{abs}} \sqrt{n_{\mathrm{eq}}}$

7. Combination of relative and absolute tolerances, see 5 and 6 for details
   $\|\Delta V\| \leq \mathrm{tol}_V^{\mathrm{rel}} \|V_{i-1}\| + \mathrm{tol}_V^{\mathrm{abs}} \sqrt{n_{\mathrm{eq}}}$, and
   $\|G(V, Q)\| \leq \mathrm{tol}_G^{\mathrm{rel}} \|G\left(V^{(0)}, Q^{(0)}\right)\| + \mathrm{tol}_G^{\mathrm{abs}} \sqrt{n_{\mathrm{eq}}}$

8. Newton tolerances based on the tolerances of the DIRK-method
   $\|\Delta V\| \leq \mathrm{tol}_V^{\mathrm{rel}} \|V^{(0)}\| + \mathrm{tol}_V^{\mathrm{abs}} \sqrt{n_{\mathrm{eq}}}$ with
   $\mathrm{tol}_V^{\mathrm{rel}} = \varepsilon_{\mathrm{r}}/100, \mathrm{tol}_V^{\mathrm{abs}} = \varepsilon_{\mathrm{a}}/100$

Setting the local Newton tolerance according to 4, i.e. starting with a rough tolerance and refining when approaching the exact solution on global level, leads in special cases to a performance increase. Unfortunately this does not hold in general due to the interference between the local and global level. This is investigated in detail in [Quint, 2004] and [Hartmann, 2005], where it is called "improved MLNA". Specifying relative and absolute tolerances as in 5 and 6 can be based on theoretical considerations as in [Kelley, 2003, p. 9]. The criterion 8 has the advantage, that the accuracy is automatically related to the user specified accuracy of the time integration.

A.4. Computation of Gradients with Respect to Different Coordinates

Gradients of scalar and vector functions are needed within finite elements to compute the right hand side and the functional matrix.

A typical example of a scalar function is the temperature θ. With the element interpolation function (5.72), the temperature gradient with respect to the current and reference configuration is given by

$$\operatorname{grad} \theta = \frac{\partial \theta}{\partial \boldsymbol{x}} = \sum_{a=1}^{n_{\mathrm{en}}} \operatorname{grad} N_a \Theta_a^e, \quad \text{and} \quad \operatorname{Grad} \theta = \frac{\partial \theta}{\partial \boldsymbol{X}} = \sum_{a=1}^{n_{\mathrm{en}}} \operatorname{Grad} N_a \Theta_a^e. \quad \text{(A.5)}$$

A typical example of a vector function is the displacement. The displacement gradient is given within one element e by

$$\operatorname{grad} \boldsymbol{u} = \sum_{a=1}^{n_{\mathrm{en}}} \mathbf{u}_a^e \otimes \operatorname{grad} N_a, \quad \text{and} \quad \operatorname{Grad} \boldsymbol{u} = \sum_{a=1}^{n_{\mathrm{en}}} \mathbf{u}_a^e \otimes \operatorname{Grad} N_a. \quad \text{(A.6)}$$

For the evaluation, the gradient of the shape function N_a has to be computed with respect to the different configurations. However, these functions are formulated in terms of the parametric coordinates $\boldsymbol{\xi}$ and a transformation into other configurations is needed

$$N_a = N_a(\boldsymbol{\xi}) = N_a(\boldsymbol{\xi}(\boldsymbol{x})) = N_a(\boldsymbol{\xi}(\boldsymbol{X})). \quad \text{(A.7)}$$

The position vectors in the current and reference configuration are related to the parametric coordinates by the element interpolation functions

$$\boldsymbol{x}(\boldsymbol{\xi}, t) = \sum_{a=1}^{n_{\mathrm{en}}} N_a(\boldsymbol{\xi}) \boldsymbol{x}_a^e(t), \quad \text{and} \quad \boldsymbol{X}(\boldsymbol{\xi}) = \sum_{a=1}^{n_{\mathrm{en}}} N_a(\boldsymbol{\xi}) \boldsymbol{X}_a^e.$$

The directional derivative[1] of the current position is given by

$$\mathrm{d}\boldsymbol{x} = \mathbf{j}\,\mathrm{d}\boldsymbol{\xi}, \quad \text{and} \quad \mathrm{d}\boldsymbol{X} = \mathbf{J}\,\mathrm{d}\boldsymbol{\xi}, \quad \text{(A.8)}$$

---

[1]See also the remarks on material elements in Sec. 3.1.2.

where the Jacobians are given by

$$\mathbf{J} = \left[\frac{\partial \boldsymbol{X}}{\partial \boldsymbol{\xi}}\right] = \operatorname{Grad}_\xi \boldsymbol{X} = \sum_{a=1}^{n_{en}} \boldsymbol{X}_a \otimes \operatorname{Grad}_\xi N_a, \qquad J_{ij} = \frac{\partial X_i}{\partial \xi_j},$$

$$\mathbf{j} = \left[\frac{\partial \boldsymbol{x}}{\partial \boldsymbol{\xi}}\right] = \operatorname{Grad}_\xi \boldsymbol{x} = \sum_{a=1}^{n_{en}} \boldsymbol{x}_a \otimes \operatorname{Grad}_\xi N_a, \qquad j_{ij} = \frac{\partial x_i}{\partial \xi_j},$$

With these preliminary results, the different gradients of N_a can be obtained by considering the directional derivative of the shape function N_a

$$\mathrm{D}N_a(\boldsymbol{\xi})[\mathrm{d}\boldsymbol{\xi}] = \mathrm{D}N_a(\boldsymbol{\xi}(\boldsymbol{x}))[\mathrm{d}\boldsymbol{x}] = \mathrm{D}N_a(\boldsymbol{\xi}(\boldsymbol{X}))[\mathrm{d}\boldsymbol{X}]. \tag{A.9}$$

Inserting the results of (A.8) leads to

$$\mathrm{D}N_a(\boldsymbol{\xi})[\mathrm{d}\boldsymbol{\xi}] = \operatorname{Grad}_\xi N_a \cdot \mathrm{d}\boldsymbol{\xi} = \operatorname{grad} N_a \cdot \mathrm{d}\boldsymbol{x} = \operatorname{grad} N_a \cdot \mathbf{j}\,\mathrm{d}\boldsymbol{\xi}. \tag{A.10}$$

The directional derivative of $\hat{N}_a$ is treated in the same manner. Finally, the gradients are given by

$$\operatorname{grad} N_a = \mathbf{j}^{-\mathrm{T}} \operatorname{Grad}_\xi N_a, \quad \text{and} \quad \operatorname{Grad} N_a = \mathbf{J}^{-\mathrm{T}} \operatorname{Grad}_\xi N_a.$$

These can be evaluated analytically only for simple elements and domains. In most cases numerical quadrature is applied and the inverse Jacobians have to be computed only at certain points, the quadrature points. In this case the inverse Jacobians are computed within the elements using dense matrix algorithms.

A.5. Additional Constitutive Models

A.5.1. Small Strain Viscoplasticity Model for POM

The small strain viscoplasticity model for polyoxymethylene (POM) was originally developed in [Hartmann, 2006b]. It is motivated by the rheological model in Fig. A.1 which implies an additive decomposition of the strain and the stress. The linearized strain tensor $\mathbf{E}$ is split into an elastic and a viscous part, $\mathbf{E} = \mathbf{E}_e + \mathbf{E}_v$, $\mathbf{E} = \mathbf{E}^\mathrm{T}$, $\mathbf{E}_e = \mathbf{E}_e^\mathrm{T}$, $\mathbf{E}_v = \mathbf{E}_v^\mathrm{T}$. Additionally, the stress-state $\mathbf{T} = \mathbf{T}^\mathrm{T}$ is assumed to consist of an equilibrium and an overstress part, $\mathbf{T} = \mathbf{T}_{eq}^e + \mathbf{T}_{eq}^h + \mathbf{T}_{ov}$, where the equilibrium stress part consists of an elastic, $\mathbf{T}_{eq}^e = \mathbf{T}_{eq}^{e\,\mathrm{T}}$, and a hysteretic part, $\mathbf{T}_{eq}^h = \mathbf{T}_{eq}^{h\,\mathrm{T}}$. The elastic equilibrium and the overstress part $\mathbf{T}_{ov} = \mathbf{T}_{ov}^\mathrm{T}$ are defined by elasticity relations

$$\mathbf{T}_{ov} = K_0(\operatorname{tr}\mathbf{E}_e)\mathbf{I} + 2G_0\mathbf{E}_e^\mathrm{D}, \tag{A.11}$$

$$\mathbf{T}_{eq}^e = (K_T f_T(\mathbf{I_E}) + K_C f_C(\mathbf{I_E}))\,\mathbf{I_E}\mathbf{I} + G(\mathbf{J_E})\,(f_T(\mathbf{I_E}) + \beta f_C(\mathbf{I_E}))\,\mathbf{E}^\mathrm{D} \tag{A.12}$$
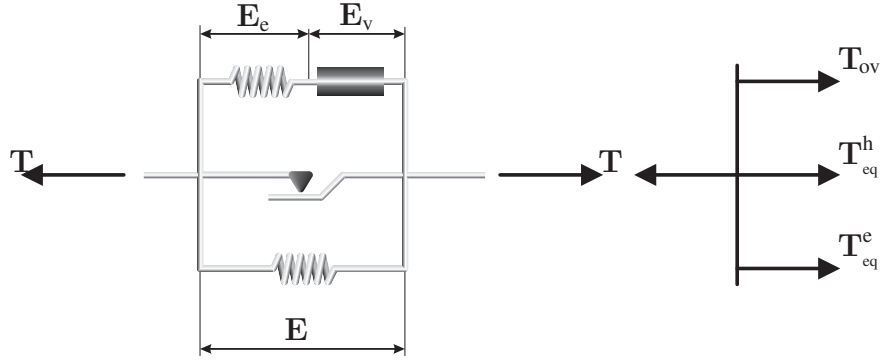
Figure A.1.: Rheological model for constitutive equations of POM

with both the deformation-dependent shear modulus $G(\mathbf{J_E})$ and the smoothing functions $f_T(\mathbf{I_E})$ as well as $f_C(\mathbf{I_E})$

$$G(\mathbf{J_E}) = \frac{\alpha_1}{\alpha_2 + \sqrt{\mathbf{J_E}}}, \quad f_T(\mathbf{I_E}) = \tfrac{1}{2}(1 + \tanh(a\mathbf{I_E})), \quad f_C(\mathbf{I_E}) = \tfrac{1}{2}(1 - \tanh(a\mathbf{I_E})).$$

Here, the invariants $\mathbf{I_E} = \operatorname{tr}\mathbf{E}$ and $\mathbf{J_E} = \mathbf{E}^D \cdot \mathbf{E}^D$ are defined Furthermore a is a smoothing parameter and K_0, G_0, K_T, K_C, α_1, and α_2 are material parameters which have to be adapted to experimental data, see [Hartmann, 2006b]. The smoothing functions are introduced to represent the tension-compression asymmetry occurring in the experiments, controlled by the material parameter β. The remaining viscous strains $\mathbf{E_v}$ and the hysteretic part of the equilibrium stresses $\mathbf{T}^h_{eq}$ are given by evolutions equations, i.e. ordinary differential equations of first order:

$$\dot{\mathbf{T}}^h_{eq} = c\dot{\mathbf{E}}^D - b\dot{s}\mathbf{T}^h_{eq} \tag{A.13}$$

$$\dot{\mathbf{E}}_v = \frac{\beta_2\|\dot{\mathbf{E}}\|^{\beta_3} + 1}{\eta_0(1 + \beta_1\|\mathbf{E}\|)}\mathbf{T}_{ov} \tag{A.14}$$

Here, a deformation-process dependent viscosity is applied. $\dot{s} = \|\dot{\mathbf{E}}\| = \sqrt{\dot{\mathbf{E}} \cdot \dot{\mathbf{E}}} \geq 0$ defines the rate of an arc-length and b, c, β_2, β_3 and η_0 are additional material parameters representing the remaining deformations and the rate-dependence as well as relaxation behavior of the material under consideration. The material parameters are compiled in Tab. A.6 In conclusion, the constitutive model fits into the structure

$$\mathbf{T} = \mathbf{h}(\mathbf{E}, \mathbf{q}) \tag{A.15}$$

$$\dot{\mathbf{q}} = \mathbf{r}(\mathbf{E}, \dot{\mathbf{E}}, \mathbf{q}), \tag{A.16}$$

with $\mathbf{q} = \{\mathbf{T}^h_{eq}, \mathbf{E_v}\}$. In the three-dimensional case $\mathbf{q}$ has the dimension 12, since both the stress and the strain tensor are symmetric. The stress state is defined by the current state of deformation and the state of the internal variables. The latter are implicitly

Table A.6.: Material parameters of small strain viscoplasticity model identified in [Hartmann, 2006b]

K_T MPa	K_C MPa	α_1 MPa	α_2 /	β /	c MPa	b /	K_0 MPa	G_0 MPa	η_0 MPa	β_1 10^5	β_2 /	β_3 /
7200	7200	35	0.04	1.8	200	10	5000	700	10^7	7	0.96	10

given by ordinary differential equations. Although the constitutive model is nonlinear, a diagonally-implicit Runge-Kutta step can be solved explicitly since the internal variables occur linearly, see [Hartmann, 2006b]. Thus, on quadrature-point level there are no iterations (see function $\boldsymbol{L}$ in equation (5.149) and Tab. 5.2), i.e. only function evaluations have to be performed on quadrature-point level.

A.5.2. Finite Strain Viscoplasticity Model for Metal at Room Temperature

In comparison much more complicated is the model of Fig. A.2, which describes finite strain viscoplasticity of metals with kinematic hardening and is originally published in [Hartmann et al., 2008a]. According to the proposals of Lion [2000] and Tsakmakis and
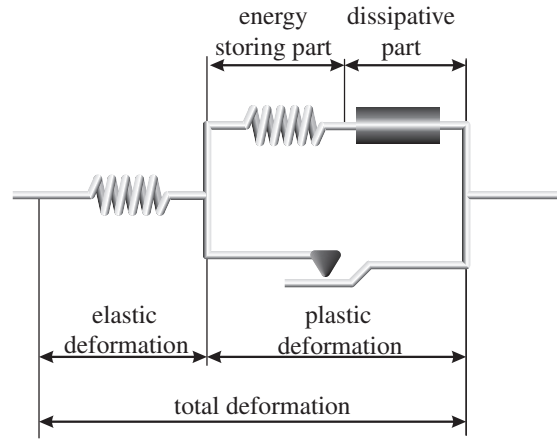

Figure A.2.: Rheological model for constitutive equations

Willuweit [2004] a multiplicative decomposition of the deformation gradient into an elastic and a viscous part is assumed, where the latter is additionally decomposed multiplicatively into an energy storing and a dissipative part: $\mathbf{F} = \hat{\mathbf{F}}_\mathrm{e}\mathbf{F}_\mathrm{p} = \hat{\mathbf{F}}_\mathrm{e}\check{\mathbf{F}}_\mathrm{s}\mathbf{F}_\mathrm{d}$. Based on this decomposition strain tensors relative to the inelastic intermediate configurations are formulated. Relative to the plastic intermediate configuration an elasticity relation is formulated, which can be expressed by quantities relative to the reference configuration. The kinematic hardening behavior is modeled by strain-like quantities, where

an additional elasticity relation defines a back-stress tensor occurring in a von Mises yield function. Both the plastic and the energy storing intermediate configurations are controlled by flow rules for strain tensors. Relative to the reference configuration they can be expressed by the plastic right Cauchy-Green tensor $\mathbf{C}_\mathrm{p} = \mathbf{F}_\mathrm{p}^\mathrm{T} \mathbf{F}_\mathrm{p}$ and the quantity $\mathbf{C}_\mathrm{d} = \mathbf{F}_\mathrm{d}^\mathrm{T} \mathbf{F}_\mathrm{d}$. The extension to viscoplasticity is done by a Perzyna-type model. In Tab. A.7 the model is summarized showing that 12 internal variables control the inelastic

Table A.7.: Constitutive model expressed with quantities relative to the reference configuration

	Elasticity	*Viscoplasticity*
Loading condition	$F \leq 0$	$F > 0$
Flow rule 1	$\dot{\mathbf{C}}_\mathrm{p} = \mathbf{0}$	$\dot{\mathbf{C}}_\mathrm{p} = \Lambda \frac{3}{2\alpha} \left(\mathbf{C}_\mathrm{p} \tilde{\mathbf{T}} \mathbf{C} - \mathbf{C}_\mathrm{d} \mathbf{Z} \mathbf{C}_\mathrm{p} - \frac{1}{3}(\mathrm{tr}(\tilde{\mathbf{T}}\mathbf{C} - \mathbf{C}_\mathrm{d}\mathbf{Z}))\mathbf{C}_\mathrm{p} \right)$
Flow rule 2	$\dot{\mathbf{C}}_\mathrm{d} = \mathbf{0}$	$\dot{\mathbf{C}}_\mathrm{d} = \Lambda \sqrt{8/3} \beta \left(\mathbf{C}_\mathrm{d} \mathbf{Z} \mathbf{C}_\mathrm{d} - (\mathrm{tr}(\mathbf{Z}\mathbf{C}_\mathrm{d}))/3\mathbf{C}_\mathrm{d} \right)$
Elasticity relation	$\tilde{\mathbf{T}} = K(J-1)J\mathbf{C}^{-1} + 2c_{10} J^{-2/3} \left(\mathbf{C}_\mathrm{p}^{-1} - \frac{1}{3}\mathrm{tr}(\mathbf{C}\mathbf{C}_\mathrm{p}^{-1})\mathbf{C}^{-1} \right)$	

Abbreviations

$$\mathbf{Z} = \frac{1}{2}\left(c_1 - \frac{c_2}{3}\right)\left(3 - \mathrm{tr}(\mathbf{C}_\mathrm{d}\mathbf{C}_\mathrm{p}^{-1})\right)\mathbf{C}_\mathrm{p}^{-1} + \frac{c_2}{2}\left(\mathbf{C}_\mathrm{p}^{-1} - \mathbf{C}_\mathrm{p}^{-1}\mathbf{C}_\mathrm{d}\mathbf{C}_\mathrm{p}^{-1}\right)$$

$$F = \sqrt{\frac{3}{2}\left((\mathbf{C}_\mathrm{p}\tilde{\mathbf{T}}\mathbf{C}\mathbf{C}_\mathrm{p}^{-1} - \mathbf{C}_\mathrm{d}\mathbf{Z}) \cdot (\tilde{\mathbf{T}}\mathbf{C} - \mathbf{C}_\mathrm{p}^{-1}\mathbf{C}_\mathrm{d}\mathbf{Z}\mathbf{C}_\mathrm{p}) - \frac{1}{3}\left(\tilde{\mathbf{T}}\mathbf{C} - \mathbf{C}_\mathrm{d}\mathbf{Z}\right)^2\right)} - k$$

$$\alpha = F + k, \quad \Lambda = 1/\eta(F/\sigma_0)^{r_v}$$

deformation process, where $\tilde{\mathbf{T}} = (\det \mathbf{F})\mathbf{F}^{-1}\mathbf{T}\mathbf{F}^{-\mathrm{T}}$ is the 2nd Piola-Kirchhoff tensor. $\mathbf{T}$ designates the Cauchy-stress tensor. The aspect of integration, particularly, the incorporation of the plastic incompressibility condition is discussed in [Hartmann et al., 2008a]. The chosen material parameters are depicted in Tab. A.8. The integration step of the

Table A.8.: Material parameters of finite strain viscoplasticity model

K MPa	μ MPa	k MPa	c_1 MPa	c_2 MPa	β_1 —	r —	σ_0 MPa	η s
166666.67	76923.08	200	6666.67	20000	0.0025	1.0	1.0	0.1

internal variables is done iteratively on quadrature-point level by solving 12 unknowns (and one for the yield function) if $F < 0$ holds. Accordingly, the numerical effort is much larger than for the small strain POM model.

A.6. Convective Heat Transfer Coefficient of Isothermal Vertical Cylinder

A body that is immersed in a moving fluid exchanges thermal energy with the fluid, this energy exchange is called heat convection. The fluids movement can be driven by external means, such as fans. In this case one speaks of forced flow and thus forced heat convection. In the presence of temperature differences, density variations result and lead to buoyancy forces. These let the fluid rise, independently of external forces. This effect is technically exploited e.g. by radiators and heat exchangers. Air that is in direct contact with the devices heats up and experiences a reduction in density. The lighter air rises and induces a vertical bulk fluid motion, where cool air flows in from the ambience.

Both mechanisms are of technical relevance, where in the present paper the free convection dominates the cooling process. The heat flux $\overline{q}_{con}$ is often approximated by a linear relationship

$$\overline{q}_{con} = h_c \left(\theta_s - \theta_\infty \right), \tag{5.19}$$

where θ_s is the absolute temperature (in K) of the surface, θ_∞ is the absolute temperature of the surrounding fluid, and h_c is the heat transfer coefficient, which reflects the mean heat transfer. In the following it is determined on the basis of analytical and experimental results.

According to Fig. 6.5a, the heat transfer coefficient of a vertical cylinder (length $L = 0.15$ m and diameter $D = 0.03$ m) has to be found. Simplifying the investigation, an isothermal setting is assumed here, in contrast to the real experiment. The convective heat transfer coefficient is related to the Nusselt number Nu and the heat conductivity of air λ by

$$h_c = \frac{Nu\lambda}{L}. \tag{A.17}$$

The Nusselt number is a dimensionless parameter that characterizes the heat transfer properties of the boundary layer. It can be expressed in terms of further dimensionless parameters of the fluid flow, namely the Grashof and the Rayleigh number. The Grashof number gives the ratio of buoyancy to viscous forces acting on the fluid

$$Gr = \frac{g\beta(\Theta_s - \theta_\infty)L^3}{\nu^2}, \tag{A.18}$$

where $g = 9.81$ m/s^2 is the gravitational acceleration and β is the volumetric thermal expansion coefficient, which can in the case of ideal gases be approximated by $\beta = 1/\theta_f$, cf. [Incropera et al., 2007, p. 564]. The parameter ν is the kinematic viscosity of air, which also depends on the fluid temperature θ_f.

In [Churchill and Chu, 1975] a correlation between Ra, Pr, and Nu is derived for laminar ($10^4 \lesssim Ra \lesssim 10^9$) and turbulent ($10^9 \lesssim Ra \lesssim 10^{13}$) flow over an isothermal vertical plate

$$Nu_P = \left[0.825 + \frac{0.387 Ra^{1/6}}{[1 + (0.492/Pr)^{9/16}]^{8/27}} \right]^2, \tag{A.19}$$

197

which is also recommended in [Gnielinski et al., 2006]. Slightly better accuracy is obtained in the case of laminar flow with the equation

$$Nu_{\mathrm{p}} = 0.68 + \frac{0.670 Ra^{1/4}}{(1 + (0.492/Pr)^{9/16})^{4/9}}, \quad Ra \lesssim 10^9, \tag{A.20}$$

cf. [Churchill and Chu, 1975]. In these expressions the similarity parameter Prandtl number $Pr = \nu \rho c_p / \lambda = Ra/Gr$ is used. Its values can be found for different temperatures for example in [Incropera et al., 2007, p. 941].

In comparison with a flat plate the curvature of a cylinder leads to an increased Nusselt number. Different analytical relations are investigated and compared with experimental data in [Popiel et al., 2007]. The authors find that the equation of Cebeci [1974] correlates best with their experimental data

$$Nu = \left(1 + B \left[32^{1/2}(Gr)^{-1/4} \left(\frac{L}{D}\right)\right]^C\right) Nu_{\mathrm{p}} \tag{A.21}$$

where

$$B = 0.0571322 + 0.20305 Pr^{-0.43},$$
$$C = 0.9165 - 0.0043 Pr^{1/2} + 0.01333 \ln(Pr) + 0.0004809/Pr.$$

Using equation (A.21), the convective heat transfer coefficient h is computed for three different surface temperatures θ_{s}. According to [Kays et al., 2005, p. 383], all properties $(Ra, Pr, \dots)$ have to be evaluated at a specific reference temperature. Almost all reported data and data correlations use the average film temperature $\theta_{\mathrm{f}} = \frac{1}{2}(\theta_{\mathrm{s}} + \theta_\infty)$, which is also employed here. The temperature at the outer edge of the boundary layer is fixed at $\theta_\infty = 290$ K. The resulting intermediate values and heat transfer coefficients are summarized in Tab. A.9 and are obtained by equations (A.17), (A.18), (A.20), and (A.21). The average heat transfer coefficient (due to free convection) of a vertical cylin-

Table A.9.: Parameter

Θ_s	θ_{f}	$\nu(\theta_{\mathrm{f}})$	$Pr(\theta_{\mathrm{f}})$	$\lambda(\theta_{\mathrm{f}})$	$h_{\mathrm{c}}(\theta_{\mathrm{f}})$
°C	K	m^2/s	-	W/mK	W/(m^{2}K)
434	500	$38.79 \cdot 10^{-6}$	0.684	$40.7 \cdot 10^{-3}$	9.61
834	700	$68.10 \cdot 10^{-6}$	0.695	$52.4 \cdot 10^{-3}$	10.51
1234	900	$102.90 \cdot 10^{-6}$	0.720	$62.0 \cdot 10^{-3}$	10.91

der at a constant temperature is between $h_{\mathrm{c}} = 9$ W/(m^{2}K) and $h_{\mathrm{c}} = 11$ W/(m^{2}K) in the range of $\Theta = 400$ °C to $\Theta = 1200$ °C.

A.7. List of Publications Related to the Present Work

1. S. Rothe, A.-W. Hamkar, K. J. Quint, S. Hartmann
   Comparison of diagonal-implicit, linear-implicit and half-explicit Runge-Kutta methods in non-linear finite element analyses
   Archive of Applied Mechanics DOI 10.1007/s00419-012-0617-5, (2012)

2. K. J. Quint, S. Hartmann, S. Rothe, N. Saba, K. Steinhoff
   Experimental validation of high-order time integration for non-linear heat transfer problems
   Computational Mechanics, Volume 48, Number 1 (2011)

3. S. Rothe, S. Hartmann, A.-W. Hamkar, K. J. Quint
   A comparison of time adaptive integration methods for small and large strain viscoelasticity
   Proceedings in Applied Mathematics and Mechanics, Volume 11, Issue 1 (2011)

4. P. Birken, K. J. Quint, S. Hartmann, A. Meister
   Chosing norms in adaptive FSI calculations
   Proceedings in Applied Mathematics and Mechanics, Volume 10, Issue 1 (2010)

5. P. Birken, K. J. Quint, S. Hartmann, A. Meister
   A time-adaptive fluid-structure interaction method for thermal coupling
   Computing and Visualization in Science, Volume 13, Number 7 (2010)

6. K. J. Quint, S. Hartmann
   Time adaptive analysis of thermo-mechanically coupled plasticity
   Int. Conf. on Computational Methods for Coupled Problems in Science and Engineering, B. Schrefler, E. Onate, and M. Papadrakakis, Eds., CD, ISBN 978-84-96736-65-8, CIMNE; Barcelona, Spain (2009)

7. S. Hartmann, J. Duintjer Tebbens, K. J. Quint, A. Meister
   Iterative solvers within sequences of large linear systems in non-linear structural mechanics
   Journal of Applied Mathematics and Mechanics, Volume 89, Issue 9 (2009)

8.   S. Hartmann, D. Kuhl, K. J. Quint
Time-Adaptive Computation of Finite Strain Thermoviscoplastic Structures
In Functionally Graded Materials in Industrial Mass Production
Verlag Wissenschaftliche Scripten, Auerbach (2009)

9.   S. Hartmann, A. Meister, P. Birken, K. J. Quint
Thermal Fluid-Structure-Interaction of Cooling Processes in Steel Forming
In Functionally Graded Materials in Industrial Mass Production
Verlag Wissenschaftliche Scripten, Auerbach (2009)

10.   P. Birken, S. Hartmann, A. Meister, K. J. Quint
On higher order time integration for thermal coupling
Numerical Analysis and Applied Mathematics, International Conference on Numerical Analysis and Applied Mathematics 2009, Volume 2, AIP Conference Proceedings, 2009, pp. 1184-1187

11.   P. Birken, K. J. Quint, S. Hartmann, A. Meister
On coupling schemes for heat transfer in FSI applications
International Workshop on Fluid-Structure Interaction: Theory, Numerics and Applications
kassel university press, Kassel (2009)

12.   K. J. Quint, S. Hartmann, J. Duintjer Tebbens, A. Meister
Efficient finite element analysis of inelastic structures with iterative solvers
Proceedings in Applied Mathematics and Mechanics, Volume 8, Issue 1 (2008)

13.   S. Hartmann, K. J. Quint, M. Arnold
On plastic incompressibility within time-adaptive finite elements combined with projection techniques
Computer Methods in Applied Mechanics and Engineering, Volume 198, Issue 2 (2008)

14.   S. Hartmann, K. J. Quint, A.-W. Hamkar
Displacement control in time-adaptive non-linear finite-element analysis
Journal of Applied Mathematics and Mechanics, Volume 88, Issue 5 (2008)

15. K. J. Quint, S. Hartmann
    The multiple intermediate configuration approach and its influence on
    DIRK/MLNA finite element procedures
    Proceedings in Applied Mathematics and Mechanics, Volume 7, Issue 1
    (2007)

16. K. J. Quint
    Numerische Behandlung plastischer Inkompressibilität
    Report of the Institute of Mechanics No.1/2007, University of Kassel

A.8. Curriculum Vitae

Persönliche Daten

Name	Karsten Jens Quint, Dipl.-Ing.
geboren am	16.12.1978 in München
Familienstand	verheiratet

Schulausbildung

09. 1985 bis 06. 1989	Grundschule „Am Goldacker", Baunatal
09. 1989 bis 07. 1995	Erich Kästner-Schule, Baunatal
08. 1995 bis 06. 1996	International High School Program, Fargo, USA
09. 1996 bis 06. 1999	Georg-Christoph-Lichtenberg-Schule, Kassel
08. 2000 bis 01. 2003	Herwig-Blankertz-Schule, Berufsschule-Wolfhagen

Zivildienst

07. 1999 bis 07. 2000	Arbeiter-Samariter-Bund e.V. in Baunatal

Berufsausbildung

08. 2000 bis 01. 2003	Industriemechaniker (Fachrichtung Maschinen- und Systemtechnik), Volkswagen Werk Kassel

Studium

10. 2000 bis 08. 2005	Studium des Maschinenbaus im Praxisverbund an der Universität Kassel und im Volkswagen Werk Kassel Diplom I in Zusammenarbeit mit der Volkswagen AG: *Luftfederdämpfer: Physikalische Modellierung und Simulation in Fahrzeugmodellen mit MATLAB und ADAMS/CAR*
08. 2005 bis 05. 2006	Fulbright-Stipendium: Studiengang „Engineering Mechanics" an der University of Texas at Austin und Zusammenarbeit mit Prof. Demkowicz am Institute for Computational Engineering and Sciences (ICES), USA
07. 2006 bis 11. 2006	Diplom II: *Numerische Behandlung plastischer Inkompressibilität bei finiter Viskoplastizität*

Auszeichnungen

1999	DPG-Buchpreis für hervorragende Leistungen im Fach Physik
2003	IHK Auszeichnung für sehr gute Prüfungsergebnisse
2005	Auszeichnung für das beste Diplom I im SS 2005
2006	Auszeichnung für das beste Diplom II im WS 2006
2007	VDI Diplompreis Nordhessen 2006

Berufliche Tätigkeiten

11. 2006 bis 08. 2009	Wissenschaftlicher Mitarbeiter am Institut für Mechanik, FG Kontinuumsmechanik, Universität Kassel: *Betreuung des Teilprojektes C1 des Sonderforschungsbereichs TRR30: Zeitadaptive Berechnung finiter thermoviskoplastischer Strukturen*
08. 2009 bis 07. 2010	Wissenschaftlicher Mitarbeiter am Institut für Baustatik und Baudynamik, FG Baumechanik/ Baudynamik, Universität Kassel: *Weiterhin Betreuung des Teilprojektes C1 des SFB TRR30. Wechsel aufgrund der Änderung der Projektleitung von Prof. Hartmann zu Prof. Kuhl*
08. 2010 bis 09. 2010	Wissenschaftlicher Mitarbeiter am Institut für Technische Mechanik, Technische Universität Clausthal: *Weiterhin inhaltliche Bearbeitung des Teilprojektes C1 bei Prof. Hartmann*
seit 10. 2010	Berechnungsingenieur in der Abteilung Fahrwerkvorentwicklung der Volkswagen AG in Wolfsburg *Untersuchung und Verbesserung der Fahrdynamik und des Fahrkomforts von PKWs*

Fachbezogene Mitgliedschaften

11. 2006 bis 08. 2010	Mitglied im interdisziplinären Promotionskolleg SCOSA, der Universität Kassel
07. 2007 bis 08. 2010	Doktorandenvertreter und Vorstandsmitglied des Sonderforschungsbereichs TRR30

Bibliography

Adam, L. and Ponthot, J.-P. A coupled thermo-viscoplastic formulation at finite strains for the numerical simulation of superplastic forming. *Journal of Materials Processing Technology*, 139(1–3):514–520, 2003. 9

Adam, L. and Ponthot, J.-P. Thermomechanical modeling of metals at finite strains: First and mixed order finite elements. *International Journal of Solids and Structures*, 42(21–22):5615–5655, 2005. 9

Agelet de Saracibar, C., Cervera, M., and Chiumenti, M. On the formulation of coupled thermoplastic problems with phase-change. *International Journal of Plasticity*, 15(1):1–34, 1999. 10, 14

Agelet de Saracibar, C., Cervera, M., and Chiumenti, M. On the constitutive modeling of coupled thermomechanical phase-change problems. *International Journal of Plasticity*, 17(12):1565–1622, 2001. 10, 12

Al-Baldawi, A. *Verifikationsbeispiele von Wärmeleitungsproblemen für die Finite Element Methode*. Master's thesis, University of Kassel, 2008. 15, 120

Alber, H.-D. Mathematische Theorie des inelastischen Materialverhaltens von Metallen. *Mitteilungen der Gesellschaft für Angewandte Mathematik und Mechanik*, 18:9–38, 1995. 84

Alexander, R. Diagonally implicit Runge-Kutta methods for stiff O.D.E.'s. *SIAM Journal on Numerical Analysis*, 14(6):1006–1021, 1977. 119, 162

Ali, Y. M. and Zhang, L. C. Relativistic heat conduction. *International Journal of Heat and Mass Transfer*, 48(12):2397–2406, 2005. 66

Alonso-Mallo, I. Runge-Kutta methods without order reduction for linear initial boundary value problems. *Numerische Mathematik*, 91(4):577–603, 2002. 120, 121

Alonso-Mallo, I. and Cano, B. Avoiding order reduction of Runge-Kutta discretizations for linear time-dependent parabolic problems. *BIT Numerical Mathematics*, 44(1):1–20, 2004. 120, 121

Altan, T., editor. *Schuler - Metal Forming Handbook*. Springer, Berlin, 1998. 1

Altan, T., Ngaile, G., and Shen, G., editors. *Cold and Hot Forging: Fundamentals and Applications*. ASM International, 2004. 1

Altenbach, H., Altenbach, J., and Münch, C. Analyse des thermomechanischen Verhaltens von Festkörpern. *Archive of Applied Mechanics*, 61(4):0939–1533, 1991. 95

Altenbach, J. and Altenbach, H. *Einführung in die Kontinuumsmechanik*. Teubner, Stuttgart, 1994. 40, 45, 49, 53

Argyris, J. H., Vaz, L. E., and Willam, K. J. Integrated finite-element analysis of coupled thermoviscoplastic problems. *Journal of Thermal Stresses*, 4(2):121–153, 1981. 9

Armero, F. and Simo, J. C. A new unconditionally stable fractional step method for non-linear coupled thermomechanical problems. *International Journal for Numerical Methods in Engineering*, 35(4):737–766, 1992. 10

Armero, F. and Simo, J. C. A priori stability estimates and unconditionally stable product formula algorithms for nonlinear coupled thermoplasticity. *International Journal of Plasticity*, 9(6):749–782, 1993. 10

Armijo, L. Minimization of functions having Lipschitz continuous first partial derivatives. *Pacific Journal of Mathematics*, 16(1):1–3, 1966. 129

Armstrong, P. J. and Frederick, C. O. A mathematical representation of the multiaxial Bauschinger effect. Technical report, G.E.G.B. Report RD/B/N731, Berkeley Nuclear Laboratories, UK, 1966. 7

Ascher, U. M. and Petzold, L. R. *Computer Methods for Ordinary Differential Equations and Differential-Algebraic Equations*. SIAM Society for Industrial and Applied Mathematics, Philadelphia, 1998. 92, 99, 109, 110, 114, 116, 122, 124

Augarde, C. E., Ramage, A., and Staudacher, J. An element-based displacement preconditioner for linear elasticity problems. *Computers & Structures*, 84:2306–2315, 2006. 13

Augarde, C. E., Ramage, A., and Staudacher, J. Element-based preconditioners for elasto-plastic problems in geotechnical engineering. *International Journal for Numerical Methods in Engineering*, 71:757–779, 2007. 13

Auricchio, F. and Taylor, R. L. Two material models for cyclic plasticity: Nonlinear kinematic hardening and generalized plasticity. *International Journal of Plasticity*, 11(1):65–98, 1995. 7

Babuška, I. and Oden, J. T. Verification and validation in computational engineering and science: Basic concepts. *Computer Methods in Applied Mechanics and Engineering*, 193:4057–4066, 2004. 4, 155

Baehr, H. D. and Stephan, K. *Wärme- und Stoffübertragung*. Springer, Berlin, 2008. 29

Barrett, R., Berry, M., Chan, T., Demmel, J., Donato, J., Dongarra, J., Eijkhout, V., Pozo, R., Romine, D., and Van der Vorst, H. *Templates for the Solution of Linear Systems: Building Blocks for Iterative Methods 1*. Philadelphia, 1994. 153

Bathe, K.-J. *Finite Element Procedures*. Prentice Hall, New Jersey, 1996. 145, 185

Becker, E. B., Carey, G. F., and Oden, J. T. *Finite Elements: An Introduction, Volume 1*. Prentice Hall, New Jersey, 1981. 5, 92, 93, 105

Belytschko, T., Liu, W. K., and Moran, B. *Nonlinear Finite Elements for Continua and Structures*. John Wiley & Sons Ltd,, Chichester, 2004. 135, 145, 185

Bergman, G. and Oldenburg, M. A finite element model for thermomechanical analysis of sheet metal forming. *International Journal for Numerical Methods in Engineering*, 59(9):1167–1186, 2004. 9

Bertram, A. Finite thermoplasticity based on isomorphisms. *International Journal of Plasticity*, 19(11):2027–2050, 2003. 11

Bier, W. and Hartmann, S. A finite strain constitutive model for metal powder compaction using a unique and convex single surface yield function. *European Journal of Mechanics A/Solids*, 2006. 75

Birken, P., Quint, K. J., Hartmann, S., and Meister, A. A time-adaptive fluid-structure interaction method for thermal coupling. *Computing and Visualization in Science*, 13(7):331–340, 2010. 14, 84

Böhm, M., Dachkovski, S., Hunkel, M., Lübben, T., and Wolff, M. Übersicht über einige makroskopische Modelle für Phasenumwandlungen im Stahl. *Reports ZeTeM*, 2003. 12

Bonet, J. and Wood, R. D. *Nonlinear Continuum Mechanics for Finite Element Analysis*. Cambridge University Press, 1997. 133

Brown, S. B., Kim, K. H., and Anand, L. An internal variable constitutive model for hot working metals. *International Journal of Plasticity*, 5:95–130, 1989. 11, 186

Büchling, B. Simulation der Materialphasenentwicklung in einer einseitig abgekühlten Stahlflachprobe aus 51CrV4 mit adiabaten Randbedingungen. Technical report, University of Kassel, Institute of Mechanics and Dynamics, 2010. 186

Burg, K., Haf, H., Wille, F., and Meister, A. *Höhere Mathematik für Ingenieure: Band I Analysis*. Teubner, Stuttgart, 2008. 102, 105

Burkhardt, L. *Eine Methodik zur virtuellen Beherrschung thermo-mechanischer Produktionsprozesse bei der Karosserieherstellung*. Ph.D. thesis, ETH Zürich, 2008. 9

Büttner, J. and Simeon, B. Runge-Kutta methods in elastoplasticity. *Applied Numerical Mathematics*, 41:443–458, 2002. 7, 8

Calvo, M. P. and Palencia, C. Avoiding the order reduction of Runge-Kutta methods for linear initial boundary value problems. *Mathematics of Computation*, 71(240):1529–1543, 2001. 120

Cameron, F. *Low-order Runge-Kutta Methods for Differential-Algebraic Equations*. Ph.D. thesis, Tampere University of Technology, Tampere, Finland, 1999. 145

Čanađija, M. and Brnić, J. Associative coupled thermoplasticity at finite strain with temperature-dependent material parameters. *International Journal of Plasticity*, 20(10):1851–1874, 2004. 9, 13

Carpenter, M. H., Gottlieb, D., Abarbanel, S., and Don, W.-S. The theoretical accuracy of Runge-Kutta time discretizations for the initial boundary value problem: A study of the boundary error. *SIAM Journal on Scientific Computing*, 16(6):1241–1252, 1995. 120

Carstens, S. and Kuhl, D. Non-linear static and dynamic analysis of tensegrity structures by spatial and temporal Galerkin methods. *Journal of the International Association for Shell and Spatial Structures*, 46(2):116–134, 2005. 93

Cash, J. R. Diagonally implicit Runge-Kutta formulae with error estimates. *IMA Journal of Applied Mathematics*, 24(3):293–301, 1979. 163, 190

Cebeci, T. Laminar-free-convective-heat transfer from the outer surface of a vertical slender circular cylinder. In *Proceedings of the fifth International Heat Transfer Conference*, volume 3, pages 15–19. 1974. 198

Celigoj, C. C. Finite deformation coupled thermomechanical problems and generalized standard materials. *International Journal for Numerical Methods in Engineering*, 42(6):1025–1043, 1998. 11

Chaboche, J. L. Cyclic viscoplastic constitutive equations, part I: A thermodynamically consistent formulation. *Journal of Applied Mechanics*, 60(4):813–821, 1993a. 62

Chaboche, J. L. Cyclic viscoplastic constitutive equations, part II: Stored energy comparison between models and experiments. *Journal of Applied Mechanics*, 60(4):822–828, 1993b. 62

Chaboche, J. L. A review of some plasticity and viscoplasticity constitutive theories. *International Journal of Plasticity*, 24(10):1642–1693, 2008. 11

Chapman, B., Jost, G., and van der Pas, R. *Using OpenMP: Portable Shared Memory Parallel Programming*. Scientific and Engineering Computation Series. The MIT Press, Cambridge, MA, 2008. 15, 131

Christov, C. I. On frame indifferent formulation of the Maxwell-Cattaneo model of finite-speed heat conduction. *Mechanics Research Communications*, 36:481–486, 2009. 66

Churchill, S. W. and Chu, H. H. S. Correlating equations for laminar and turbulent free convection from a vertical plate. *International Journal of Heat and Mass Transfer*, 18:1323–1329, 1975. 197, 198

Clark, M. *Pragmatisch Programmieren: Projekt-Automatisierung*. Hanser Fachbuch, München, 2006. 15

Clemens, M., Wilke, M., and Weiland, T. Efficient extrapolation methods for electro- and magneto-quasistatic field simulations. *Advances in Radio Science*, 1:81–86, 2003. 145

Cools, R. An encyclopaedia of cubature formulas. *Journal of Complexity*, 19(3):445–453, 2003. 188

Cottrell, J. A., Hughes, T. J. R., and Bazilevs, Y. *Isogeometric Analysis: Toward Integration of CAD and FEA*. John Wiley & Sons, Chichester, 2009. 92, 93

Crisfield, M. A. *Finite Elements and Solution Procedures for Structural Analysis*. Pineridge Press, Swansea, 1986. 12

Damjanić, F. and Owen, D. R. J. Practical considerations for thermal transient finite element analysis using isoparametric elements. *Nuclear Engineering and Design*, 69(1):109–126, 1982. 5

Davis, T. A. and Duff, I. S. A combined/multifrontal method for unsymmetric sparse matrices. Technical Report TR-97-016 (REP-1997-252), Computer and Information Science and Engineering Department, University of Florida, Gainesville, Florida, 1997. 12, 150

Dembot, R., Eisenstat, E., and Steihaug, T. Inexact Newton methods. *SIAM Journal on Numerical Analysis*, 19, 1982. 153

Demmel, J. W., Eisenstat, S. C., Gilbert, J. R., Li, X. S., and Liu, J. W. H. A supernodal approach to sparse partial pivoting. *SIAM Journal on Matrix Analysis and Applications*, 20(3):720–755, 1999. 12

Dennis, J. E. and Schnabel, R. B. *Numerical methods for unconstrained optimization and nonlinear equations*, volume 16 of *Classics in Applied Mathematics*. SIAM Society for Industrial and Applied Mathematics, Philadelphia, 1996. 129

Dettmer, W. and Reese, S. On the theoretical and numerical modelling of armstrong-frederick kinematic hardening in the finite strain regime. *Computer Methods in Applied Mechanics and Engineering*, 193:87–116, 2004. 7

Deuflhard, P. and Bornemann, F. A. *Numerische Mathematik II: Gewöhnliche Differentialgleichungen*. de Gruyter, Berlin, 2008. 126

Dhatt, G. and Touzot, G. *The Finite Element Method Displayed*. John Wiley & Sons Ltd, England, Chichester, 1985. 81, 95, 102, 104, 105, 189

Dhondt, G. *The Finite Element Method for Three-dimensional Thermomechanical Applications*. John Wiley & Sons Ltd, Chichester, 2004. 81, 90

Diebels, S., Ellsiepen, P., and Ehler, W. Error-controlled Runge-Kutta time integration of a viscoplastic hybrid two-phases model. *Technische Mechanik*, 19:19–27, 1999. 126

Dunne, F. and Petrinic, N. *Introduction to Computational Plasticity*. Oxford University Press, USA, 2005. 6

Eckart, C. The thermodynamics of irreversible processes. IV. The theory of elasticity and anelasticity. *Physical Review*, 73(4):373–382, 1948. 54

Eckert, S., Baaser, H., Gross, D., and Scherf, O. A BDF2 integration method with step size control for elasto-plasticity. *Computational Mechanics*, 34(5):377–386, 2004. 8, 109

Eisenstat, S. C. and Walker, H. F. Choosing the forcing terms in an inexact Newton method. *SIAM Journal on Scientific Computing*, 17(1):16–32, 1996. Special issue on iterative methods in numerical linear algebra (Breckenridge, CO, 1994). 153

Ellsiepen, P. *Zeit- und ortsadaptive Verfahren angewandt auf Mehrphasenprobleme poröser Medien*. Ph.D. thesis, Universität Stuttgart, 1999. 162, 190

Ellsiepen, P. and Hartmann, S. Remarks on the interpretation of current non-linear finite element analyses as differential-algebraic equations. *International Journal for Numerical Methods in Engineering*, 51:679–707, 2001. 7, 8, 14, 94, 96, 100, 129

Eriksson, K. and Johnson, C. Adaptive finite element methods for parabolic problems I: A linear model problem. *Society for Industrial and Applied Mathematics*, 28(1):43–77, 1991. 6

Eriksson, K. and Johnson, C. Adaptive finite element methods for parabolic problems IV: Nonlinear problems. *Society for Industrial and Applied Mathematics*, 32(6):1729–1749, 1995. 6

Eriksson, K., Johnson, C., and Thomee, V. Time discretization of parabolic problems by the discontinuous Galerkin method. *Modélisation mathématique et analyse numérique*, 19(4):611–643, 1985. 108

Esche, S. K., Kinzel, G. L., and Altan, T. Issues in convergence improvements for non-linear finite element programs. *International Journal for Numerical Methods in Engineering*, 40:4577–4594, 1997. 145

Faragó, I. and Horváth, R. A review of reliable numerical models for three-dimensional linear parabolic problems. *International Journal for Numerical Methods in Engineering*, 70(1):25–45, 2007. 6

Felippa, C. A. and Park, K. C. Staggered transient analysis procedures for coupled mechanical systems: Formulation. *Computer Methods in Applied Mechanics and Engineering*, 24(1):61 – 111, 1980. 9

Felippa, C. A., Park, K. C., and Farhat, C. Partitioned analysis of coupled mechanical systems. *Computer Methods in Applied Mechanics and Engineering*, 190(24–25):3247–3270, 2001. 9

Ferencz, R. M. and Hughes, T. J. R. Iterative finite element solutions in nonlinear solid mechanics. In Ciarlet, P. G. and Lions, J. L., editors, *Numerical Methods for Solids (Part 3)*, volume VI of *Handbook of Numerical Analysis*, pages 3–179. Elsevier Science, 1998. 12

Flory, P. J. Thermodynamic relations for high elastic materials. *Transaction of the Faraday Society*, 57:829–838, 1961. 62

Fritsch, A. *Finite Thermoplastizität Materialmodellierung und Numerik thermoplastischer Werkstoffe bei finiten Deformationen*. Ph.D. thesis, Institut für Mechanik der Fakultät Luft- und Raumfahrttechnik der Universität der Bundeswehr München, Fortschritt-Berichte VDI, Reihe 18, Nr. 290, 2004. 10, 62, 90

Fritzen, P. *Numerische Behandlung nichtlinearer Probleme der Elastizitäts- und Plastizitätstheorie*. Ph.D. thesis, Technische Universität Darmstadt, 1997. 8, 80, 84, 94, 96

Fritzen, P. and Wittekindt, J. Numerical solution of viscoplastic constitutive equations with internal state variables. Part I: Algorithms and implementation. *Mathematical Methods in the Applied Sciences*, 20:1411–1425, 1997. 8

Fujii, H. Some remarks on finite element analysis of time-dependent field problems. In *Theory and Practice in Finite Element Structural Analysis*, pages 91–106. University of Tokyo Press, Tokyo, 1973. 5

Fung, T. C. Third order complex-time-step methods for transient analysis. *Computer Methods in Applied Mechanics and Engineering*, 190(22–23):2789–2802, 2001. 6

Gabbert, U. *Die Finite-Element-Methode in den Ingenieurwissenschaften unter dem Aspekt der rechentechnischen Realisierung im Rahmen universeller Programmsysteme*. Ph.D. thesis, TU Magdeburg, 1987. 95

Gallopoulos, A., E. Sameh. CSE: content and product. *Computing in Science and Engineering*, 4(2):39–43, 1997. 3, 4

Gallopoulos, E., Houstis, E., and Rice, J. R. Computer as thinker/doer: Problem-solving environments for computational science. *Computing in Science and Engineering*, 1(2):11–23, 1994. 3, 4

Ganapathysubramanian, S. and Zabaras, N. A continuum sensitivity method for finite thermo-inelastic deformations with applications to the design of hot forming processes. *International Journal for Numerical Methods in Engineering*, 55(12):1391–1437, 2002. 11

Gerhold, T., Friedrich, O., Evans, J., and Galle, M. Calculation of complex three-dimensional configurations employing the DLR-τ-code. In *35th Aerospace Sciences Meeting & Exhibit*, volume 97-0167. AIAA, 1997. 186

Glaser, S. *Berechnung gekoppelter thermomechanischer Prozesse*. Ph.D. thesis, Universität Stuttgart, 1992. 10, 11

Gnielinski, V., Kabelac, S., Kind, M., Martin, H., Mewes, D., Schaber, K., and Stephan, P., editors. *VDI-Wärmeatlas*. Springer, Berlin, 2006. 27, 198

Golub, G. H. and van Loan, C. F. *Matrix Computation*. The Johns Hopkins University Press, Baltimore, 3rd edition, 1996. 12, 149

Gould, N. I. M., Scott, J. A., and Hu, Y. A numerical evaluation of sparse direct solvers for the solution of large sparse symmetric linear systems of equations. *ACM Transactions on Mathematical Software*, 33(2):10, 2007. 150

Greenberg, M. *Advanced Engineering Mathematics*. Prentice Hall, New Jersey, 1998. 63, 80, 81, 84, 88, 119, 120, 130, 141

Greenberg, M. D. *Foundations of Applied Mathematics*. Prentice Hall, 1978. 84

Griewank, A. and Walther, a. *Evaluating Derivatives: Principles and Techniques of Algorithmic Differentiation*. SIAM Society for Industrial and Applied Mathematics, Philadelphia, 2008. 111

Großmann, C. and Roos, H.-G. *Numerische Behandlung partieller Differentialgleichungen*. Teubner, Stuttgart, 2005. 91, 93, 95, 105, 168

Guo, Z., Kang, G., and Saunders, N. Modelling materials properties critical to simulation of hot stamping. In *The 13th International Conference on Metal Forming*. Toyohashi, Japan, 2010. 73

Guo, Z., Saunders, N., Schillé, J. P., and Miodownik, A. P. Material properties for process simulation. *Materials Science and Engineering A*, 499:7–13, 2009. 73

Gustafsson, K. Control theoretic techniques for stepsize selection in explicit Runge-Kutta methods. *Transactions on Mathematical Software*, 17:533–554, 1991. 127

Gustafsson, K. Control-theoretic techniques for stepsize selection in implicit Runge-Kutta methods. *Transactions on Mathematical Software*, 20(4):496–517, 1994. 127

Gustafsson, K., Lundh, M., and Söderlind, G. A PI stepsize control for the numerical solution of ordinary differential equations. *BIT Numerical Mathematics*, 28(2):270–287, 1988. 126

Hackbusch, W. *Multigrid Methods and Applications*, volume 4 of *Computational Mathematics*. Springer, Berlin, 1985. 149

Hadamard, J. *Lectures on Cauchy's Problem in Linear Partial Differential Equations*. Dover Publications, Mineola, NY, 2003. 86

Haines, P. J. *Thermal Methods of Analysis: Principles, Applications and Problems*. Blackie Academic and Professional, Glasgow, 1995. 26

Hairer, E., Norsett, S. P., and Wanner, G. *Solving Ordinary Differential Equations I: Nonstiff Problems*. Springer, Berlin, 2000. 6, 109, 113, 126, 162

Hairer, E. and Wanner, G. *Solving Ordinary Differential Equations II: Stiff and Differential-Algebraic Problems*. Springer, Berlin, 2002. 108, 109, 119, 126, 190

Hairer, E., Wanner, G., and Lubich, C. *Geometric Numerical Integration: Structure-Preserving Algorithms for Ordinary Differential Equations*. Springer, Berlin, 2002. 6, 8

Hakansson, P., Wallin, M., and Ristinmaa, M. Comparison of isotropic hardening and kinematic hardening in thermoplasticity. *International Journal of Plasticity*, 21(7):1435–1460, 2005. 9, 11, 54

Hammer, P. and Stroud, A. Numerical evaluation of multiple integrals II. *Mathematical Tables and Other Aids to Computation*, 12:272–280, 1958. 107, 187

Hansen, E. and Ostermann, A. Unconditional convergence of DIRK schemes applied to dissipative evolution equations. *Applied Numerical Mathematics*, 60(1–2):55–63, 2010. 6

Hartmann, S. Computation in finite-strain viscoelasticity: Finite elements based on the interpretation as differential-algebraic equations. *Computer Methods in Applied Mechanics and Engineering*, 191(13–14):1439–1470, 2002. 8, 14

Hartmann, S. Finite-Elemente Berechnung inelastischer Kontinua: Interpretation als Algebro-Differentialgleichungssysteme. Habilitationsschrift, 2003. 94, 96, 122

Hartmann, S. A remark on the application of the Newton-Raphson method in non-linear finite element analysis. *Computational Mechanics*, 36(2):100–116, 2005. 8, 127, 192

Hartmann, S. TASA-FEM: Ein Finite-Elemente Programm für raum-zeitadaptive gekoppelte Strukturberechnungen, Version 1.0. Mitteilung des Instituts für Mechanik 1/ 06, Institut für Mechanik, Universität Kassel, 2006a. 8, 15, 81

Hartmann, S. A thermomechanically consistent constitutive model for polyoxymethylene. *Archive of Applied Mechanics*, 76(5–6):349–366, 2006b. 164, 166, 193, 194, 195

Hartmann, S. and Bier, W. High-order time integration applied to metal powder. *International Journal of Plasticity*, 24(1):17–54, 2008. 8

Hartmann, S., Duintjer Tebbens, J., Quint, K. J., and Meister, A. Iterative solvers within sequences of large linear systems in non-linear structural mechanics. *Journal of Applied Mathematics and Mechanics*, 89(9):711–728, 2009a. 131, 151, 154

Hartmann, S. and Hamkar, A.-W. Rosenbrock-type methods applied to finite element computations within finite strain visco- elasticity. *Computer Methods in Applied Mechanics and Engineering*, 199(23–24):1455–1470, 2010. 8

Hartmann, S. and Haupt, P. Stress computation and consistent tangent operator using non-linear kinematic hardening models. *International Journal for Numerical Methods in Engineering*, 36:3801–3814, 1993. 7

Hartmann, S., Kuhl, D., and Quint, K. J. Time-adaptive computation of finite strain thermoviscoplastic structures. In Steinhoff, K., Maier, K.-J., and Svendsen, B., editors, *Functionally Graded Materials in Industrial Mass Production*, chapter 4.1, pages 269–282. Verlag Wissenschaftliche Scripten, Auerbach, 2009b. 75

Hartmann, S., Lührs, G., and Haupt, P. An efficient stress algorithm with applications in viscoplasticity and plasticity. *International Journal for Numerical Methods in Engineering*, 40:991–1013, 1997. 7, 62

Hartmann, S., Meister, A., Birken, P., and Quint, K. J. Thermal fluid-structure-interaction of cooling processes in steel forming. In Steinhoff, K., Maier, K.-J., and Svendsen, B., editors, *Functionally Graded Materials in Industrial Mass Production*, chapter 4.2, pages 283–292. Verlag Wissenschaftliche Scripten, Auerbach, 2009c. 14, 84

Hartmann, S. and Neff, P. Polyconvexity of generalized polynomial-type hyperelastic strain energy functions for near-incompressibility. *International Journal of Solids and Structures*, 40(11):2767–2791, 2003. 62, 183

Hartmann, S., Quint, K. J., and Arnold, M. On plastic incompressibility within time-adaptive finite elements combined with projection techniques. *Computer Methods in Applied Mechanics and Engineering*, 198(2):178–193, 2008a. 8, 14, 164, 166, 195, 196

Hartmann, S., Quint, K. J., and Hamkar, A.-W. Displacement control in time-adaptive non-linear finite-element analysis. *Journal of Applied Mathematics and Mechanics*, 88(5):342–364, 2008b. 7, 125

Hartmann, S. and Wensch, J. Finite element analysis of viscoelastic structures using Rosenbrock-type methods. *Computational Mechanics*, 40(2):383–398, 2007. 8

Haupt, P. *Continuum Mechanics and Theory of Materials*. Springer, Berlin, 2000. 31, 33, 36, 43, 46, 50, 51, 55, 56, 57, 58, 67, 68, 72, 80, 82

Haupt, P. and Lion, A. Experimental identification and mathematical modeling of viscoplastic material behavior. *Continuum Mechanics and Thermodynamics*, 7(1):73–96, 1995. 18, 54

Heimes, T. Thermohyperelastisches Material mit Zwischenkonfiguration. Technical report, Universität der Bundeswehr München, 2003. 90, 91

Heimes, T. *Finite Thermoinelastizität: Experimente, Materialmodellierung und Implementierung in die FEM am Beispiel einer technischen Gummimischung*. Ph.D. thesis, Universität der Bundeswehr München, 2005. 90

Hellen, T. K. Effective quadrature rules for quadratic solid isopatametric finite elements. *International Journal for Numerical Methods in Engineering*, 4:597–599, 1972. 107, 187

Helm, D. Experimentelle Untersuchung und phänomenologische Modellierung thermomechanischer Kopplungseffekte in der Metallplastizität. In Hartmann, S. and Tsakmakis, C., editors, *Aspekte der Kontinuumsmechanik und Materialtheorie*, number 1 in Berichte des Instituts für Mechanik, pages 81–105. Gesamthochschul-Bibliothek, 1998. 59, 62, 67

Helm, D. *Formgedächtnislegierungen: Experimentelle Untersuchung, phänomenologische Modellierung und numerische Simulation der themomechanischen Materialeigenschaften*. Ph.D. thesis, Institut für Mechanik, Universität Kassel, 2001. 66, 68

Helm, D. Kontinuumsmechanik I, Skript zur Vorlesung des WS 2003/04 Institut für Mechanik, Universität Kassel. 2003. 43

Helm, D. Stress computation in finite thermoviscoplasticity. *International Journal of Plasticity*, 22:1699–1727, 2006. 7, 11, 13, 54, 55, 62, 183

Hemminger, W. and Höhne, G. *Grundlagen der Kalorimetrie*. Verlag Chemie, Weinheim, 1979. 25, 26

Hestenes, M. R. and Stiefel, E. Methods of conjugate gradients for solving linear systems. *Journal of Research of the National Bureau of Standards, Section B*, 49:409–436, 1952. 13

Hibbit, H. D. Some follower forces and load stiffness. *International Journal for Numerical Methods in Engineering*, 14(6):937–941, 1979. 82

Hinnant, H. C. A fast method of numerical quadrature for p-version finite element matrices. *International Journal for Numerical Methods in Engineering*, 37(21):3723–3750, 1994. 108

Hohenemser, K. and Prager, W. Über die Ansätze der Mechanik isotroper Kontinua. *Journal of Applied Mathematics and Mechanics*, 12(4):216–226, 1932. 61

Höhne, G., Hemminger, W. F., and Flammersheim, H.-J. *Differential Scanning Calorimetry*. Springer, Berlin, 2003. 25, 26

Hömberg, D. A mathematical model for the phase transitions in eutectoid carbon steel. *IMA Journal of Applied Mathematics*, 54:31–57, 1995. 12

Hömberg, D. A numerical simulation of the Jominy end-quench test. *Acta Metallurgica*, 11:4375–4385, 1996. 12

Huétink, J. On anisotropy, objectivity and invariance in finite thermo-mechanical deformations. In Juster, N. and Rosochowski, A., editors, *ESAFORM 2006*, pages 355–358. Publishing Hous Akapit, Krakow, 2006. 11

Hughes, T. J. R. *The Finite Element Method: Linear Static and Dynamic Finite Element Analysis*. Dover Publications, Mineola, NY, 2000. 5, 81, 86, 93, 94, 95, 97, 99, 100, 101, 102, 104, 105, 106, 108, 136, 189

Hunt, A. and Thomas, D. *Der Pragmatische Programmierer*. Hanser Fachbuch, München, 2003. 15

Hunt, A. and Thomas, D. *Pragmatisch Programmieren: Unit-Tests mit JUnit*. Hanser Fachbuch, München, 2005. 15

Hutter, K. and Jöhnk, K. *Continuum Methods of Physical Modeling. Continuum Mechanics, Dimensional Analysis, Turbulence*. Springer, Berlin, 2004. 31, 40, 42, 43

Ibrahimbegovic, A. and Chorfi, L. Covariant principal axis formulation of associated coupled thermoplasticity at finite strains and its numerical implementation. *International Journal of Solids and Structures*, 39(2):499–528, 2002. 11

Incropera, F. P., Dewitt, D. P., Bergman, T. L., and Lavine, A. S. *Fundamentals of Heat and Mass Transfer*. John Wiley & Sons, Hoboken, NJ, 6th edition, 2007. 28, 29, 80, 84, 161, 197, 198

Irons, B. M. Quadrature rules for brick based finite elements. *International Journal for Numerical Methods in Engineering*, 3:293–294, 1971. 107, 187

Jansohn, W. *Formulierung und Integration von Stoffgesetzen zur Beschreibung großer Deformationen in der Thermoplastizität und -viskoplastizität*. Ph.D. thesis, Forschungszentrum Karlsruhe, Institut für Materialforschung, 1997. 11, 62, 68, 70, 184

Jeltsch-Fricker, R. Variationsrechnung. Skript zur Vorlesung in den Technikstudiengängen der Universität Kassel, 2007. 87, 98

Johnson, C. *Numerical Solution of Partial Differential Equations by the Finite Element Method*. Dover Publications, 2009. 108

Kassiotis, C., Colliat, J.-B., Ibrahimbegovic, A., and Matthies, H. G. Multiscale in time and stability analysis of operator split solution procedures applied to thermomechanical problems. *Engineering Computations*, 26(1/2):205–223, 2009. 10

Kays, W. M., Crawford, M. E., and Weigand, B. *Convective Heat and Mass Transfer*. McGraw-Hill, New York, 2005. 161, 198

Kelley, C. T. *Iterative Methods for Linear and Nonlinear Equations*. SIAM Society for Industrial and Applied Mathematics, Philadelphia, 1995. 128, 146, 147, 153, 154, 167

Kelley, C. T. *Solving Nonlinear Equations with Newton's Method*. Fundamentals of Algorithms. SIAM Society for Industrial and Applied Mathematics, Philadelphia, 2003. 146, 192

Kelley, C. T. and Keyes, D. E. Convergence analysis of pseudo-transient continuation. *SIAM Journal on Numerical Analysis*, 35(2):508–523, 1998. 129

Kieback, B., Neubrand, A., and Riedel, H. Processing techniques for functionally graded materials. *Materials Science and Engineering A*, 362(1–2):81–106, 2003. 1

Kim, C. G. and Suri, M. On the p version of the finite element method in the presence of numerical integration. *Numerical Methods for Partial Differential Equations*, 9(6):593–629, 1993. 106

Kirchner, E. and Simeon, B. A higher-order time integration method for viscoplasticity. *Computer Methods in Applied Mechanics and Engineering*, 175:1–18, 1999. 7, 109

Kloosterman, G. *Contact Methods in Finite Element Simulations*. Ph.D. thesis, University of Twente, 2002. 81

Koizumi, M. FGM activities in japan. *Composites Part B: Engineering*, 28(1–2):1–4, 1997. 1

Kojić, M. and Bathe, J.-K. The effective-stress-function algorithm for thermo-elastoplasticity and creep. *International Journal for Numerical Methods in Engineering*, 24(8):1509–1532, 1987. 9

Kreisselmeier, G. and Steinhauser, R. Systematische Auslegung von Reglern durch Optimierung eines vektoriellen Gütekriteriums. *Regelungstechnik*, 3:76–79, 1979. 75

Kreyszig, E. *Introductory Functional Analysis with Applications*. John Wiley & Sons, Hoboken, NJ, 1989. 102, 107

Kuhl, D. Modellierung und Simulation von Mehrfeldproblemen der Strukturmechanik. Habilitationsschrift, 2004a. 8, 93

Kuhl, D. Thermomechanical analysis using fintie element methods with particular emphasis on rocket combustion chambers. In Neittaanmäki, P., Rossi, T., Korotov, S., Oñate, E., Périaux, J., and Knörzer, D., editors, *Fourth European Congress on Computational Methods in Applied Sciences and Engineering*. Jyväskylä, 2004b. 9

Kuhl, D. and Meschke, G. Numerical analysis of dissolution processes in cementitious materials using discontinuous and continuous Galerkin time integration schemes. *International Journal for Numerical Methods in Engineering*, 69:1775–1803, 2007. 93

Kuhl, D., Riccius, J., and Haidn, O. Thermomechanical analysis and optimization of cryogenic liquid rocket engines. *Journal of Propulsion and Power*, 18:835–846, 2002. 9

Kujawski, J. and Wiberg, N.-E. Least-squares schemes for time integration of thermal problems. *International Journal for Numerical Methods in Engineering*, 24:159–175, 1987. 5

Lambers, H.-G., Tschumak, S., Maier, H., and Canadinc, D. Role of austenitization and pre-deformation on the kinetics of the isothermal bainitic transformation. *Metallurgical and Materials Transactions A*, 40(6):1073–5623, 2009. 17

Lambers, H.-G., Tschumak, S., Maier, H., and Canadinc, D. Pre-deformation-transformation plasticity relationship during martensitic transformation. *Materials Science and Engineering: A*, 527:625–633, 2010. 17

Lämmer, H. *Thermoplastizität und Thermoviskoplastizität mit Schädigung bei kleinen und großen Deformationen*. Ph.D. thesis, Forschungszentrum Karlsruhe, Institut für Materialforschung, 1998. 7, 11, 62

Lang, J. and Verwer, J. G. ROS3P - an accurate third-order Rosenbrock solver designed for parabolic problems. *BIT Numerical Mathematics*, 41(4):731–738, 2001. 6

Lang, J. and Verwer, J. G. On global error estimation and control for initial value problems. *Society for Industrial and Applied Mathematics*, 29(4):1460–1475, 2007. 124

Läpple, V. *Wärmebehandlung des Stahls: Grundlagen, Verfahren und Werkstoffe*. Europa-Lehrmittel, Haan-Gruiten, 2006. 30

Lee, E. Elastic-plastic deformation at finite strains. *Journal of Applied Mechanics*, 36:1–6, 1969. 54, 68

Lewis, R. W., Morgan, K., Thomas, H. R., and Seetharamu, K. N. *The Finite Element Method in Heat Transfer Analysis*. John Wiley & Sons, Chichester, 1996. 5

Lion, A. *Materialeigenschaften der Viskoplastizität*. Ph.D. thesis, Institut für Mechanik, Universität Kassel, 1994. 19, 23

Lion, A. Constitutive modelling in finite thermoviscoplasticity: A physical approach based on nonlinear rheological models. *International Journal of Plasticity*, 16:469–494, 2000. 7, 11, 13, 53, 54, 55, 195

Loureiro, F. S. and Mansur, W. J. A new family of time integration methods for heat conduction problems using numerical Green's functions. *Computational Mechanics*, 44(4):519–531, 2009. 6

Lu, S. C. H. and Pister, K. S. Decomposition of deformation and representation of the free energy function for isotropic thermoelastic solids. *International Journal of Solids and Structures*, 11(7–8):927–934, 1975. 55

Lubarda, V. A. Constitutive theories based on the multiplicative decomposition of deformation gradient: Thermoelasticity, elastoplasticity, and biomechanics. *Applied Mechanics Reviews*, 57(2):95–108, 2004. 54

Lubich, C. and Ostermann, A. Runge-Kutta methods for parabolic equations and convolution quadrature. *Mathematics of Computation*, 60(201):105–131, 1993. 116

Lubliner, J. *Plasticity Theory*. Dover Publications, Mineola, NY, 2008. 18, 19, 21, 54, 60, 61, 68, 74, 81

Lührs, G. *Randwertaufgaben der Viskoplastizität: Modellierung, Simulation und Vergleich mit experimentellen Daten aus zyklischen Prozessen und Umformvorgängen.* Ph.D. thesis, Universität Kassel, Institut für Mechanik, 1997. 7, 68

Lührs, G., Hartmann, S., and Haupt, P. On the numerical treatment of finite deformations in elastoviscoplasticity. *Computer Methods in Applied Mechanics and Engineering*, 144:1–21, 1997. 68

Madhusudana, C. V. *Thermal Contact Conductance*. Springer, Berlin, 1996. 160

Mahnken, R. and Schneidt, A. A thermodynamics framework and numerical aspects for transformation-induced plasticity at large strains. *Archive of Applied Mechanics*, 80:229–253, 2010. 12

Mahnken, R., Schneidt, A., and Antretter, T. Macro modelling and homogenization for transformation induced plasticity of a low-alloy steel. *International Journal of Plasticity*, 25:183–204, 2009. 12

Maier, H. J., Tschumak, S., Weidig, U., and Steinhoff, K. Functional gradation of low alloy steel by differentially controlled phase transformation. *Steel Research International*, 79(2):105–110, 2008. 17

Maikranz-Valentin, M., Weidig, U., Schoof, U., Becker, H.-H., and Steinhoff, K. Components with optimised properties due to advanced thermo-mechanical process strategies in hot sheet metal forming. *Steel Research Internationa*, 79(2):92–97, 2008. 1

Mancuso, M., Ubertini, F., and Momanyi, F. X. Time continuous Galerkin methods for linear heat conduction problems. *Computer Methods in Applied Mechanics and Engineering*, 189(1):91–106, 2000. 6

Marsden, J. E. and Hughes, T. J. R. *Mathematical Foundations of Elasticity*. Dover Publications, Inc., Mineola, N.Y., Mineola, NY, 1994. 33, 80

Matthies, H. G., Niekamp, R., and Steindorf, J. Algorithms for strong coupling procedures. *Computer Methods in Applied Mechanics and Engineering*, 195:2028–2049, 2006. 186

Mattuck, A. *Introduction to Analysis*. Prentice Hall, Upper Saddle River, NJ, 1999. 112

Meggyes, Á. Multiple decomposition in finite deformation theory. *Acta Mechanica*, 146(3–4):169–182, 2001. 55

Meirovitch, L. *Fundamentals of Vibrations*. McGraw-Hill, New York, 2001. 80

Meister, A. *Numerik linearer Gleichungssysteme*. Vieweg Verlag, Wiesbaden, 3rd edition, 2008. 12

Miehe, C. *Zur numerischen Behandlung thermomechanischer Prozesse*. Ph.D. thesis, Universität Hannover, 1988. 10, 90, 91

Miehe, C. *Kanonische Modelle multiplikativer Elasto-Plastizität. Thermodynamische Formulierung und numerische Implementation*. Ph.D. thesis, Universität Hannover, 1993. 10

Miehe, C. A theory of large-strain isotropic thermoplasticity based on metric transformation tensors. *Archive of Applied Mechanics*, 66(1–2):45–64, 1995. 10

Miehe, C. Multisurface thermoplasticity for single crystals at large strains in terms of eulerian vector updates. *International Journal of Solids and Structures*, 33(20-22):3103–3130, 1996. 10

Miller, K. Nonlinear Krylov and moving nodes in the method of lines. *Journal of Computational and Applied Mathematics*, 183:275–287, 2005. 145

Miyamoto, Y., editor. *Functionally Graded Materials: Design, Processing and Applications*. Kluwer Academic Press Inc, 1999. 1

Münch, C. *Die Analyse thermomechanischer Vorgänge mit der Finite-Element-Methode*. Ph.D. thesis, TU Magdeburg, 1989. 9

Muschik, W. Irreversibility and second law. *Journal of Non-Equilibrium Thermodynamics*, 23(1):87–98, 1998. 50

Neff, P. and Wieners, C. Comparison of models for finite plasticity. *Computing and Visualization in Sience*, 6:23–35, 2003. 13

Nemkov, V. *Handbook of Thermal Process Modeling of Steels*, chapter 10. Modeling of Induction Hardening Processes, pages 427–498. CRC Press, 2009. 173

Neuer, G. Messung des Gesamtemissionsgrades von Graphit, Molybdän, Tantal und Wolfram bei Temperaturen zwischen 1200 K und 2400 K. *Wärme- und Stoffübertragung*, 4:133–141, 1971. 30

Neuer, G. Total normal and spectral emittance of refractory materials for high temperature ovens. *Thermochimica Acta*, 218:211–219, 1993. 30

Neuer, G. and Hoch, M. Spectral emittance and temperature determination of carbon/SiC and SiC/SiC composites. *Thermochimica Acta*, 218:305–315, 1993. 30

Nicolas, Y. Hot stamping - a new hot forming technology. *ThyssenKrupp techforum*, 7:40–47, 2005. 1

Noll, W. Five contributions to natural philosophy - On the principle of material frame-indifference. Posted on the authors website, 2004. 31

Oden, J. T. The promise of computational sciences: Will it be kept? *IACM Expressions*, (12):12–15, 2002. 3, 155

Ogden, R. W. *Non-Linear Elastic Deformations*. Dover Publications, Inc., Mineola, N.Y., Mineola, NY, 1997. 35, 46, 59, 80, 84

Oñate, E. *Structural Analysis with the Finite Element Method: Linear Statics*, volume 1 of *Lecture Notes on Numerical Methods in Engineering and Sciences*. Springer, Berlin, 2009. 81, 148

Orlich, J., Rose, A., and Wiest, P. *Atlas zur Wärmebehandlung der Stähle, Band 3*. Verlag Stahleisen M.B.H., Düsseldorf, 1973. 17

Pantuso, D., Bathe, K. J., and Bouzinov, P. A. A finite element procedure for the analysis of thermo-mechanical solids in contact. *Computers & Structures*, 75(6):551–573, 2000. 186

Parisch, H. *Festkörper-Kontinuumsmechanik: Von den Grundgleichungen zur Lösung mit Finiten Elementen*. Teubner, Stuttgart, 2003. 10, 90

Parks, M., de Sturler, M., G., M., D., J., and Maiti, S. Recycling Krylov subspaces for sequences of linear systems. *SIAM Journal on Scientific Computing*, 28(5):1651–1674, 2006. 186

Pathria, D. The correct formulation of intermediate boundary conditions for Runge-Kutta time integration of initial boundary value problems. *SIAM Journal on Scientific Computing*, 18(5):1255–1266, 1997. 120

Perić, D. and Owen, D. R. J. *Encyclopedia of Computational Mechanics: Computational Modeling of Forming Processes*, volume 2, chapter 14, pages 461–511. John Wiley & Sons, Chichester, 2004. 9, 90, 186

Perzyna, P. The constitutive equations for rate sensitive plastic materials. *Quartely of Applied Mathematics*, 20:321–332, 1963. 61

Peterson, J. W. Analytical formulae for two of A.H. Stroud's quadrature rules. *ArXiv e-prints*, 2009. 187

Pietzsch, R., Brzoza, M., Kaymak, Y., Specht, E., and Bertram, A. Simulation of the distortion of long steel profiles during cooling. *Journal of Applied Mechanics*, 74(3):427–437, 2007. 12

Popiel, C. O. and Wojtkowiak, J. Experiments on free convective heat transfer from side walls of a vertical square cylinder in air. *Experimental Thermal and Fluid Science*, 29(1):1–8, 2004. 161

Popiel, C. O., Wojtkowiak, J., and Bober, K. Laminar free convective heat transfer from isothermal vertical slender cylinder. *Experimental Thermal and Fluid Science*, 32(2):607–613, 2007. 161, 198

Post, D. E. The promise of science-based computational engineering. *Computing in Science and Engineering*, 11(3):3–4, 2009. 3, 155

Press, W. H., Teukolsky, S. A., Vetterling, W. T., and Flannery, B. P. *Numerical Recipes in Fortran 77: The Art of Scientific Computing*. Cambridge University Press, 1992. 133

Quint, K. J. Vergleichende Studien unterschiedlicher Newton-Verfahren in der Methode der finiten Elemente nichtlinearer Kontinua. Studienarbeit, 2004. 179, 192

Quint, K. J. and Hartmann, S. The multiple intermediate configuration approach and its influence on DIRK/MLNA finite element procedures. *PAMM*, 7(1):4060005–4060006, 2007. 164

Quint, K. J. and Hartmann, S. Time-adaptive analysis of thermo-mechanically coupled plasticity. In Schrefler, B., Onate, E., and Papadrakakis, M., editors, *Int. Conf. on Computational Methods for Coupled Problems in Science and Engineering*. 2009. 10

Quint, K. J., Hartmann, S., Rothe, S., Saba, N., and Steinhoff, K. Experimental validation of high-order time integration for non-linear heat transfer problems. *Computational Mechanics*, 48(1):81–96, 2011.

Rabbat, N. B. G., Sangiovanni-Vincentelli, A. L., and Hsieh, H. Y. A multilevel Newton algorithm with macromodeling and latency for the analysis of large-scale nonlinear circuits in the time domain. *IEEE Transactions on Circuits and Systems*, 26(9):733–740, 1979. 8, 129

Rank, E., Katz, C., and Werner, H. On the importance of the discrete maximum principle in transient analysis using finite element methods. *International Journal for Numerical Methods in Engineering*, 19(12):1771–1782, 1983. 5, 188

Raßbach, S. and Lehnert, W. Investigations of deformation of FGM. *Computational Materials Science*, 19(1–4):298–303, 2000. 1

Reddy, J. N. *An Introduction to Nonlinear Finite Element Analysis*. 2004. 136

Reddy, J. N. and Gartling, D. K. *The Finite Element Method in Heat Transfer and Fluid Dynamics*. CRC Press, Boca Raton, FL, 2000. 5

Rieger, A. *Adaptive Algorithmen für thermomechanisch gekoppelte Kontaktprobleme*. Ph.D. thesis, Institut für Baumechanik und Numerische Mechanik, Universität Hannover, 2002. 9

Rieger, A. and Wriggers, P. Adaptive methods for thermomechanical coupled contact problems. *International Journal for Numerical Methods in Engineering*, 59(6):871–894, 2004. 81, 186

Rincon, M. A., Límaco, J., and Liu, I.-S. Existence and uniqueness of solutions of a nonlinear heat equation. *TEMA Tend. Mat. Apl. Comput.*, 6(2):273–284, 2005. 84

Rincon, M. A., Límaco, J., and Liu, I.-S. A nonlinear heat equation with temperature-dependent parameters. *Mathematical Physics Electronic Journal*, 12, 2006. 84

Roos, H.-G., Stynes, M., and Tobiska, L. *Robust Numerical Methods for Singularly Pertubed Differential Equations*. Springer, Berlin, 2008. 95

Rösler, J., Harders, H., and Bäker, M. *Mechanisches Verhalten der Werkstoffe*. Vieweg+Teubner, 3. edition, 2008. 60, 61, 72, 74

Rothe, S. *Zeitadaptive Finite-Elemente-Berechnung von thermischen Prozessen zur Herstellung funktional gradierter Strukturen*. Master's thesis, University of Kassel, 2010. 15, 111, 186

Ryabkov, N., Jackel, F., van Putten, K., and Hirt, G. Production of blanks with thickness transitions in longitudinal and lateral direction through 3d-strip profile rolling. *International Journal of Material Forming*, 1:391–394, 2008. 1

Saad, Y. ILUT: a dual threshold incomplete *LU* factorization. *Numer. Linear Algebra Appl.*, 1(4):387–402, 1994a. 168

Saad, Y. SPARSKIT: A basic tool-kit for sparse matrix computations. Technical report, University of Minnesota, Department of Computer Science and Engineering, 1994b. 153

Saad, Y. *Iterative Methods for Sparse Linear Systems*. SIAM Society for Industrial and Applied Mathematics, Philadelphia, 2nd edition, 2003. 12, 148, 154

Saad, Y. and Schultz, M. H. GMRES: A generalized minimal residual algorithm for solving nonsymmetric linear systems. *SIAM Journal on Scientific and Statistical Computing*, 7:856–869, 1986. 12, 152

Sadd, M. H. *Elasticity: Theory, Applications, and Numerics*. Elsevier Butterworth-Heinemann, Burlington, MA, 2005. 84

Saint-Georges, P., Warzee, G., Beauwens, R., and Notay, Y. High-performance PCG solvers for FEM structural analysis. *International Journal for Numerical Methods in Engineering*, 39:1313–1340, 1996. 13

Sandwell, D. T. Biharmonic spline interpolation of GEOS-3 and SEASAT altimeter data. *Geophysical Research Letters*, 14, 2:139–142, 1987. 159

Sanz-Serna, J. M., Verwer, J. G., and Hundsdorfer, W. H. Convergence and order reduction of Runge-Kutta schemes applied to evolutionary problems in partial differential equations. *Numerische Mathematik*, 40(4):405–148, 1986. 116

Saunders, N., Guo, Z., Li, X., Miodownik, A. P., and Schillé, J. P. Using JMatPro to model materials properties and behavior. *JOM*, pages 60–65, 2003. 73

Schäfer, M. *Computational Engineering : Introduction to Numerical Methods*. Springer, Berlin, 2006. 4, 92

Schenk, O. and Gärtner, K. Solving unsymmetric sparse systems of linear equations with pardiso. *Future Generation Computer Systems*, 20(3):475–487, 2004. 150

Schenk, O. and Gärtner, K. On fast factorization pivoting methods for sparse symmetric indefinite systems. *Electronic Transactions on Numerical Analysi*, 23:158–179, 2006. 151

Schenk, O., Gärtner, K., and Fichtner, W. Efficient sparse LU factorization with left-right looking strategy on shared memory multiprocessors. *BIT*, 40(1):158–176, 1999. 12, 150

Schiesser, W. E. *The Numerical Method of Lines: Integration of Partial Differential Equations*. Academic Press Inc, San Diego, CA, 1991. 91

Schiesser, W. E. and Griffiths, G. W. *A Compendium of Partial Differential Equation Models: Method of Lines Analysis with Matlab*. Cambridge University Press, New York, NY, 2009. 92

Schlichting, H. and Gersten, K. *Grenzschicht-Theorie*. Springer, Berlin, 2006. 161

Schrefler, B. A. *Encyclopedia of Computational Mechanics: Multifield Problems*, volume 2, chapter 17, pages 575–603. John Wiley & Sons, Chichester, 2004. 8

Schwarz, H. R. and Köckler, N. *Numerische Mathematik*. Teubner, Stuttgart, 2004. 102, 106

Simo, J. C. *Handbook of Numerical Analysis: The Coupled Thermomechanical Problem*, volume 6, chapter 5, pages 433–499. Elsevier Science & Technology, 1998. 10, 14, 15

Simo, J. C. and Hughes, T. J. R. *Computational Inelasticity*. Springer, Berlin, 2000. 64, 87, 94, 129, 140

Simo, J. C. and Miehe, C. Associative coupled thermoplasticity at finite strains: Formulation, numerical analysis and implementation. *Computer Methods in Applied Mechanics and Engineering*, 98:41–104, 1992. 7, 10, 11, 13

Simo, J. C. and Taylor, R. L. Consistent tangent operators for rate-independent elastoplasticity. *Computer Methods in Applied Mechanics and Engineering*, 48(1):101–118, 1985. 129

Simo, J. C., Taylor, R. L., and Pister, K. S. Variational and projection methods for the volume constraint in finite deformation elasto-plasticity. *Computer Methods in Applied Mechanics and Engineering*, 51:177–208, 1985. 7

Simo, J. C., Taylor, R. L., and Wriggers, P. A note on finite-element implementation of pressure boundary loading. *Communications in Applied Numerical Methods*, 7(7):513–525, 1991. 82

Simsir, C. and Gür, C. H. A mathematical framework for the simulation of thermal processing of materials: application to steel quenching. *Turkish J. Eng. Env. Sci.*, 32:85–100, 2008. 12

Snydera, M. D. and Bathe, K.-J. A solution procedure for thermo-elastic-plastic and creep problems. *Nuclear Engineering and Design*, 64(1):49–80, 1981. 9

Söderlind, G. Automatic control and adaptive time-stepping. *Numerical Algorithms*, 31(1–4):281–310, 2002. 127

Sommerville, I. *Software Engineering*. Pearson Studium, München, 2007. 15

Srikanth, A. and Zabaras, N. A computational model for the finite element analysis of thermoplasticity coupled with ductile damage at finite strains. *International Journal for Numerical Methods in Engineering*, 45(11):1569–1605, 1999. 11

Steinhoff, K., Maier, K.-J., and Svendsen, B., editors. *Functionally Graded Materials in Industrial Mass Production*. Verlag Wissenschaftliche Scripten, Auerbach, 2009. 2

Steinhoff, K., Weidig, U., Scholtes, B., and Zinn, W. Innovative flexible metal forming processes based on hybrid thermo-mechanical interaction. *Steel Research Internationa*, 76(2/3):154–159, 2005. 2

Stephan, P., Schaber, K., Stephan, K., and Mayinger, F. *Thermodynamik: 1 Einstoffsysteme*. Springer-Verlag, Berlin, 2009. 25, 49

Strang, G. and Fix, G. J. *An Analysis of the Finite Element Method*. Prentice Hall, New Jersey, 1973. 87, 94, 95, 96, 97, 106

Strehmel, K. and Weiner, R. *Numerik gewöhnlicher Differentialgleichungen*. Teubner, Stuttgart, 1995. 99, 109, 110, 111, 113, 114, 116, 123

Stricklin, J. A., Haisler, W. E., and von Riesemann, W. A. Evaluation of solution procedures for material and for geometrically nonlinear structural analysis. *American Institute of Aeronautics and Astronautics*, 11:292–299, 1973. 145

Stroud, A. H. Some fifth degree integration formulas for symmetric regions II. *Numerische Mathematik*, 9(5):460–468, 1967. 187

Stüben, K. Algebraic multigrid (AMG): An introduction with applications. Technical Report 70, GMD – Forschungszentrum Informationstechnik GmbH, Sankt Augustin, 1999. 149

Sumathi, S. and Surekha, P. *LabVIEW based Advanced Instrumentation Systems*. Springer, Berlin, 2007. 156

Surm, H., Kessler, O., Hoffmann, F., and Zoch, H.-W. Modelling of austenitizing with non-constant heating rate in hypereutectoid steels. *International Journal of Microstructure and Materials Properties*, 3:35–48, 2008. 12

Surm, H., Kessler, O., Hunkel, M., Hoffmann, F., and Mayr, P. Modelling the ferrite/carbide $\rightarrow$ austenite transformation of hypoeutectoid and hypereutectoid steels. *Journal de Physique IV*, 120:111–119, 2004. 12

Svendsen, B., Arndt, S., Klingbeil, D., and Sievert, R. Hyperelastic models for elasto-plasticity with non-linear isotropic and kinematic hardening at large deformation. *International Journal of Solids and Structures*, 35(25):3363–3389, 1998. 7

Szabó, B. and Babuška, I. *Finite Element Analysis*. John Wiley & Sons, New York, 1991. 4, 105

Szabó, I. *Geschichte der mechanischen Prinzipien und ihrer wichtigsten Anwendungen*. Birkhäuser Verlag, Basel, 1996. 40, 46

Taylor, G. I. and Quinney, H. The latent energy remaining in a metal after cold working. *Proceedings of the Royal Society of London*, 143(849):307–326, 1934. 11, 59

Taylor, J. R. *An Introduction to Error Analysis*. University Science Books, Sausalito, CA, 1997. 157

Thomas, H. R. and Zhou, Z. Minimum time-step size for diffusion problem in FEM analysis. *International Journal for Numerical Methods in Engineering*, 40(20):3865–3880, 1997. 5

Truesdell, C. A. The computer: Ruin of science and threat to mankind. In *An Idiot's Fugitive Essays on Science*, pages 594–631. Springer, Berlin, 1984. 3

Truesdell, C. A. *A First Course in Rational Continuum Mechanics*. Academic Press Inc, San Diego, CA, 2nd edition, 1991. 44

Truesdell, C. A. and Noll, W. *The Non-Linear Field Theories of Mechanics*. Springer, Berlin, 2004. 58

Tsakmakis, C. Methoden zur Darstellung inelastischen Materialverhaltens bei kleinen Deformationen. Habilitationsschrift, 1994. 21

Tsakmakis, C. Kinematic hardening rules in finite plasticity. Part I: A constitutive approach. *Continuum Mechanics and Thermodynamics*, 8:215–231, 1996. 7

Tsakmakis, C. Energiehaushalt des elastisch-plastischen Körpers, 1998. Presented in the symposium: Aspekte der Kontinuumsmechanik und Materialtheorie, Kassel. 62

Tsakmakis, C. and Willuweit, A. Use of the elastic predictor-plastic corrector method for integrating finite deformation plasticity laws. In Hutter, K. and Baaser, H., editors, *Deformation and Failure of Metallic Materials*, pages 79–106. Springer, Berlin, 2003. 7

Tsakmakis, C. and Willuweit, A. A comparative study of kinematic hardening rules at finite deformations. *International Journal of Non-Linear Mechanics*, 39:539–554, 2004. 7, 60, 195

Tušek, J., Kampuš, Z., and Suan, M. Welding of tailored blanks of different materials. *Journal of Materials Processing Technology*, 119(1–3):180–184, 2001. 1

Überhuber, W. *Numerical Computation 2: Methods, Software, and Analysis*. Springer, Berlin, 1997. 106, 150

van den Boogaard, A., Meinders, T., and Huétink, J. Efficient implicit finite element analysis of sheet forming processes. *International Journal for Numerical Methods in Engineering*, pages 1083–1107, 2003. 13

van der Vorst, H. A. BI-CGSTAB: A fast and smoothly converging variant of BI-CG for the solution of nonsymmetric linear systems. *SIAM Journal on Scientific and Statistical Computing*, 13:631–644, 1992. 12, 152

Verwer, J. G. Convergence and order reduction of diagonally implicit Runge-Kutta schemes in the method of lines. In Griffiths, D. F. and Watson, G. A., editors, *Numerical Analysis*, number 140 in Pitman Research Notes in Mathematics, pages 220–237. Longman Scientific and Technical, Essex, 1986. 116

Videla, L., Baloa, T., Griffiths, D. V., and Cerrolaza, M. Exact integration of the stiffness matrix of an 8-node plane elastic finite element by symbolic computation. *Numerical Methods for Partial Differential Equations*, 24:249–261, 2007. 105

Visintin, A. Mathematical model of solid-solid phase transitions in steel. *IMA Journal of Applied Mathematics*, 39:143–157, 1987. 12

Vladimirov, I. N., Pietryga, M. P., and Reese, S. On the modelling of non-linear kinematic hardening at finite strains with application to springback - comparison of time integration algorithms. *International Journal for Numerical Methods in Engineering*, 74, 2007. 7

Watson, E. S. and O'Neil, M. J. Differential microcalorimeter. 1966. 25

Watson, L. T., Billups, S. C., and Morgan, A. P. Algorithm 652: HOMPACK: A suite of codes for globally convergent homotopy algorithms. *ACM Transactions on Mathematical Software*, 13:281–310, 1987. 129

Weber, G. and Anand, L. Finite deformation constitutive equations and a time integration procedure for isotropic, hyperelastic-viscoplastic solids. *Computer Methods in Applied Mechanics and Engineering*, 79:173–202, 1990. 7

Weidig, U., Hübner, K., and Steinhoff, K. Bulk steel products with functionally graded properties produced by differential thermo-mechanical processing. *Steel Research International*, 79(1):59–65, 2008. 2, 156

Weidig, U., Saba, N., and Steinhoff, K. Functional gradation by differential thermo-mechanical treatment. *International Journal of Microstructure and Materials Properties*, 4(5/6):649–663, 2009. 2

Wever, F., Rose, A., Peter, W., Strassburg, W., and Rademacher, L. *Atlas zur Wärmebehandlung der Stähle, Band 1*. Verlag Stahleisen M. B. H., Düsseldorf, 1961. 17

Wieners, C., Ammann, M., Diebels, S., and Ehlers, W. Parallel 3-d simulations for porous media models in solid mechanics. *Computational Mechanics*, 29:75–87, 2002. 13

Wieners, C., Ammann, M., Graf, T., and Ehlers, W. Parallel Krylov methods and the application to 3-d simulations of a triphasic porous media model in soil mechanics. *Computational Mechanics*, 36:409–420, 2005. 13

Wittekindt, J. *Die numerische Lösung von Anfangs-Randwertproblemen zur Beschreibung inelastischen Werkstoffverhaltens*. Ph.D. thesis, Technische Hochschule Darmstadt, 1991. 94, 96, 109

Wolff, M., Böhm, M., and Helm, D. Material behavior of steel - modeling of complex phenomena and thermodynamic consistency. *International Journal of Plasticity*, 24(5):746–774, 2008. 12, 14, 186

Wriggers, P. *Nonlinear Finite Element Methods*. Springer, Berlin, 2009. 13, 82, 93, 94, 101, 106, 132, 133, 135, 144, 145, 185, 189

Xing, H. L. and Makinouchi, A. FE modeling of thermo-elasto-plastic finite deformation and its application in sheet warm forming. *Engineering Computations*, 19(4):392–410, 2002. 9

Yang, C. and Gu, Y. Minimum time-step criteria for the Galerkin finite element methods applied to one-dimensional parabolic partial differential equations. *Numerical Methods for Partial Differential Equations*, 22(2):259–273, 2005. 5

Zeidler, E. *Nonlinear Functional Analysis and its Applications III: Variational Methods and Optimization*. Springer, Berlin, 1985. 87

Zienkiewicz, O. C. Origins, milestones and directions of the finite element method – a personal view. *Archives of Computational Methods in Engineering*, 2(1):1–48, 1995. 101

Zienkiewicz, O. C. and Taylor, R. L. *The Finite Element Method: The Basis*, volume 1. Butterworth-Heinemann, 5 edition, 2000. 136

Zienkiewicz, O. C. and Taylor, R. L. *The Finite Element Method: Its Basis and Fundamentals*. Butterworth-Heinemann, Burlington, MA, 6 edition, 2005. 5, 106, 108

Zienkiewicz, O. C., Taylor, R. L., and Zhu, J. Z. *The Finite Element Method for Solid and Structural Mechanics*. Butterworth-Heinemann, Burlington, MA, 6 edition, 2005. 86, 133